5-2019

Understanding and modeling the formation of syngas contaminants during biomass gasification

Oluwafemi Ademola Oyedeji
University of Tennessee, ooyedeji@vols.utk.edu

To the Graduate Council:

I am submitting herewith a dissertation written by Oluwafemi Ademola Oyedeji entitled "Understanding and modeling the formation of syngas contaminants during biomass gasification." I have examined the final electronic copy of this dissertation for form and content and recommend that it be accepted in partial fulfillment of the requirements for the degree of Doctor of Philosophy, with a major in Biosystems Engineering.

Nourredine Abdoulmoumine, Major Professor

We have read this dissertation and recommend its acceptance:

Nicole Labbe, Stuart Daw, Paul Ayers

Accepted for the Council:

Dixie L. Thompson

Vice Provost and Dean of the Graduate School

(Original signatures are on file with official student records.)

Understanding and modeling the formation of syngas contaminants during biomass gasification

A Dissertation Presented for the
Doctor of Philosophy
Degree
The University of Tennessee, Knoxville

Oluwafemi Ademola Oyedeji
May 2019

ACKNOWLEDGEMENTS

I would like to appreciate my Ph.D. advisor and mentor, Dr. Nourredine Abdoulmoumine, for giving me the invaluable opportunity to work on this dissertation and his unwavering support through it. I am also extremely grateful to my Ph.D. committee members--Drs. Stuart Daw, Nikki Labbé, and Paul Ayers--for their erudite advice and expertise, without which this dissertation would not have been possible.

My greatest appreciation goes to my dearest wife. Oluwafemifola, I could not have asked for a better source of inspiration. Thank you for believing in me. To my amazing dad, mum, and siblings, “ẹ̀ sé púpó” for encouraging me throughout this work. I would not have finish well without your consistent love, support, and motivation.

I would like to express my profound gratitude to the entire faculty, staff, and students of the Department of Biosystems Engineering and Soil Science at the University of Tennessee. Likewise, my research group members--Ross Houston, Qiaoming Liu, Ekramul Ehite, and Skye Lee--for helping me hone my research and communication skills.

I am extremely thankful to Mark and Janet, Ashley, Tesfaye, Marcia, Uche, and Da for being an integral part of my journey through the University of Tennessee. The years flew by fast because of you.

To God be the glory!

ABSTRACT

The focus of this dissertation was to understand and model how inorganic contaminants (mainly H_2S, COS, NH_3, and HCN) are formed during biomass gasification to provide information for effective contaminant abatement and producer gas remediation. This dissertation was partitioned into five research studies with specify objectives. In the first study, a simple thermo-gravimetric approach coupled with CHN analyzer and inductively coupled plasma optical emission spectrometry (ICP-OES) was used to track the conversion profile of C, H, N, S, and O during the pyrolysis stage of biomass gasification. The activation energy for the sulfur and nitrogen conversion was drastically lower at 800 °C compared to 600 and 700 °C. Additionally, the elemental concentrations of sulfur and nitrogen were higher for pyrolyzed biomass compared to fresh biomass. In the second study, a non-stoichiometric equilibrium model of biomass gasification was implemented. We demonstrated that the yields of CO, CO_2, and H_2 during gasification were equilibrium-controlled. However, the yields of CH_4 and contaminant species were kinetically-limited. Furthermore, we establish that $NH_3 + CO \leftrightarrow HCN + H_2O$ and $H_2S + CO_2 \leftrightarrow COS + H_2O$ reactions were important to nitrogen and sulfur species distribution, respectively. In the third, an inert fluidized bed system was simulated using computational fluid dynamics and discrete element method (CFD-DEM). Also, experimental validation of the developed model was performed on three important hydrodynamic variables of fluidized bed systems (pressure drop, minimum fluidization velocity, and bed height). The CFD-DEM model produced a realistic representation of the particle motion and reasonably predicted the hydrodynamics properties of the experimental system. The fourth and fifth studies were designed to simulate the formation of nitrogen (NH_3 and HCN) and sulfur (H_2S, COS, SO_2) contaminants, respectively, by coupling the developed CFD-DEM model in the third study with appropriate chemical reactions, heat transfer, and particle shrinkage models. We found that the proposed CFD-DEM model gave reasonably prediction for the selected contaminants species. Hence, the proposed model is a valuable tool for gaining insight into the formation and extent of producer gas contaminants.

TABLE OF CONTENTS

LIST OF TABLES

LIST OF FIGURES

CHAPTER I
INTRODUCTION

Gasification of lignocellulosic biomass to producer gas, *i.e.* carbon monoxide (CO), hydrogen (H_2), carbon dioxide (CO_2) and methane (CH_4), has gained increasing attention in recent decades. The two major constituents of producer gas, CO and H_2, are essential building blocks used to produce renewable fuels and chemicals via chemical synthesis routes, e.g. Fischer−Tropsch (FT) and methanol syntheses. As a result of their importance in industrial chemical processes, mixtures of these two constituents has historically been called synthesis gas or syngas. Besides fuels and chemicals, producer gas can be utilized to generate combined heat and power (CHP) using internal combustion (IC) engines and gas or steam turbines.[1]

Thus far, gasification has been investigated on a wide variety of lignocellulosic biomass feedstocks including agricultural residues and wastes, forest resources, and dedicated energy crops under various environments.[2-4] Based on these research activities, the foremost challenge associated with contemporary gasification technologies is the co-production of contaminants alongside producer gas.[2, 5-7] These contaminants include particulate matter, tars, sulfur compounds, nitrogen compounds, trace metals, and halides and their concentrations are affected by the type of gasifier type, gasification conditions, *i.e.* temperature, gasification agents etc., and feedstock properties.[8] The presence of contaminants reduces the value of producer gas and increases the cost associated with producing fuel, power, and chemicals in downstream applications.[5] Specifically, contaminants inhibit catalyst activity, cause corrosion and clogging of equipment, reduce downstream process efficiency, and generate gaseous species that are precursors to regulated pollutants.[9] As a consequence of their negative impacts, downstream applications have recommended tolerances for contaminants as illustrated in Table 1.1.

Producer gas contaminants

Particulate matter

Particulate matter contaminants are solid materials entrained as the producer gas exits the gasifier and vary from incompletely decomposed biomass particles to fragmented catalyst or inert bed materials, and inorganic compounds. Particulate matter leads to corrosion and erosion of equipment, as well as fouling.[15]

Tar

The definition of tars is still debated. Among several definitions that have been proposed, one which has gained traction in recent years defines tars as a group of condensable organic compounds, which have a molecular weight greater than benzene's.[16] Tar species are categorized using several approaches depending on their detectability by gas chromatography (GC) systems, solubility in water, condensation temperature, and cyclic rings into the following categories:

Table 1.1. Downstream applications and the contaminant tolerance.[10-14]

Contaminant	IC engines*	Gas turbine	MeOH synthesis	FT synthesis*
Tar	10-50 mg/m^3	< 5 mg/Nm^3	< 0.1 mg/m^3	< 1 ppmV
Sulfur		< 1 ppm	< 1 mg/m^3	< 1 ppmV
Nitrogen		< 50 µl/l	< 0.1 mg/m^3	< 1 ppmV
Halides		< 0.5 ppm	< 0.1 mg/m^3	< 10 ppbV
Metals		< 50 ppb		< 10 ppbV

*IC: Internal combustion, MeOH: Methanol, FT: Fischer-Tropsch.

- **Class I**. Tar compounds belonging to this class are not detectable by GC equipped with flame ionization detector (FID) or mass spectrometer (MS) using non-polar capillary column. Tar compounds of this class are often loosely called “GC-undetectable tars”.

- **Class II**. Tar components of this class are heterocyclic compounds characterized by a high-water solubility. Example of Class II tar components are phenol, pyridine, and cresol.

- **Class III**. Tar components of this class are one-ring aromatic compounds like xylene, styrene or toluene and light hydrocarbons, which do not pose significant condensation issues.

- **Class IV**. Tar components of this class are light polyaromatic (2-3 rings) hydrocarbons that condense at relatively high concentrations and intermediate temperatures.

- **Class V**. Tar components of this class are heavy polyaromatic (4-7 rings) hydrocarbons that condense at relatively high temperatures at low concentrations. Examples of compounds in this class are fluoranthene, pyrene, or coronene.

Tar is significant among all contaminants because it is the most abundant[17], condenses on surfaces resulting in fouling and clogging of pipes and filters[18] and results in catalyst deactivation due to coking in downstream operations.

Sulfur

Gaseous sulfur contaminants exist as hydrogen sulfide (H_2S), carbonyl sulfide (COS), and carbon disulfide (CS_2), with hydrogen sulfide being the most prominent. Sulfur contamination is usually affected by biomass type and pre-gasification processes.[19] The presence of sulfur compounds, even in small concentration, *i.e.* parts per million (ppm) to parts per billion (ppb) range, leads to severe catalyst poisoning, corrosion of equipment, and air pollution by contributing to the production oxides of sulfur (SO_x).

Nitrogen

Nitrogen containing contaminants are primarily ammonia (NH_3) and secondarily hydrogen cyanide (HCN) and nitrogen oxides (NO_x). These contaminants cause catalyst poisoning in addition to air pollution due to their tendencies to form nitrous oxides (NO_x) in downstream oxidative processes.[20]

Metal

Physiological biomass metals and post-harvest addition to feedstock play a negative role during gasification by leading to catalyst deactivation. In addition, biomass derived metals can form salts leading to ash fouling, high-temperature metal corrosion, and air pollution.[21] Furthermore, ash metals can agglomerate and lead to bed de-fluidization in fluidized bed gasifier.[22]

Statement of research problems and gaps

The presence of contaminants is a significant problem to the commercialization of biomass gasification because it drastically increases the economic risks associated with investing in biomass gasification projects.[5] Among the barriers to the commercialization of biomass gasification technologies, the presence of syngas contaminants and the higher cost associated with its cleanup, and environmental issues involved with the treatment and disposal of waste streams from syngas cleanup are considered major hurdles.[23-24] Three groups of strategies are applicable to overcoming the problem of syngas contaminants: primary, secondary, and tertiary strategies.[7, 25] The reduction or complete elimination of syngas contaminants by in-situ or ex-situ catalytic gasification approaches including thermal and catalytic processes is the emphasis of primary strategies.[25] Secondary strategies emphasize ex-situ removal of syngas contaminants to the tolerable concentrations,[26] whereas tertiary strategies focus on the design of downstream processes and systems that are contaminant tolerant**.** One major problem militating against the successful deployment of these strategies is the limited understanding of the fundamentals of biomass syngas contaminants formation. The challenge is further compounded by

the anisotropic nature of biomass that affects the concentration of contaminant precursors.

Experimental studies to provide insight into the formation of syngas contaminants are expensive and laborious.[27] Additionally, most experimental studies on biomass gasification focus on the yield of the major gas products of biomass gasification, resulting in paucity in literature regarding the yield of syngas contaminants.[28] The few available literature on the yield of syngas contaminant during gasification of biomass lacks an in-depth analysis of the interaction between the hydrodynamics and transport phenomena.[29-31] The consequence of these issues is that there are no tools available for accurate and fast prediction of syngas contaminant yield during gasification. The implication of this is that scientist and engineers are not equipped with analytical tools to adequately inform the selection of process variables during gasification and prepare for syngas remediation step after gasification.

Statement of research objectives

The goal of this study is to investigate the fundamentals of the formation producer gas contaminants and develop modeling tools that connect lignocellulosic biomass properties with concentration of contaminants. Hence, this study focuses on the following specific objectives:

Objective 1. Investigate the kinetics of switchgrass pyrolysis leading to the release of contaminant precursors.

Rationale: Pyrolysis is the commencing chemical reaction during gasification and make up a significant part of gasification mechanistic framework. Therefore, kinetic information on the release of elemental precursors of syngas contaminant during pyrolysis is crucial to understanding how syngas contaminants are formed. This objective provides information to estimate the rate of release of elemental precursors of syngas contaminant during pyrolysis.

Hypothesis: We hypothesize that the rate and extent of release of elemental precursors of syngas contaminant during pyrolysis is different for each elemental precursor of syngas contaminant.

Goal: The goal of this objective is to track the release profile of selected elemental precursors of syngas contaminant during pyrolysis and thereafter use the resulting data to obtain kinetic parameters.

Objective 2. Non-stoichiometric equilibrium modeling of syngas contaminant formation during biomass gasification.

Rationale: All reactions approach chemical equilibrium. Therefore, determining the equilibrium position of biomass gasification is the logical first step in understanding

the formation of syngas contaminants during gasification. Identifying the equilibrium position of biomass gasification as affected by operating variables and feedstock properties provides necessary information for understanding the fundamental trends associated with the formation of syngas contaminant during biomass gasification.

Hypothesis: We hypothesize that the formation of syngas primary constituents (CO, H_2, CO_2) are thermodynamically controlled while that of contaminants (NH_3, H_2S, HCN, COS) are kinetically controlled.

Goal: Develop a non-stoichiometric equilibrium model for predicting syngas contaminant formation by minimizing the Gibbs's free energy of the overall gasification reaction. Then compare predicted concentrations of syngas contaminants to corresponding experimental data.

Objective 3. CFD-DEM simulation and validation of the hydrodynamics behavior of an inert fluidized bed system.

Rationale: Experimental validation of the developed CFD-DEM model is crucial to ensure its accuracy. The approach in this objective is to validate the hydrodynamics properties (bed height, minimum fluidization velocity, and pressure drop) through experiments data because these properties are critical to biomass gasification performance.

Hypothesis: We hypothesize that the simulation data from CFD-DEM modeling of an inert fluidized bed system statistically comparable to corresponding experimental data collected in well-controlled environments.

Goal: The aim of this objective is to validate our simulation experimentally to assess the accuracy of predictions. Experimental data on the hydrodynamics behavior of fluidized bed will be compared to simulation results, using appropriate qualitative and statistical methods

Objective 4. Develop a computational fluid dynamics and discrete element model to simulate the formation of nitrogen-containing contaminants during biomass gasification.

Rationale: Biomass gasification is a complex multiscale process and its accurate simulation therefore requires a careful implementation of a network of small-scale process model involving chemical and physical transformation of biomass particles coupled with the detailed hydrodynamic behavior inside the reactor. Computational fluid dynamics and discrete element (CFD-DEM) modeling was selected as an approach because it allows us to capture the complex physics in fluidized bed systems while also incorporating chemistry for primary syngas constituents as well as nitrogen contaminants. Our attention was focused in particular on the formation

of NH_3 and HCN because they are two most prominent and notorious nitrogen-containing contaminants during gasification.

Hypothesis: We hypothesize that incorporating a mechanistic chemical kinetics information for nitrogen-containing contaminants (NH_3 and HCN) into the CFD-DEM model will improve the accuracy of concentration predictions when compared to the equilibrium modeling predictions.

Goal: The aim of this objective is to develop a reactor-level computational model for a fluidized bed gasifier that accounts for syngas primary constituents and contaminant formation. The model will take the physiochemical properties of switchgrass and gasification conditions as input parameters and will be able to estimate the concentration of primary producer gas constituents (CO, H_2, CO_2, CH_4) and the major nitrogen-containing contaminant species (NH_3 and HCN) at the gasifier outlet as well as their distribution in the reactor.

Objective 5. Develop a computational fluid dynamics and discrete element model to simulate the formation of sulfur-containing contaminants during biomass gasification.

Rationale: The prediction of the concentration of sulfur-containing contaminants in syngas during gasification is important to designing appropriate downstream remediation systems and avoid the technical challenges associated with sulfur contaminants. As in the previous objective, computational fluid dynamics and discrete element (CFD-DEM) modeling was selected as an approach because it allows us to capture the complexity of our reacting system with a high fidelity. This objective mainly focused on modeling the formation of H_2S and COS because they are the two most important sulfur-containing contaminants during gasification.

Hypothesis: We hypothesize that incorporating the mechanistic chemical kinetics information for H_2S and COS into the CFD-DEM model will improve the accuracy of concentration predictions when compared to the equilibrium modeling prediction.

Goal: The aim of this objective is to develop a reactor-level computational model for a fluidized bed gasifier that accounts for primary constituents and contaminant formation. The model will take the physiochemical properties of switchgrass and gasification conditions as input parameters and is able to estimate the concentration of major sulfur-containing contaminant species (H_2S, COS, and SO_2) at the gasifier outlet as well as their distribution in the reactor.

Organization of the dissertation

The notation adopted in this dissertation distinguished between mathematical equations and chemical reactions. The caption for mathematical equations is included in parentheses, e.g. (1.1), whereas that of chemical reactions are included

in brackets, e.g. [1.1]. Both mathematical equations and chemical reactions are prefixed with the chapter number, a dot and the equation or reaction number in descending order of appearance in the chapter. An illustration of this notation is shown below for the law of conservation of mass by Equation (1.1) (in-text citation) and the oxidation reaction of carbon and oxygen to carbon dioxide Reaction [1.1] (in-text citation):

$$\sum m^{in} = \sum m^{out} \tag{1.1}$$

$$C + O_2 \rightarrow CO_2 \tag{1.1}$$

The American Society of Chemistry (ACS) style guide was used in the text as well for the bibliographies. Organizationally, this dissertation is divided into seven chapters. Chapter 1 presents a succinct summary of the dissertation project, its objectives, rationale, and hypotheses. In Chapter 2, a comprehensive literature review is presented on gasification, in general, and, gasification modeling, in particular. Chapter 3 encapsulates Objective 1 and discusses the investigation of the devolatilization of contaminant precursors and its resulting kinetic study. Chapter 4 encapsulates Objective 2, summarizing the approach used for non-stoichiometric equilibrium modeling of the formation of syngas contaminants. Chapter 5 encapsulates Objective 3 and summarizes the simulation of an inert fluidized bed system using computational fluid dynamics and discrete element method (CFD-DEM). Chapter 6 and 7 encapsulates Objectives 4 and 5. They outline our CFD modeling approach and findings on the formation of nitrogen and sulfur contaminants. Finally, Chapter 8 presents the overall conclusions of the doctoral project and future recommendations for improvements or expansion of our studies.

References

1. Basu, P., *Combustion and Gasification in Fluidized Beds*. 1st ed.; Taylor & Francis Group, LLC: Florida, USA, 2006.
2. Abdoulmoumine, N.; Adhikari, S.; Kulkarni, A.; Chattanathan, S., A review on biomass gasification syngas cleanup. *Appl Energ* **2015,** *155* (1), 294-307.
3. Karlström, O.; Costa, M.; Brink, A.; Hupa, M., CO2 gasification rates of char particles from torrefied pine shell, olive stones and straw. *Fuel* **2015,** *158* (1), 753-763.
4. Zhai, M.; Zhang, Y.; Dong, P.; Liu, P., Characteristics of rice husk char gasification with steam. *Fuel* **2015,** *158* (1), 42-49.
5. Heyne, S.; Liliedahl, T.; Marklund, M. *Biomass gasification - a synthesis of technical barriers and current research issues for deployment at large scale*; The Swedish Knowledge Centre for Renewable Transportation Fuels: Göteborg, Sweden, 2013, 2013.
6. Torres, W.; Pansare, S. S.; Goodwin, J. G., Hot Gas Removal of Tars, Ammonia, and Hydrogen Sulfide from Biomass Gasification Gas. *Catalysis Reviews* **2007,** *49* (4), 407-456.
7. Woolcock, P. J.; Brown, R. C., A review of cleaning technologies for biomass-derived syngas. *Biomass and Bioenergy* **2013,** *52* (1), 54-84.
8. Kumar, A.; Jones, D. D.; Hanna, M. A., Thermochemical Biomass Gasification: A Review of the Current Status of the Technology. *Energies* **2009,** *2* (3), 556-581.
9. Sharma, S. D.; Dolan, M.; Ilyushechkin, A.; McLennan, K.; Nguyen, T.; Chase, D., Recent developments in dry hot syngas cleaning processes. *Fuel* **2010,** *89* (4), 817-826.
10. Boerrigter, H.; Den Uil, H.; Calis, H.-P., Green diesel from biomass via Fischer-Tropsch synthesis: new insights in gas cleaning and process design. Citeseer: 2003; pp 371-383.
11. Baker, E.; Brown, M.; Moore, R.; Mudge, L.; Elliott, D. *Engineering analysis of biomass gasifier product gas cleaning technology*; Pacific Northwest Lab., Richland, WA (USA): 1986.
12. Milne, T. A.; Abatzoglou, N.; Evans, R. J., *Biomass Gasifier "Tars": Their Nature, Formation, and Conversion*. National Renewable Energy Laboratory Golden, CO: 1998; Vol. 570.
13. Bridgwater, A., The technical and economic feasibility of biomass gasification for power generation. *Fuel* **1995,** *74* (5), 631-653.
14. Asadullah, M., Biomass gasification gas cleaning for downstream applications: A comparative critical review. *Renewable and Sustainable Energy Reviews* **2014,** *40*, 118-132.
15. Stahlberg, P.; Lappi, M.; Kurkela, E.; Simell, P.; Oesch, P.; Nieminen, M. *Sampling of contaminants from product gases of biomass gasifier*; VTT Research Notes 1903; VTT Technical Research Centre of Finland: Espoo, Finland, 1998, 1998.

16. Ma, Z.; Chen, D.; Gu, J.; Bao, B.; Zhang, Q., Determination of pyrolysis characteristics and kinetics of palm kernel shell using TGA–FTIR and model-free integral methods. *Energy Conversion and Management* **2015,** *89*, 251-259.
17. Asadullah, M., Biomass gasification gas cleaning for downstream applications: A comparative critical review. *Renewable and Sustainable Energy Reviews* **2014,** *40* (1), 118-132.
18. Li, C.; Suzuki, K., Tar property, analysis, reforming mechanism and model for biomass gasification—An overview. *Renewable and Sustainable Energy Reviews* **2009,** *13* (3), 594-604.
19. Gupta, R. P.; Turk, B. S.; Portzer, J. W.; Cicero, D. C., Desulfurization of syngas in a transport reactor. *Environmental Progress* **2004,** *20* (3), 187-195.
20. Molina, A.; Eddings, E.; Pershing, D.; Sarofim, A., Char nitrogen conversion: implications to emissions from coal-fired utility boilers. *Progress in Energy and Combustion Science* **2000,** *26* (4), 507-531.
21. Dayton, D. C.; French, R. J.; Milne, T. A., Direct Observation of Alkali Vapor Release during Biomass Combustion and Gasification. 1. Application of Molecular Beam/Mass Spectrometry to Switchgrass Combustion. *Energy and Fuels* **1995,** *9* (5), 855-865.
22. Göransson, K.; Söderlind, U.; He, J.; Zhang, W., Review of syngas production via biomass DFBGs. *Renewable and Sustainable Energy Reviews* **2011,** *15* (1), 482-492.
23. Werle, S.; Dudziak, M., Influence of wastewater treatment and the method of sludge disposal on the gasification process. *Ecological Chemistry and Engineering S* **2014,** *21* (2), 255-268.
24. Swanson, R. M.; Platon, A.; Satrio, J. A.; Brown, R. C., Techno-economic analysis of biomass-to-liquids production based on gasification. *Fuel* **2010,** *89* (1), S11-S19.
25. Bhaduri, S.; Contino, F.; Jeanmart, H.; Breuer, E., The effects of biomass syngas composition, moisture, tar loading and operating conditions on the combustion of a tar-tolerant HCCI (Homogeneous Charge Compression Ignition) engine. *Energy* **2015,** *87* (1), 289-302.
26. Bhandari, P. N.; Kumar, A.; Huhnke, R. L. In *Review of Syngas Contaminants removal using Carbon-based Catalysts*, 2012 Dallas, Texas, July 29-August 1, 2012, American Society of Agricultural and Biological Engineers: 2012; p 1.
27. Pepiot, P.; Dibble, C. J.; Foust, T. D., Computational fluid dynamics modeling of biomass gasification and pyrolysis. In *Computational Modeling in Lignocellulosic Biofuel Production*, 1st ed.; American Chemical Society: 2010; Vol. 1052, pp 273-298.
28. Broer, K. M.; Woolcock, P. J.; Johnston, P. A.; Brown, R. C., Steam/oxygen gasification system for the production of clean syngas from switchgrass. *Fuel* **2015,** *140*, 282-292.
29. Abdoulmoumine, N.; Kulkarni, A.; Adhikari, S., Effects of Temperature and Equivalence Ratio on Pine Syngas Primary Gases and Contaminants in a Bench-Scale Fluidized Bed Gasifier. *Ind. Eng. Chem. Res.* **2014,** *53* (14), 5767-5777.

30. Aljbour, S. H.; Kawamoto, K., Bench-scale gasification of cedar wood – Part II: Effect of Operational conditions on contaminant release. *Chemosphere* **2013,** *90* (4), 1501-1507.
31. Kulkarni, A.; Baker, R.; Abdoulmomine, N.; Adhikari, S.; Bhavnani, S., Experimental study of torrefied pine as a gasification fuel using a bubbling fluidized bed gasifier. *Renewable Energy* **2016,** *93*, 460-468.

CHAPTER II
LITERATURE REVIEW

Introduction

Fossil-based fuels (petroleum, coal, and natural gas) are the main energy source in the United States, accounting for at least 70% of the total annual energy consumption.[1] The utilization of fossil-based fuels for energy generation has however raised serious concerns over the past few decades, such as global warming, pollution, energy cost volatility, and non-renewability.[2] Carbon dioxide (CO_2), the primary driver of climate change among greenhouse gases, is released into the atmosphere when fossil-based fuels are combusted to generate electricity or heat.[3] Similarly, air pollutants and acid rain precursors, such as sulfur dioxide and nitrogen oxides, are also released, especially in the case of coal.[3] Thus, it is imperative to adopt viable, clean, and renewable energy sources to alleviate the concerns surrounding the use of fossil-based fuels.

Biomass is one of the most important renewable energy sources. It made up approximately half of the total renewable energy production in the United States in 2017.[1] In addition, biomass is the only renewable source of liquid transportation fuels. Several thermochemical processes (combustion, gasification, and pyrolysis) have been used to extract fuel and energy from biomass.[4] The prospects of biomass gasification are encouraging because it allows for the production of primarily synthesis gas or syngas, i.e. CO and H_2, which can be subsequently used as reactants in the production of liquid transportation fuels as well as valuable chemicals.[5] Biomass gasification can be described as the intermediate process between complete combustion and pyrolysis of biological materials. It involves the chemical depolymerization of biomass feedstock in the presence of a limited oxidizing agent at elevated temperatures, typically higher than 600 °C, inside a reactor known as a gasifier.[6]

In the last two decades, biomass gasification has significantly evolved on many fronts. Biomass gasification studies have explored and reported several gasification technologies, mathematical models, reaction mechanisms, and operation optimization schemes. During this period, few literature review papers have summarized these advances in biomass gasification. Patra et al.[7] and Baruah[8] presented an extensive discussion of biomass gasification models. Abdoulmoumine et al.[9] and Woolcock et al.[10] provided detailed reviews of syngas cleanup processes. Other review papers have analyzed tar evolution and other major advances in biomass gasification technologies.[11-13] However, the scope of these reviews did not synthesize the growing body of work on *i)* biomass gasification reaction mechanisms; *ii)* detail kinetic rate equations and parameters, which are increasingly used for gasification modeling and simulation; and *iii)* the lessons learned over the years. The present literature review presents a holistic review of the state-of-the-art of biomass gasification chemistry, kinetics, and modeling to address the aforementioned limitations. Furthermore, this chapter ties together the various advancements, critical challenges, and contemporary opportunities in biomass

gasification in the section titled Biomass gasification: Challenges and future perspectives.

Overview of lignocellulosic biomass thermochemical conversion processes

Pyrolysis

In the context of this work, pyrolysis is the thermal decomposition of lignocellulosic biomass in the absence of oxygen at temperatures below 650 °C. Lignocellulosic biomass pyrolytic processes produce three main products: a liquid product known as bio-oil, a solid residue of biomass known as biochar, and a gas product. These processes can be grouped into three distinct categories based on their operating temperatures and vapor residence times: fast, intermediate and slow pyrolysis. Fast pyrolysis occurs at very high heating rates between 1000 to 10000 °C/s and low residence time, < 2 seconds.[14-15] It is typically carried out between 425 to 550 °C and as high as 650 °C.[15-16] Due to its high heating rate and short vapor residence time, secondary vapor cracking reactions are minimized, and bio-oil yield is maximized. Intermediate pyrolysis is similar to fast pyrolysis with regards to the heating rate and operating temperatures.[14] However, the pyrolytic vapors reside much longer in the reactor during intermediate pyrolysis than during fast pyrolysis. As a result, intermediate pyrolysis bio-oil yield is lower than that typically observed in fast pyrolysis. Nonetheless, bio-oil is the major product while the solid and gas product yield are virtually identical. In contrast to fast and intermediate pyrolysis, slow pyrolysis occurs at a much slower heating, lower temperature and vapor residence times significantly longer than 30 seconds. These conditions maximize the biochar yield. Slow pyrolysis minimizes the liquid product yield due to low devolatilization and extensive secondary cracking of large volatiles into non-condensable gases. The typical operating conditions and product yields of these processes are summarized in Table 2.1.

Combustion

In its simplest form, combustion is the full oxidation of a fuel, e.g. carbon or hydrogen, to release heat as originally discovered by French chemist Antoine Lavoisier in 1772.[18] In the context of lignocellulosic biomass, combustion is a complex process that occurs at temperatures between 850 and 1150°C in excess air relative to its stoichiometric requirement.[19] Its primary product is flue gas which contains carbon dioxide, water vapor, residual air and trace amounts of carbon monoxide, sulfur and nitrogen oxides, particulates.[5] Besides flue gas, combustion also produces approximately 5 wt. % of fly ash.[5] It can be broadly divided into four processes: heating and drying, pyrolysis or devolatilization, gas phase oxidation and finally char oxidation. Heating and drying occurs when biomass is introduced into the combustion vessel and heated up from its ambient temperature to the onset temperature of pyrolysis approximately between 200-225 °C.[20-21]

Table 2.1. Pyrolysis modes and typical yields[14-15, 17]

Pyrolysis category	Typical conditions	Product yield, wt. %		
		Liquid	Solid	Gas*
Fast	Heating rate 1000 - 10000 °C/s, 425-500 °C, Vapor residence time < 2 s	75	12	13
Intermediate	425-500 °C, Vapor residence time 2-30 s	50	25	25
Slow	< 300 °C, < 7 °C/min, vapor residence time > 30 s	15	80	5

*Gas represents non-condensable gases.

In the pyrolysis phase, biomass is devolatilized into condensable and non-condensable gases, resulting in a rapid mass loss between 200 to 400 °C.[22] Volatiles and char produced during the pyrolysis phase further undergo oxidation to produce and release heat in the process. Overall, lignocellulosic biomass combustion can be represented by the reaction below:

$$C_{\alpha}H_{\beta}O_{\gamma}S_{\phi}N_{\kappa} + m(O_2 + 3.76N_2) \rightarrow aCO_2 + bH_2O + cSO_2 + dN_2 \qquad [2.1]$$

In this reaction, the coefficient for nitrogen (N_2), 3.76, represents the number of moles of nitrogen in air for every mole of oxygen. The coefficients α, β, γ, θ and κ are determined from the elemental composition of lignocellulosic biomass as determined from the ultimate analysis. The coefficients a, b, c, d, and m are unknown and can be determined through a species balance. Thus, based on the reaction above, the following set of algebraic expressions can be deduced for the unknown coefficients:

C balance: $\alpha = a \quad => \quad a = \alpha$

H balance: $\beta = 2b$ => $b = \frac{\beta}{2}$

S balance: $\phi = c$ => $c = \phi$

O balance: $\gamma + 2m = 2a + b + 2c$ => $m = \frac{2a + b + 2c + \gamma}{2}$

=> $m = \alpha + \frac{\beta}{4} + \phi - \frac{\gamma}{2}$

N balance: $\kappa + 3.76(2 \times m) = 2d$ => $d = 3.76m + \frac{\kappa}{2}$

Thus, the general reaction can be rewritten as shown below

$$C_\alpha H_\beta O_\gamma S_\phi N_\kappa + (\alpha + \frac{\beta}{4} + \theta - \frac{\gamma}{2})(O_2 + 3.76N_2) \rightarrow \alpha CO_2 + \frac{\beta}{2} H_2O + \theta SO_2 + \left(3.76 + \frac{\kappa}{2}\right) N_2 \quad [2.2]$$

In most lignocellulosic biomass feedstocks used in thermochemical conversion, nitrogen and sulfur contents are small and their products are customarily ignored. Accordingly, $m = \alpha + \frac{\beta}{4} - \frac{\gamma}{2}$ and $d = 3.76m$. The combustion scientific community has defined a dimensionless number to conveniently present the quantity of air required for complete combustion in terms of a ratio based on unit mass of fuel. The theoretical ratio (stoichiometric ratio) of mass of air to mass of biomass, $\left(\frac{A}{B}\right)_{stoichiometric}$, and can be calculated according to Equation (2.1) using the coefficients of the balanced reaction [2].

$$\left(\frac{A}{B}\right)_{stoichiometric} = \frac{m_{air}}{m_{biomass}} = \frac{(n_i M_i)_{air}}{(n_i M_i)_{biomass}} = \frac{m(M_{O_2} + 3.76M_{N_2})}{\alpha M_C + \beta M_H + \lambda M_O + \theta M_S + \kappa M_N} \quad (2.1)$$

where, M_i is molecular weight of constituents i. Another ratio which is often encountered in the combustion scientific literature is the equivalence ratio, λ, and is a measure of actual oxygen supplied to the combustion process to that required stoichiometrically as outlined in Equation (2.2).

$$\lambda = \frac{\left(\frac{A}{B}\right)_{actual}}{\left(\frac{A}{B}\right)_{stoichiometric}} \quad (2.2)$$

where, $\left(\frac{A}{B}\right)_{actual}$ and $\left(\frac{A}{B}\right)_{stoichiometric}$ are the actual and stoichiometric air to biomass ratios, respectively.

In the context of lignocellulosic biomass combustion, the air/biomass equivalence ratio is used to define combustion regimes. In a lignocellulosic biomass rich regime, insufficient air is available for complete combustion and $\lambda < 1$. When excess air is supplied, $\lambda > 1$ and the regime is deemed lignocellulosic biomass-lean. If the stoichiometric amount of oxygen required for complete combustion is supplied, there is no excess air and $\lambda = 1$. Thus, the term "e", expressed in percentage, is used to determine the excess air in the combustion process and is defined as [23]:

$$e = 100(\lambda - 1) \tag{2.3}$$

Gasification

Gasification lies between pyrolysis and combustion with regards to oxygen requirements and temperatures. It is defined as a thermal decomposition process that occurs in the presence of sub-stoichiometric amount of oxygen, relative to that required for full combustion, at high temperatures, typically between 650 and 1500^{o}C to yield producer gas and biochar.[24-25] Producer gas is composed primary gases and gas contaminants. Producer gas primary gases or constituents refers to the four most abundant species, i.e. carbon monoxide (CO), hydrogen (H_2), methane (CH_4) and CO_2). The species are commonly found at percent volume concentration rather than parts per millions or billions.

As in combustion, a dimensionless number, equivalence ratio (ER), is used to measure the proportion of oxygen supplied during this process relative to the stoichiometric need for full combustion. The equivalence ratio is the ratio of the actual air to biomass ratio supplied during gasification to that required for complete combustion. Because gasification occurs in an oxygen deprived environment, ER varies between 0 and 1, where 0 indicates a pyrolysis mode and 1 or more, a combustion mode. It is expressed as shown in Equation (2.5) and generally varies between 0.20 and 0.30 for biomass.

$$\phi = \frac{\left(\frac{A}{B}\right)_a}{\left(\frac{A}{B}\right)_s} \tag{2.4}$$

The stoichiometric air to biomass ratio $\left(\frac{A}{B}\right)_s$ can be represented as

$$\left(\frac{A}{B}\right)_s = \frac{m_{air}}{m_{biomass}} = \frac{m\left(M_{O_2} + 3.76M_{N_2}\right)}{\alpha M_C + \beta M_H + \theta M_S} \quad (2.5)$$

Several sources can be used to supply oxygen in gasification including air, air, and steam or O_2 and steam mixtures and, steam. The oxygen source is referred as the oxidizing or gasifying media or agents. When air is used as gasifying agent, considerable amount of nitrogen could appear in the producer gas thus diluting the concentration of other components. A wide variety of reactor technologies have been applied in biomass gasification. Biomass gasification using fixed bed gasifiers (downdraft and updraft), fluidized bed gasifiers (circulating and bubbling), and entrained flow gasifiers comprise the majority of conventional technologies. Table 2.2 summarizes these technologies and their major features. A more detailed description can be found in Basu [26-27]

Chemistry of gasification producer gas primary constituents

When exposed to the high temperatures during gasification, biomass particles are rapidly heated and begin decomposing. Water vapor is released as the temperature of the particles approaches or exceeds the vaporization temperature of water (100 – 200°C).[7] This initial drying stage usually continues until the moisture content of the biomass particles is less than 5%.[12, 28] Continued heating of the dried biomass particles leads to the devolatilization or pyrolysis stage. Devolatilization involves the thermal decomposition of biomass molecules in the absence of oxygen to liberate volatile gases and primary tar, leaving behind a solid aggregate of char and ash.[29] The volatile gases produced during the devolatilization stage include CO, CO_2, H_2, CH_4, H_2S, and NH_3.[30] Primary tar is also released and is composed of a complex composite of heavier organic compounds that are unstable. Because they are unstable, the constituents of primary tar are susceptible to thermal cracking, producing additional volatile gases and a more stable and refractory tar known as secondary and tertiary tar as illustrated in Figure 2.1.[31]

After devolatilization, char is exothermically oxidized during gasification when exposed to sub-stoichiometric oxygen levels, producing CO and CO_2 (Reactions [2.3] and [2.4] in Table 2.3). The heat released by char oxidation is consumed by other simultaneous endothermic reactions such that the net heat of gasification is typically small.[26] Solid char may also react with H_2O, H_2, and CO_2, as shown in Reactions [2.5], [2.6], and [2.7], respectively. In addition, several homogenous (gas phase) chemical reactions (Reactions [2.8] – [2.12]) occur at gasification temperatures before gaseous products leave the gasification reactor. As would be expected, the extent to which each chemical reaction occurs during biomass gasification is influenced by the reactor operating parameters, including those that control the gas and solid particle residence times.

Table 2.2. Summary of conventional biomass gasification technology.

Technology	Description	Benefits	Limitations
Updraft	Counter-current flow reactor. Biomass particles flow downward whereas gasifying agent flows upward.	a. Low sensitivity to biomass properties. b. Simple design.	a. Low syngas quality and high tar content. b. Frequent clogging of gasifier grate.
Downdraft	Co-current flow reactor. Biomass particles and gasifying agent flow downward.	a. Relatively low tar. b. Suitable for high-volatile biomass.	a. High particulate matters. b. Low heating value syngas c. Can only handle low moisture content biomass.
Fluidized bed (FB)	Biomass particles are mixed in a fluid-like state. Bed material, typically sand or catalyst, promotes heat transfer.	a. Highly adaptable to commercial scale process. b. High thermal efficiency. c. High carbon conversion efficiency, in the case of circulating FB.	a. Biomass particle size and moisture content control are needed for effective fluidization. b. Channeling and agglomeration issues.
Entrained flow	Biomass is introduced into the gasifier suspended in a stream of gasifying agent. Operated at high temperatures (> 1000 °C) and low residence time.	a. Highly adaptable to commercial scale process. b. High tar cracking and gasification efficiency.	a. Highly controlled biomass size. b. Grinding cost is high. c. Frequent slagging of ash.

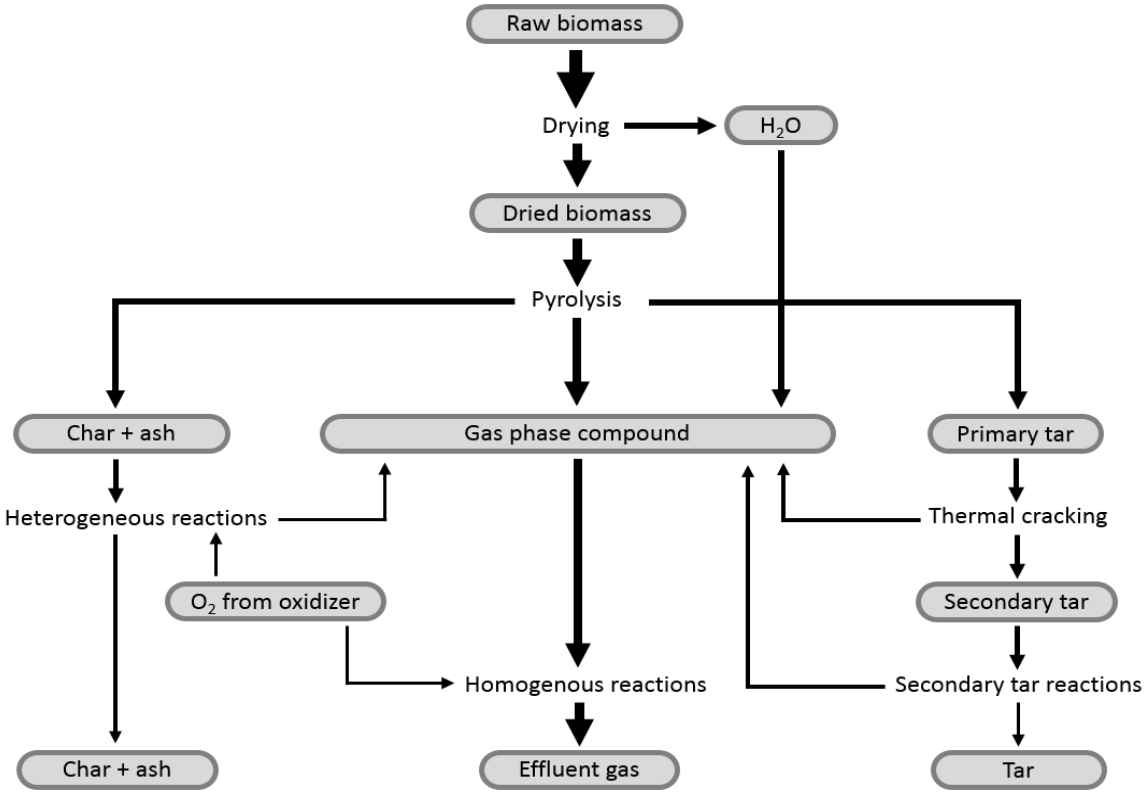

Figure 2.1. A conventional biomass gasification process. The arrow weight qualitatively depicts the mass fraction of intermediate and final products.

Table 2.3. Important lignocellulosic biomass gasification reactions.[32-36]

Name	Stoichiometry	ΔH (kJ/mol)	No.
Carbon partial oxidation	$C + 0.5O_2 \rightarrow CO$	-111	[2.3]
Carbon complete oxidation	$C + O_2 \rightarrow CO_2$	-394	[2.4]
Water-gas reaction	$C + H_2O \rightarrow CO + H_2$	+131	[2.5]
Hydrogasification reaction	$C + 2H_2 \rightarrow CH_4$	-75	[2.6]
Boudouard reaction	$C + CO_2 \rightarrow 2CO$	+172	[2.7]
Hydrogen oxidation	$H_2 + 0.5O_2 \rightarrow H_2O$	-242	[2.8]
Carbon monoxide oxidation	$CO + 0.5O_2 \rightarrow CO_2$	-284	[2.9]
Water-gas shift reaction	$CO + H_2O \leftrightarrow CO_2 + H_2$	-41	[2.10]
Methane steam reforming	$CH_4 + H_2O \leftrightarrow CO + 3H_2$	+206	[2.11]
Methane dry reforming	$CH_4 + CO_2 \leftrightarrow 2CO + 2H_2$	+247	[2.12]

ΔH: heat of reaction, No.: reaction number.

Chemistry of gasification producer gas impurities

Producer gas nitrogen impurities

A substantial portion of the nitrogen contained in biomass is released as NH_3, HCN, and nitric oxides[37]. Broer et al.[38] demonstrated that approximately 40–65% of biomass-nitrogen was converted into NH_3 and HCN during gasification of switchgrass, with NH_3 being the dominant nitrogen species. Generally, the formation of nitrogen compounds is undesirable during gasification because these compounds cause catalyst deactivation and pollution in post-gasification processes.[39]

Present knowledge on the evolution of biomass-nitrogen is limited. The earliest insight into the evolution of biomass-nitrogen arises from studies on coal-nitrogen evolution. It has been proposed that coal-nitrogen decomposes to form HCN and HCNO during the pyrolysis stage of gasification and NH_3 formation results from the secondary reactions of HCN and HCNO (Reactions [2.13] and [2.14], Table 2.4).[40] From a biomass gasification standpoint, the main drawback to this reaction mechanism is associated with the difference in the nature of coal-nitrogen and biomass-nitrogen. Nitrogen in coal exists mainly in heterocyclic compounds such as pyridine and pyrrole.[41-42] However, the general hypothesis about the nature of biomass-nitrogen is that it is primarily bound to protein and amino acids in biomass, and in small part, to alkaloids, chlorophyll, and nucleic acid.[43-44] This hypothesis fundamentally shapes the other mechanisms that have been proposed for the evolution of biomass-nitrogen.

There is evidence that a part of biomass-nitrogen is released into the gas phase as volatile-nitrogen (NH_3, HCN, HCNO, and tar-nitrogen) during the pyrolysis stage of biomass gasification and the remainder is held in the solid particle as char-nitrogen.[30, 45] The release of volatile-nitrogen and the formation of char-nitrogen are presumed to follow a series of primary and secondary reactions of protein and amino acids. First, protein and amino acid undergo dehydration and decarboxylation reactions to form cyclic amides (mainly 2,5-diketopiperazine) and amines, respectively, during pyrolysis (Figure 2.2).[46-47] Cyclic amides are similar to the heterocyclic compounds found in coal; hence they are presumably cracked to produce HCN and HCNO, with HCN being the major product. In addition to cracking of cyclic amides, cleavage of its functional groups occurs, yielding diverse products (including tar-nitrogen, i.e., nitrogen-containing tar compounds).[48] The amines are hypothesized to decompose to NH_3,[49] and char-nitrogen formed through polymerization reactions of nitrogen-containing compounds.[48-49] The concentration of nitrogen in char-nitrogen typically decreases with increasing temperature and equivalence ratio.[50-51] Tar-nitrogen may be cracked to produce NH_3, HCN, and HCNO at high temperatures (Figure 2.2). Furthermore, the interactions of hemicellulose, cellulose, and lignin with biomass-nitrogen are proposed to play a major role in determining biomass-nitrogen release during pyrolysis.[48, 52-53]

Table 2.4. Chemical reactions of biomass-nitrogen during gasification.[142]

Stoichiometry	ΔH (kJ/mol)	Number
$HCN + H_2O \rightarrow NH_3 + CO$	-47.71	[2.13]
$HNCO + H_2O \rightarrow NH_3 + CO_2$	-79.55	[2.14]
$NH_3 + 2.5O_2 \rightarrow NO + 1.5H_2O$	-225.54	[2.15]
$2NH_3 \leftrightarrow 3H_2 + N_2$	+91.87	[2.16]
$2N_2 + 2H_2O + 4CO \leftrightarrow 4HCN + 3O_2$	+1458	[2.17]
$2N + xO_2 \leftrightarrow 2NO_x$	> +68.38	[2.18]

ΔH: heat of reaction.

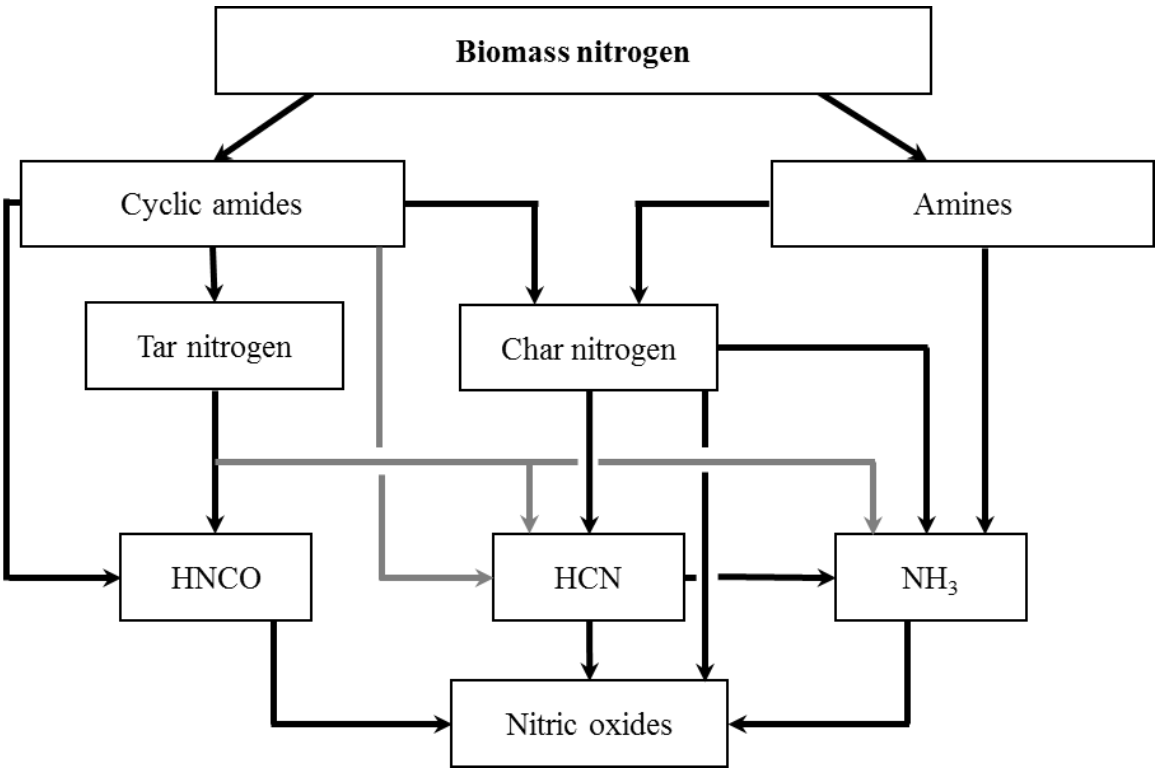

Figure 2.2. Summary of the evolution of biomass-nitrogen during gasification according to information available in literature.[65-69, 74-75]

Additional NH_3 is formed after pyrolysis through the hydrogenation reactions of char-nitrogen and HCN. These reactions are favored in the presence of steam.[54] Conversely, NH_3 decomposition is enhanced as temperature increases and in the presence of ash. Abdoulmoumine et al.[55] found that the ammonia yield decreased from 1.63 to 1.00 mg/kg dry biomass when the gasification temperature of pine was raised from 790 to 1078 °C. The authors in this study ascribed the reduction in ammonia yield to thermal decomposition (Reaction [2.16], Table 2.4). Furthermore, oxidation of NH_3, HCN, HCNO, and char-nitrogen into nitric oxides is expected at high equivalent ratios and favorable temperatures (Reaction [2.18], Table 2.4).

Producer gas sulfur impurities

Sulfur compounds (mostly H_2S, COS, CS_2, and SO_2) are another undesirable chemical species formed during biomass gasification. Typically, the concentration of sulfur compounds in biomass-derived syngas is lower compared to that of coal-derived syngas.[56] However, the concentration of sulfur compounds in biomass-derived syngas (typically > 40 ppmV)[55, 57-59] is still at levels that can cause severe catalyst deactivation, deposition and metal corrosion in post-gasification processes.

The most common viewpoint on the nature of biomass-sulfur is that biomass-sulfur is partitioned into organic and inorganic sulfur, with the latter being more thermally stable. Although plants generally take in sulfur as inorganic sulfates via their roots, sulfur is reduced and transformed into organic sulfur (basic amino acids cysteine and methionine) during protein synthesis in plant leaves.[60] There are two potential implications of this view. First, the ratio of organic to inorganic sulfur is dependent on plant type and growth conditions. Second, the release of biomass-sulfur during a thermochemical process is a two-step activity. The first step would involve the degradation of organic sulfur during pyrolysis (Figure 2.3).[61] Johansen et al.[62] suggested that the onset temperature for the degradation of organic sulfur is approximately 200 °C based on the decomposition temperature of cysteine and methionine. Some part of the released organic sulfur is likely captured on the active sites in the char matrix as char-sulfur.[63]

The second step of biomass-sulfur release would involve the transformation of inorganic sulfur (mostly metal sulfates) into metal sulfides and char-sulfur (Figure 2.3).[63] which later undergo heterogeneous reactions with gas phase compounds during char gasification (Reactions [2.20] – [2.22], Table 2.5). This would occur at temperatures above 500°C. Some inorganic sulfur (mainly K_2SO_4) might still be retained in the ash and probably would decompose at temperatures above 1000 °C.[65]

Knudsen et al.[63] proposed that organic sulfur is mainly released as H_2S and COS, whereas inorganic sulfur is mainly released as SO_2. Sulfur-containing tar compounds such as mercaptans, disulfides, and thiophenes (tar-sulfur) are also likely released during pyrolysis of organic sulfur. The hydrogenation reaction of mercaptans and disulfides, as well as thermal cracking of thiophenes, may

contribute to the formation of H_2S.[64, 68] The final yield of sulfur compounds in the syngas is ultimately determined by the homogenous gas-phase reactions sulfur that compounds undergo after pyrolysis and char reaction. The expected homogenous reactions are listed in Table 2.5.

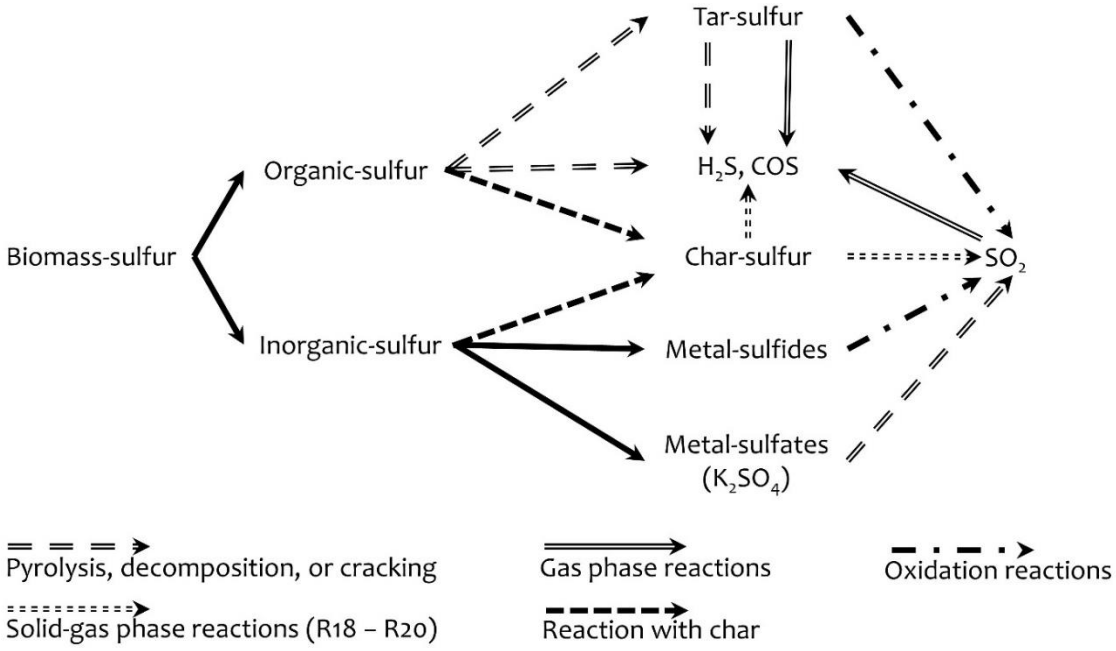

Figure 2.3. Summary of the evolution of biomass-sulfur during gasification according to information available in literature.[61-65]

Table 2.5. Chemical reactions of biomass-sulfur during gasification.[66-67]

Stoichiometry	ΔH (kJ/mol)	Number
$S_{(s)} + O_2 \rightarrow SO_2$	-296.79	[2.19]
$S_{(s)} + CO_2 \rightarrow COS + \ldots$		[2.20]
$S_{(s)} + H_2O \rightarrow H_2S + \ldots$		[2.21]
$H_2S + 1.5O_2 \rightarrow SO_2 + H_2O$	-518.02	[2.22]
$H_2S + CO_2 \leftrightarrow COS + H_2O$	+30.57	[2.23]
$H_2S + CO \leftrightarrow COS + H_2$	-10.56	[2.24]
$H_2S + COS \leftrightarrow CS_2 + H_2O$	+37.16	[2.25]
$SO_2 + 3H_2 \leftrightarrow H_2S + 2H_2O$	-207.46	[2.26]
$SO_2 + 2CO \leftrightarrow S + 2CO_2$	-269.12	[2.27]
$2H_2S + SO_2 \rightarrow 3S + 2H_2O$	-233.64	[2.28]

ΔH: heat of reaction.

Effect of operating parameters on gasification performance

Effect of feedstock properties

The chemical and physical properties of biomass feedstock contribute to its reactivity and ultimately influence the final composition of gasification products. For instance, biomass with small particle size have large surface area to volume ratio which enhances solid-gas interaction and chemical reaction rate.[69] High moisture content of biomass feedstock lowers the gasification temperature because of the corresponding increase in the drying magnitude and endothermic water-gas and methane steam reforming reactions (Reactions [2.5] and [2.11]). The resulting low gasification temperature favors the consumption of CO to produce CO_2 via the forward water-gas shift reaction (R8). In their study, Zainal et al.[70] gasified woodchips at 800 °C in a downdraft gasifier and quantified the effect of feedstock moisture content on syngas composition. It was observed that as the moisture content of the feedstock increased from 0% to 40%, CO concentration decreased from about 28% to 15% and CO_2 concentration increased from about 5% to 15%. Similarly, Antonopoulos et al.[71] measured the syngas composition from the gasification of Miscanthus at 1000 °C. They reported that the concentration of CO decreased from 22% to 14.8% as the moisture content was increased from 0% - 40%. An opposite trend was reported for the concentration of CO_2.

However, high moisture content of biomass feedstock results in a desirable increase in the H_2 concentration of syngas. Pellegrini and Oliveira[72] studied the gasification of sugarcane bagasse and reported that H_2 concentration in syngas increased from about 26% to about 33% when the moisture content of sugarcane bagasse was increased from 20% to 50%. Similarly, Kuo et al.[73] observed that regardless of the equivalent ratio (ER) used, raw bamboo produced syngas with higher H_2 concentration when compared to torrefied bamboo. This was ascribed to the fact that the moisture content of raw bamboo was higher than the moisture content of torrefied bamboo. At ER of 0.2, the H_2 concentration of the syngas from the gasification of raw bamboo was 29.23% while it was 27.22% and 23.34% for bamboo torrefied at 250 °C for one hour and 300 °C for one hour, respectively. These aforementioned studies demonstrate that the choice of the moisture content level of biomass for gasification is important and dependent on the need of downstream applications, especially from a H_2:CO ratio standpoint. However, biomass gasifiers are usually designed to handle low moisture content feedstock (<30%) because ignition difficulty, reduced efficiency, and low calorific value of syngas are associated with high moisture content feedstock.[74]

Volatile matter is another important biomass property that influences gasification performance and syngas composition. Biomass containing high volatile matter are highly reactive, easy to gasify, and produce less char.[27] Also, high volatile matter in biomass enhances the porosity and reactivity of biomass char. In theory, however, tar yield during gasification is proportional to the amount of volatile matter in solid

fuel. Typically, biomass feedstocks (with >60% volatile matter content) would produce more tar than coal feedstocks (with <40% volatile matter content), which would lead to more severe fouling issues downstream.[75] Saw and Pang[76] used a solid fuel blend (a mixture of lignite coal and radiata pine) to establish that higher volatile matter content feedstock yield more tar. Feedstock with volatile matter content of 77.4%, 48.5%, and 32.9% produced tar yield of 6.6 $g/kg_{dry\ fuel}$, 2.7 $g/kg_{dry\ fuel}$, and 2.3 $g/kg_{dry\ fuel}$, respectively. At the devolatilization stage, volatile matter content also contributes to the production syngas contaminants such as H_2S and NH_3 that are responsible for catalyst deactivation in downstream applications.[77]

Effect of gasification temperature

Temperature plays a critical role in determining the magnitude and composition of syngas from biomass gasification as well as the carbon conversion efficiency. Higher gasification temperature tends to increase syngas yield by increasing the extent of devolatilization and thermal tar cracking. Abdoulmoumine et al.[55] investigated the influence of gasification temperature on the air gasification of pine. Their result showed that, at ER of 0.25, syngas yield increased from 73.06 wt.% to 84.16 wt.% as the gasification temperature was increased from 790K to 1078K. Similar trend was reported by Skoulou et al.[78] for the gasification of olive tree cuttings and olive kernels in a downdraft fixed-bed gasifier.

According to Le Chatelier's principle, increase in temperature causes the chemical equilibrium to shift to the right in endothermic reactions and to the left in exothermic reactions. During gasification, the products of the most prominent endothermic reactions (water-gas reaction, Boudouard reaction, methane steam reforming reaction, and methane dry reforming reaction) are H_2 and/or CO. Therefore, in addition to the increase in syngas yield with increasing gasification temperature, H_2 and CO content of syngas simultaneously increase with increasing gasification temperature. Also, carbon conversion to gaseous products is enhanced as gasification temperature increases mainly because of corresponding increase in the rate of water-gas reaction and Boudouard reaction. A study by Sadhwani et al.[79] on the gasification of loblolly pine using CO_2 reported that the H_2 and CO content of syngas increased by a factor of 3.94 and 1.96 as gasification temperature increased from 700K to 934K. Average carbon conversion increased from 61.37% to 81.9% over the same increment in gasification temperature.

Low heating value (LHV), which is a measure of gasification efficiency and the most desirable property of syngas intended for combustion applications, reduces as gasification temperature increases.[80-81] This may be explained by the reduction in the concentration of high energy containing hydrocarbon gases (mainly CH_4) via steam and dry reforming reaction as gasification temperature increases. When He et al.[82] investigated the catalytic gasification of waste polyethylene, they reported that the LHV of the syngas produced was reduced from 12.44 MJ/N m^3 to 11.31 MJ/N m^3 as the gasification temperature was raised from 973K to 1173K.

Effect of oxidizing media

Several oxidizing media including air, oxygen, steam, and CO_2 have been utilized and studied for biomass gasification. Air is the most commonly used oxidizing media for biomass gasification because it is cheap and convenient. However, the LHV and H_2 concentration of the resulting syngas is typically low when compared to oxygen-gasification and steam-gasification. The heating value and H_2 concentration of air-gasification syngas is generally lower than 7 MJ/N m^3 and 14%, respectively, whereas those of steam-gasification syngas can be up to 16 MJ/N m^3 and 60%, respectively.[83-84] Nitrogen dilution is another drawback associated with air-gasification. In the case of steam-gasification, however, the energy requirement is high because supplementary energy is needed to maintain the gasification temperature. This is because the prevalence of endothermic water-gas and steam reforming reactions tends to lower the gasification temperature during steam-gasification.[85] The additional cost needed for oxygen supply is the major deterrent to the use of oxygen-gasification.

Some studies have used a combined stream of air and steam as the oxidizing media for biomass gasification. The air-steam gasification process is self-sufficient from an energy standpoint because oxygen in the air partakes in exothermic oxidation reaction and provide the heat necessary for endothermic water-gas and steam reforming reactions involving steam. The resulting syngas has relatively higher heating value, higher H_2 content, and lower nitrogen content compared to air-gasification.[86] Similarly, steam-oxygen gasification the biomass has been explored to improve syngas quality, but the high capital cost of oxygen supply makes the process unattractive for industrial implementation.[87-88] Researchers have also reported CO_2-gasification of biomass as an environmental friendly process. The major drawback limiting CO_2 only gasification is that external heat source is needed. The ratio of CO_2 inflow rate to biomass feed rate significantly affects syngas yield and composition and carbon conversion.

For air-gasification, equivalence ratio (ER) has been found to significantly influence biomass gasification performance and syngas properties. ER is the actual air-fuel ratio divided by the stoichiometric air-fuel ratio. Complete biomass combustion is ideally achieved at ER of 1 while biomass pyrolysis is ideally achieved at ER of 0. Biomass gasification lies between combustion and pyrolysis, typically occurring at ER values between 0.2 and 0.4.[89-92] Increase in ER during biomass gasification enhances the oxidation of high calorific gases (CO, H_2, and CH_4) to produce low calorific gases (CO_2 and H_2O). In addition, the nitrogen content of syngas increases with increasing ER because nitrogen is the major component of air. Below a certain threshold of ER (usually 0.2), exothermic oxidation reactions are diminished, and gasification temperature is severely reduced. The syngas yield at this ER regime is low while tar yield is high, mainly because the rate of thermal cracking and reforming reactions of tar is lowered.[93]

Guo et al.[94] investigated the effect of ER on biomass gasification. They used corn stalk and varied ER from 0.18 to 0.37. Tar yield was about 2.5 g/Nm^3 at ER of 0.2 and linearly decreased to 0.52 g/Nm^3 at ER of 0.32. They also observed that the higher the ER used, the higher the temperature measured across the gasifier due to the release of heat from oxidation reactions. The increase in temperature because of increasing ER initially caused the concentration of H_2 and CO to increase up to a peak value of 12.89% at ER of 0.25 and 19.41% at ER of 0.27, respectively. Further increase in temperature as ER increases after the peak caused the oxidation of H_2 and CO, and therefore subsequent drop in their concentration. Gai et al.[95] reported a similar polynomial relationship between ER and the concentration of H_2 and CO for the gasification of corn straw in a downdraft gasifier. They observed that the concentration of H_2 initially increased from 6.9% at ER of 0.18 to 13.51% at ER of 0.32, then decreased to 10.58% when ER was further increased to 0.41. The concentration of CO also initially increased from 11.35% at ER of 0.18 to 19.81% at ER of 0.32, then decreased to 15.16% when ER was further increased to 0.41. Likewise, the LHV was 2.69 MJ/N m^3, 5.39 MJ/N m^3, and 3.69 MJ/N m^3 at ER of 0.18, 0.32, and 0.41, respectively. Xue et al.[96] used a narrower ER range in their study, therefore only reported a linear pattern. Their result shows that the concentration of H_2 and CO decreased from 10.2% to 6.4% and 17.0% to 14.5%, respectively when ER was increased from 0.18 to 0.26.

Steam to biomass (S/B) ratio is one of the most important operational parameters in steam-gasification of biomass. It is the ratio of steam inflow rate to biomass feed rate. At small S/B ratio, high amount of CH_4 and char is produced. However, as S/B ratio is increased CH_4 and char are oxidized to produce H_2 and CO via water-gas and methane steam reforming reactions. Excessive steam may lead to the further oxidization of CO to CO_2 and lowering of the temperature which tends to increase tar yield. There is therefore the need to identify and use optimized S/B ratio for biomass gasification with respect to downstream applications.

Chen et al.[97] revealed that syngas yield gradually increased when S/B ratio was increased from 0 to 7.3. The H_2 content increased from 38.40% to 45.58% as S/B ratio was increased from 1.3 to 5.3, then slightly decreased as S/B ratio was further increased to 7.3. Hejazi et al.[98] reported that the concentration of H_2 and CO_2 increased as S/B ratio was increased, but the concentration of CO and CH_4 decreased as S/B ratio was increased. Sharma and Sheth[99] investigated the air-steam gasification of waste sesame wood. They established that above a S/B ratio threshold of 0.8 the H_2 and CO content, as well as heating value of syngas, decreased with increasing S/B ratio.

Effect of catalysts

Different catalysts have been used in-situ and ex-situ during biomass gasification to enhance the production of or selectivity for particular products. Among the many catalysts that have been commonly used during biomass gasification are alkaline

metals catalysts (dolomite, olivine, CaO, and MgO), Fe-based catalysts, Ni-based catalysts, and Zn-based catalysts. The conversion of tar to produce H_2-rich gas has been the focus of interest in the use of in-situ catalysts biomass gasification. Dolomite and olivine are natural occurring and have been widely demonstrated to exhibit some tar conversion activity during biomass gasification, with dolomite being the more effective.[100-101] In addition to showing tar conversion activity, dolomite and olivine also show ammonia removal ability.[101] Ni-based catalysts are effective for tar decomposition and have good steam reforming and water gas shift activity.[102] However, the poisoning of Ni-based catalysts by sulfur compound and deactivation by coke deposition are major concerns.[103]

Kimura et al.[102] developed and tested different Ni-based catalysts for the conversion of tar during steam-gasification of biomass. They reported that $Ni/CeO_2/Al_2O_3$ catalysts prepared via co-impregnation method performed best among the catalysts, producing the least tar yield and highest gaseous product yield. Hu et al. tested a NiO catalyst supported on modified dolomite (NiO/MD) for steam co-gasification of wet sewage sludge and pine sawdust. The NiO/MD catalyst showed 83.8% tar removal efficiency. Also, syngas yield was increased by 39.4% in the presence of the NiO/MD catalyst compared to co-gasification without catalysts. Some studies have investigated the utility of the intrinsic alkaline and alkaline earth metals in bio-char for catalytic tar conversion during biomass gasification.[104-110] The activity of biochar is affected by its physicochemical properties as dictated by biomass type.[111] Yao et al.[109] used activated carbon and biochar from three biomass feedstocks (namely: wheat straw, rice husk, and cotton stalk) to enhance H2 production during biomass gasification. It was established that biochar from cotton stalk produced the highest H2 yield due to its high content of alkaline and alkaline earth metals. The activity of the bio-chars and activated carbon according to hydrogen production were observed to follow this order: cotton stalk > wheat straw > activated carbon > rice husk. In subsequent experiments, they reported that the addition of nickel significantly enhanced the catalytic activity of the bio-chars and activated carbon, following the same order of activity. Shen et al.[106] were able to achieve about 93% tar conversion using Ni-char catalyst. At the same time, they observed an increase in the yield of syngas, H2, and CO compared to uncatalyzed biomass gasification.

Thermodynamics equilibrium and kinetic modeling

Thermodynamic equilibrium modeling

Thermodynamic equilibrium models are based on determining the final thermodynamic state in which the concentrations of chemical species in the reactor no longer change with time (i.e., the final thermodynamic states in which the consumption and production reactions associated with each chemical species are balanced). Therefore, thermodynamic equilibrium models generally predict the theoretical maximum yield of the gasification process at chemical equilibrium

conditions where the Gibbs free energy of the reacting system is minimized. However, the probability of reaching thermodynamic equilibrium during an actual gasification process is low due to less than infinite contact times between the reactants. Simulations from thermodynamic equilibrium models fit experimental data better when the gasification temperature is high (> 1500 K) and the residence time is long with respect to the reaction time scale.[112-113] because thermodynamic equilibrium is more achievable under these conditions.

Because thermodynamic equilibrium models for gasification depend only on the thermodynamic properties of the initial and final species, they are independent of the specific details of the reactor. Hence, some important details about mechanism and rate of the gasification process, such as gasifier type and geometry, cannot be captured using these models.[114] However, they are still useful for establishing the maximum possible limits for gasifiers not limited by chemical reaction rates or mass, heat, and momentum transport. Thus, they provide an assessment of the best possible performance that can be achieved given specific assumptions about the feed stream compositions and the reactor operating temperature and pressure
Two types of constraints are typically used to determine chemical equilibrium in biomass gasification. One approach, referred to as the 'stoichiometric' approach, applies both the explicit reaction stoichiometries for all the possible reactions as well as the thermodynamic properties of the reactants and products. In this case, the species balances imposed by the reactions are included when the Gibbs free energy of the final reaction mixture is minimized. It is convenient to achieve this result using the equilibrium constants illustrated by Equations (2.6) and (2.7). Solving these equations simultaneously guarantees that both the species balances and free energy state required for chemical equilibrium are satisfied:[115]

$$\Delta G_j^o = -RT\ln K_j \tag{2.6}$$

$$K_j = \prod_i \left(\frac{P_i}{P_o}\right)^{v_{i,j}} \tag{2.7}$$

In the case of the non-stoichiometric approach, the concentration of each chemical species is estimated through the direct minimization of the Gibbs free energy alone, after assuming some relationship (typically empirical) between the species balances between reactants and products of the reactions.

$$G_{total} = \sum_{i=1}^{N} n_i \Delta G_{i,total}^o + RT \sum_{i=1}^{N} n_i \ln\left[\frac{n_i}{\sum n_i}\right] \tag{2.8}$$

Hence, the non-stoichiometric approach is often referred to as the Gibbs free energy minimization approach. The stoichiometric approach requires that all independent chemical species and reactions involved in the gasification process be specified (including all possible phases), in order to provide the complete species balance constraints needed to solve the final product species and phase compositions.[70,116] In practice, however, only a subset of the significant chemical reactions can be specified because the number of chemical reactions and phases simultaneously occurring during gasification process is large and often not completely known. This lack of information about the possible reactions and phases increases the probability of model prediction errors. The non-stoichiometric approach does not require the identification of all the possible attendant chemical reactions, but it requires some additional information about constraints between the reactant and product species and the possible phases present. Often these constraints are empirical and can still require sophisticated numerical analysis tools to solve the high-dimensional minimization problem.[117]

Several previous studies have used some type of thermodynamic models to estimate the performance of biomass gasification systems based on chemical equilibrium. One example is that by Sharma and Sheth[99], who developed an equilibrium model to predict the syngas composition of air-steam gasification of sesame wood assuming three important biomass gasification reactions (water-gas shift reaction, steam reforming, and methanation reactions). Although the equilibrium model predictions showed good agreement with experimental data from Sheth and Babu[91] and Dogru et al.[90], the equilibrium model predictions poorly fitted experimental data collected by the authors themselves. They ascribed this poor fit between their equilibrium model and experimental data to the non-equilibrium phenomenon inside the gasifier as shown by the continuous variation in temperature inside the gasifier. In a similar work, George et al.[118] developed a stoichiometric thermodynamic equilibrium model, which was used to evaluate the suitability of various biomass feedstock for producing H_2-rich syngas. The model was compared with experimental measurements from steam gasification[119] of rice husk and air-steam gasification[120] of sawdust. In both cases, the model predictions were closely in agreement with the experimental data.

Modification of biomass gasification equilibrium models to account for non-equilibrium effects has been the focus of other recent studies. For example, Ghassemi and Shahsavan-Markadeh[121] modified an equilibrium model based on Gibbs free energy minimization by incorporating the models developed by Azzone et al.[122] for carbon conversion efficiency and Barman et al.[123] for tar formation. The original and modified equilibrium models were used to evaluate the effects of ER, gasification temperature, moisture content, biomass feedstock, and gasifying agent on higher heating value (HHV) and gasification cold gas efficiency, as well as the effect of ER on syngas composition. Ghassemi and Shahsavan-Markadeh demonstrated that with their modifications, increased model prediction accuracy

could be obtained compared to the experimental data from Narvaez et al.[93] and Subramanian et al.[124].

Lim and Lee[125] defined a quasi-equilibrium model that integrates non-equilibrium factors with a thermodynamic equilibrium model. The non-equilibrium factors were estimated from empirical data and equations as functions of ER to address the deviation of the real gasification process from the thermodynamic equilibrium assumptions. In another work, Kangas et al.[126] described a constrained free energy-based thermodynamic equilibrium model that incorporates extent of reaction constraints to account for gasification process variables. The model concurrently resolves enthalpy and chemical species during biomass gasification as a restricted partial equilibrium with a one calculation step. Kangas et al.[126] reported that the prediction result for major syngas species (CO, CO_2, H_2, H_2O, and CH_4) fits experimental data but the prediction result for minor syngas species (C_2H_2, C_2H_4, C_2H_6, C_3H_8, C_6H_6) did not fit experimental data.

Kinetic rate modeling

Kinetic rate models are more difficult to formulate than thermodynamic equilibrium models because they consider the actual rates of chemical reactions as well as the effects of macro, meso, and microscale heat and mass transport phenomena inside the reactor. The difficulties arise because chemical reaction rates depend on both the local temperature at species concentrations at the reaction sites, which can often be at solid surfaces inside catalyst and/or biomass particles. When such models are utilized, the resulting prediction accuracies can be remarkably enhanced, but their practical applicability can be problematic due to unknown parameters and the computational expense involved in determining the actual conditions at the point of reaction. This difficulty increases with the size and design complexity of gasification reactor system, the complexity of the biomass chemical composition, and the amount of desired detail that needs to be predicted.

One common technique used to simplify the numerical complexity kinetic rate modeling of biomass gasification is the separation of the overall process into distinct small-scale processes or reactions that can be studied under more ideal or tightly specified conditions. For example, it can be assumed that the overall gasification process can be divided into the distinct stages of devolatilization, oxidation, reduction, and tar-cracking. During each of these stages, reaction rates can be determined by rate laws (e.g., Arrhenius kinetics) that express the rates of each reaction as a function of a temperature dependent reaction rate constant and the concentration of the reactants and products raised to appropriate powers.[127] The reaction rate constant is typically a crucial parameter because it often reflects a very strong dependence of the reaction rate on temperature. For Arrhenius kinetics, this is usually expressed as:

$$r = A\,T^{a} e^{\left(\frac{-E_a}{RT}\right)} f(C) \qquad (2.9)$$

Non-Arrhenius type temperature effects have also been observed.[128] Table 2.6 lists a wide range of biomass gasification models where reaction kinetics were found to be useful and the corresponding references from which they were obtained. An example of how reaction kinetics have been used for biomass gasification is found in the results reported by Inayat et al.[149], who investigated the production of hydrogen from steam gasification of wood with in-situ CO_2 adsorption. The influence of temperature, sorbent/biomass ratio, and steam/biomass ratio on the production of H_2, CO, CO_2, and CH_4 were reported and interpreted using kinetic arguments. Hydrogen production was reported to initially increase with temperature, but then decreased as temperature increased for temperatures above 950 K. This work assumed that tar and ash production were negligible and only char gasification, Boudouard, methanation, methane reforming, water gas shift, and carbonation reactions were proposed to occur. However, the reported hydrogen concentration fits the empirical data from Mahishi and Goswami[150] better than the result from the equilibrium modeling conducted by Florin and Harris[151]. Also, Giltrap et al.[152] combined kinetic models and mass and energy balance equations to simulate the gasification of char in a downdraft gasifier. The simulation was limited to the reduction zone of the gasifier and output gas was tracked for CO_2, CO, CH_4, H_2O H_2, and N_2 concentration. Although the predicted concentration of gas species agreed with experimental results, the concentration of CH_4 was over-predicted. This over-prediction problem was attributed to the fact that the methane-oxidation reaction was not involved in the modeled reaction scheme.

To account for the complex molecular composition of biomass, distributed activated energy models (DAEM) have emerged as powerful kinetic modeling tools because they can be used to represent the disperse activation energies involved as the multiple types of molecules in the raw biomass and evolving char and volatiles react. The unique characteristic of DAEM models is that they assume a range of values (i.e., probability distribution) for the activation energies of the tracked reactions. Therefore, the activation energies of one or more reactions are described using probability density functions, such as the Gaussian distribution and Logistic distribution (Equations (2.10) and (2.11), respectively).[153] Meng et al.[154] developed DAEM for the pyrolysis and gasification of solid wastes components in a macro-TGA. Using experimental data, they derived activation energy distributions for the pyrolysis and gasification of the model solid waste components used. Khonde and Chaurasia[155] described the formation of primary gases (CH_4, CO, H_2, and CO_2) and tar cracking using single-reaction model and DAEM. Single-reaction model is the conventional Arrhenius kinetics with one value of activation energy. They concluded that tar cracking improved H_2 production and DAEM produced better fit to the experimental data than SRM.

Table 2.6. Kinetic rate models for different gasification reactions.

Stoichiometry	Kinetic models	
CELL → Vg + Pt + CHAR	$1.09 \times 10^{06} \exp\left(\frac{-192000}{RT_p}\right)(1-\alpha)$	129
	$6.22 \times 10^{10} \exp\left(\frac{-137231}{RT_p}\right)(1-\alpha)^{1.01}$	30
	$1.84 \times 10^{17} \exp\left(\frac{-230100}{RT_p}\right)(1-\alpha)$	130
HCELL → Vg + Pt + CHAR	$2.69 \times 10^{04} \exp\left(\frac{-133000}{RT_p}\right)(1-\alpha)$	129
	$9.30 \times 10^{09} \exp\left(\frac{-141546}{RT_p}\right)(1-\alpha)^{1.06}$	30
	$1.98 \times 10^{11} \exp\left(\frac{-149700}{RT_p}\right)(1-\alpha)$	130
LIG → Vg + Pt + CHAR	$2.22 \times 10^{01} \exp\left(\frac{-87000}{RT_p}\right)(1-\alpha)$	129
	$9.77 \times 10^{00} \exp\left(\frac{-38795}{RT_p}\right)(1-\alpha)^{2.53}$	30
	$5.14 \times 10^{09} \exp\left(\frac{-154300}{RT_p}\right)(1-\alpha)^{2.60}$	130
Pt → Vg + St	$9.55 \times 10^{04} \exp\left(\frac{-1.12 \times 10^{4}}{T}\right) \rho_{\text{primary tar}}$	

CELL: Cellulose, HCELL: Hemicellulose, Pt: Primary tar, CHAR: bio-char, St: Secondary tar, LIG: Lignin

Table 2.6. Continued.

Stoichiometry	Kinetic models	
$C + H_2O \rightarrow CO + H_2$	$\frac{k_1 P_{H_2O}}{1 + k_2 P_{H_2O} + k_3 P_{H_2}}$ $k_1 = 4.93 \times 10^{03} \exp\left(\frac{-18522}{T_p}\right)$ $k_2 = 1.11 \times 10^{01} \exp\left(\frac{-3548}{T_p}\right)$ $k_3 = 1.53 \times 10^{-9} \exp\left(\frac{25161}{T_p}\right)$	131
$C + H_2O \rightarrow CO + H_2$	$2.47 \times 10^{02} \exp\left(\frac{-21060}{T_p}\right)$	132
$C + H_2O \rightarrow CO + H_2$	$4.56 \times 10^{01} \exp\left(\frac{-43.7}{RT_p}\right) T_p$	133
$C + H_2O \rightarrow CO + H_2$	$2.00 \times 10^{-3} \exp\left(\frac{-1.96 \times 10^8}{RT_p}\right)$	134
$C + H_2O \rightarrow CO + H_2$	$6.33 \times 10^{01} \exp\left(\frac{-14051}{T}\right)$	135
$C + H_2O \rightarrow CO + H_2$	$1.52 \times 10^{04} \exp\left(\frac{-121620}{RT}\right)$	136
$C + CO_2 \rightarrow 2CO$	$2.47 \times 10^{02} \exp\left(\frac{-21060}{T_p}\right)$	132

Table 2.6. Continued.

Stoichiometry	Kinetic models	
$C + CO_2 \rightarrow 2CO$	$8.30 \times 10^{00} \exp\left(\frac{-43.7}{RT_p}\right) T_p$	133
$C + CO_2 \rightarrow 2CO$	$3.00 \times 10^{-1} \exp\left(\frac{-2.00 \times 10^{8}}{RT_p}\right)$	134
$C + CO_2 \rightarrow 2CO$	$2.08 \times 10^{03} \exp\left(\frac{-18036}{T}\right)$	135
$C + CO_2 \rightarrow 2CO$	$3.62 \times 10^{01} \exp\left(\frac{-77390}{RT}\right)$	136
$C + O_2 \rightarrow CO_2$	$8.71 \times 10^{03} \exp\left(\frac{-17967}{T_p}\right)$	132
$C + 0.5O_2 \rightarrow CO$	$\left(-1.68 \times 10^{-2} + \left(1.32 \times 10^{-5} T_p\right)\right) T_p$	133
$C + 0.5O_2 \rightarrow CO$	$2.51 \times 10^{-3} \exp\left(\frac{-7.48 \times 10^{7}}{RT_p}\right)$	134
$C + 0.5O_2 \rightarrow CO$	$5.96 \times 10^{02} T_p \exp\left(\frac{-1800}{T}\right)$	135
$C + 2H_2 \rightarrow CH_4$	$1.20 \times 10^{-1} \exp\left(\frac{-17921}{T_p}\right)$	132
$C + 2H_2 \rightarrow CH_4$	$4.19 \times 10^{-3} \exp\left(\frac{-19210}{RT}\right)$	136

Table 2.6. Continued.

Stoichiometry	Kinetic models	
$H_2 + 0.5O_2 \rightarrow H_2O$	$2.20 \times 10^{09} \exp\left(\frac{-109000}{RT}\right) C_{H_2}^{1} C_{O_2}^{1}$	137
$H_2 + 0.5O_2 \rightarrow H_2O$	$2.78 \times 10^{03} \exp\left(\frac{-1510}{T}\right)(K)$ $K = C_{CO} C_{H_2O} - \frac{C_{CO_2} C_{H_2}}{0.0265 \exp\left(\frac{3968}{T}\right)}$	135
$CO + H_2O \leftrightarrow CO_2 + H_2$	$2.78 \times 10^{03} \exp\left(\frac{-12560}{RT}\right) C_{CO}^{1} C_{H_2O}^{1}$	138
$CO + H_2O \rightarrow CO_2 + H_2$	$2.75 \times 10^{09} \exp\left(\frac{-8.37 \times 10^{7}}{RT}\right) C_{CO}^{1} C_{H_2O}^{1}$	139
$CO + H_2O \rightarrow CO_2 + H_2$	$5.16 \times 10^{15} \exp\left(\frac{-3430}{T}\right) T^{-1.5} C_{CO} C_{O_2}^{0.5}$	135
$CO + 0.5O_2 \rightarrow CO_2$	$2.32 \times 10^{12} \exp\left(\frac{-167000}{RT}\right) C_{CO}^{1} C_{O_2}^{0.25} C_{H_2O}^{0.5}$	140
$CO + 0.5O_2 \rightarrow CO_2$	$1.30 \times 10^{11} \exp\left(\frac{-126000}{RT}\right) C_{CO}^{1} C_{O_2}^{0.5} C_{H_2O}^{0.5}$	141
$CO + 0.5O_2 \rightarrow CO_2$	$4.78 \times 10^{08} \exp\left(\frac{-66900}{RT}\right) C_{CO}^{1} C_{O_2}^{0.3} C_{H_2O}^{0.5}$	142
$CO + 0.5O_2 \rightarrow CO_2$	$1.28 \times 10^{17} \exp\left(\frac{-289000}{RT}\right) C_{CO}^{1} C_{O_2}^{0.25} C_{H_2O}^{0.5}$	143

Table 2.6. Continued.

Stoichiometry	Kinetic models	
$CO + 0.5O_2 \rightarrow CO_2$	$1.00 \times 10^{10} \exp\left(\frac{-126000}{RT}\right) C_{CO}^{1} C_{O_2}^{0.5} C_{H_2O}^{0.5}$	144
$CO + 0.5O_2 \rightarrow CO_2$	$1.00 \times 10^{15} \exp\left(\frac{-16000}{T}\right) C_{CO} C_{O_2}^{0.5}$	135
$CH_4 + H_2O \rightarrow CO + 3H_2$	$3.12 \times 10^{02} \exp\left(\frac{-30000}{RT}\right)$	132
$CH_4 + H_2O \rightarrow CO + 3H_2$	$3.30 \times 10^{10} \exp\left(\frac{-2.40 \times 10^{5}}{RT}\right) C_{CH_4}^{1.7} C_{H_2}^{-0.8}$	145
$CH_4 + H_2O \rightarrow CO + 3H_2$	$7.30 \times 10^{01} \exp\left(\frac{-36150}{RT}\right) (K)$ $K = C_{CH_4}^{1} C_{H_2O}^{1} - \frac{C_{CO}^{1} C_{H_2}^{3}}{k_{eq,4}}$	136
$CH_4 + H_2O \rightarrow CO + 3H_2$	$3.00 \times 10^{08} \exp\left(\frac{-1.26 \times 10^{8}}{RT}\right) C_{CH_4}^{1} C_{H_2O}^{1}$	139
$CH_4 + 0.5O_2 \rightarrow CO + 2H_2$	$4.40 \times 10^{11} \exp\left(\frac{-1.26 \times 10^{8}}{RT}\right) C_{CH_4}^{0.5} C_{O_2}^{1.25}$	139
$CH_4 + 2O_2 \rightarrow CO_2 + 2H_2O$	$3.00 \times 10^{05} \exp\left(\frac{-15042}{T}\right) C_{H_2O} C_{CH_4}$	135
$CH_4 + 0.5CO_2 + 0.5H_2O \rightarrow 1.5CO + 2.5H_2$	$4.50 \times 10^{10} \exp\left(\frac{-2.50 \times 10^{5}}{RT}\right) C_{CH_4}$	146

Table 2.6. Continued.

Stoichiometry	Kinetic models	
$C_2H_4 + O_2 \xrightarrow{*} 2CO + 2H_2O$	$1.58 \times 10^{20} \exp\left(\frac{-19977.82}{RT}\right) C_{C_2H_4}^{0.7} C_{O_2}^{0.8}$	147
$C_2H_6 + O_2 \rightarrow 2CO + 3H_2$	$4.20 \times 10^{11} \exp\left(\frac{-1.26 \times 10^{8}}{RT}\right) C_{C_2H_6}^{0.5} C_{O_2}^{1.25}$	139
$C_3H_8 + 1.5O_2 \rightarrow 3CO + 4H_2$	$4.00 \times 10^{11} \exp\left(\frac{-1.26 \times 10^{8}}{RT}\right) C_{C_3H_8}^{0.5} C_{O_2}^{1.25}$	139
$C_4H_{10} + 2O_2 \rightarrow 4CO + 5H_2$	$3.80 \times 10^{11} \exp\left(\frac{-1.26 \times 10^{8}}{RT}\right) C_{C_4H_{10}}^{0.5} C_{O_2}^{1.25}$	139
$C_6H_6 + 3CO_2 + 3H_2O \rightarrow 9CO + 6H_2$	$2.00 \times 10^{11} \exp\left(\frac{-1.96 \times 10^{5}}{RT}\right) C_{C_6H_6}$	146
$C_6H_6 + H_2 + H_2O \rightarrow CH_4 + CO_2 + 2CO + 4H_2 + C_2H_4$	$2.00 \times 10^{16} \exp\left(\frac{-4.43 \times 10^{5}}{RT}\right) C_{C_6H_6}^{1.3} C_{H_2}^{-0.4} C_{H_2O}^{0.2}$	148
$C_7H_8 + H_2 + H_2O \rightarrow CH_4 + CO_2 + 3CO + 6H_2 + C_2H_4$	$3.30 \times 10^{10} \exp\left(\frac{-2.47 \times 10^{5}}{RT}\right) C_{C_7H_8}^{1} C_{H_2}^{0.5}$	148
$C_{10}H_8 + 5CO_2 + H_2O \rightarrow 15CO + 9H_2$	$4.30 \times 10^{13} \exp\left(\frac{-3.32 \times 10^{5}}{RT}\right) C_{C_{10}H_8}^{0.2} C_{H_2}^{0.3}$	146
$1.2C_{10}H_8 + 1.7H_2 + 1.5H_2O \rightarrow C_6H_6 + CH_4 + C_2H_4 + H_2 + CO + CO_2 + C$	$1.70 \times 10^{14} \exp\left(\frac{-3.50 \times 10^{5}}{RT}\right) C_{C_{10}H_8}^{1.6} C_{H_2}^{-0.5}$	148

$$f(E) = \frac{1}{\sigma\sqrt{2\pi}} \exp\left(\frac{-(\overline{E} - E_0)^2}{2\sigma^2}\right) \quad (2.10)$$

$$f(E) = \frac{\pi}{\sigma\sqrt{3}} \left(\frac{\exp\left(-\pi(\overline{E} - E_0)/\left(\sigma\sqrt{3}\right)\right)}{\left(1 + \exp\left(-\pi(\overline{E} - E_0)/\sigma\sqrt{3}\right)\right)^2}\right) \quad (2.11)$$

Multiphase modeling of gasification

Computational fluid dynamics modeling provides a numerical approach for combining the effects of complex hydrodynamic mixing with chemical kinetics and mass and heat transport in multiphase flow reactors. The key challenge in accounting for all these effects simultaneously is that it imposes a huge computational burden. Nevertheless, over the last decades, computational fluid dynamics (CFD) modeling of biomass gasification systems have become attractive, mainly because of the fast advances in computing power. CFD models combine the laws of conservation of mass, momentum, energy, and chemical species to numerically predict the distribution of physical, thermal, and chemical quantities across the reactor volume. When coupled with the correct mathematical description of the physics and chemistry of the gasification system (sub-models), CFD models provide accurate and detailed simulations. Figure 2.4 shows a network of conservation laws and sub-models that can be incorporated in the CFD modeling of biomass gasification, with the conservation laws being the backbone of the network.

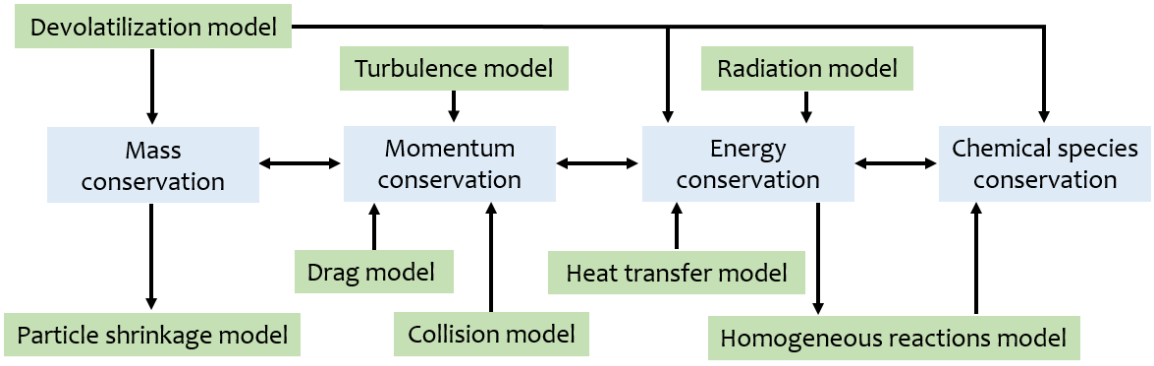

Figure 2.4. CFD sub-models involved in biomass gasification.

For reactor systems involving both solid and gas phase flows, such as in biomass gasification, CFD models are mainly divided into Eulerian-Eulerian and Eulerian-Lagrangian frames of reference. With the Eulerian-Eulerian framework, all phases are considered as inter-penetrating continuum and their flow behavior is explained using the Navier-Stokes equations linked with the volume fraction of each phase. Granular particle models, such as the kinetic theory of granular flows (KTGF), are used to describe the interactions within the solid phase (particle-particle interactions). KTGF is a derivative of the kinetic theory of gases and includes energy transfer during particle collisions. However, the Eulerian-Lagrangian framework considers the gas phase as a continuum and tracks particles or groups of particles in the solid phase as discrete elements using Newton's laws of motion. Eulerian-Lagrangian method is more accurate and detailed than Eulerian-Eulerian method, but it is more computationally expensive. Thus, computational cost and simulation time must be considered when considering which of these frameworks to use.

Both commercial (Barracuda®, ANSYS FLUENT, COMSOL, and simFlow) and non-commercial (OpenFOAM, OVERFLOW, and CFL3D) CFD codes are in widespread use for multiphase flow reactors. Numerically, differential balances with reactors are solved using multiple numerical methods including the finite volume method (FVM), finite difference method (FDM), and finite element method (FEM). FVM is the most common method used because it conserves computational memory and relates most directly to the governing heat, mass, and momentum balances. Several CFD models have been reportedly used for biomass and coal gasification.[29, 31, 127, 156-162]

Oevermann et al.[163] and Ku et al.[156] have conducted Eulerian-Lagrangian simulations of biomass gasification in fluidized bed reactors using OpenFOAM. They solved particle (biomass and bed material) motion using the discrete element method (DEM), in which the Hertz-Mindlin particle contact model was used to describe the particle collisional behavior (Figure 2.5). To handle biomass particle size variations, they assumed that the diameter of the biomass particles shrinks proportionally to their mass (Equation (2.12)). Their simulation results for the concentration of CO and H_2 showed good fit with experimental data.

$$d_p = \sqrt[3]{6\frac{m_p}{\pi\rho_p}} \qquad (2.12)$$

Liu et al.[164] simulated a pilot-scale dual fluidized-bed biomass gasifier using Multiphase Particle-In-Cell (MP-PIC) method. The gas phase was resolved by Large Eddy Simulation (LES) and interphase transport coefficient was described following Wen and Yu[165] model. The solid phase motion modeling followed a blended acceleration model approach as described by O'Rourke et al.[166]. Their CFD model was developed in Barracuda Virtual Reactor software and was used to predict the effects of gasification temperature, steam-to-biomass ratio, and equivalence ratio. A good fit of the prediction results with experimental data was also reported.

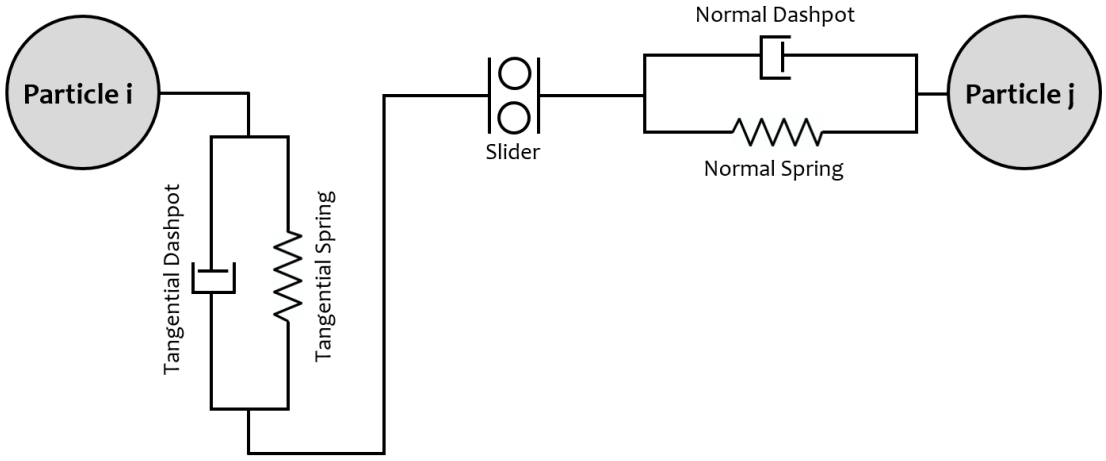

Figure 2.5. Hertz-Mindlin particle contact model.

Gerber et al.[167] presented a 2D CFD simulation of wood gasification in a fluidized bed using char as bed material. The behavior of the dispersed solid phase (wood and char particles) was assumed to follow the kinetic theory of granular material coupled with Syamlal-O'Brien drag model. Using this approach, the authors evaluated the influence of operating conditions (such as initial bed height and wood feeding rate) and model parameters (such as boundary conditions and pyrolysis kinetics) on product gas and temperature distribution. They reported that the concentration of primary tar increased and the temperature at the reactor outlet decreased with increasing heat exchange coefficient.

Ku et al.[168] investigated the effect of torrefaction on the performance of biomass (forest residue and spruce) gasification using a 3D CFD model with Eulerian-Lagrangian framework. The equivalence ratio (0.25 – 0.35), steam-to-biomass ratio (0 – 1), and biomass particle size (0.3 – 0.7 mm) were varied whereas the operating temperature was fixed at 1400 °C. They concluded that torrefaction notably decreased carbon conversion efficiency and H_2 concentration. Also, H_2 concentration increased as steam-to-biomass ratio increased.

Turbulent heat and mass transport in biomass gasification reactors are key features that need to be resolved in CFD models A significant portion of research on CFD modeling of biomass gasification has relied on large eddy simulations (LES) and Reynolds-averaged Navier-Stokes (RANS) turbulence models to account for these effects. RANS models decompose flow values into steady and unsteady (turbulence) components. Using the Boussinesq hypothesis, RANS models

describe the turbulence (in terms of effective Reynolds stresses) as a function of the effective viscosity of the fluid and the velocity field gradient. In LES models, the continuum and momentum balances in unsteady flow with a length scale larger than the local mesh size (large-scale turbulence) is explicitly resolved and small-scale turbulence is described using approximate mathematical models to achieve sub-scale closure of the momentum balances. Abani and Ghoniem[133] found that LES model captures unsteady flow structures inside the gasifier better than RANS model. Consequently, they reported that LES model is more accurate than RANS model in predicting char-conversion efficiency and gas product distributions.

The increasing relevance of CFD modeling to many kinds of research across the world, coupled with the advancement in computational power, make CFD modeling of biomass gasification an indispensable tool. CFD modeling of biomass gasification is therefore key to enhancing our current understanding of biomass gasification, which is needed for the commercial deployment of biomass gasification.

Biomass gasification: Challenges and future perspectives

Various strategies have emerged over the past years to study the chemistry of biomass gasification and ensure high biomass gasification performance and syngas quality in a cost-effective manner. However, several challenges still exist that inhibit the commercial deployment of biomass gasification. This section highlights some important lessons learned from different projects and studies, challenges faced by biomass gasification technologies, and suggested approaches to ensure progress.

Biomass gasification challenges may be broadly classified as pre-gasification, gasification, and post-gasification issues, with all being inter-connected and critical to the overall performance of biomass gasification. Flowability problems, because of wide size distribution and large aspect ratio of biomass particles after grinding, may cause downtime due to clogging of grinders, conveyors, and feeders. Although grinding dried feedstocks has been found to improve flow behavior, the flowability problems are not completely eradicated.[69, 169] It is imperative to explore technologies that can produce easily flowing particulate biomass. Such technologies will not only resolve flowability problems and reduce downtime risk, but they will enhance intra-particle heat flux during gasification and fluidization behavior, in the case of fluidized beds.

A careful examination of biomass gasification studies shows that there is high variability in biomass gasification performance and syngas quality (Table 2.7). This is mostly due to the inherent and logistics-related variations in the properties of biomass feedstock and the sensitivity of biomass gasification performance and syngas quality to biomass gasification process variables. [170] The high variability in biomass gasification performance and syngas quality significantly raises the risks associated with the commercialization of biomass gasification. It is therefore important to create a robust approach to predict biomass gasification performance and syngas quality through a synergetic combination of available modeling

approaches. Biomass gasification models need to account for deviation from ideal assumptions that simplify them. For example, more models are needed to account for particle shape, particle size distribution, particle attrition, slagging, particle shrinkage, and particle elutriation rate to produce improved and realistic simulations of biomass gasification.

There is far-reaching information on the mechanistic transformation of syngas contaminants during gasification, but their abatement measures are still limited. The presence of syngas contaminant in syngas is therefore the foremost challenge faced by post-gasification processes.[172] According to a recent techno-economic analysis, syngas makes up the largest share of the capital cost and a significant share of the operating cost.[173]

There are three practical strategies that have been used to address syngas contaminant issues (primary, secondary, and tertiary strategies). Primary strategies are one-pot approaches focused on the in-situ destruction (partial or complete) of syngas contaminants during biomass gasification by selecting optimum operating conditions and catalysts. Although decades of biomass gasification studies have led to significant progress in reducing syngas contaminants during gasification, primary strategies still do not meet the recommended syngas contaminant tolerances for most downstream processes (Table 2.8). The ineffectiveness of primary strategies is addressed by secondary strategies, which are focused on the use of ex-situ syngas cleanup processes to remove syngas contaminants. Tertiary strategies emphasize the creation of novel post-gasification processes and systems that are highly tolerant to syngas contaminants. A demonstration of the tertiary strategy is the introduction and assessment of a tar-tolerant homogeneous charge compression ignition (HCCI) engine by Bhaduri et al.[174]

Secondary approaches are the most common solution to syngas contaminants and are broadly categorized as cold and hot gas cleanup. Cold gas cleanup uses liquid adsorbents to wash contaminants from syngas at low temperatures (< 100 °C). This method has been demonstrated to have high contaminant removal efficiency but low thermal efficiency due to cooling of the syngas. Water is a cheap and effective syngas washing adsorbent for removing light tars, ammonia, hydrogen cyanide and particulate matter. The major downside to the water washing of syngas is wastewater disposal and treatment. Throughout the last decades, efforts have therefore been devoted to non-polar washing adsorbents, such as engine oil, rapeseed oil methyl ester, and diesel fuel.[38, 179] Despite the success of cold gas cleanup (especially from a tar removal standpoint), the loss of heat drastically reduces its economic viability. Hot gas cleanup has therefore attracted more interest in recent studies.

Table 2.7. Summary of some syngas composition reported in the literature from the gasification of pine wood.

Feed rate (g/min)	Temperature (°C)	Gasifying agent	Gas composition (vol.%)				Tar (g/Nm^3)	
			CO	CO_2	H_2	CH_4		
4.30	800	S/B = 0.52	21.7	37.8	27.2	9.2	3.89	[171]
4.07	800	S/B = 0.66	15.7	47.0	24.9	8.6	3.04	[171]
4.10	800	S/B = 0.64	16.9	43.6	27.3	8.5	3.41	[171]
4.07	800	S/B = 0.68	18.4	40.5	27.9	9.2	3.42	[171]
4.35	750	S/B = 0.52	22.9	35.4	27.6	9.9	5.70	[100]
4.30	800	S/B = 0.52	21.7	37.8	27.2	9.2	3.88	[100]
4.02	850	S/B = 0.57	18.7	42.0	26.7	8.8	2.62	[100]
9.00	790	ER = 0.25	9.32	11.0	3.5	11.2	1.56	[59]
9.00	935	ER = 0.25	11.8	10.1	6.9	5.4	3.87	[59]
9.00	1000	ER = 0.25	12.3	9.4	7.6	4.6	2.08	[59]
N/A	790	ER = 0.25	34.7	27.2	24.9	12.0	9.70	[55]
N/A	934	ER = 0.35	35.8	30.4	26.6	7.2	2.50	[55]
204*	800	ER = 0.32	36.2	34.9	18.1	7.8	1.76*	[93]
195*	800	ER = 0.37	31.2	36.0	22.8	6.5	4.21*	[93]
138*	810	ER = 0.47	29.9	35.8	23.9	7.2	1.35*	[93]
242*	800	ER = 0.26	31.2	36.0	22.8	6.5	0.97*	[93]
231*	790	ER = 0.36	31.2	36.0	22.8	6.5	1.23*	[93]
240*	800	ER = 0.32	32.7	24.6	17.3	8.2	11.53*	[93]

ER: Equivalence ratio, S/B: steam to biomass ratio (g H_2O/g biomass dry), *: Feed rate unit is in $kg/h.m^2$ and Tar unit is in (g/kg of daf biomass)

Table 2.8. Downstream applications and the contaminant tolerance.[25, 175-178]

Contaminant	IC engines*	Gas turbine	MeOH synthesis	FT synthesis*
Tar	10-50 mg/m^3	< 5 mg/Nm^3	< 0.1 mg/m^3	< 1 ppmV
Sulfur		< 1 ppm	< 1 mg/m^3	< 1 ppmV
Nitrogen		< 50 µl/l	< 0.1 mg/m^3	< 1 ppmV
Halides		< 0.5 ppm	< 0.1 mg/m^3	< 10 ppbV
Metals		< 50 ppb		< 10 ppbV

*IC: Internal combustion, MeOH: Methanol, FT: Fischer-Tropsch.

Hot gas cleanup focuses on the decomposition and reforming (thermal and catalytic) of syngas contaminants at high temperatures (< 400 °C). Hot gas cleanup is thermally efficient, but catalyst deactivation and regeneration are common occurrence. The successful deployment of hot gas cleanup technology will require continued and sustained improvement of available catalysts and sorbents with activity for removing syngas contaminant. Apart from developing a catalyst that is cost-effective from earth-abundant materials, this improvement needs to be focused on the development of *i)* a single catalyst capable of removing all or most contaminants; *ii)* highly deactivation resistant catalysts; and *iii)* efficient catalyst regeneration processes. Furthermore, extensive modeling studies are needed to establish the contributions of gasification process variables to syngas contaminant yield. This must be preceded by the development of useful kinetics models for syngas contaminants that have been hitherto scarce.

Nomenclature

A	Arrhenius pre-exponential parameter (s^{-1})
CM	Char matrix
DP	Degree of polymerization (dimensionless)
d_p	Diameter of particle (m)
E_a	Activation energy (J/mol)
$f(C)$	Function of conversion factor and concentration of chemical species
K_j	Equilibrium constant of reaction j
m_p	Mass of particle (kg)
R	Gas constant

r	Rate of reaction (mol/s)
T	Temperature (K)
a	Exponent of temperature term (dimensionless)
T_p	Temperature of particle (K)
ρ_p	Density of particle (kg/m^3)
ΔG_j^o	Variation of standard Gibbs free energy reaction j as function of temperature
$\rho_{\text{primary tar}}$	Density of primary tar (kg/m^3)
daf	dry ash free basis

References

1. EIA *March 2018 - Monthly energy review*; U.S. Energy Information Administration: Washington, DC, 2018; pp 2 - 244.
2. Brutschin, E.; Fleig, A., Innovation in the energy sector – The role of fossil fuels and developing economies. *Energy Policy* **2016,** *97*, 27-38.
3. EPA Overview of greenhouse gases. https://www.epa.gov/ghgemissions/overview-greenhouse-gases (accessed 09-19).
4. McKendry, P., Energy production from biomass (part 1): overview of biomass. *Bioresource Technology* **2002,** *83* (1), 37-46.
5. Demirbas, A., Combustion characteristics of different biomass fuels. *Progress in Energy and Combustion Science* **2004,** *30* (2), 219-230.
6. Matsumura, Y.; Kato, A.; Sasaki, H.; Yoshida, T., Gasification of liquidized biomass in supercritical water using partial oxidation. In *Progress in Thermochemical Biomass Conversion*, 1st ed.; Bridgwater, A. V., Ed. Blackwell Science Ltd: Oxford, England, 2001; pp 237–251.
7. Patra, T. K.; Sheth, P. N., Biomass gasification models for downdraft gasifier: A state-of-the-art review. *Renewable and Sustainable Energy Reviews* **2015,** *50* (1), 583-593.
8. Baruah, D.; Baruah, D., Modeling of biomass gasification: a review. *Renewable and Sustainable Energy Reviews* **2014,** *39*, 806-815.
9. Abdoulmoumine, N.; Adhikari, S.; Kulkarni, A.; Chattanathan, S., A review on biomass gasification syngas cleanup. *Appl Energ* **2015,** *155* (1), 294-307.
10. Woolcock, P. J.; Brown, R. C., A review of cleaning technologies for biomass-derived syngas. *Biomass and Bioenergy* **2013,** *52* (1), 54-84.
11. Palma, C. F., Modelling of tar formation and evolution for biomass gasification: a review. *Appl Energ* **2013,** *111*, 129-141.
12. Puig-Arnavat, M.; Bruno, J. C.; Coronas, A., Review and analysis of biomass gasification models. *Renewable and Sustainable Energy Reviews* **2010,** *14* (9), 2841-2851.
13. Sikarwar, V. S.; Zhao, M.; Clough, P.; Yao, J.; Zhong, X.; Memon, M. Z.; Shah, N.; Anthony, E. J.; Fennell, P. S., An overview of advances in biomass gasification. *Energy & Environmental Science* **2016,** *9* (10), 2939-2977.
14. Bridgwater, A. V., Pyrolysis of biomass. *Transformations to Effective Use: Biomass Power for the World" eds. W. van Swaaij, S. Kersten and W. Palz* **2015,** *6*, 473-514.
15. Bridgwater, A. V., Renewable fuels and chemicals by thermal processing of biomass. *Chemical Engineering Journal* **2003,** *91* (2), 87-102.
16. Mohan, D.; Pittman, C. U.; Steele, P. H., Pyrolysis of Wood/Biomass for Bio-oil: A Critical Review. *Energy & Fuels* **2006,** *20* (3), 848-889.
17. Goyal, H. B.; Seal, D.; Saxena, R. C., Bio-fuels from thermochemical conversion of renewable resources: A review. *Renewable and Sustainable Energy Reviews* **2008,** *12* (2), 504-517.
18. Hendry, R. F., Antoine Lavoisier (1743–1794). In *Philosophy of Chemistry*, Elsevier: 2012; pp 63-70.

19. Nussbaumer, T., Combustion and Co-combustion of Biomass: Fundamentals, Technologies, and Primary Measures for Emission Reduction. *Energy & Fuels* **2003,** *17* (6), 1510-1521.
20. Tillman, D. A.; Rossi, A. J.; Kitto, W. D., *Wood combustion. Principles, processes, and economics*. Academic Press.: New York, New York, 1981.
21. Basu, P., *Biomass gasification and pyrolysis: practical design and theory*. Academic press: 2010.
22. Brown, R. C., *Thermochemical processing of biomass: conversion into fuels, chemicals and power*. Wiley: Hoboken, New Jersey, 2011; Vol. 12.
23. Annamalai, K.; Puri, I. K., *Combustion science and engineering*. CRC press: 2007; Vol. 7.
24. Moens, L., Chapter 9 Renewable feedstocks. In *Sustainability Science and Engineering*, Abraham, M. A., Ed. Elsevier: 2006; Vol. Volume 1, pp 177-199.
25. Bridgwater, A., The technical and economic feasibility of biomass gasification for power generation. *Fuel* **1995,** *74* (5), 631-653.
26. Basu, P., *Biomass Gasification and Pyrolysis*. 1st ed.; Elsevier: Oxford, England, 2010.
27. Basu, P., *Combustion and Gasification in Fluidized Beds*. 1st ed.; Taylor & Francis Group, LLC: Florida, USA, 2006.
28. Adeyemi, I.; Janajreh, I., Modeling of the entrained flow gasification: Kinetics-based ASPEN Plus model. *Renewable Energy* **2015,** *82* (1), 77-84.
29. Liu, H.; Elkamel, A.; Lohi, A.; Biglari, M., Computational fluid dynamics modeling of biomass gasification in circulating fluidized-bed reactor using the Eulerian–Eulerian approach. *Ind. Eng. Chem. Res.* **2013,** *52* (51), 18162-18174.
30. Lee, S.-B.; Fasina, O., TG-FTIR analysis of switchgrass pyrolysis. *Journal of analytical and applied pyrolysis* **2009,** *86* (1), 39-43.
31. Wu, Y.; Zhang, Q.; Yang, W.; Blasiak, W., Two-dimensional computational fluid dynamics simulation of biomass gasification in a downdraft fixed-bed gasifier with highly preheated air and steam. *Energy Fuels* **2013,** *27* (6), 3274-3282.
32. Gómez-Barea, A.; Leckner, B., Modeling of biomass gasification in fluidized bed. *Progress in Energy and Combustion Science* **2010,** *36* (4), 444-509.
33. Higman, C.; Van der Burgt, M., *Gasification*. Gulf professional publishing: 2011.
34. Klass, D. L., *Biomass for renewable energy, fuels, and chemicals*. Academic press: 1998.
35. Knoef, H.; Ahrenfeldt, J., *Handbook biomass gasification*. BTG biomass technology group The Netherlands: 2005.
36. Pakhare, D.; Spivey, J., A review of dry (CO 2) reforming of methane over noble metal catalysts. *Chemical Society Reviews* **2014,** *43* (22), 7813-7837.
37. Oyedeji, O.; Daw, C. S.; Labbe, N.; Ayers, P.; Abdoulmoumine, N., Kinetics of the release of elemental precursors of syngas and syngas contaminants during devolatilization of switchgrass. *Bioresource Technology* **2017,** *244*, 525-533.

38. Broer, K. M.; Woolcock, P. J.; Johnston, P. A.; Brown, R. C., Steam/oxygen gasification system for the production of clean syngas from switchgrass. *Fuel* **2015,** *140*, 282-292.
39. Bain, R. L.; Dayton, D. C.; Carpenter, D. L.; Czernik, S. R.; Feik, C. J.; French, R. J.; Magrini-Bair, K. A.; Phillips, S. D., Evaluation of catalyst deactivation during catalytic steam reforming of biomass-derived syngas. *Ind. Eng. Chem. Res.* **2005,** *44* (21), 7945-7956.
40. Haynes, B., Reactions of ammonia and nitric oxide in the burnt gases of fuel-rich hydrocarbon-air flames. *Combustion and Flame* **1977,** *28*, 81-91.
41. Solomon, P. R.; Colket, M. B., Evolution of fuel nitrogen in coal devolatilization. *Fuel* **1978,** *57* (12), 749-755.
42. Duan, Y.; Duan, L.; Anthony, E. J.; Zhao, C., Nitrogen and sulfur conversion during pressurized pyrolysis under CO2 atmosphere in fluidized bed. *Fuel* **2017,** *189*, 98-106.
43. Tian, F.-J.; Yu, J.; McKenzie, L. J.; Hayashi, J.-i.; Li, C.-Z., Conversion of fuel-N into HCN and NH3 during the pyrolysis and gasification in steam: a comparative study of coal and biomass. *Energy Fuels* **2007,** *21* (2), 517-521.
44. Yuan, S.; Zhou, Z.-j.; Li, J.; Chen, X.-l.; Wang, F.-c., HCN and NH3 released from biomass and soybean cake under rapid pyrolysis. *Energy Fuels* **2010,** *24* (11), 6166-6171.
45. Chen, H.; Wang, Y.; Xu, G.; Yoshikawa, K., Fuel-N evolution during the pyrolysis of industrial biomass wastes with high nitrogen content. *Energies* **2012,** *5* (12), 5418-5438.
46. Basiuk, V. A., Pyrolysis of valine and leucine at 500 C: Identification of less-volatile products using gas chromatography-Fourier transform infrared spectroscopy-mass spectrometry. *Journal of Analytical and Applied Pyrolysis* **1998,** *47* (2), 127-143.
47. Becidan, M.; Skreiberg, Ø.; Hustad, J. E., NO x and N2O Precursors (NH3 and HCN) in Pyrolysis of Biomass Residues. *Energy Fuels* **2007,** *21* (2), 1173-1180.
48. Samuelsson, J. I. Conversion of nitrogen into a fixed burning biofuel bed. Chalmers University of Technology, Göteborg, Sweden, 2006.
49. Hansson, K.-M.; Åmand, L.-E.; Habermann, A.; Winter, F., Pyrolysis of poly-l-leucine under combustion-like conditions☆. *Fuel* **2003,** *82* (6), 653-660.
50. Broer, K. M.; Brown, R. C., Effect of Equivalence Ratio on Partitioning of Nitrogen during Biomass Gasification. *Energy Fuels* **2015,** *30* (1), 407-413.
51. Zhou, J.; Masutani, S. M.; Ishimura, D. M.; Turn, S. Q.; Kinoshita, C. M., Release of fuel-bound nitrogen during biomass gasification. *Ind. Eng. Chem. Res.* **2000,** *39* (3), 626-634.
52. Chen, H.; Si, Y.; Chen, Y.; Yang, H.; Chen, D.; Chen, W., NOx precursors from biomass pyrolysis: Distribution of amino acids in biomass and Tar-N during devolatilization using model compounds. *Fuel* **2017,** *187*, 367-375.
53. Ren, Q.; Zhao, C.; Chen, X.; Duan, L.; Li, Y.; Ma, C., NOx and N2O precursors (NH3 and HCN) from biomass pyrolysis: Co-pyrolysis of amino acids and

cellulose, hemicellulose and lignin. *Proceedings of the Combustion Institute* **2011,** *33* (2), 1715-1722.
54. Mckenzie, L. J.; Tian, F.-J.; Li, C.-Z., NH3 formation and destruction during the gasification of coal in oxygen and steam. *Environmental science & technology* **2007,** *41* (15), 5505-5509.
55. Abdoulmoumine, N.; Kulkarni, A.; Adhikari, S., Effects of Temperature and Equivalence Ratio on Pine Syngas Primary Gases and Contaminants in a Bench-Scale Fluidized Bed Gasifier. *Ind. Eng. Chem. Res.* **2014,** *53* (14), 5767-5777.
56. Asadullah, M., Biomass gasification gas cleaning for downstream applications: A comparative critical review. *Renewable and Sustainable Energy Reviews* **2014,** *40* (1), 118-132.
57. Aljbour, S. H.; Kawamoto, K., Bench-scale gasification of cedar wood – Part II: Effect of Operational conditions on contaminant release. *Chemosphere* **2013,** *90* (4), 1501-1507.
58. Kern, S.; Pfeifer, C.; Hofbauer, H., Co-gasification of wood and lignite in a dual fluidized bed gasifier. *Energy Fuels* **2013,** *27* (2), 919-931.
59. Kulkarni, A.; Baker, R.; Abdoulmoumine, N.; Adhikari, S.; Bhavnani, S., Experimental study of torrefied pine as a gasification fuel using a bubbling fluidized bed gasifier. *Renewable Energy* **2016,** *93*, 460-468.
60. De Kok, L. J. In *Sulfur nutrition and assimilation in higher plants*, Workshop on Sulfur Metabolism in Higher Plants 1992: Garmisch-Partenkirchen, Germany), SPB Academic: 1993.
61. Tchoffor, P. A.; Moradian, F.; Pettersson, A.; Davidsson, K. O.; Thunman, H., Influence of Fuel Ash Characteristics on the Release of Potassium, Chlorine, and Sulfur from Biomass Fuels under Steam-Fluidized Bed Gasification Conditions. *Energy Fuels* **2016,** *30* (12), 10435-10442.
62. Johansen, J. M.; Jakobsen, J. G.; Frandsen, F. J.; Glarborg, P., Release of K, Cl, and S during pyrolysis and combustion of high-chlorine biomass. *Energy Fuels* **2011,** *25* (11), 4961-4971.
63. Knudsen, J. N.; Jensen, P. A.; Lin, W.; Frandsen, F. J.; Dam-Johansen, K., Sulfur transformations during thermal conversion of herbaceous biomass. *Energy Fuels* **2004,** *18* (3), 810-819.
64. Gai, C.; Dong, Y.; Zhang, T., Distribution of sulfur species in gaseous and condensed phase during downdraft gasification of corn straw. *Energy* **2014,** *64*, 248-258.
65. van Lith, S. C.; Jensen, P. A.; Frandsen, F. J.; Glarborg, P., Release to the gas phase of inorganic elements during wood combustion. Part 2: influence of fuel composition. *Energy Fuels* **2008,** *22* (3), 1598-1609.
66. Liu, K.; Song, C.; Subramani, V., *Hydrogen and Syngas Production and Purification Technologies*. 1st ed.; Wiley Online Library: Hoboken, N.Y., 2010.
67. Meng, X. Biomass gasification: the understanding of sulfur, tar, and char reaction in fluidized bed gasifiers. TU Delft, Delft University of Technology, 2012.

68. Kaufman Rechulski, M. D.; Schildhauer, T. J.; Biollaz, S. M. A.; Ludwig, C., Sulfur containing organic compounds in the raw producer gas of wood and grass gasification. *Fuel* **2014,** *128*, 330-339.
69. Oyedeji, O.; Fasina, O., Impact of drying-grinding sequence on loblolly pine chips preprocessing effectiveness. *Industrial Crops and Products* **2017,** *96* (1), 8-15.
70. Zainal, Z. A.; Ali, R.; Lean, C. H.; Seetharamu, K. N., Prediction of performance of a downdraft gasifier using equilibrium modeling for different biomass materials. *Energy Conversion and Management* **2001,** *42* (12), 1499-1515.
71. Antonopoulos, I. S.; Karagiannidis, A.; Gkouletsos, A.; Perkoulidis, G., Modelling of a downdraft gasifier fed by agricultural residues. *Waste Management* **2012,** *32* (4), 710-718.
72. Pellegrini, L. F.; Oliveira, S., Exergy analysis of sugarcane bagasse gasification. *Energy* **2007,** *32* (4), 314-327.
73. Kuo, P.; Wu, W.; Chen, W., Gasification performances of raw and torrefied biomass in a downdraft fixed bed gasifier using thermodynamic analysis. *Fuel* **2014,** *117, Part B* (1), 1231-1241.
74. McKendry, P., Energy production from biomass (part 3): Gasification technologies. *Bioresource Technology* **2002,** *83* (1), 55-63.
75. Bhavya, B.; Singh, R.; Bhaskar, T., Preparation of feedstocks for gasification for synthetic liquid fuel production. In *Gasification for Synthetic Fuel Production*, 1st ed.; Woodhead Publishing: Cambridge, England, 2015; p 61.
76. Saw, W. L.; Pang, S., Co-gasification of blended lignite and wood pellets in a 100 kW dual fluidized bed steam gasifier: The influence of lignite ratio on producer gas composition and tar content. *Fuel* **2013,** *112* (1), 117-124.
77. Syamlal, M.; Bissett, L. A. *METC Gasifier Advanced Simulation (MGAS) Model*; DOE/METC--92/4108; Office of Fossil Energy, U.S. Department of Energy: Morgantown, West Virginia, 1992, 1992.
78. Skoulou, V.; Zabaniotou, A.; Stavropoulos, G.; Sakelaropoulos, G., Syngas production from olive tree cuttings and olive kernels in a downdraft fixed-bed gasifier. *International Journal of Hydrogen Energy* **2008,** *33* (4), 1185-1194.
79. Sadhwani, N.; Adhikari, S.; Eden, M. R., Biomass Gasification Using Carbon Dioxide: Effect of Temperature, CO2/C Ratio, and the Study of Reactions Influencing the Process. *Ind. Eng. Chem. Res.* **2016,** *55* (10), 2883-2891.
80. Ptasinski, K. J.; Prins, M. J.; Pierik, A., Exergetic evaluation of biomass gasification. *Energy* **2007,** *32* (4), 568-574.
81. Zhou, J.; Chen, Q.; Zhao, H.; Cao, X.; Mei, Q.; Luo, Z.; Cen, K., Biomass–oxygen gasification in a high-temperature entrained-flow gasifier. *Biotechnology Advances* **2009,** *27* (5), 606-611.
82. He, M.; Xiao, B.; Hu, Z.; Liu, S.; Guo, X.; Luo, S., Syngas production from catalytic gasification of waste polyethylene: influence of temperature on gas yield and composition. *International Journal of Hydrogen Energy* **2009,** *34* (3), 1342-1348.

83. Delgado, J.; Aznar, M. P.; Corella, J., Biomass gasification with steam in fluidized bed: Effectiveness of CaO, MgO, and CaO− MgO for hot raw gas cleaning. *Ind. Eng. Chem. Res.* **1997,** *36* (5), 1535-1543.
84. Lv, P.; Xiong, Z.; Chang, J.; Wu, C.; Chen, Y.; Zhu, J., An experimental study on biomass air–steam gasification in a fluidized bed. *Bioresource Technology* **2004,** *95* (1), 95-101.
85. Umeki, K.; Yamamoto, K.; Namioka, T.; Yoshikawa, K., High temperature steam-only gasification of woody biomass. *Appl Energ* **2010,** *87* (3), 791-798.
86. Campoy, M.; Gómez-Barea, A.; Vidal, F. B.; Ollero, P., Air–steam gasification of biomass in a fluidised bed: process optimisation by enriched air. *Fuel Processing Technology* **2009,** *90* (5), 677-685.
87. Gil, J.; Aznar, M. P.; Caballero, M. A.; Francés, E.; Corella, J., Biomass gasification in fluidized bed at pilot scale with steam− oxygen mixtures. Product distribution for very different operating conditions. *Energy Fuels* **1997,** *11* (6), 1109-1118.
88. Wang, Y.; Kinoshita, C., Experimental analysis of biomass gasification with steam and oxygen. *Solar Energy* **1992,** *49* (3), 153-158.
89. Kirsanovs, V.; Zandeckis, A.; Blumberga, D.; Veidenbergs, I. In *The influence of process temperature, equivalence ratio and fuel moisture content on gasification process: A review*, Proceedings of 27th International Conference on Efficiency, Cost, Optimization, Simulation and Environmental Impact of Energy Systems, 2014; pp 15-19.
90. Dogru, M.; Howarth, C.; Akay, G.; Keskinler, B.; Malik, A., Gasification of hazelnut shells in a downdraft gasifier. *Energy* **2002,** *27* (5), 415-427.
91. Sheth, P. N.; Babu, B., Experimental studies on producer gas generation from wood waste in a downdraft biomass gasifier. *Bioresource Technology* **2009,** *100* (12), 3127-3133.
92. Zainal, Z.; Rifau, A.; Quadir, G.; Seetharamu, K., Experimental investigation of a downdraft biomass gasifier. *Biomass and bioenergy* **2002,** *23* (4), 283-289.
93. Narvaez, I.; Orio, A.; Aznar, M. P.; Corella, J., Biomass gasification with air in an atmospheric bubbling fluidized bed. Effect of six operational variables on the quality of the produced raw gas. *Ind. Eng. Chem. Res.* **1996,** *35* (7), 2110-2120.
94. Guo, F.; Dong, Y.; Dong, L.; Guo, C., Effect of design and operating parameters on the gasification process of biomass in a downdraft fixed bed: An experimental study. *International Journal of Hydrogen Energy* **2014,** *39* (11), 5625-5633.
95. Gai, C.; Dong, Y., Experimental study on non-woody biomass gasification in a downdraft gasifier. *International Journal of Hydrogen Energy* **2012,** *37* (6), 4935-4944.
96. Xue, G.; Kwapinska, M.; Horvat, A.; Kwapinski, W.; Rabou, L. P. L. M.; Dooley, S.; Czajka, K. M.; Leahy, J. J., Gasification of torrefied Miscanthus × giganteus in an air-blown bubbling fluidized bed gasifier. *Bioresource Technology* **2014,** *159*, 397-403.

97. Chen, G.; Yao, J.; Yang, H.; Yan, B.; Chen, H., Steam gasification of acid-hydrolysis biomass CAHR for clean syngas production. *Bioresource Technology* **2015,** *179*, 323-330.
98. Hejazi, B.; Grace, J. R.; Bi, X.; Mahecha-Botero, A., Kinetic model of steam gasification of biomass in a bubbling fluidized bed reactor. *Energy Fuels* **2017**.
99. Sharma, S.; Sheth, P. N., Air–steam biomass gasification: Experiments, modeling and simulation. *Energy Conversion and Management* **2016,** *110*, 307-318.
100. García-Labiano, F.; Gayán, P.; De Diego, L.; Abad, A.; Mendiara, T.; Adánez, J.; Nacken, M.; Heidenreich, S., Tar abatement in a fixed bed catalytic filter candle during biomass gasification in a dual fluidized bed. *Applied Catalysis B: Environmental* **2016,** *188*, 198-206.
101. Corella, J.; Toledo, J. M.; Padilla, R., Olivine or dolomite as in-bed additive in biomass gasification with air in a fluidized bed: which is better? *Energy Fuels* **2004,** *18* (3), 713-720.
102. Kimura, T.; Miyazawa, T.; Nishikawa, J.; Kado, S.; Okumura, K.; Miyao, T.; Naito, S.; Kunimori, K.; Tomishige, K., Development of Ni catalysts for tar removal by steam gasification of biomass. *Applied Catalysis B: Environmental* **2006,** *68* (3), 160-170.
103. Engelen, K.; Zhang, Y.; Draelants, D. J.; Baron, G. V., A novel catalytic filter for tar removal from biomass gasification gas: improvement of the catalytic activity in presence of H 2 S. *Chemical Engineering Science* **2003,** *58* (3), 665-670.
104. Sattar, A.; Leeke, G. A.; Hornung, A.; Wood, J., Steam gasification of rapeseed, wood, sewage sludge and miscanthus biochars for the production of a hydrogen-rich syngas. *biomass and bioenergy* **2014,** *69*, 276-286.
105. Shen, Y., Chars as carbonaceous adsorbents/catalysts for tar elimination during biomass pyrolysis or gasification. *Renewable and Sustainable Energy Reviews* **2015,** *43*, 281-295.
106. Shen, Y.; Zhao, P.; Shao, Q.; Ma, D.; Takahashi, F.; Yoshikawa, K., In-situ catalytic conversion of tar using rice husk char-supported nickel-iron catalysts for biomass pyrolysis/gasification. *Applied Catalysis B: Environmental* **2014,** *152–153*, 140-151.
107. Song, Y.; Wang, Y.; Hu, X.; Hu, S.; Xiang, J.; Zhang, L.; Zhang, S.; Min, Z.; Li, C.-Z., Effects of volatile–char interactions on in situ destruction of nascent tar during the pyrolysis and gasification of biomass. Part I. Roles of nascent char. *Fuel* **2014,** *122*, 60-66.
108. Yan, F.; Luo, S.-y.; Hu, Z.-q.; Xiao, B.; Cheng, G., Hydrogen-rich gas production by steam gasification of char from biomass fast pyrolysis in a fixed-bed reactor: Influence of temperature and steam on hydrogen yield and syngas composition. *Bioresource Technology* **2010,** *101* (14), 5633-5637.
109. Yao, D.; Hu, Q.; Wang, D.; Yang, H.; Wu, C.; Wang, X.; Chen, H., Hydrogen production from biomass gasification using biochar as a catalyst/support. *Bioresource Technology* **2016,** *216*, 159-164.

110. Krerkkaiwan, S.; Mueangta, S.; Thammarat, P.; Jaisat, L.; Kuchonthara, P., Catalytic Biomass-Derived Tar Decomposition Using Char from the Co-pyrolysis of Coal and Giant Leucaena Wood Biomass. *Energy Fuels* **2015,** *29* (5), 3119-3126.
111. Liu, N.; Charrua, A. B.; Weng, C.-H.; Yuan, X.; Ding, F., Characterization of biochars derived from agriculture wastes and their adsorptive removal of atrazine from aqueous solution: a comparative study. *Bioresource Technology* **2015,** *198*, 55-62.
112. Altafini, C. R.; Wander, P. R.; Barreto, R. M., Prediction of the working parameters of a wood waste gasifier through an equilibrium model. *Energy Conversion and Management* **2003,** *44* (17), 2763-2777.
113. Baratieri, M.; Baggio, P.; Fiori, L.; Grigiante, M., Biomass as an energy source: Thermodynamic constraints on the performance of the conversion process. *Bioresource Technology* **2008,** *99* (15), 7063-7073.
114. Li, X.; Grace, J. R.; Watkinson, A. P.; Lim, C. J.; Ergüdenler, A., Equilibrium modeling of gasification: a free energy minimization approach and its application to a circulating fluidized bed coal gasifier. *Fuel* **2001,** *80* (2), 195-207.
115. Rodrigues, R.; Secchi, A. R.; Marcílio, N. R.; Godinho, M., Modeling of Biomass Gasification Applied to a Combined Gasifier-Combustor Unit: Equilibrium and Kinetic Approaches. In *Computer Aided Chemical Engineering*, Rita Maria de Brito Alves, C. A. O. d. N.; Evaristo Chalbaud, B., Eds. Elsevier: 2009; Vol. Volume 27, pp 657-662.
116. Castello, D.; Fiori, L., Supercritical water gasification of biomass: A stoichiometric thermodynamic model. *International Journal of Hydrogen Energy* **2015,** *40* (21), 6771-6781.
117. Shabbar, S.; Janajreh, I., Thermodynamic equilibrium analysis of coal gasification using Gibbs energy minimization method. *Energy Conversion and Management* **2013,** *65* (1), 755-763.
118. George, J.; Arun, P.; Muraleedharan, C., Stoichiometric Equilibrium Model Based Assessment of Hydrogen Generation through Biomass Gasification. *Procedia Technology* **2016,** *25*, 982-989.
119. Loha, C.; Chatterjee, P. K.; Chattopadhyay, H., Performance of fluidized bed steam gasification of biomass–modeling and experiment. *Energy Conversion and Management* **2011,** *52* (3), 1583-1588.
120. Turn, S.; Kinoshita, C.; Zhang, Z.; Ishimura, D.; Zhou, J., An experimental investigation of hydrogen production from biomass gasification. *International Journal of Hydrogen Energy* **1998,** *23* (8), 641-648.
121. Ghassemi, H.; Shahsavan-Markadeh, R., Effects of various operational parameters on biomass gasification process; a modified equilibrium model. *Energy Conversion and Management* **2014,** *79*, 18-24.
122. Azzone, E.; Morini, M.; Pinelli, M., Development of an equilibrium model for the simulation of thermochemical gasification and application to agricultural residues. *Renewable Energy* **2012,** *46*, 248-254.

123. Barman, N. S.; Ghosh, S.; De, S., Gasification of biomass in a fixed bed downdraft gasifier–A realistic model including tar. *Bioresource Technology* **2012,** *107*, 505-511.
124. Subramanian, P.; Sampathrajan, A.; Venkatachalam, P., Fluidized bed gasification of select granular biomaterials. *Bioresource Technology* **2011,** *102* (2), 1914-1920.
125. Lim, Y.-i.; Lee, U.-D., Quasi-equilibrium thermodynamic model with empirical equations for air–steam biomass gasification in fluidized-beds. *Fuel Processing Technology* **2014,** *128*, 199-210.
126. Kangas, P.; Hannula, I.; Koukkari, P.; Hupa, M., Modelling super-equilibrium in biomass gasification with the constrained Gibbs energy method. *Fuel* **2014,** *129*, 86-94.
127. Ahmed, T. Y.; Ahmad, M. M.; Yusup, S.; Inayat, A.; Khan, Z., Mathematical and computational approaches for design of biomass gasification for hydrogen production: A review. *Renewable and Sustainable Energy Reviews* **2012,** *16* (4), 2304-2315.
128. Sreejith, C. C.; Muraleedharan, C.; Arun, P., Air–steam gasification of biomass in fluidized bed with CO2 absorption: A kinetic model for performance prediction. *Fuel Processing Technology* **2015,** *130*, 197-207.
129. Radmanesh, R.; Courbariaux, Y.; Chaouki, J.; Guy, C., A unified lumped approach in kinetic modeling of biomass pyrolysis. *Fuel* **2006,** *85* (9), 1211-1220.
130. Bartocci, P.; Anca-Couce, A.; Slopiecka, K.; Nefkens, S.; Evic, N.; Retschitzegger, S.; Barbanera, M.; Buratti, C.; Cotana, F.; Bidini, G., Pyrolysis of pellets made with biomass and glycerol: Kinetic analysis and evolved gas analysis. *Biomass and Bioenergy* **2017,** *97*, 11-19.
131. Mühlen, H.-J.; van Heek, K. H.; Jüntgen, H., Kinetic studies of steam gasification of char in the presence of H2, CO2 and CO. *Fuel* **1985,** *64* (7), 944-949.
132. Govind, R.; Shah, J., Modeling and simulation of an entrained flow coal gasifier. *AIChE Journal* **1984,** *30* (1), 79-92.
133. Abani, N.; Ghoniem, A. F., Large eddy simulations of coal gasification in an entrained flow gasifier. *Fuel* **2013,** *104*, 664-680.
134. Ku, X.; Li, T.; Løvås, T., Eulerian–lagrangian simulation of biomass gasification behavior in a high-temperature entrained-flow reactor. *Energy Fuels* **2014,** *28* (8), 5184-5196.
135. Couto, N. D.; Silva, V. B.; Monteiro, E.; Rouboa, A.; Brito, P., An experimental and numerical study on the Miscanthus gasification by using a pilot scale gasifier. *Renewable Energy* **2017,** *109*, 248-261.
136. Wang, Y.; Kinoshita, C., Kinetic model of biomass gasification. *Solar Energy* **1993,** *51* (1), 19-25.
137. Mitani, T.; Williams, F., Studies of cellular flames in hydrogen oxygen nitrogen mixtures. *Combustion and Flame* **1980,** *39* (2), 169-190.
138. Macak, J.; Malecha, J., Mathematical Model for the Gasification of Coal under Pressure. *Industrial & Engineering Chemistry Process Design and Development* **1978,** *17* (1), 92-98.

139. Jones, W.; Lindstedt, R., Global reaction schemes for hydrocarbon combustion. *Combustion and flame* **1988,** *73* (3), 233-249.
140. Dryer, F.; Glassman, I. In *High-temperature oxidation of CO and CH4*, Symposium (International) on combustion, Elsevier: 1973; pp 987-1003.
141. Howard, J.; Williams, G.; Fine, D. In *Kinetics of carbon monoxide oxidation in postflame gases*, Symposium (International) on Combustion, Elsevier: 1973; pp 975-986.
142. Hottel, H.; Williams, G.; Nerheim, N.; Schneider, G. In *Kinetic studies in stirred reactors: combustion of carbon monoxide and propane*, Symposium (International) on Combustion, Elsevier: 1965; pp 111-121.
143. Yetter, R.; Dryer, F.; Rabitz, H. In *Complications of one-step kinetics for moist CO oxidation*, Symposium (International) on Combustion, Elsevier: 1988; pp 749-760.
144. Hannes, J. P., *Mathematical modelling of circulating fluidized bed combustion*. TU Delft, Delft University of Technology: 1996.
145. Jess, A., Reaktionskinetische untersuchungen zur thermischen zersetzung von modellkohlenwasserstoffen. *Erdöl, Erdgas, Kohle* **1995,** *111* (11), 479-484.
146. Jess, A., Catalytic upgrading of tarry fuel gases: A kinetic study with model components. *Chemical Engineering and Processing: Process Intensification* **1996,** *35* (6), 487-494.
147. Groppi, G.; Tronconi, E.; Forzatti, P.; Berg, M., Mathematical modelling of catalytic combustors fuelled by gasified biomasses. *Catalysis Today* **2000,** *59* (1), 151-162.
148. Jess, A., Mechanisms and kinetics of thermal reactions of aromatic hydrocarbons from pyrolysis of solid fuels. *Fuel* **1996,** *75* (12), 1441-1448.
149. Inayat, A.; Ahmad, M. M.; Yusup, S.; Mutalib, M. I. A., Biomass steam gasification with in-situ CO2 capture for enriched hydrogen gas production: a reaction kinetics modelling approach. *Energies* **2010,** *3* (8), 1472-1484.
150. Mahishi, M. R.; Goswami, D., An experimental study of hydrogen production by gasification of biomass in the presence of a CO2 sorbent. *International Journal of Hydrogen Energy* **2007,** *32* (14), 2803-2808.
151. Florin, N. H.; Harris, A. T., Hydrogen production from biomass coupled with carbon dioxide capture: the implications of thermodynamic equilibrium. *International Journal of Hydrogen Energy* **2007,** *32* (17), 4119-4134.
152. Giltrap, D. L.; McKibbin, R.; Barnes, G. R. G., A steady state model of gas-char reactions in a downdraft biomass gasifier. *Solar Energy* **2003,** *74* (1), 85-91.
153. Xiong, Q.; Zhang, J.; Xu, F.; Wiggins, G.; Daw, C. S., Coupling DAEM and CFD for simulating biomass fast pyrolysis in fluidized beds. *Journal of Analytical and Applied Pyrolysis* **2016,** *117*, 176-181.
154. Meng, A.; Chen, S.; Long, Y.; Zhou, H.; Zhang, Y.; Li, Q., Pyrolysis and gasification of typical components in wastes with macro-TGA. *Waste Management* **2015,** *46*, 247-256.

155. Khonde, R.; Chaurasia, A., Rice husk gasification in a two-stage fixed-bed gasifier: Production of hydrogen rich syngas and kinetics. *International Journal of Hydrogen Energy* **2016,** *41* (21), 8793-8802.
156. Ku, X.; Li, T.; Løvås, T., CFD–DEM simulation of biomass gasification with steam in a fluidized bed reactor. *Chemical Engineering Science* **2015,** *122*, 270-283.
157. Pepiot, P.; Dibble, C. J.; Foust, T. D., Computational fluid dynamics modeling of biomass gasification and pyrolysis. In *Computational Modeling in Lignocellulosic Biofuel Production*, 1st ed.; American Chemical Society: 2010; Vol. 1052, pp 273-298.
158. Reddy, R. K.; Joshi, J. B., CFD modeling of solid–liquid fluidized beds of mono and binary particle mixtures. *Chemical Engineering Science* **2009,** *64* (16), 3641-3658.
159. Singh, R. I.; Brink, A.; Hupa, M., CFD modeling to study fluidized bed combustion and gasification. *Applied Thermal Engineering* **2013,** *52* (2), 585-614.
160. Tu, J.; Yeoh, G. H.; Liu, C., *Computational Fluid Dynamics: A Practical Approach*. 2nd ed.; Butterworth-Heinemann: Oxford, United Kingdom, 2013.
161. Wang, Y.; Yan, L., CFD studies on biomass thermochemical conversion. *International journal of molecular sciences* **2008,** *9* (6), 1108-1130.
162. Zhang, Y.; Lei, F.; Xiao, Y., Computational fluid dynamics simulation and parametric study of coal gasification in a circulating fluidized bed reactor. *Asia-Pac. J. Chem. Eng.* **2015,** *10* (2), 307-317.
163. Oevermann, M.; Gerber, S.; Behrendt, F., Euler–Lagrange/DEM simulation of wood gasification in a bubbling fluidized bed reactor. *Particuology* **2009,** *7* (4), 307-316.
164. Liu, H.; Cattolica, R. J.; Seiser, R., CFD studies on biomass gasification in a pilot-scale dual fluidized-bed system. *International Journal of Hydrogen Energy* **2016,** *41* (28), 11974-11989.
165. Wen, C. Y.; Yu, Y. H., Mechanics of fluidization. *Chem. Eng. Prog. Symp* **1966,** *62* (1), 100–110.
166. O'Rourke, P. J.; Brackbill, J. U.; Larrouturou, B., On Particle-Grid Interpolation and Calculating Chemistry in Particle-in-Cell Methods. *Journal of Computational Physics* **1993,** *109* (1), 37-52.
167. Gerber, S.; Behrendt, F.; Oevermann, M., An Eulerian modeling approach of wood gasification in a bubbling fluidized bed reactor using char as bed material. *Fuel* **2010,** *89* (10), 2903-2917.
168. Ku, X.; Lin, J.; Yuan, F., Influence of Torrefaction on Biomass Gasification Performance in a High-Temperature Entrained-Flow Reactor. *Energy Fuels* **2016,** *30* (5), 4053-4064.
169. Oyedeji, O.; Fasina, O.; Adhikari, S.; McDonald, T.; Taylor, S., The effect of storage time and moisture content on grindability of loblolly pine (Pinus taeda L.). *European Journal of Wood and Wood Products* **2016,** *74* (6), 857-866.
170. Kenney, K. L.; Smith, W. A.; Gresham, G. L.; Westover, T. L., Understanding biomass feedstock variability. *Biofuels* **2013,** *4* (1), 111-127.

171. de Diego, L. F.; García-Labiano, F.; Gayán, P.; Abad, A.; Mendiara, T.; Adánez, J.; Nacken, M.; Heidenreich, S., Tar abatement for clean syngas production during biomass gasification in a dual fluidized bed. *Fuel Processing Technology* **2016,** *152*, 116-123.
172. Heyne, S.; Liliedahl, T.; Marklund, M. *Biomass gasification - a synthesis of technical barriers and current research issues for deployment at large scale*; The Swedish Knowledge Centre for Renewable Transportation Fuels: Göteborg, Sweden, 2013, 2013.
173. Tan E. C. D.; Talmadge M.; Dutta A.; Hensley J.; Schaidle J.; Biddy M.; Humbird D.; Snowden-Swan L. J.; Ross J.; Sexton D.; Yap R.; J., L. *Process Design and Economics for the Conversion of Lignocellulosic Biomass to Hydrocarbons via Indirect Liquefaction*; 2015.
174. Bhaduri, S.; Contino, F.; Jeanmart, H.; Breuer, E., The effects of biomass syngas composition, moisture, tar loading and operating conditions on the combustion of a tar-tolerant HCCI (Homogeneous Charge Compression Ignition) engine. *Energy* **2015,** *87* (1), 289-302.
175. Boerrigter, H.; Den Uil, H.; Calis, H.-P., Green diesel from biomass via Fischer-Tropsch synthesis: new insights in gas cleaning and process design. Citeseer: 2003; pp 371-383.
176. Baker, E.; Brown, M.; Moore, R.; Mudge, L.; Elliott, D. *Engineering analysis of biomass gasifier product gas cleaning technology*; Pacific Northwest Lab., Richland, WA (USA): 1986.
177. Milne, T. A.; Abatzoglou, N.; Evans, R. J., *Biomass Gasifier "Tars": Their Nature, Formation, and Conversion*. National Renewable Energy Laboratory Golden, CO: 1998; Vol. 570.
178. Asadullah, M., Biomass gasification gas cleaning for downstream applications: A comparative critical review. *Renewable and Sustainable Energy Reviews* **2014,** *40*, 118-132.
179. Zwart, R.; Van der Drift, A.; Bos, A.; Visser, H.; Cieplik, M.; Könemann, H., Oil-based gas washing—Flexible tar removal for high-efficient production of clean heat and power as well as sustainable fuels and chemicals. *Environmental Progress & Sustainable Energy* **2009,** *28* (3), 324-335.

CHAPTER III
KINETICS OF THE RELEASE OF ELEMENTAL PRECURSORS OF SYNGAS AND SYNGAS CONTAMINANTS DURING DEVOLATILIZATION OF SWITCHGRASS

A version of this chapter was originally published by Oyedeji et al.:

Oyedeji, O. A., Daw, C. S., Labbé, N., Ayers, P, D., and Abdoulmoumine, N. H. (2017). Kinetics of the release of elemental precursors of syngas and syngas contaminants during switchgrass devolatilization. Bioresource Technology 244(1): 525-533

Oluwafemi Oyedeji performed the experiments, conducted data analysis and modeling, and wrote the first draft of the manuscript. Dr. Stuart Daw, Dr. Nicole Labbé, and Dr. Paul Ayers assisted with some experimental design, data modeling, and manuscript reviewing. Additionally, Dr. Nicole Labbé supervised the sample elemental characterization experimental. Dr. Nourredine Abdoulmoumine oversaw the experimental design, assisted with data analysis and modeling, and edited the manuscript.

Abstract

In this study, the results from laboratory measurements of the devolatilization kinetics of switchgrass in a rapidly heated fixed bed reactor flushed with argon and operated at constant temperatures between 600 and 800 °C was reported. Results indicate that switchgrass decomposes in two sequential stages during pyrolysis: stage I involves the evaporation and devolatilization of water and extractives and stage II involves that of hemicellulose, cellulose, and lignin. The estimated global activation energy for stage II increased from 52.80 – 59.39 kJ/mol as the reactor temperature was increased from 600 – 800 °C. The maximum conversion of carbon, hydrogen, oxygen, sulfur, and nitrogen ranged from 0.68 – 0.70, 0.90 – 0.95, 0.88 – 0.91, 0.70 – 0.80, and 0.55 – 0.66, respectively. The retention of alkali and alkaline earth metal (AAEM) species in the solid char after complete pyrolysis was significantly higher than in the original feed, indicating the importance of AAEM species in subsequent char processing.

Keywords: Biomass, thermochemical conversion, Arrhenius parameters, char, alkaline earth contaminants.

Introduction

Pyrolysis and gasification are the two most common thermochemical conversion methods used to convert lignocellulosic biomass into fuels, chemicals, and materials to significantly displace the world demand for crude oil and coal.[1-2] In the context of lignocellulosic thermochemical conversion, pyrolysis involves the thermal decomposition of biomass in the absence of oxygen to produce bio-oil as the major product, alongside biochar and pyrolytic gases.[3] In contrast to pyrolysis, gasification is the thermal decomposition of biomass in the presence of limited and sub-stoichiometric oxygen levels to yield producer gases as the major product followed by biochar.[4] Although occurring in different environments, pyrolysis (also referred to

as devolatilization) is the commencing chemical step during gasification which leads to the formation of volatiles that later undergo secondary reactions (intra- and extra-particle) to produce the final producer gases.[2]

Lignocellulosic biomass is a complex composite of water, volatiles, ash, and char from a thermochemical conversion standpoint. During pyrolysis, lignocellulosic biomass first reacts endothermically and irreversibly to produce a mixture of primary gases (CO, CO_2, H_2O, H_2, and CH_4) and primary tars. Subsequently, the primary tar constituents are further cracked into secondary and tertiary tars as well as primary gases at temperatures typically observed for gasification (Figure 3.1).[5] In addition to the production of primary constituents, gases generated during pyrolysis usually contain minor but significant quantity of undesirable contaminants. These contaminants include sulfur containing compounds (such as H_2S and COS), nitrogen containing compounds (such as NH_3 and HCN), and trace amounts of metals (such as K and Ca).[6] The presence of contaminant compounds in the main gas products is one of the major concerns for the commercial deployment of gasification technologies because they are difficult and expensive to remove.[7] A recent techno-economic analysis demonstrated that gas cleaning to remove contaminants accounts for the largest share of the capital cost and a significant share of the operating cost.[8]

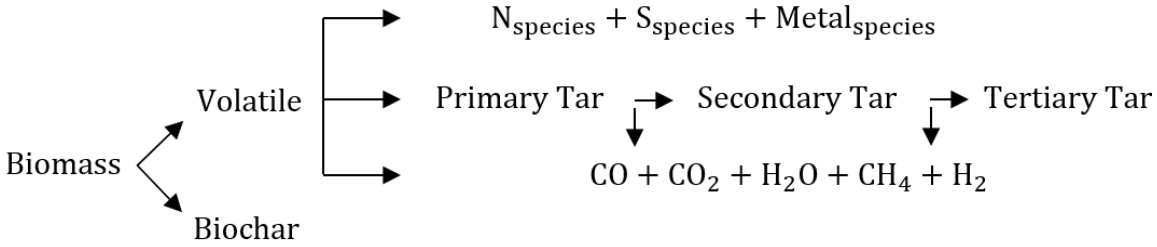

Figure 3.1. Biomass decomposition during pyrolysis.

Thus, understanding biomass pyrolysis behavior and kinetics is essential to maximize desirable products and minimize contaminant compounds during biomass gasification. Hyphenated thermogravimetric analysis (TGA) techniques, such as TGA coupled with Fourier transform infrared (FTIR), gas chromatography (GC), or mass spectrometry (MS), are common methods used to study the fundamentals of biomass pyrolysis. Such studies have been carried out with thin layered samples in mostly non-isothermal conditions.[9-12] Although TGA techniques are convenient for biomass pyrolysis modeling, resulting kinetic parameters have been criticized because of the inherent inability to accurately access the kinetic parameters obtained from TGA and the high sensitive of kinetic parameters to experimental noise.[13]

Other investigators have utilized fixed-bed reactors to study biomass pyrolysis. Bilbao, et al. [14] achieved heating rates ranging from 2 to 53 °C/min during the pyrolysis of cellulose and pine sawdust in a tubular reactor. They found that gas yield increased as the pyrolysis temperature and heating rate increased. Raveendran, et al. [15] demonstrated that the distribution of pyrolysis products was unaffected by the interactions among individual biomass components by studying pyrolysis of several isolated biomass components (cellulose, lignin, hemicellulose, and extractives) and biomass feedstocks in a fixed-bed pyrolyzer.

Several reaction kinetics models have been proposed for biomass pyrolysis. Radmanesh, et al. [16] employed a model with three independent parallel reactions to explain the production of char during the pyrolysis of Canadian beech wood, sawdust, and Chinese rice husk. The authors assumed a simple first-order rate equation to model the generation of H_2, CH_4, CO, and CO_2. Seo, et al. [17] also modeled the formation of gases from the pyrolysis of sawdust using the same kinetic model. In another study, Sadhukhan, et al. [18] proposed a parallel-series kinetic model to predict the pyrolysis behavior of coal–biomass blends. These and other similar models suffer from the fact that they do not resolve details about the species in the reaction products. Instead, they lump the pyrolysis products (e.g., light gases, oils, and char) because of the hundreds of molecular species that are produced.[19] In some other cases, only the major gas products (CO, CO_2, H_2, and CH_4) were accounted for. Hence, it is not possible to derive any significant information about potential contaminant species that might be present in the initial pyrolysis products.

The objective in this study was to improve the understanding of the rates and distributions of syngas and contaminant precursor species that are released from switchgrass during pyrolysis. The methodology used was based on a two-fold approach: *i)* to experimentally measure the release of selected elements during the pyrolysis of switchgrass that contribute to potential syngas and syngas contaminant species in the products and; *ii)* to develop global kinetic rate expressions for the release of these elements during experimental switchgrass pyrolysis.

This study was focused on the tracking of carbon, hydrogen, oxygen, nitrogen, sulfur, potassium, calcium, and magnesium due to their importance in syngas and syngas contaminant species in pyrolysis products or their derivatives.

Materials and methods

Figure 3.2a illustrates the experimental flowchart followed in this study. Switchgrass (*Panicum virgatum*) was used for this work because of the forecasted importance of herbaceous biomass to a sustainable biomass supply system and its abundance in the United States. Switchgrass samples were ground with a knife mill (model no. 3, Thomas Wiley, Swedesboro, NJ) fitted with a 2 mm screen size. Then, the samples were sorted by size with a Ro-Tap screen shaker (model RX – 29, W.S. Tyler, Mentor, Ohio) fitted with 4 ISO screens (2.36 mm, 0.850 mm, 0.425 mm, and 0.180 mm). The moisture content was determined following ASABE Standard S358.3[20] and was 4.34 wt. % (wet basis) with a standard deviation of 0.17 wt. %. Additionally, the volatile matter content was determined according to ASTM Standard D3175-11[21] and was 82.24 wt. % (dry basis) with a standard deviation of 0.05 wt. %. The ash content was measured according to NREL method[22] and was 4.31 wt. % (dry basis) with a standard deviation of 0.09 wt. %. Finally, the fixed carbon content was calculated by difference from the values of volatile matter content and ash content and was 13.45 wt. % (dry basis) with standard deviation of 0.09 wt. %.

Pyrolysis methodology

Switchgrass samples were pyrolyzed in an up-flow tubular fixed-bed reactor (0.5 in./1.27 cm O.D. and 3 in./7.62 cm high) illustrated in Figure 3.2b. The reactor was constructed from stainless steel pipes and fittings, and its mass was 172.58 ± 5.90 g. Argon carrier gas was introduced into the reactor through a bottom inlet tube (0.125 in./0.32 cm O.D.) to dilute and rapidly flush the pyrolysis products out of the reactor. Exhaust gases exited the reactor through a 0.25 in. (0.64 cm) O.D. tube for collecting pyrolysis products. The reactor tube was inserted inside a muffle furnace (model F47915, Thermo-Fisher Scientific, Waltham, MA) to supply the pyrolysis heat.

For each experiment, approximately 0.50 g of ground switchgrass was placed on a quartz wool plug positioned at the base of the reactor and purged with argon (carrier gas) for 60 seconds to remove ambient air in the reactor. Under a constant stream of argon, the reactor tube was then placed in the muffle furnace maintained at one of three set temperatures 600, 700, and 800 °C through the vent port at the top of the furnace. The temperature inside the sample bed was continuously measured and logged every second with a type K thermocouple, and the reactor tube was maintained in the furnace for predetermined times, ranging from 30 to 360 s.

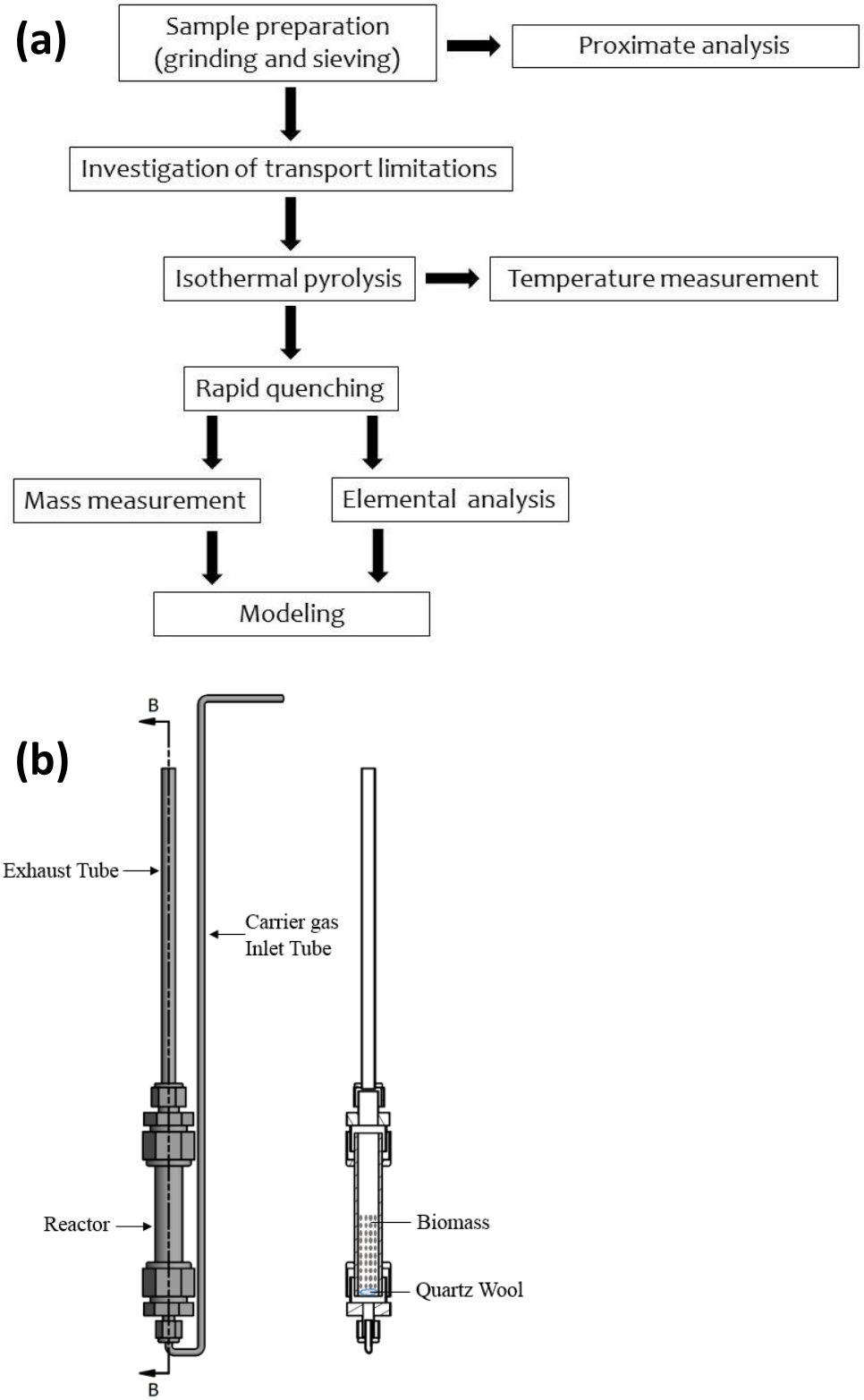

Figure 3.2. a) The biomass pyrolyser used in this study and cross-sectional view of the reactor and b) experimental flowchart.

At the end of the experiment, the reactor tube was quickly removed from the muffle furnace and rapidly quenched in a liquid nitrogen bath under a continuous flow of carrier gas until the pyrolyser and its content attained temperatures below 100 °C, ensuring that devolatilization was completely terminated. The mass of the sample before and after each experiment was measured using a digital balance with 0.1 mg readability (model SI-215D, Denver Instrument, Denver, CO). The exhaust tube was removed before each mass measurement to ensure that tar condensates on the walls were not included in the mass measurement.

Specification of particle size and gas flow rate

Depending on the reactor conditions, biomass pyrolysis behavior can be a strong function of particle size because of heat and mass transfer inside individual particles as well as gas residence time in the reactor.[23] Consequently, to account for these effects, the transport effects were minimized by conducting preliminary screening experiments to identify a carrier gas flow rate and biomass particle size for the pyrolysis experiments.[24] The screening experiments included measuring the impact of gas flow rate and sample particle size on devolatilization rate with a furnace temperature of 800 °C.

As pointed out by Branca, et al. [25], higher gas flow rate increases the mass transfer rate between the carrier gas and the biomass particles. Likewise, as particle size decreases, intra-particle concentration and temperature gradients are reduced, so that reaction rates closely approach those expected for the bulk bed conditions. Therefore, by identifying reactor operating conditions at which the observed devolatilization rates were unaffected by particle size and gas flow, the conditions for estimating consistent intrinsic Arrhenius rate parameters were established.

Elemental analysis

Elemental carbon, hydrogen, and nitrogen (CHN) and an inductively coupled plasma optical emission spectroscopy (ICP-OES) analyses were carried out for both the unpyrolysed switchgrass and residual char following pyrolysis. The CHN analysis was performed with a PerkinElmer CHN analyzer (model 2400II, Waltham, MA), and sulfur, potassium, calcium, and magnesium content were measured with an Optima 7300 DV spectrometer (ICP–OES, PerkinElmer, Waltham, MA) after digestion[26] of the sample. Approximately 0.3 g of each sample were digested using a microwave digester (Multiwave 3000 digester) with 10 ml of HNO_3 (67-70%), 3 ml of HCl (35%), and 1 ml of HF (51%) at 180 – 210 °C for 100 min. To complex residual HF and dissolved precipitated fluorides, 5 ml of H_3BO_3 (4%) were added after digestion. Deionized water was added to dilute the solutions to 50 ml, then the solutions was filtrated through a 0.2 µm syringe filter before being analyzed by ICP-OES.[27] Oxygen content of each sample was calculated by difference. Unless otherwise stated, each chemical analysis was at least performed in duplicate and average values are reported on dry basis throughout this study.

Analytical methodology

Total and elemental species mass loss (conversion) vs. time profiles generated in the experiments were interpolated using the Piecewise Cubic Hermite Interpolating Polynomial (PCHIP) function in MATLAB R2016a. The average value of triplicates was used for the interpolation process. Experimental time derivatives (conversion rates) were then determined from the interpolated profiles.

The overall devolatilization rate was modeled as a function of the activation energy, pre-exponential parameter, and instantaneous volatile matter content, as follows:

$$\frac{d\alpha}{dt} = Ae^{-E_a/RT}(1-\propto)^n \tag{3.1}$$

$$\propto = \frac{m_0 - m_t}{m_0 - m_\infty} \tag{3.2}$$

where A is pre-exponential constant for total pyrolysis (s^{-1}); E_a is activation energy for total pyrolysis (J mol^{-1}); $\propto$ is Conversion factor (dimensionless); m_0 is mass of sample before pyrolysis (mg); m_t is mass of sample at time t during pyrolysis (mg); m_∞ is mass of sample after pyrolysis (mg); n is reaction order for total pyrolysis (dimensionless); R is universal gas constant, 8.315 (kJ mol^{-1} K^{-1}); t is time (s); and T is local bed temperature (K).

Similarly, the release of chemical elements (i = C, H, O, N, S, K, Ca, and Mg) during pyrolysis was modeled using an nth-order Arrhenius equation (Equation (3.3)). The instantaneous conversion rate of each element ($\frac{dW_i}{dt}$) was calculated as a product of instantaneous concentration of each element and time derivative of conversion factor (Equation (3.4)).

$$\frac{dW_i}{dt} = A_i e^{-E_{ai}/RT}\left(1 - x_{i,t}\right)^{n_i} \tag{3.3}$$

$$\frac{dW_i}{dt} = Y_i \frac{d\alpha}{dt} \tag{3.4}$$

$$x_{i,t} = \frac{W_{i,0} - W_{i,t}}{W_{i,0}} \tag{3.5}$$

where A_i is Pre-exponential constant for elemental precursor i (s^{-1}); E_{ai} is activation energy for elemental precursor i (kJ mol^{-1}); n_i is reaction order for elemental precursor I (dimensionless); R is universal gas constant, 8.315 (kJ mol^{-1} K^{-1}); T is time (s); T is local bed temperature (K); W_i is total mass of elemental precursor i in

sample (mg); $W_{i,t}$ is total mass of elemental precursor i in sample at time t (mg); $W_{i,0}$ is total mass of elemental precursor i in sample before pyrolysis (mg); $x_{i,t}$ is conversion of elemental precursor i at time t (dimensionless); Y_i is mass concentration of elemental precursor i in sample (mg/g); and $\propto$ is conversion factor (dimensionless).

The reaction rate parameters were determined by fitting the above rate expressions (this assumes that the fixed bed behaves as a differential reactor) with the observed measurements to minimize the root mean square error (RMSE), mean absolute error (MAE), and quality of fit (FIT) as defined by Equations (3.6), (3.7), and (3.8), respectively.[28] In addition, all statistical tests were carried out in SAS 9.4 using PROC GLM and Tukey's multiple comparison tests. The significance level of all the tests performed was 5% unless otherwise stated.

$$\mathrm{RMSE} = \sqrt[2]{\frac{1}{N}\sum_{j=i}^{N}\left(\mathrm{experimental}_j - \mathrm{predicted}_j\right)^2} \tag{3.6}$$

$$\mathrm{MAE} = \frac{1}{N}\sum_{j=i}^{N}\left|\mathrm{experimental}_j - \mathrm{predicted}_j\right| \tag{3.7}$$

$$\mathrm{FIT} = 100\,\frac{\sum_{j=1}^{N}\left((\mathrm{experimental}_j - \mathrm{predicted}_j)^2\right)/N^2}{\mathrm{experimental}_{max}} \tag{3.8}$$

where N is the number of observations; experimental and $\mathrm{predicted}_j$ are the experimental and predicted values for observation j; and $\mathrm{experimental}_{max}$ is the maximum value among all observations.

Results and discussion

Experimental particle size and gas flow rate

As depicted in Figure 3.3a, the screening experiments revealed that switchgrass conversion after 90 and 120 s did not change significantly ($p < 0.05$) as the flow rate of carrier gas was changed from 50 to 200 ml/min. This implied that particle-to-gas mass transfer and overall reactor effects were not significant as long as gas flow was kept in this range. Figure 3.3b shows that the average switchgrass conversion after 90 s initially increased from 0.63 to 0.68 when the biomass particle diameter was decreased from 0.85 to 0.43 mm. However, further reduction in particle size from 0.43 to 0.10 mm did not affect conversion significantly ($p < 0.05$). A similar trend was observed for the average switchgrass conversion after 120 s. It was

therefore concluded from this result that intraparticle gradients were negligible for particles ≤ 0.43 mm. Based on the above observations, a gas flow of 200 ml/min and a particle size of 0.180 mm were selected as the target conditions for generating kinetic parameter estimates.

Pyrolysis profile characteristics

The heating rate of biomass bed initially increased due to the magnitude of the temperature difference between the biomass bed and the furnace chamber. However, when the temperature of the biomass bed attained a threshold value, the heating rate of the biomass bed gradually decreased. For example, at a furnace temperature of 800 °C, the heating rate of switchgrass bed increased from 0 to 299.0 °C/min when the temperature of the switchgrass bed increased from 28 to 362.2 °C. Then the heating rate of the switchgrass bed decreased as its temperature further increased to attain the furnace temperature (Figure 3.4). The peak heating rate achieved ranged from 136.0 to 263.7 °C/min and increased with increasing furnace temperature (Figure 3.4). This observation expresses the fundamental flaw in the generation of biomass pyrolysis kinetic information at constant heating rate, which makes up majority of the biomass pyrolysis studies.[13]

Furthermore, it was observed that heating rate sharply decreased as the biomass bed temperature approached 100 °C before it continued to increase again. This behavior was attributed to moisture evaporation because heat absorbed at this point was consumed to change the state of biomass moisture to vapor at constant temperature.

Pyrolysis profiles are useful in the design of reactors components and selection of optimum operating conditions. The pyrolysis profiles for switchgrass obtained in this study are shown in Figure 3.5a. Similar profiles have been reported for studies conducted using multiple types of reactors and heating techniques for other types of biomass.[29-31] In this study, the decomposition of switchgrass reached asymptotic levels at around 180 s (for 700 and 800 °C) and 300 s (for 600 °C). The rate and extent of decomposition of samples increased as furnace temperature was raised, which is consistent with the finding of González, et al. [30] for cherry stones. The change in overall volatile conversion rate and extent were ascribed to increased heat flux inside the biomass particle as pyrolysis temperature is increased.[32] Approximately 78, 80, and 81% of decomposition was observed at furnace temperature 600, 700, and 800 °C, respectively. These levels of decomposition represent the removal of 95–99% of the total volatiles and moisture content of the sample

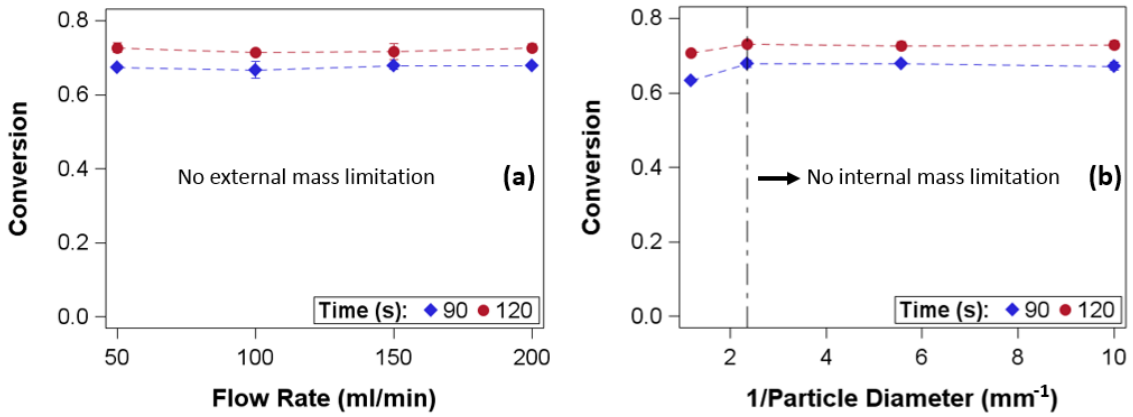

Figure 3.3. Effect of (a) the carrier gas flow rate and (b) the particle diameter of switchgrass on conversion after 90 and 120 s at furnace temperature of 800 °C.

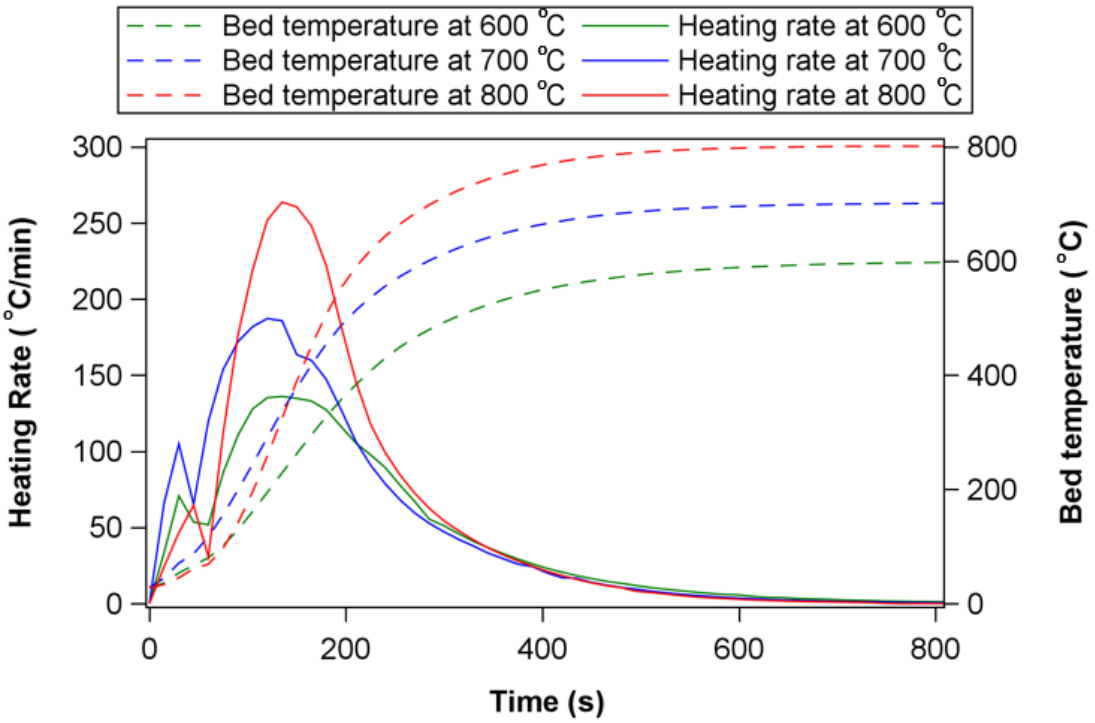

Figure 3.4. Temperature and heating rate profile of biomass bed at different furnace temperature.

Figure 3.5b shows the total conversion rate for switchgrass obtained using Equation (3.2). The conversion rate profiles were deconvoluted into two distributions using an open-source C++ library (Fityk software[33]). The initial phase of mass loss was ascribed to moisture and extractives release, whereas the second phase of mass loss was ascribed to the decomposition of cellulose, hemicellulose, and lignin. These different phases are referred to as stage I and stage II, respectively, in subsequent sections of this study (Figure 3.5c).

It is difficult to distinguish separate peaks for the decomposition of cellulose, hemicellulose, and lignin in this study as has been commonly reported for other biomass pyrolysis profiles in literature. There are two potential reasons for this. First, the temporal resolution of the profiles may simply be inadequate to resolve the parallel decomposition of biomass cellulose, hemicellulose, and lignin. Secondly and more likely, it may be that at the heating rates in this study, the decomposition of biomass cellulose, hemicellulose, and lignin may be not be readily distinguished. This seems to be consistent with the results reported by Wu, et al. [34] and Wongsiriamnuay and Tippayawong [35].

The peak mass loss rates observed during experimental pyrolysis were 0.71, 1.03, and 1.59 min^{-1} for furnace temperature of 600, 700, and 800 °C, respectively. Lee and Fasina [31] reported a peak mass loss rate for switchgrass of ~0.35 min^{-1} at a heating rate of 40 °C/min in their experiments. This kind of difference is expected for lower heating rates. Although there are no switchgrass pyrolysis studies in the literature for heating rates comparable to this study, Wu, et al. [36] reported comparable peak mass loss rates for pyrolysis of rice straw, pelletized corncob, and pelletized corn straw at similar heating rates.

Estimation of Arrhenius kinetic parameters

Total mass loss

Table 3.1 lists the effective Arrhenius parameters for total mass loss in stages I and II at different furnace temperatures. The estimated values of parameters for stage II measurements are comparable with values that have been reported for isothermal pyrolysis of other types of biomass.[37-39] For stage II, the apparent activation energy (E_a) and pre-exponential parameter (A) values increased with increasing furnace temperature. This observation agrees with the finding of Liu, et al. [40] on the pyrolysis of Fir lignin. The reaction order (n) however decreased as furnace temperature increased.

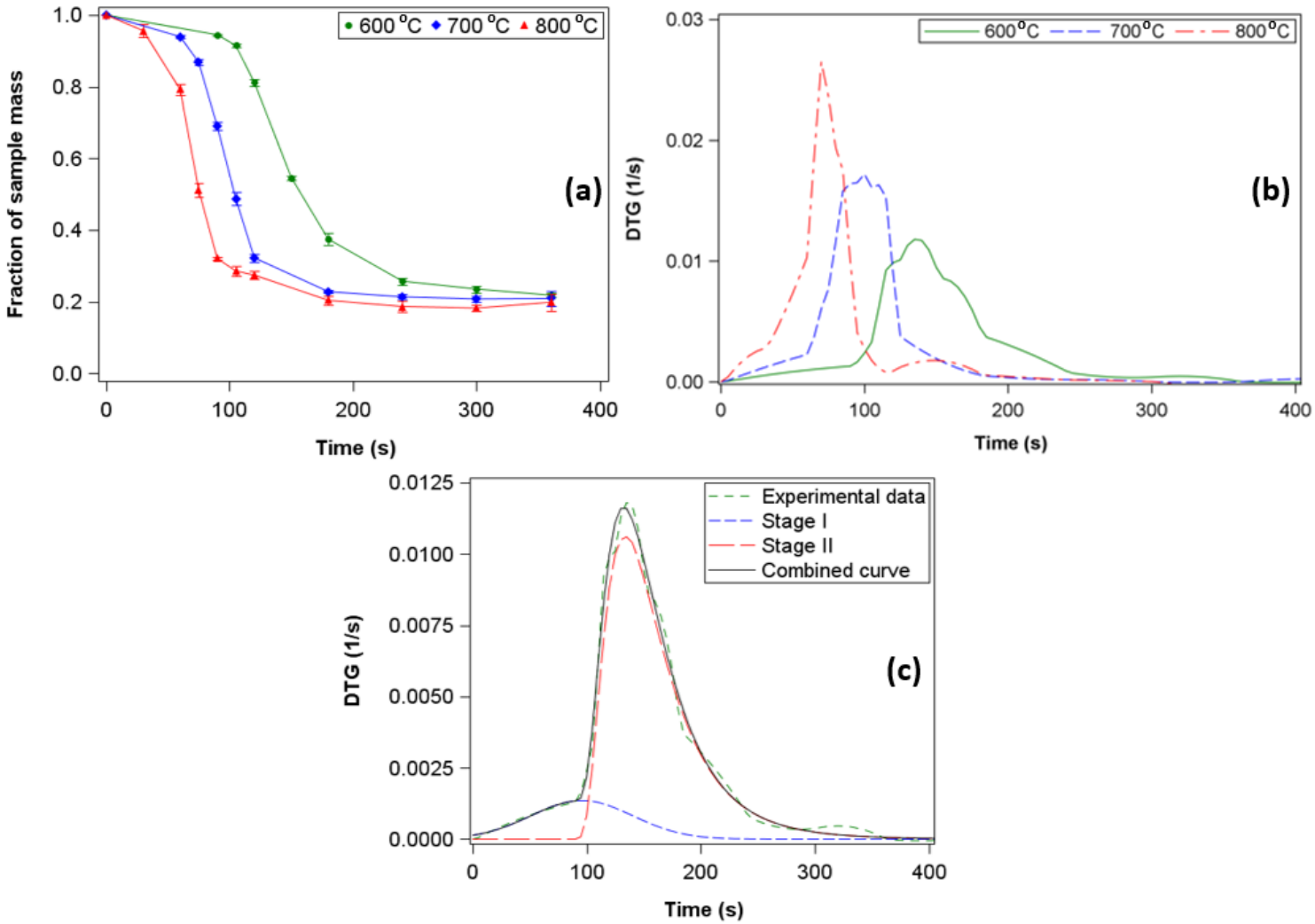

Figure 3.5. a) Pyrolysis profile of switchgrass at different pyrolysis temperatures; b) Conversion rate curve of switchgrass at different pyrolysis temperature; and c) Deconvolution of conversion rate curve at furnace temperature of 600 °C**.**

Table 3.1. Estimate of kinetics parameters for total devolatilization (Equation (3.1)).

Furnace temperature (°C)	Stage I			Stage II			RMSE	MAE	FIT
	ln(A), s^{-1}	E_a, kJ/mol	n	ln(A), s^{-1}	E_a, kJ/mol	n			
600	1.50	24.47	0.014	8.92	52.80	2.36	0.015	0.013	0.146
700	9.60	45.60	0.013	10.86	55.38	2.04	0.013	0.010	0.146
800	7.23	36.24	0.041	11.88	59.39	1.35	0.041	0.032	0.485

RMSE: root mean square error (s^{-1}), MAE: mean absolute error (s^{-1}), FIT: quality of fit (%).

It was conjecture that the apparent parameter variations with furnace temperature described above are due to the presence of hundreds of species and reactions occurring simultaneously at each point in time. When there are different heating rates, the resulting product species and reaction states present should vary widely at each given temperature, resulting in effective composite rate parameters that are likely to be significantly different. Therefore, the actual heating rate at which Arrhenius parameters are determined can be a key factor in explaining the diverse results in the literature, even for the same types of biomass.

The agreement between the experimental weight loss rate data and the predictions based on the above Arrhenius parameters appears reasonable, although the goodness of fit was less at 800 °C (Figure 3.6a and Table 3.3). The values of RMSE and FIT also indicate that a reaction order > 1 is needed at all the temperatures. The agreement observation between the experimental and predicted data in this study is better than those reported by Branca, et al. [41].

Elemental carbon, hydrogen, and oxygen release

The ultimate analysis of unpyrolysed switchgrass and solid residue after complete pyrolysis are presented in Table 3.2. The values shown are within the range that has been reported for unpyrolysed switchgrass.[42-45] During pyrolysis, fuel-carbon is released as CO, CO_2, CH_4, COS, and CS_2 and fuel-hydrogen is released as H_2, H_2O, CH_4, NH_3, and H_2S, and the instantaneous conversion of each element observed in this study (as expressed in Equation (3.5)) is depicted in Figures 6b-d. As expected, the instantaneous conversion of elemental carbon, hydrogen, and oxygen increased as the furnace temperature was raised, implying an increased rate of conversion for each of these elements with higher reaction temperature.

Also as expected, the carbon content of the remaining char at the end of pyrolysis was significantly higher ($p < 0.05$) than that of unpyrolysed switchgrass, and the hydrogen and oxygen content of the char was significantly lower ($p < 0.05$) (Table 3.2). Since the cleavage of C–C bond requires higher energy compared to C–H and R'–R" bonds (R' and R" are radical groups of carbon and other elements), this trend is not surprising.

Similarly, it was observed that approximately 88–91% of the oxygen content in switchgrass were converted to the gas-phase during pyrolysis and the concentration of oxygen in the solid residue after pyrolysis was approximately 50% lower than in unpyrolysed switchgrass. The simultaneous decrease in the elemental concentration of hydrogen and oxygen during pyrolysis (Table 3.2) suggests that the conversion of elemental hydrogen and oxygen is mainly due to the cleavage of hydroxyl functional groups (–OH).

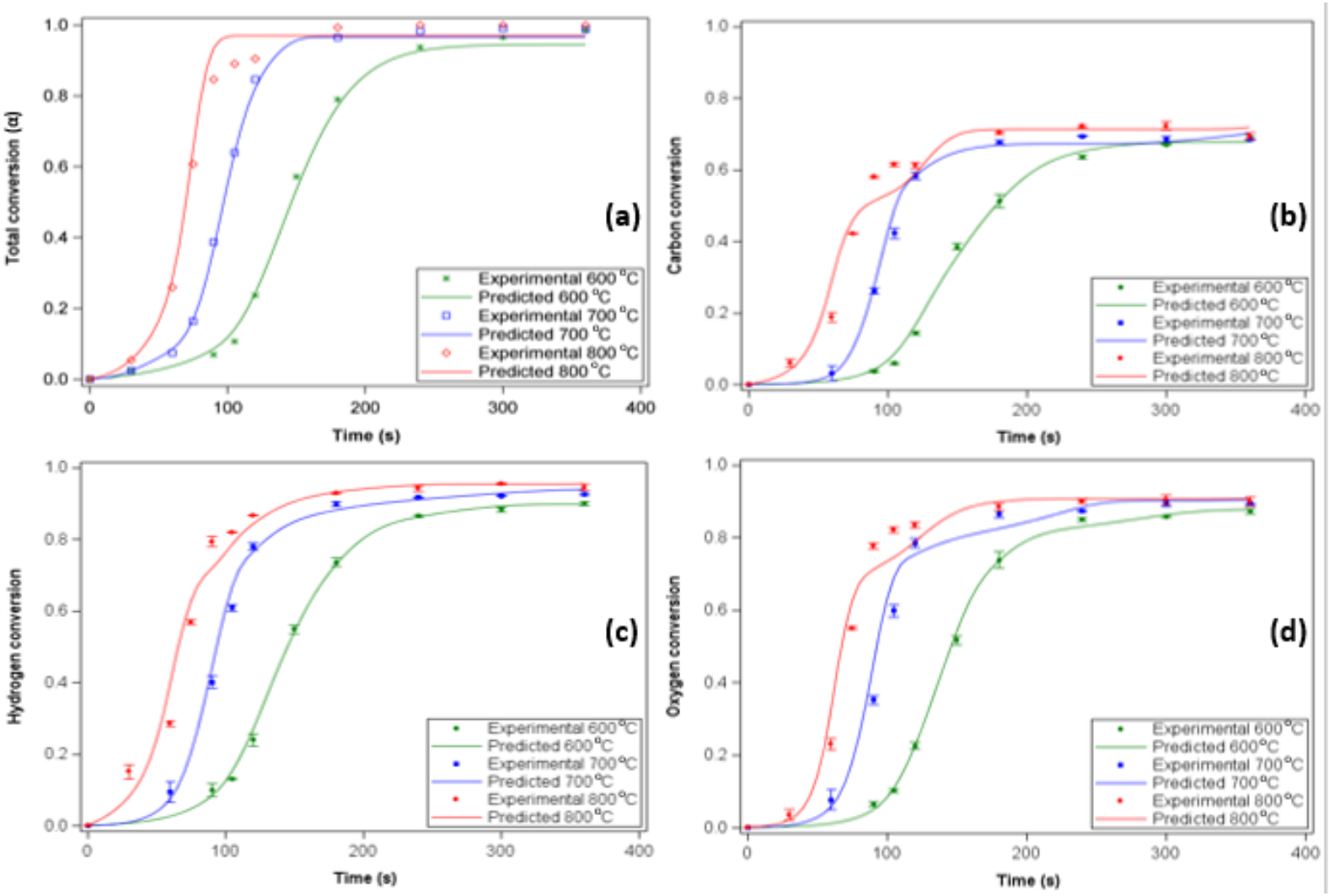

Figure 3.6. Comparison of prediction data with experimental data at different furnace temperature a) total pyrolysis (volatile release); b) carbon release; c) hydrogen release; d) oxygen release; e) nitrogen release; f) sulfur release; and g) AAEM species release.

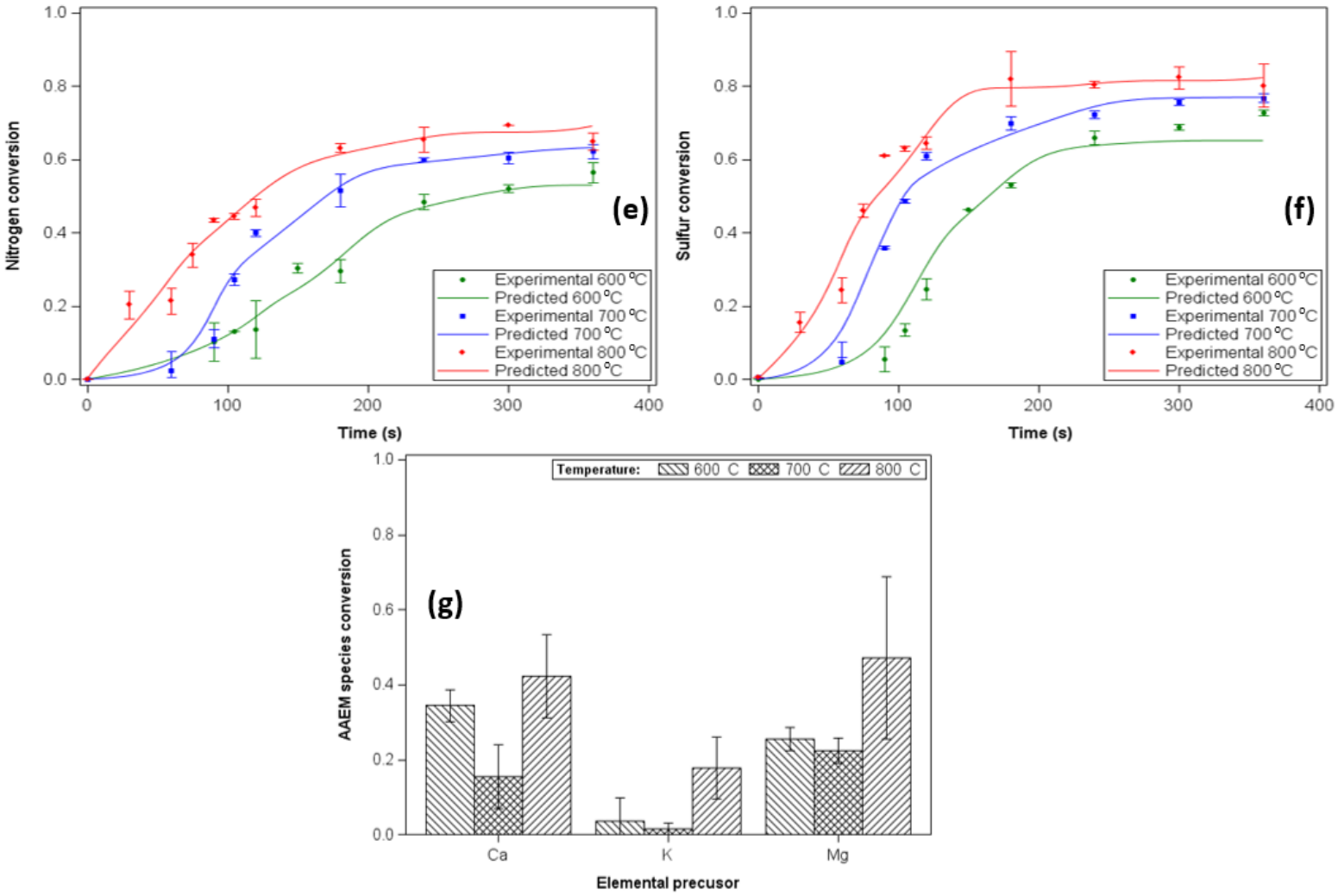

Figure 3.6. Continued.

Table 3.2. Ultimate analysis of unpyrolysed switchgrass and solid residue after pyrolysis.

Element	Unpyrolysed switchgrass	Solid residue after pyrolysis		
		600 °C	700 °C	800 °C
C (mg/g)	464.8 ± 17.7	683.8 ± 22.8	707.2 ± 22.9	717.5 ± 20.7
H (mg/g)	63.4 ± 1.3	29.1 ± 4.7	19.8 ± 1.0	17.3 ± 2.8
N (mg/g)	4.7 ± 0.3	9.8 ± 0.2	8.1 ± 0.4	8.4 ± 0.6
S (mg/g)	0.6 ± 0.0	0.8 ± 0.0	0.6 ± 0.0	0.6 ± 0.2
K (mg/g)	2.0 ± 0.0	8.7 ± 1.4	10.0 ± 0.2	8.4 ± 0.9
Ca (mg/g)	4.5 ± 0.5	15.1 ± 1.5	18.8 ± 1.9	13.0 ± 2.5
Mg (mg/g)	1.59 ± 0.0	5.7 ± 0.3	6.2 ± 0.3	4.3 ± 1.7
O (mg/g)	458.4 ± 19.8	246.8 ± 31.0	229.1 ± 26.7	230.3 ± 29.5

As with the overall mass loss, all the Arrhenius least-squared fitting results for the elemental volatilization rates implied greater than first-order reactions (Table 3.3). The activation energy of elemental carbon was higher than the activation energy of elemental hydrogen throughout all the furnace temperatures. This is consistent with the general observation that the release of elemental hydrogen tends to be more rapid than the release of elemental carbon during biomass pyrolysis.

Elemental nitrogen and sulfur release

Nitrogen and sulfur compounds in biomass volatiles make up a significant part of potential contaminants in the pyrolysis products. Fuel-nitrogen is primarily released as HCN and NH_3, and fuel-sulfur is primarily released as H_2S, COS, and CS_2.[6] The net conversion of sulfur after complete pyrolysis of the switchgrass was higher (ranging from 0.70 to 0.80) than that of nitrogen (ranging from 0.55 to 0.66) at all three furnace temperatures (Figure 3.6e and Figure 3.6f). However, since the total mass of elemental nitrogen in unpyrolysed switchgrass was about eight times larger than the total mass of the elemental sulfur in unpyrolysed switchgrass (Table 3.2), the quantity of nitrogen containing compounds released during pyrolysis is expected to be higher than the quantity of sulfur containing compounds. The sulfur retained in the residual char after pyrolysis is typically inorganic sulfur in sulfate form and are thermally stable at temperatures below 1000°C.[46]

The elemental sulfur concentration in the residual char after pyrolysis was slightly higher than the elemental sulfur concentration in unpyrolysed switchgrass. However, elemental nitrogen concentration in the residual char after pyrolysis was about twice the value of elemental nitrogen concentration in unpyrolysed switchgrass (Table 3.2). This indicates the increased importance of nitrogen in heterogeneous reactions after pyrolysis.

The estimated Arrhenius parameters for the release kinetics of elemental sulfur and nitrogen are listed in Table 3.3. The values of RMSE and FIT obtained with these estimates indicate acceptable fits. There are no published kinetics for release of sulfur and nitrogen from biomass pyrolysis that can be compared with these results. Yet, kinetic parameters, like the ones reported in this study, are routinely needed in numerical models. This highlights the importance of the findings in this study which present information that can be used to quantitatively account for the total release of sulfur and nitrogen during the pyrolysis stage of biomass gasification, which is hitherto not available.

Table 3.3. Estimate of kinetics parameters for the release of element C, H, O, N, and S during devolatilization (Equation (3.3)).

Furnace temperature	Element	$\ln(A_i)$, s^{-1}	E_{ai}, kJ/mol	n_i	RMSE	MAE	FIT
600 °C	C	5.75	40.18	2.29	0.012	0.010	0.176
	H	4.62	34.31	1.81	0.012	0.008	0.132
	N	-2.14	13.20	1.25	0.023	0.018	0.421
	S	5.16	34.74	3.00	0.046	0.037	0.637
	O	7.52	45.15	2.22	0.011	0.008	0.124
700 °C	C	12.48	60.45	2.90	0.018	0.013	0.277
	H	10.72	51.57	2.91	0.017	0.013	0.201
	N	4.12	33.24	3.00	0.025	0.017	0.411
	S	6.36	36.37	3.00	0.029	0.022	0.400
	O	11.94	56.38	3.00	0.032	0.022	0.382
800 °C	C	5.69	32.96	3.00	0.033	0.022	0.534
	H	3.59	25.18	2.14	0.035	0.021	0.432
	N	-4.17	2.69	1.00	0.029	0.020	0.468
	S	-1.21	11.05	1.43	0.032	0.022	0.461
	O	9.67	46.17	3.00	0.034	0.019	0.441

RMSE: root mean square error (s^{-1}), MAE: mean absolute error (s^{-1}), FIT: quality of fit (%).

Elemental potassium, calcium, and magnesium release

Biomass typically contains small but significant amounts of alkali and alkaline earth metallic (AAEM) species such as K, Ca, and Mg from nutrients uptake during plant growth and deposition during harvest operation. AAEM species form chlorides, hydroxides, and sulfates that may cause extensive fouling and corrosion in downstream processes.[47]

Figure 3.6g shows the final conversion for AAEM species (K, Ca, and Mg) during the pyrolysis measurements of switchgrass. High variability was observed among the measured AAEM values and thus the ability to obtain reliable Arrhenius parameter estimates for these species was compromised. Therefore, only the final conversions of the AAEM species after pyrolysis was reported here. The mean final conversion of AAEM species during pyrolysis ranged from 0.02 to 0.47 (Figure 3.6), with the highest level occurring at the highest furnace temperature. The retention of AAEM species in the residual char after pyrolysis was also significantly higher when compared with the retention of C, H, O, N, and S and higher than in the unpyrolysed biomass (Table 3.2). This demonstrates the relatively high thermal stability of the AAEM species in the switchgrass and implies that these species are likely to be important in any further processing of the char (e.g., where gasification follows pyrolysis). The presence of high levels of AAEM in char is additionally complicated because of the potential catalytic effects of these species. For example, previous studies have shown that AAEM species enhance char-gasification and tar decomposition.[48-49] It is therefore essential to account for the change in the concentration of AAEM species when applying mathematical tools like computational fluid dynamic simulations to effectively capture the resulting change in the rate of char-gasification and tar decomposition.

The conversion of AAEM species (especially K and Mg) remained roughly unchanged as furnace temperature was increased from 600°C to 700°C. Table 3.2 however shows that the concentration of AAEM species is highest at 700°C. This can be explained by the fact that AAEM species are thermally stable. The increase in the concentration of AAEM species is because while the final conversion of AAEM species remained roughly constant between 600°C to 700°C, the final conversion of other elements linearly increased between 600°C to 700°C. As the furnace temperature is further increased to 800°C more AAEM species are released, causing the reduction on their concentration.

Conclusions

A comprehensive picture of the release of elemental precursors of syngas and syngas contaminants during pyrolysis was presented. Total mass loss measurements revealed two distinct stages. Kinetics modeling shows that non-first-order Arrhenius reaction kinetics fit the observed conversion rates for total volatiles, carbon, hydrogen, oxygen, sulfur, and nitrogen. The estimates for the kinetic parameters varied with temperature due to the activation of different chemical

reactions at the different temperatures. The developed kinetic models will be useful for tracking the amount of elemental C, H, O, N, and S in the solid and gas phase during the pyrolysis stage of gasification.

Acknowledgement

This research was supported by Southeastern Sun Grant Center and the US Department of Transportation, Research and Innovative Technology Administration, Grant No. DTO559-07-G-00050.

References

1. Oyedeji, O.; Fasina, O.; Adhikari, S.; McDonald, T.; Taylor, S., The effect of storage time and moisture content on grindability of loblolly pine (Pinus taeda L.). *European Journal of Wood and Wood Products* **2016,** *74* (6), 857-866.
2. McKendry, P., Energy production from biomass (part 2): conversion technologies. *Bioresource Technology* **2002,** *83* (1), 47-54.
3. Basu, P., *Biomass Gasification and Pyrolysis*. 1st ed.; Elsevier: Oxford, England, 2010.
4. Abdoulmoumine, N.; Kulkarni, A.; Adhikari, S., Effects of Temperature and Equivalence Ratio on Pine Syngas Primary Gases and Contaminants in a Bench-Scale Fluidized Bed Gasifier. *Ind. Eng. Chem. Res.* **2014,** *53* (14), 5767-5777.
5. Milne, T. A.; Abatzoglou, N.; Evans, R. J., *Biomass gasifier" tars": Their nature, formation, and conversion*. National Renewable Energy Laboratory Golden, CO: 1998; Vol. 570.
6. Abdoulmoumine, N.; Adhikari, S.; Kulkarni, A.; Chattanathan, S., A review on biomass gasification syngas cleanup. *Appl Energ* **2015,** *155* (1), 294-307.
7. Heyne, S.; Liliedahl, T.; Marklund, M. *Biomass gasification - a synthesis of technical barriers and current research issues for deployment at large scale*; The Swedish Knowledge Centre for Renewable Transportation Fuels: Göteborg, Sweden, 2013, 2013.
8. Tan, E. C.; Talmadge, M.; Dutta, A.; Hensley, J.; Schaidle, J.; Biddy, M.; Humbird, D.; Snowden-Swan, L. J.; Ross, J.; Sexton, D. *Process Design and Economics for the Conversion of Lignocellulosic Biomass to Hydrocarbons via Indirect Liquefaction. Thermochemical Research Pathway to High-Octane Gasoline Blendstock Through Methanol/Dimethyl Ether Intermediates*; NREL (National Renewable Energy Laboratory (NREL), Golden, CO (United States)): 2015.
9. Bui, H.-H.; Tran, K.-Q.; Chen, W.-H., Pyrolysis of microalgae residues–A kinetic study. *Bioresource Technology* **2016,** *199*, 362-366.
10. Di Blasi, C.; Branca, C., Kinetics of primary product formation from wood pyrolysis. *Ind. Eng. Chem. Res.* **2001,** *40* (23), 5547-5556.
11. Lv, P.; Chang, J.; Wang, T.; Wu, C.; Tsubaki, N., A kinetic study on biomass fast catalytic pyrolysis. *Energy Fuels* **2004,** *18* (6), 1865-1869.
12. Wang, S.; Jiang, X.; Wang, N.; Yu, L.; Li, Z.; He, P., Research on pyrolysis characteristics of seaweed. *Energy Fuels* **2007,** *21* (6), 3723-3729.
13. White, J. E.; Catallo, W. J.; Legendre, B. L., Biomass pyrolysis kinetics: a comparative critical review with relevant agricultural residue case studies. *Journal of Analytical and Applied Pyrolysis* **2011,** *91* (1), 1-33.
14. Bilbao, R.; Arauzo, J.; Salvador, M. L., Kinetics and modeling of gas formation in the thermal decomposition of powdery cellulose and pine sawdust. *Ind. Eng. Chem. Res.* **1995,** *34* (3), 786-793.
15. Raveendran, K.; Ganesh, A.; Khilar, K. C., Pyrolysis characteristics of biomass and biomass components. *Fuel* **1996,** *75* (8), 987-998.
16. Radmanesh, R.; Courbariaux, Y.; Chaouki, J.; Guy, C., A unified lumped approach in kinetic modeling of biomass pyrolysis. *Fuel* **2006,** *85* (9), 1211-1220.

17. Seo, D. K.; Park, S. S.; Hwang, J.; Yu, T.-U., Study of the pyrolysis of biomass using thermo-gravimetric analysis (TGA) and concentration measurements of the evolved species. *Journal of Analytical and Applied Pyrolysis* **2010,** *89* (1), 66-73.
18. Sadhukhan, A. K.; Gupta, P.; Goyal, T.; Saha, R. K., Modelling of pyrolysis of coal–biomass blends using thermogravimetric analysis. *Bioresource Technology* **2008,** *99* (17), 8022-8026.
19. Tihay, V.; Gillard, P., Pyrolysis gases released during the thermal decomposition of three Mediterranean species. *Journal of Analytical and Applied Pyrolysis* **2010,** *88* (2), 168-174.
20. ASABE, S358.3: Moisture Measurement — Forages. ASABE: St. Joseph, Mich., 2012.
21. ASTM, D3175 - 11: Standard test method for volatile matter in the analysis sample of coal and coke. ASTM International: West Conshohocken, Pa., 2011.
22. NREL, Determination of Ash in Biomass. National Renewable Energy Laboratory: Golden, Colo., 2005.
23. Di Blasi, C.; Lanzetta, M., Intrinsic kinetics of isothermal xylan degradation in inert atmosphere. *Journal of Analytical and Applied Pyrolysis* **1997,** *40*, 287-303.
24. Fogler, S. H., External Diffusion Effects on Heterogeneous Reactions. In *Elements of Chemical Reaction Engineering*, 3rd ed.; Prentice-Hall of India: New Delhi, India, 2004; pp 686-726.
25. Branca, C.; Di Blasi, C.; Russo, C., Devolatilization in the temperature range 300–600 K of liquids derived from wood pyrolysis and gasification. *Fuel* **2005,** *84* (1), 37-45.
26. USEPA, Method 3052: Microwave assisted acid digestion of siliceous and organically based matrices. *Test Methods for Evaluating Solid Waste* **1995**.
27. Kim, P.; Johnson, A.; Edmunds, C. W.; Radosevich, M.; Vogt, F.; Rials, T. G.; Labbé, N., Surface functionality and carbon structures in lignocellulosic-derived biochars produced by fast pyrolysis. *Energy Fuels* **2011,** *25* (10), 4693-4703.
28. Granada, E.; Eguía, P.; Comesaña, J.; Patiño, D.; Porteiro, J.; Miguez, J., Devolatilization behaviour and pyrolysis kinetic modelling of Spanish biomass fuels. *Journal of thermal analysis and calorimetry* **2013,** *113* (2), 569-578.
29. Di Blasi, C.; Branca, C.; Lombardi, V.; Ciappa, P.; Di Giacomo, C., Effects of particle size and density on the packed-bed pyrolysis of wood. *Energy Fuels* **2013,** *27* (11), 6781-6791.
30. González, J. F.; Encinar, J. M.; Canito, J. L.; Sabio, E.; Chacón, M., Pyrolysis of cherry stones: energy uses of the different fractions and kinetic study. *Journal of Analytical and Applied Pyrolysis* **2003,** *67* (1), 165-190.
31. Lee, S.-B.; Fasina, O., TG-FTIR analysis of switchgrass pyrolysis. *Journal of analytical and applied pyrolysis* **2009,** *86* (1), 39-43.
32. Kumar, S.; Dasappa, S., Modeling and analysis of single particle conversion of biomass in a packed bed gasification system. *Applied Thermal Engineering* **2017,** *112*, 1382-1395.
33. Wojdyr, M., Fityk: a general-purpose peak fitting program. *Journal of Applied Crystallography* **2010,** *43* (5), 1126-1128.

34. Wu, C.; Budarin, V. L.; Gronnow, M. J.; De Bruyn, M.; Onwudili, J. A.; Clark, J. H.; Williams, P. T., Conventional and microwave-assisted pyrolysis of biomass under different heating rates. *Journal of Analytical and Applied Pyrolysis* **2014,** *107*, 276-283.
35. Wongsiriamnuay, T.; Tippayawong, N., Non-isothermal pyrolysis characteristics of giant sensitive plants using thermogravimetric analysis. *Bioresource Technology* **2010,** *101* (14), 5638-5644.
36. Wu, W.-G.; Chen, Y.; Hu, L.-Y.; Luo, Y.-H. In *Isothermal pyrolysis of biomass by macro-TG*, Power and Energy Engineering Conference, 2009. APPEEC 2009. Asia-Pacific, IEEE: 2009; pp 1-5.
37. Babu, B., Biomass pyrolysis: a state-of-the-art review. *Biofuels, Bioproducts and Biorefining* **2008,** *2* (5), 393-414.
38. Roberts, A., A review of kinetics data for the pyrolysis of wood and related substances. *Combustion and flame* **1970,** *14* (2), 261-272.
39. Samolada, M.; Vasalos, I., A kinetic approach to the flash pyrolysis of biomass in a fluidized bed reactor. *Fuel* **1991,** *70* (7), 883-889.
40. Liu, Q.; Wang, S.; Zheng, Y.; Luo, Z.; Cen, K., Mechanism study of wood lignin pyrolysis by using TG–FTIR analysis. *Journal of Analytical and Applied Pyrolysis* **2008,** *82* (1), 170-177.
41. Branca, C.; Albano, A.; Di Blasi, C., Critical evaluation of global mechanisms of wood devolatilization. *Thermochimica Acta* **2005,** *429* (2), 133-141.
42. Bridgeman, T. G.; Darvell, L. I.; Jones, J. M.; Williams, P. T.; Fahmi, R.; Bridgwater, A. V.; Barraclough, T.; Shield, I.; Yates, N.; Thain, S. C.; Donnison, I. S., Influence of particle size on the analytical and chemical properties of two energy crops. *Fuel* **2007,** *86* (1–2), 60-72.
43. Carpenter, D. L.; Bain, R. L.; Davis, R. E.; Dutta, A.; Feik, C. J.; Gaston, K. R.; Jablonski, W.; Phillips, S. D.; Nimlos, M. R., Pilot-scale gasification of corn stover, switchgrass, wheat straw, and wood: 1. Parametric study and comparison with literature. *Ind. Eng. Chem. Res.* **2010,** *49* (4), 1859-1871.
44. Carter, C. L.; Abdoulmoumine, N.; Kulkarni, A.; Adhikari, S.; Fasina, O., Physicochemical properties of thermally treated biomass and energy requirement for torrefaction. *Transactions of the ASABE* **2013,** *56* (3), 1093 - 1100.
45. Weiland, N. T.; Means, N. C.; Morreale, B. D., Product distributions from isothermal co-pyrolysis of coal and biomass. *Fuel* **2012,** *94*, 563-570.
46. Knudsen, J. N.; Jensen, P. A.; Dam-Johansen, K., Transformation and release to the gas phase of Cl, K, and S during combustion of annual biomass. *Energy Fuels* **2004,** *18* (5), 1385-1399.
47. Woolcock, P. J.; Brown, R. C., A review of cleaning technologies for biomass-derived syngas. *Biomass and Bioenergy* **2013,** *52* (1), 54-84.
48. Sadhwani, N.; Adhikari, S.; Eden, M. R.; Wang, Z.; Baker, R., Southern pines char gasification with CO 2—Kinetics and effect of alkali and alkaline earth metals. *Fuel Processing Technology* **2016,** *150*, 64-70.

49. Shen, Y.; Yoshikawa, K., Tar conversion and vapor upgrading via in situ catalysis using silica-based nickel nanoparticles embedded in rice husk char for biomass pyrolysis/gasification. *Ind. Eng. Chem. Res.* **2014,** *53* (27), 10929-10942.

CHAPTER IV
PARAMETRIC INVESTIGATION OF THE FORMATION OF BIOMASS DERIVED PRODUCER GAS AND INORGANIC CONTAMINANTS THROUGH NON-STOICHIOMETRIC EQUILIBRIUM MODELING

This chapter is a draft version of the following article:

Oyedeji, O. A., Daw, C. S., Labbé, N., Ayers, P, D., and Abdoulmoumine, N. H. (draft). Parametric investigation of the formation of biomass derived producer gas and inorganic contaminants through non-stoichiometric equilibrium modeling. Sustainable Chemistry & Engineering or Transaction of ASABE.

Oluwafemi Oyedeji constructed the equilibrium model, wrote the computer code, conducted data analysis and visualization, and wrote the first draft of the manuscript. Dr. Stuart Daw, Dr. Nicole Labbé, and Dr. Paul Ayers helped with parametric study design, model verification process, and edited the manuscripts. Dr. Nourredine Abdoulmoumine supervised the model implementation, assisted with data analysis and visualization, and edited the manuscripts.

Abstract

Gasification generates producer gas to produce renewable fuel and chemicals. The producer gas from biomass gasification contains CO, CO_2, H_2, CH_4, and H_2O, and several deleterious contaminants (NH_3, HCN, H_2S, and COS), whose yields are significantly influenced by several operating variables. This study presents an extensive parametric study, using a non-stoichiometric equilibrium modeling approach, to provide a comprehensive picture of biomass gasification gaseous products. The non-stoichiometric equilibrium directly minimizes the Gibbs free energy of the system based on the elemental composition of biomass feedstock. The effects of gasification temperature, equivalence ratio, and moisture content of the feedstock on producer gas composition and lower heating value were investigated. The predicted concentrations of CO, CO_2, and H_2 were comparable to experimentally measured concentrations. However, those of CH_4, NH_3, HCN, H_2S, and COS were considerably different from experimentally measured data, signifying that the formation of these gases is kinetically controlled in real systems. The established trends nevertheless were comparable with experimentally observed trends. At equilibrium, large fraction of biomass-nitrogen is desirably converted to N_2. Biomass-sulfur was mostly transformed into H_2S and smaller quantities of COS. Finally, the formation of all H_2S, COS, and HCN were predominantly influenced by moisture content.

Keywords: Gasification, lignocellulosic biomass, producer gas, contaminants, non-stoichiometric model, thermodynamic equilibrium.

Introduction

Approximately 97 quadrillion Btu of energy is consumed annually in the United States with more than 80% of the energy consumption accounted for by nonrenewable, unsustainable, fossil-based sources.[1] This huge energy demand, despite diminishing fossil-based energy reserves, makes the quest for renewable, sustainable energy sources imperative.[2] Lignocellulosic biomass provides an

exclusive opportunity to displace a substantial quota of the fossil-based energy because they are renewable, ubiquitous, and capable of producing diverse alternative fuels.[3] One of the methods used to extract energy and fuel from lignocellulosic biomass is gasification. The gasification of biomass primarily generates producer gas, which can be used as building block to synthesize liquid transportation fuels and alcohols or can be directly combusted to produce heat and power.[4] The major gases in producer gas are CO, CO_2, H_2, CH_4, and H_2O.

Additionally, lignocellulosic biomass contains nitrogen and sulfur, among other elements, which are converted into inorganic contaminants during gasification leading to undesirable consequences downstream.[5] These contaminants may produce severe corrosion of equipment parts, catalyst deactivation, and environmental pollution.[6] Tan et al.[7] reported that gas cleaning to remove contaminants makes up a significant share of the capital and operating cost. It is consequently important to reduce the extent of gas cleaning needed by, among other options, minimizing the production of contaminants species during biomass gasification in the first place.

The formation of producer gas and contaminants is influenced by biomass gasification operating variables and biomass properties.[8-9] The total gas yield increases when the gasification temperature is raised because the decomposition of biomass molecules and heavy hydrocarbons is favored.[10] However, the lower heating value (LHV) of the producer gas, which is the most desirable property of producer gas intended for combustion, reduces as gasification temperature increases.[11]

Equivalence ratio (ER) also influences gasification performance. ER is the actual air-to-biomass ratio divided by the stoichiometric air-to-biomass ratio. Biomass gasification typically occur at ER values between 0.2 and 0.4.[12] Increasing ER favors exothermic oxidation reactions that elevate the temperature and reduce energy input but produce more completely oxidized chemical species such as CO_2, H_2O, SO_2, and NO_x with lower LHV. Similarly, the moisture content of biomass is an important variable. Biomass containing higher moisture desirably generates more H_2 compared to biomass containing lower moisture. However, ignition difficulty and severe efficiency loss are experienced when the moisture content of biomass is above a certain threshold (typically 30%).[13]

In summary, several factors influence gasification performance and tradeoffs are unavoidable. This coupled with the anisotropic nature of biomass makes the optimization of operating variable via experimental investigation toilsome and expensive. Non-stoichiometric equilibrium modeling of biomass gasification is a valuable tool that can be used to perform an in-depth parametric study inexpensively and fast. Non-stoichiometric equilibrium modeling directly minimizes the Gibbs free energy of the system using numerical optimization techniques.[14]

Many researchers have developed equilibrium models to predict the composition of major gases in producer gas whereas only few have reported the prediction of nitrogen and sulfur species.[15-18] The current gaps addressed by this study are: *i)* scarcity of equilibrium modeling of producer gas contaminants, and *ii)* parametric study of producer gas contaminants at equilibrium. Thus, our objective is to present a detailed parametric study of biomass gasification using a non-stoichiometric equilibrium model approach based on the measured proximate and ultimate properties and a range of operating conditions. This work presents extensive data that can inform the selection of operating variables and provide a comprehensive picture of the interactions among operating variables that is otherwise not available in published literature. Furthermore, this study provides a tool that can be used by engineers and scientists to predict the gasification performance of new solid fuels. The operating variables that were considered are gasification temperature, ER, biomass moisture content, and biomass elemental composition. The effects of these variables on producer gas composition (CO, CO_2, CH_4, H_2, H_2O, N_2, NH_3, HCN, H_2S, and COS), and LHV were evaluated.

Materials and method

Model assumptions and formulation

Figure 4.1 outlines the sequence of actions taken to effectively implement the non-stoichiometric equilibrium model for biomass gasification in this study. The following assumptions were made in the development of the non-stoichiometric equilibrium model:

1. Pressure drop across the gasifier height is negligible.
2. All chemical species are homogeneously mixed and maintained at gasification temperature.
3. All gas phase chemical species are regarded as ideal gases.
4. The global gasification reaction is as expressed in Reaction [4.1].

$$\begin{aligned} CH_aO_bN_cS_d + eH_2O + fO_2 + gN_2 \xrightarrow{\text{Heat}} C_\alpha + x_1H_2 + x_2H_2O + x_3CO \\ + x_4CO_2 + x_5CH_4 + x_6N_2 + x_7O_2 + x_8NH_3 + x_9HCN \\ + x_{10}H_2S + x_{11}COS \end{aligned} \quad [4.1]$$

These assumptions simplify the modeling procedure and are typical for equilibrium modeling.[15-19] In Reaction [4.1], $CH_aO_bN_cS_d$ represents the simplified molecular formula for the biomass used, based on an atom of carbon. Equilibrium models typically assume that all the atoms contained in the solid fuel are converted to gas phase chemical species. However, this is not the case in practice, because solid residue (C_α) is characteristically obtained after gasification. Hence, this simulation approach takes into account the production of char using an experimentally determined equation (Equation (4.1).[20] The water molecules present in the reactant side of reaction R1 account for the moisture contained in the biomass. Its coefficient

(e) was therefore calculated as a function of the initial moisture content of biomass (Equation (4.2). The values of coefficients f and g were calculated based on selected ER and carrier gas (N_2) flow rate, respectively. Therefore, for a selected set of operating variables, all coefficients in the reactant side of reaction R1 are constant and known. The coefficients on the product side of Reaction [4.1] was then estimated via direct minimization of Gibbs free energy of the system.

$$\alpha = 0.25 + 0.75\left(1 - e^{-ER/0.23}\right) \quad (4.1)$$

$$e = \frac{M_{biomass}\varphi}{M_{water}(1-\varphi)} \quad (4.2)$$

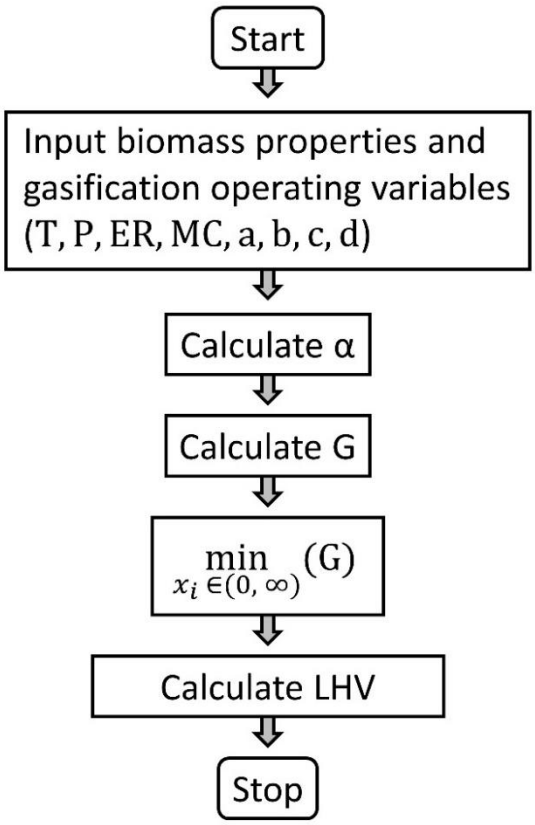

Figure 4.1. Model development flowchart. (see nomenclature section for the definition of terms).

The Gibbs free energy of the system was computed as expressed in Equation (4.3). The number of mole of each chemical species was then numerically optimized with the goal of minimizing the value of Gibbs free energy, subject to two class of constraints (Equations (4.6) – (4.11)). Lagrange method of undetermined multipliers was applied to reduce the computation cost and accelerate convergence rate. This involved the formulation of a Lagrangian function, which imports an underdetermined multiplier for each chemical element (Equation (4.12)). The minimization of the Lagrangian function is achieved when its partial derivatives equal zero (Equation (4.13)).

$$G = \sum_{i=1}^{N_c} x_i \mu_i \tag{4.3}$$

$$\mu_i = \mu_i^o + RT\ln\left(\frac{x_i P}{x_t P^o}\right) \tag{4.4}$$

$$\mu_i^o = \bar{g}_i^o = \bar{h}_i^o - T\bar{s}_i^o \tag{4.5}$$

Non-negativity constraint:

$$x_i \geq 0 \tag{4.6}$$

Conversation of moles constraints:

$$1 = \alpha + x_3 + x_4 + x_5 + x_9 + x_{11} \tag{4.7}$$

$$a + 2e = 2x_1 + 2x_2 + 4x_5 + 3x_8 + x_9 + 2x_{10} \tag{4.8}$$

$$b + e + 2f = x_2 + x_3 + 2x_4 + 2x_7 + x_{11} \tag{4.9}$$

$$c + 2g = 2x_6 + x_8 + x_9 \tag{4.10}$$

$$d = x_{10} + x_{11} \tag{4.11}$$

Lagrangian underdetermined multipliers formulation:

$$F_l = G - \sum_{j=1}^{N_e} \lambda_j \sum_{i=1}^{N_c} \left(e_{i,j} x_i - W_j\right) \tag{4.12}$$

$$\frac{\partial F_l}{\partial x_i} = \mu_i + \sum_{j=1}^{N_e} \lambda_j e_{i,j} = 0 \quad (4.13)$$

Lower heating value calculation

The heating value of generated producer gas after biomass gasification is often a measure of biomass gasification performance. Therefore, the LHV of producer gas was calculated after the composition of producer gas was determined as outlined in Equation (4.14). Since, nitrogen- and sulfur-containing species are expected to be removed through gas cleaning before the utilization of producer gas in post-gasification processes, these species were not included in the calculation of LHV of the producer gas.

$$\mathrm{LHV} = \sum_{i=1}^{N_c - N_{ns}} x_i \, \mathrm{LHV}_i \quad (4.14)$$

Model implementation

This optimization problem was solved using Engineering Equation Solver (EES) software because of the unique integration of an optimization system with an extensive thermodynamic library in EES software.[21] Each simulation was completed in less than 5 seconds using a desktop computer with 3.50 GHz, Intel i3 processor, and 4 GB RAM.

A $18 \times 5 \times 10$ factorial parametric study (total number of cases = 900) was carried out following the levels of each operating variable listed in Table 4.1. The properties of the biomass sample used are listed in Table 4.2 as adopted from Abdoulmoumine et al.[22] Before the parametric study was carried out, the developed model was first compared to selected empirically data from Abdoulmoumine et al.[22] and Aljbour and Kawamoto[23-24]. Finally, the beta coefficient from multiple linear regression model was obtained using SAS 9.4 and used to quantitatively determine the relative importance of each operating variable to each response quantity (concentration of each chemical species).

Table 4.1. Process parameters and associated levels used in this study.

Variables	Range	Levels
Temperature (K)	800 - 1500	18
ER (-)	0.20 - 0.40	5
Moisture content (%)	5 - 50	10

Table 4.2. Physical and chemical properties of biomass sample used.

Properties	Value
Biomass feedstock	Pine wood
Proximate analysis (%, wet basis)	
Moisture content	7.94
Ash content	0.31
Fixed carbon content	15.30
Volatile matter content	77.02
HHV (MJ/kg)	20.18
Ultimate analysis (%, dry basis)	
C	47.14
H	6.52
N	0.44
S	0.10
O (by difference)	45.80
Simplified molecular formula	$CH_{1.6}O_{0.7}N_{0.008}S_{0.001}$

*HHV value for biomass was not reported by author. The assumed value in this work was adapted from Fasina[25]

Results and discussion

Model verification

The prediction from the equilibrium model was compared to two sets of experimental data found in literature. The first experimental data compared with the equilibrium model prediction is from Abdoulmoumine et al.[22], in which pine wood (MC = 7.9%) was gasified at 1323 K and ER of 0.25. Whereas, the second experimental data compared with the equilibrium model prediction is from Aljbour and Kawamoto[23-24], in which Japanese cedar wood (MC = 8.9%) was gasified at 1123 – 1223 K and ER of 0.2. These two studies were selected because of the range of biomass properties both studies represent. Table 4.3 outlines the comparison between the model's prediction with the experimental data. For CO and CO_2, there was good agreement between the model prediction and experimental data. The predicted concentration of these species was within the range of the reported experimental data. In the case of H_2, the equilibrium model prediction was close but a little higher than the range of the reported experimental data (Table 4.3). The predicted concentration of CH_4 was drastically lower than the concentration observed under experimental conditions. This deviation of the equilibrium model prediction from experimental data has been reported by several equilibrium modelers.[16, 26] At equilibrium state, nearly all CH_4 is thermally cracked or reformed, but non-equilibrium effects are important in real systems. This demonstrate that the formation of CH_4 during biomass gasification is kinetically controlled rather than equilibrium controlled. The quantitative information from equilibrium models gives the picture of what is expected when the gasification system reaches equilibrium. However, qualitative information (parametric relationship) from equilibrium model is useful in understanding what happens to gasification performance when one or more gasification operation variables are modified. The qualitative information is also useful in making informed inference about the influence of gasification sub-reactions (such as water–gas shift, Boudouard, methanation, and oxidation reactions).[4] In the subsequent sections, the parametric relationship between gasification operation variables and producer gas composition is discussed.

The predicted concentration of NH_3 and HCN was also lower than the value reported in the experimental studies considered (Table 4.3). This observation points to a beneficial feature of achieving equilibrium during gasification because it implies that the concentration of NH_3 and HCN can be significantly reduced by enhancing gasification system to attain equilibrium. Reducing the concentration of NH_3 and HCN directly reduces the extent and cost of gas cleanup needed after gasification. However, the predicted concentration of H_2S and COS was higher than the experimentally measured concentration (Table 4.3). The reason for this difference is because sulfur contained in tar is expected to be converted to light sulfur compounds (H_2S, COS, SO_2, and CS_2) at thermodynamic equilibrium. However, the predicted concentration of SO_2 and CS_2 in this study was negligible, therefore, H_2S and COS are the main sulfur species formed at thermodynamic equilibrium.

Summarily, the comparison of the predicted data from the developed equilibrium model to experimental data indicates that the formation of CO, H_2, and CO_2 in real systems approach equilibrium concentrations. This implies that equilibrium modeling is sufficient for the prediction of these chemical species in real system. However, the concentration CH_4, NH_3, HCN, H_2S, and COS are governed by non-equilibrium effects in real systems because the predicted data from the developed equilibrium model deviate from the experimental data. The implication of this is that simulations involving kinetic information (such as computational fluid dynamics and multi-scale models)[27] are needed to effectively predict the concentration of CH_4, NH_3, HCN, H_2S, and COS.

Table 4.3. Comparison of equilibrium model prediction with experimental values.

Producer gas component	Reference 1[22]		Reference 2[23-24]	
	Experimental	Predicted	Experimental	Predicted
H_2 (%vol.)	38.3 ± 2.3	41.8	39.38 ± 2.23	41.90
CO (%vol.)	44.3 ± 4.2	45.5	47.33 ± 5.52	46.90
CO_2 (%vol.)	12.5 ± 1.1	12.6	8.63 ± 4.84	11.19
CH_4 (%vol.)	3.3 ± 1.0	~0.01	6.03 ± 2.72	~0.01
H_2S (ppmv)	26.0 ± 2.1	509.9	39	47.19
COS (ppmv)	na	23.6	<2	1.1
NH_3 (ppmv)	312.4 ± 40.6	13.8	505	36.7
HCN (ppmv)	27.9 ± 3.4	0.57	6	1.1

na: Data were not reported in the corresponding literature.

Prediction of major constituents and parametric analysis

Hydrogen is one of the most important component of producer gas for its contribution to the overall energy density.[29-30] Therefore, information on its yield is essential in biomass gasification processes. Figure 4.2 shows the concentration of H_2 in producer gas at thermodynamic equilibrium and how gasification operating variables shift the equilibrium concentration of H_2.

The predicted concentration of H_2 in the producer gas initially increased with increasing temperature but later decreased after a certain temperature value was attained (Figure 4.2). The temperature value where the inflection was observed ranged between 900 and 1000 K, depending on the moisture content of the biomass. This implies that there is a noticeable interaction effect between the temperature and feedstock moisture content. Additionally, the formation of H_2 linearly increased when the moisture content of biomass was raised. These observations can be used to explain the relative shift in the equilibrium position of the major reactions involving H_2. The initial increase in the formation of H_2 can be ascribed mainly to the production of H_2 via dry- and steam-reforming reactions of CH_4. However, after the inflection point, reserve water-gas-shift reaction ($CO_2 + H_2 \rightarrow CO + H_2O$) is more favored as seen in the corresponding increase in CO and H_2O concentrations (Figure 4.3 and Figure 4.4, respectively).

Equivalence ratio also played a significant role in the formation of H_2. The concentration of H_2 was inversely proportional to ER within the limits considered in this study. This is directly related to the shift in equilibrium towards the forward direction of H_2 oxidation reaction ($2H_2 + O_2 \rightarrow 2H_2O$) due to increase in the concentration of O_2.[31] The comparison of the beta coefficients from multiple linear regression revealed that ER (with beta coefficient = -0.612) was the most important variable to concentration of H_2, implying that the concentration of H_2 is more sensitive to ER than to moisture content and temperature.

Carbon monoxide is an essential building block for several post-gasification processes (e.g., methanol synthesis, Fischer-Tropsch synthesis). As temperature was raised, the formation of CO increased, whereas as moisture content increased the formation of CO decreased (Figure 4.3). The increase in CO formation with temperature further supports the proposition that reserve water-gas shift reaction is more dominant at higher gasification temperature. Additionally, CO oxidation reaction, being an exothermic reaction, is inhibited at high temperature. When the moisture content of feedstock is increased, additional H_2O in the form of biomass moisture is injected into the system, shifting the equilibrium towards the product of the water-gas shift reaction.

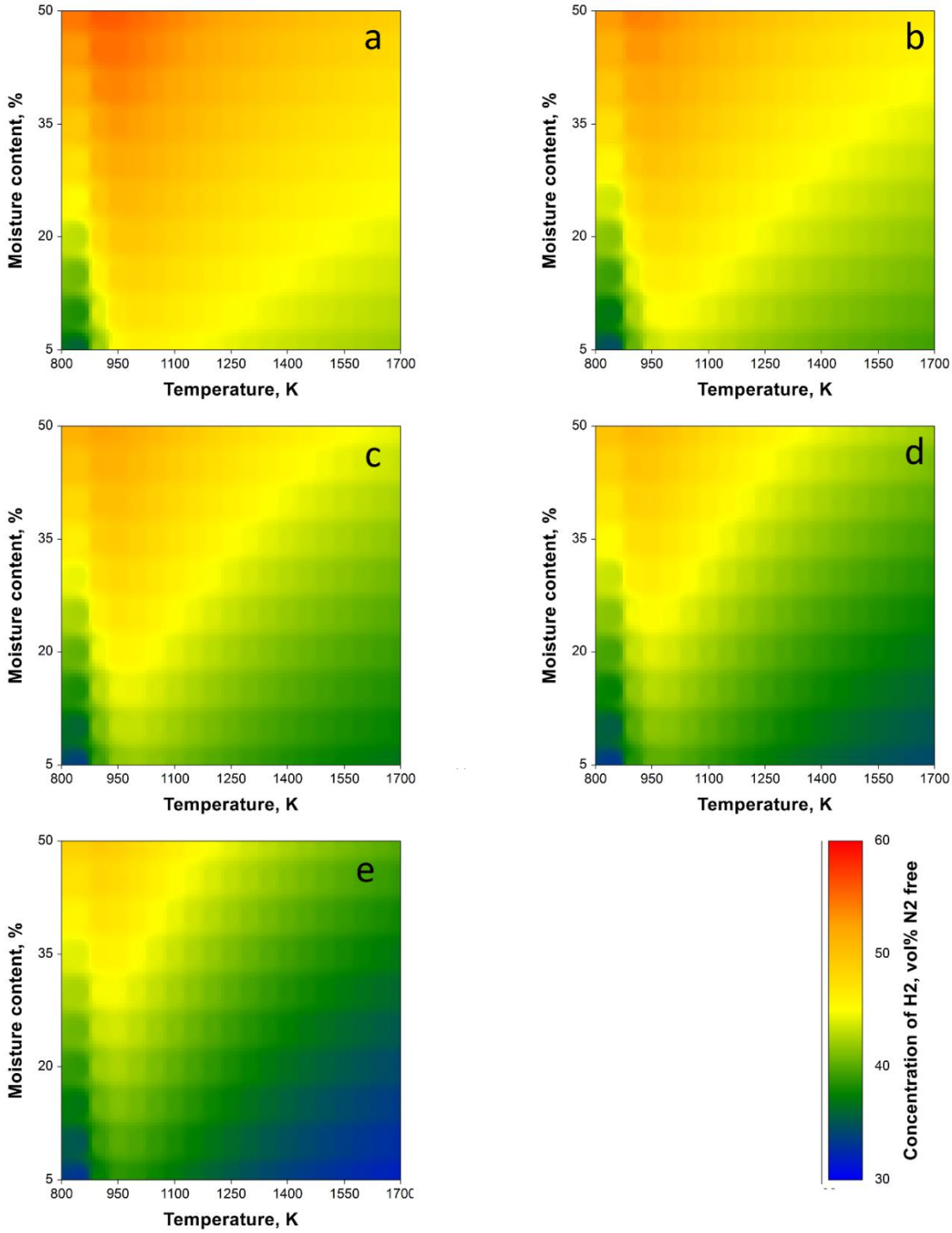

Figure 4.2. Effects of temperature, moisture content, and equivalence ratio on H_2 concentration. a) ER = 0.20, b) ER = 0.25, c) ER = 0.30, d) ER = 0.35, and e) ER = 0.40. Values are reported on a % vol/vol dry, N_2-free basis.

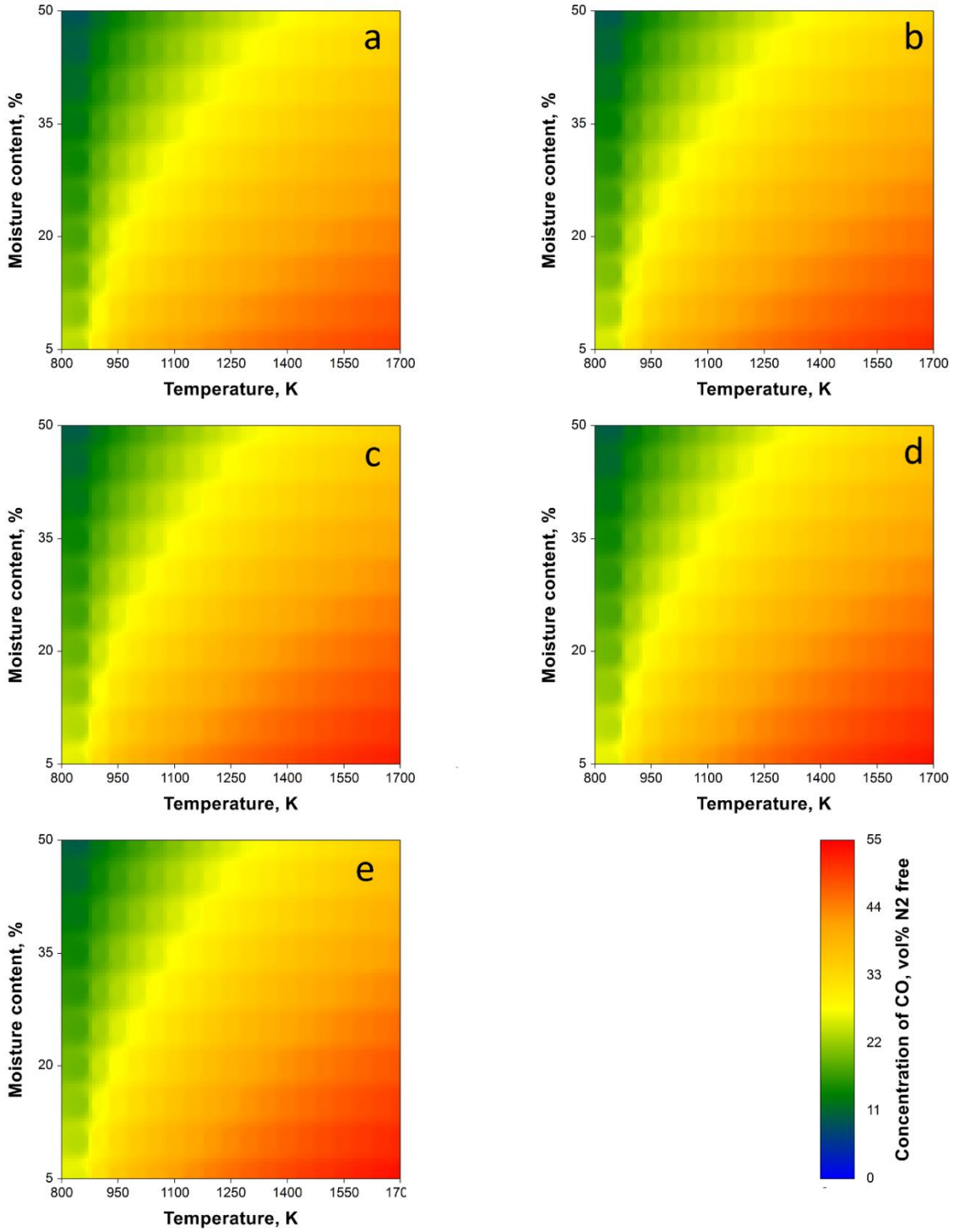

Figure 4.3. Effects of temperature, moisture content, and equivalence ratio on CO concentration. a) ER = 0.20, b) ER = 0.25, c) ER = 0.30, d) ER = 0.35, and e) ER = 0.40. Values are reported on a % vol/vol dry, N_2-free basis.

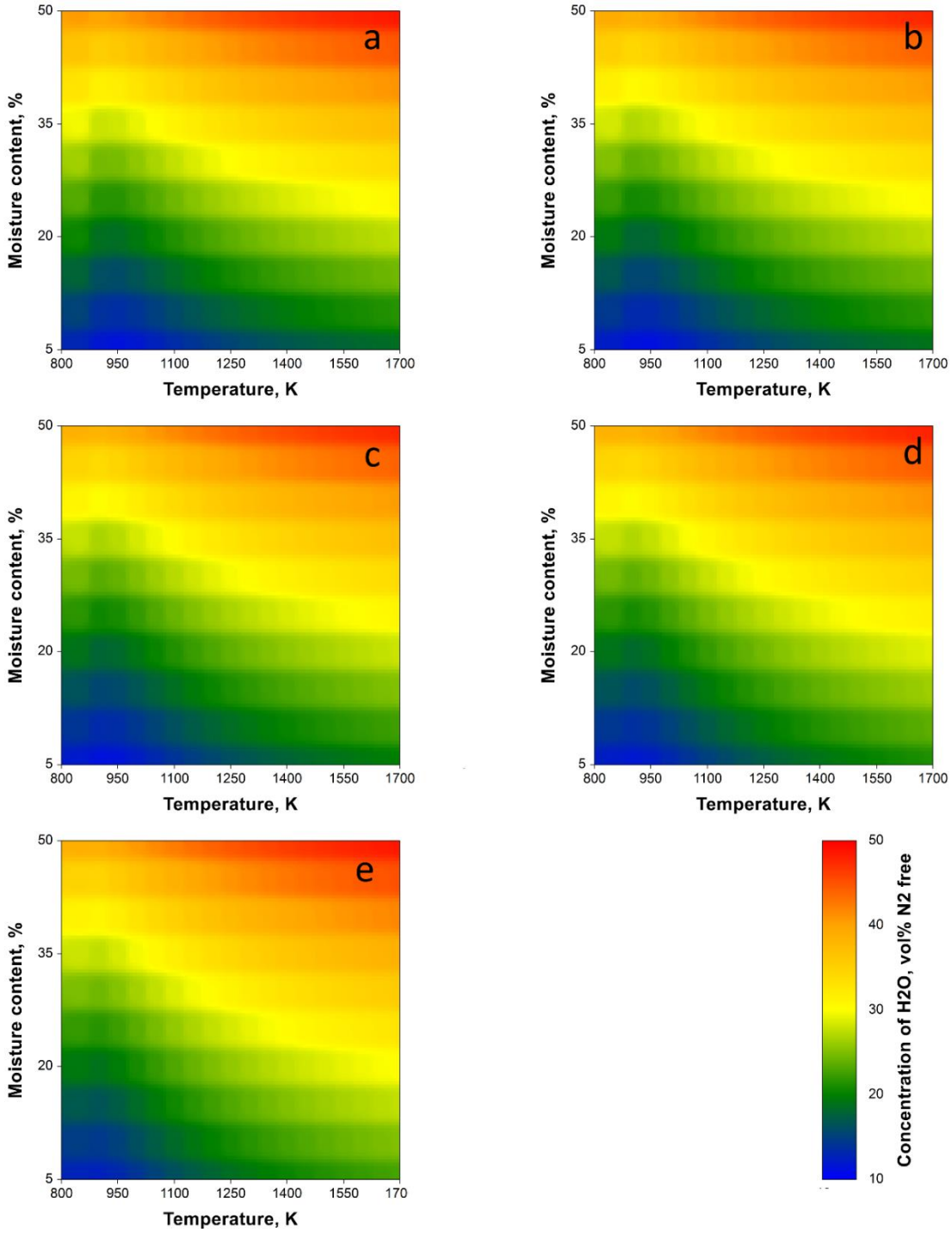

Figure 4.4. Effects of temperature, moisture content, and equivalence ratio on H_2O concentration. a) ER = 0.20, b) ER = 0.25, c) ER = 0.30, d) ER = 0.35, and e) ER = 0.40. Values are reported on a % vol/vol wet, N_2-free basis.

The concentration of CO increased with increasing ER (Figure 4.3) as a direct consequence of the implementation of Equation (4.1). As ER is increased, carbon conversion and carbon partial oxidation ($2C + O_2 \rightarrow 2CO$) increases. However, regression analysis showed that ER was the least important variable to the concentration of CO in producer gas among the three variables considered in this study. The beta coefficient associated with ER was 0.071, whereas those associated with temperature and moisture content were 0.743 and -0.632, respectively (Table 4.4).

The concentrations of H_2O, CO_2, and CH_4 as affected by gasification operating variables are shown in Figure 4.4, Figure 4.5, and Figure 4.6, respectively. These species are also considered as primary components of producer gas but are less important than CO and H_2. However, information on the concentration of CO_2, H_2O, and CH_4 is important to obtain a systematic understanding of the gasification mechanism and its chemical reaction dynamics.

The equilibrium model predicts that the higher the gasification temperature, the lower the concentration of CO_2 (Figure 4.5). This trend can be ascribed to lower production of CO_2, via exothermic CO oxidation reaction at higher temperature.[9] The concentration of CO_2 increased approximately linearly with moisture content and ER. However, the influence of moisture content on the concentration of CO_2 is more prominent compared to that of ER (Table 4.4). This indicates that the water gas shift reaction, being less exothermic, progresses faster than CO oxidation reaction at the higher temperatures.

The concentration of H_2O mostly increased with increasing temperature (Figure 4.4). This is complementary to the decrease in the concentration of H_2 with increasing temperature because of H_2 oxidation and reserve water gas shift reactions. Between temperatures of 850 and 950 K, the concentration of H_2O decreased when temperature increased, supporting the notion of the prominence of methane steam reforming reaction within this temperature range. The effect of ER on the concentration of H_2O was minimal (Figure 4.4). The predicted relationship between the concentration of H_2O and ER is similar to the experimental trend observed by Broer et al.[32] The concentration of H_2O generally reduced as ER was raised from 0.2 to 0.3 then increased as ER was further raised from 0.3 to 0.4. Finally, the concentration of H_2O increased as moisture content was augmented mainly because the amount of H_2O on the reactant side of the biomass gasification reaction increases with moisture content.

The concentration of CH_4 generally reduced with increasing temperature, moisture content, and ER, indicating the consumption of CH_4 via cracking, reforming, and oxidation reactions, respectively. The predicted concentration of CH_4 was small because reactions consuming CH_4 have high equilibrium constants and are expected to go to completion at thermodynamic equilibrium state (Figure 4.6). This

is in consonant with the result reported by several modelers.[16,26] As aforementioned, it affirms that the formation of CH_4 is more controlled by non-equilibrium effects during experimental gasification process. However, at lower temperatures and moisture content (≤850 K and ≤10%, respectively), the predicted concentration of CH_4 was approximately 10 vol% (Figure 4.6) and consistent with the experimental findings of Abdoulmoumine et al.[22] and Broer et al.[32] at similar temperatures.

Prediction of contaminant species and parametric analysis

Sulfur containing species (H_2S, COS, CS_2, and SO_2) in producer gas are notorious for causing catalyst deactivation and equipment part corrosion. Only the concentrations of H_2S and COS are discussed in this section because the upper limit of the concentration of CS_2 and SO_2 obtained during preliminary studies were in the order of 10^{-3} ppb. Furthermore, experimental investigations have shown that these two species are the most abundant sulfur species.[9, 33]

The concentration of H_2S initially decreased as gasification temperature was raised. However, it later increased with increasing temperature above 1000 K (Figure 4.7). It was also observed that the concentration of H_2S ranged between 159.00 (at temperature = 1700 K, moisture content = 50%, and ER = 0.40) to 345.70 ppmv (at temperature = 850 K, moisture content = 5%, and ER = 0.20). The range of the predicted concentration of H_2S overlaps with the range reported in literature.[34-36] The concentration of H_2S increases when ER was decreased, which is similar to the relationship between ER and the concentrations of H_2 and CO. The implication of this observation is that when ER is reduced to maximize the yield of H_2 and CO, the concentration of H_2S is simultaneously increased. The effect of moisture content on the concentration of H_2S was most severe, with more H_2S being produced by feedstocks with lower moisture content.

The concentration of COS however was higher at higher gasification temperature (Figure 4.8) This suggest that as temperature is raised, more H_2S is converted to form COS with H_2S decreasing with increasing temperature. Additionally, the concentration of COS decreased when the moisture content of biomass is increased, suggesting that higher H_2O impedes the formation of COS. These observations demonstrate that the endothermic reaction between H_2S and CO2 to form COS and H_2O ($H2S + CO2 \leftrightarrow COS + H_2O$) is important to the distribution of sulfur-containing contaminants in producer gas. The effect of ER on the concentration of COS was minimal (Figure 4.8). This was supported by the low beta coefficient obtained from the multiple linear regression analysis.

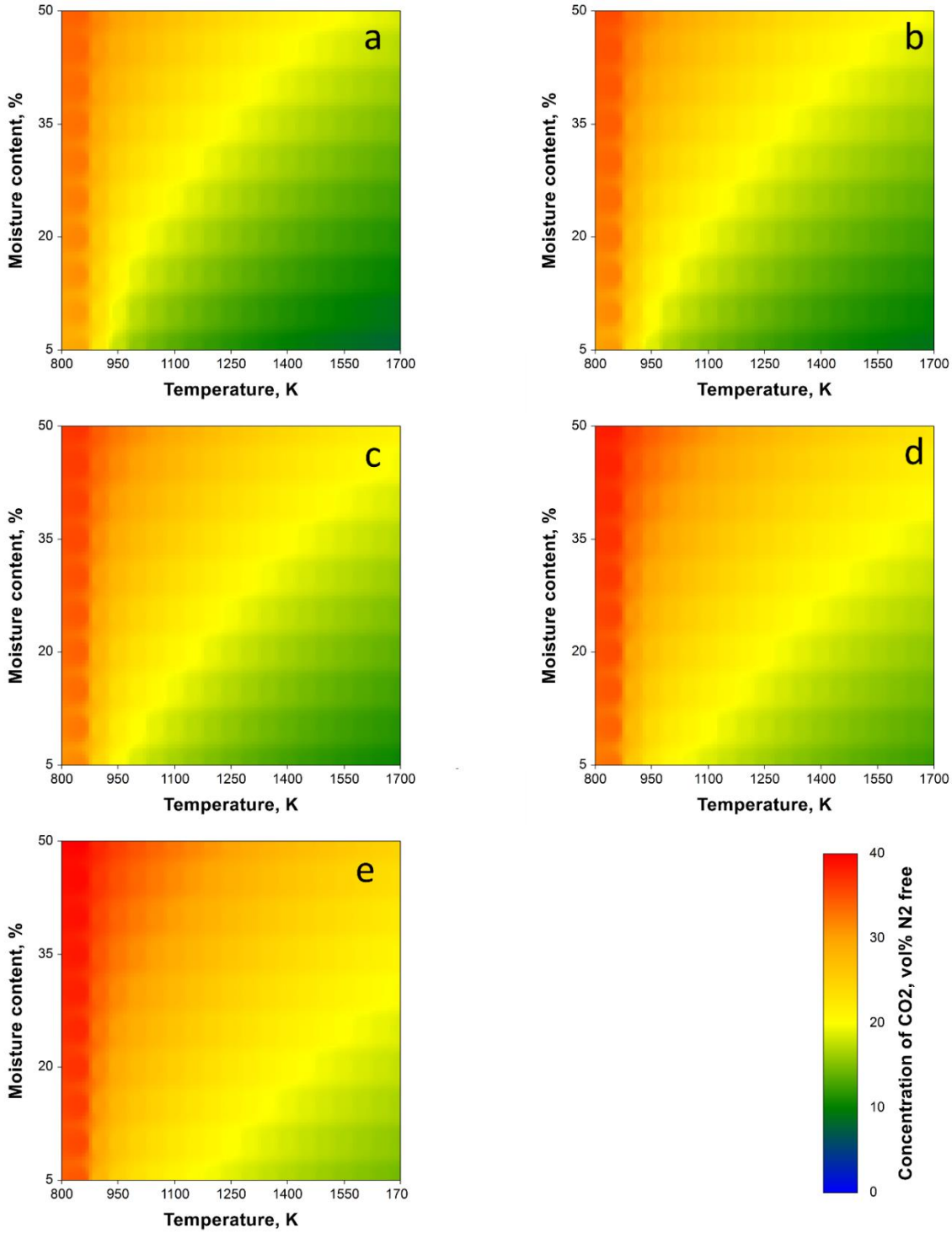

Figure 4.5. Effects of temperature, moisture content, and equivalence ratio on CO_2 concentration. a) ER = 0.20, b) ER = 0.25, c) ER = 0.30, d) ER = 0.35, and e) ER = 0.40. Values are reported on a % vol/vol dry, N_2-free basis.

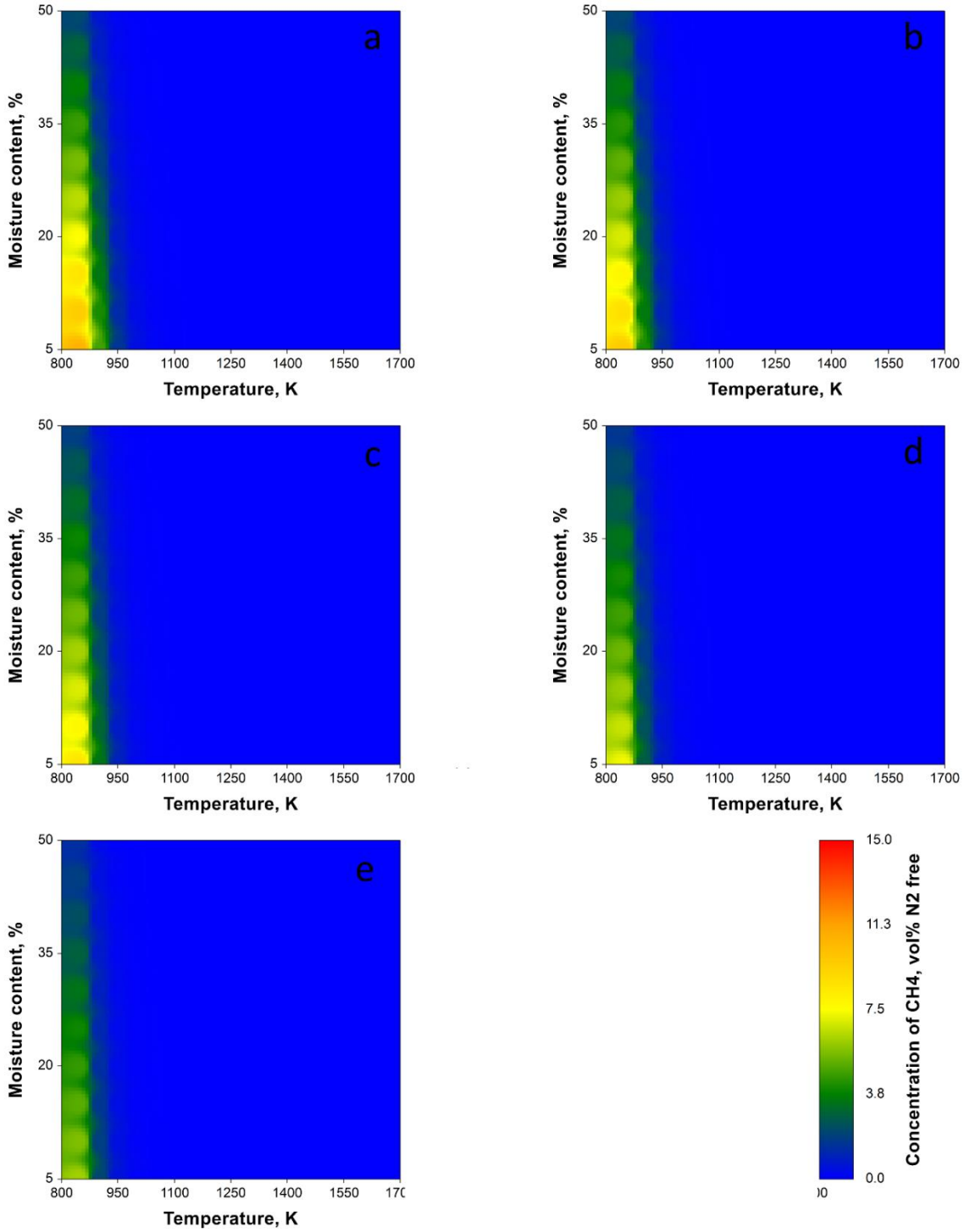

Figure 4.6. Effects of temperature, moisture content, and equivalence ratio on CH_4 concentration. a) ER = 0.20, b) ER = 0.25, c) ER = 0.30, d) ER = 0.35, and e) ER = 0.40. Values are reported on a % vol/vol dry, N_2-free basis.

Table 4.4. Standardized regression coefficients showing the relative importance of equivalence ratio, temperature, and moisture content of feedstock.

Producer gas component	Beta coefficient			Order of importance	r^2
	T	MC	ER		
H_2	-0.418	0.607	-0.612	ER > MC > T	0.92
H_2O	0.34	0.93	0.05	MC > T > ER	0.99
CO	0.743	-0.632	0.071	T > MC > ER	0.96
CO_2	-0.715	0.537	0.350	T > MC > ER	0.92
H_2S	0.426	-0.665	-0.451	MC > ER > T	0.83
COS	0.630	-0.744	0.171	MC > T > ER	0.98
NH_3	-0.805	0.030	-0.032	T > ER > MC	0.65
HCN	0.222	-0.864	-0.144	MC > T > ER	0.82

ER: Equivalence ratio, T: Temperature, MC: Moisture content of feedstock.

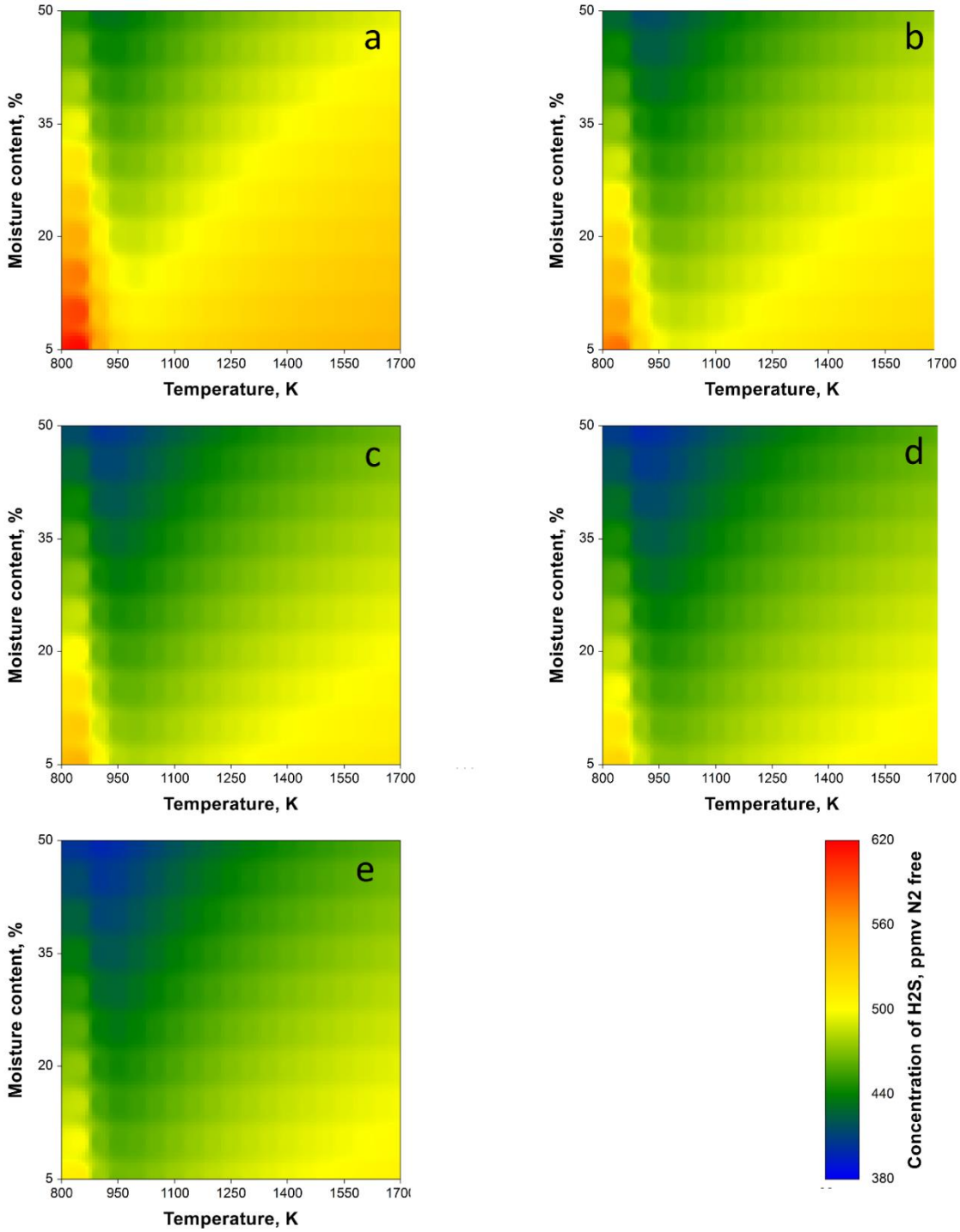

Figure 4.7. Effects of temperature, moisture content, and equivalence ratio on H_2S concentration. a) ER = 0.20, b) ER = 0.25, c) ER = 0.30, d) ER = 0.35, and e) ER = 0.40. Values are reported on a % vol/vol dry, N_2-free basis.

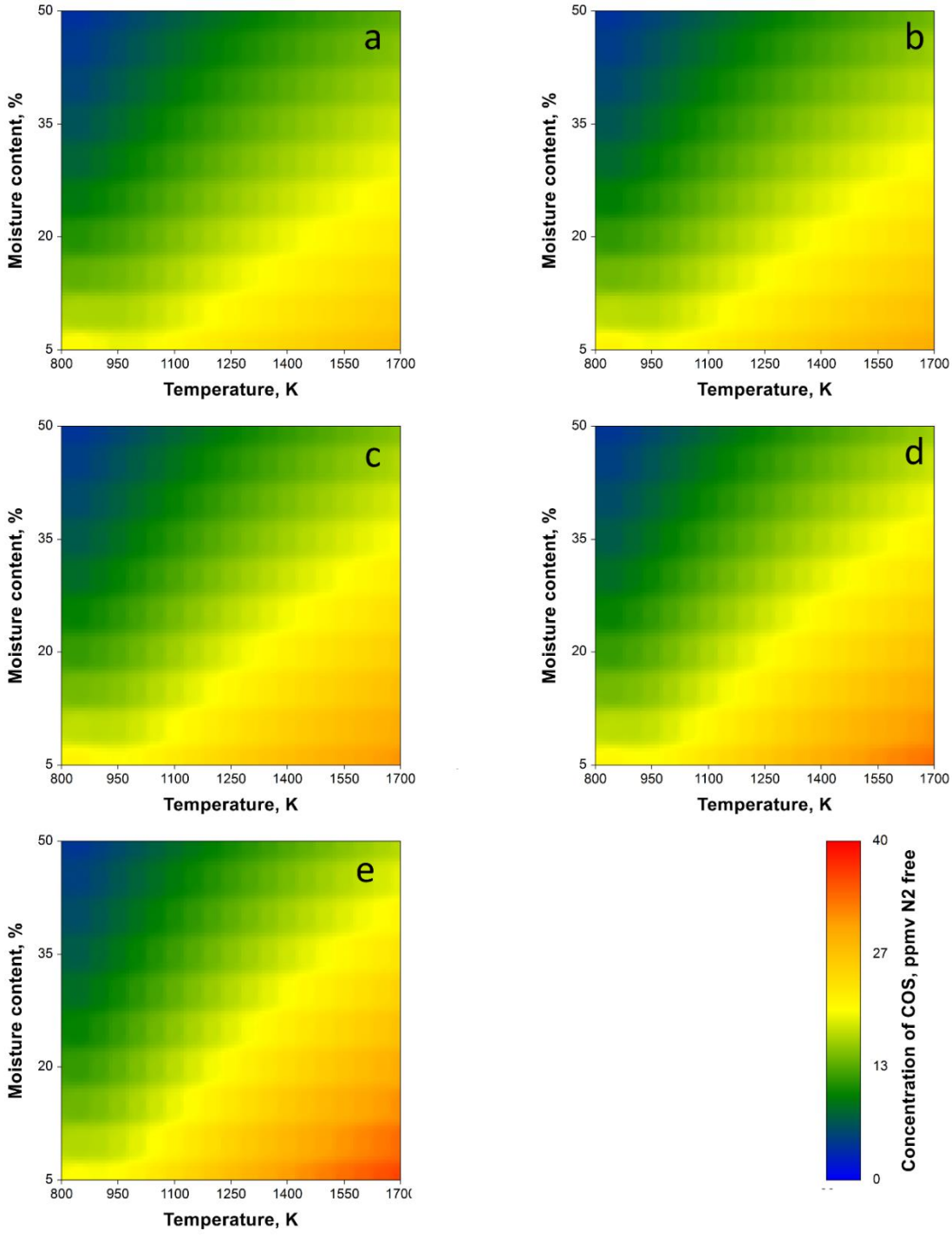

Figure 4.8. Effects of temperature, moisture content, and equivalence ratio on COS concentration. a) ER = 0.20, b) ER = 0.25, c) ER = 0.30, d) ER = 0.35, and e) ER = 0.40. Values are reported on a % vol/vol dry, N_2-free basis.

Biomass-bound nitrogen makes its way into producer gas during gasification as NH_3 and HCN, with NH_3 being the most abundant. Additionally, NH_3 may be later decomposed into diatomic nitrogen and hydrogen at high temperatures. The effects of temperature, ER, and moisture content on the concentration of NH_3 in producer gas are shown in Figure 4.9. It is evident that the concentration of NH_3 can be decreased by raising the gasification temperature and ER. This trend is in consonant with the result of many experimental studies.[22, 32, 37] The thermal decomposition and oxidation of NH_3 are enhanced when temperature and ER are raised, respectively, both causing the reduction of NH_3. At temperatures greater or equal to 1100 K, the concentration of NH_3 was lower than the level required for some post gasification applications (e.g., methanol synthesis).[34] Similarly, increasing the moisture content of the feedstock generally caused the reduction of the concentration of NH_3, except in the case of the 850 and 900 K temperature where the concentration of NH_3 initially increased with moisture content before subsequent reduction. The multiple linear regression model developed explained only about 65% of the variability in the concentration of NH_3, with temperature being the most important variable (Table 4.4).

The formation of HCN initially increased with increasing temperature up to 950 K and later reduced with further increase in temperature (Figure 4.10). Also, the formation of HCN decreased with increasing moisture content and ER. The interaction effect between moisture content and temperature was noticeable as evidenced by the decrease in the temperature-HCN concentration gradient as moisture content increased. For example, at moisture content of 10%, the concentration of HCN changed considerably with changing temperature. However, at moisture content of 50%, the concentration of HCN only slightly changed with changing temperature. The close observation of the concentration profiles for NH_3 and HCN suggests that there is an association between the concentration of NH_3 and HCN through the reaction $HCN + H_2O \leftrightarrow NH_3 + CO$.

Prediction of LHV

The effects of temperature, moisture content, and ER on LHV of the producer gas are presented in Figure 4.11. The predicted LHV of producer gas for the range of temperature, moisture content, and ER considered in this study was between 6.97 and 10.79 MJ/Nm^3. It was observed that increasing moisture content caused the LHV of resulting producer gas to linearly decrease due to the corresponding decline in the concentration of CO and CH_4. Similarly, LHV of producer gas decreased with increasing ER. These observations are in in agreement with the parametric trends established via several experimental studies.[31, 38-39] The relationship between the temperature and LHV of producer was not linear. Generally, the LHV of producer initially decreases with increasing temperature between 800 and 950 K. However above 1000 K, the LHV of producer increases with increasing temperature. The implication of this is that carrying out gasification process at relatively low temperature is beneficial from a thermal efficiency standpoint.

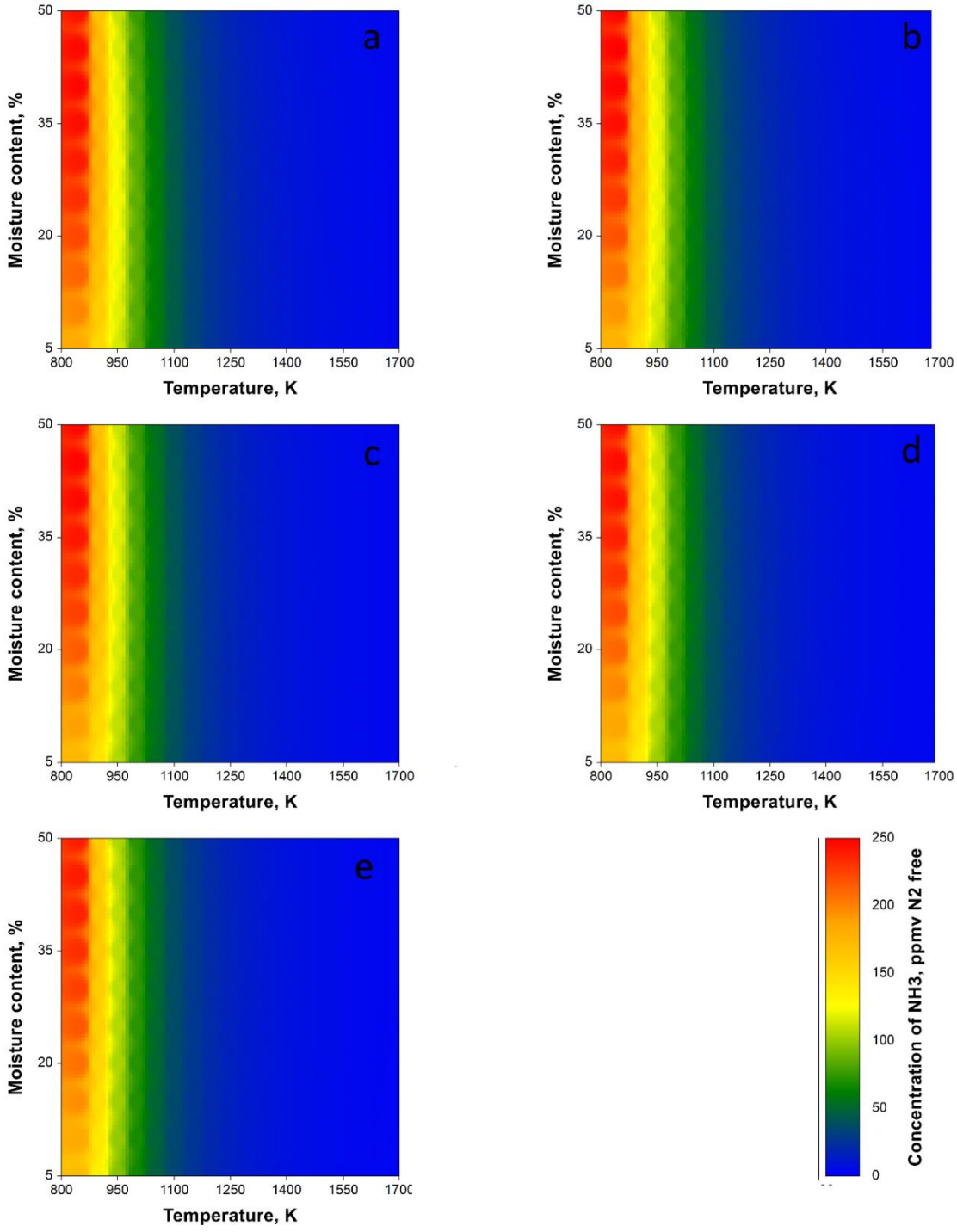

Figure 4.9. Effects of temperature, moisture content, and equivalence ratio on NH_3 concentration. a) ER = 0.20, b) ER = 0.25, c) ER = 0.30, d) ER = 0.35, and e) ER = 0.40. Values are reported on a % vol/vol dry, N_2-free basis.

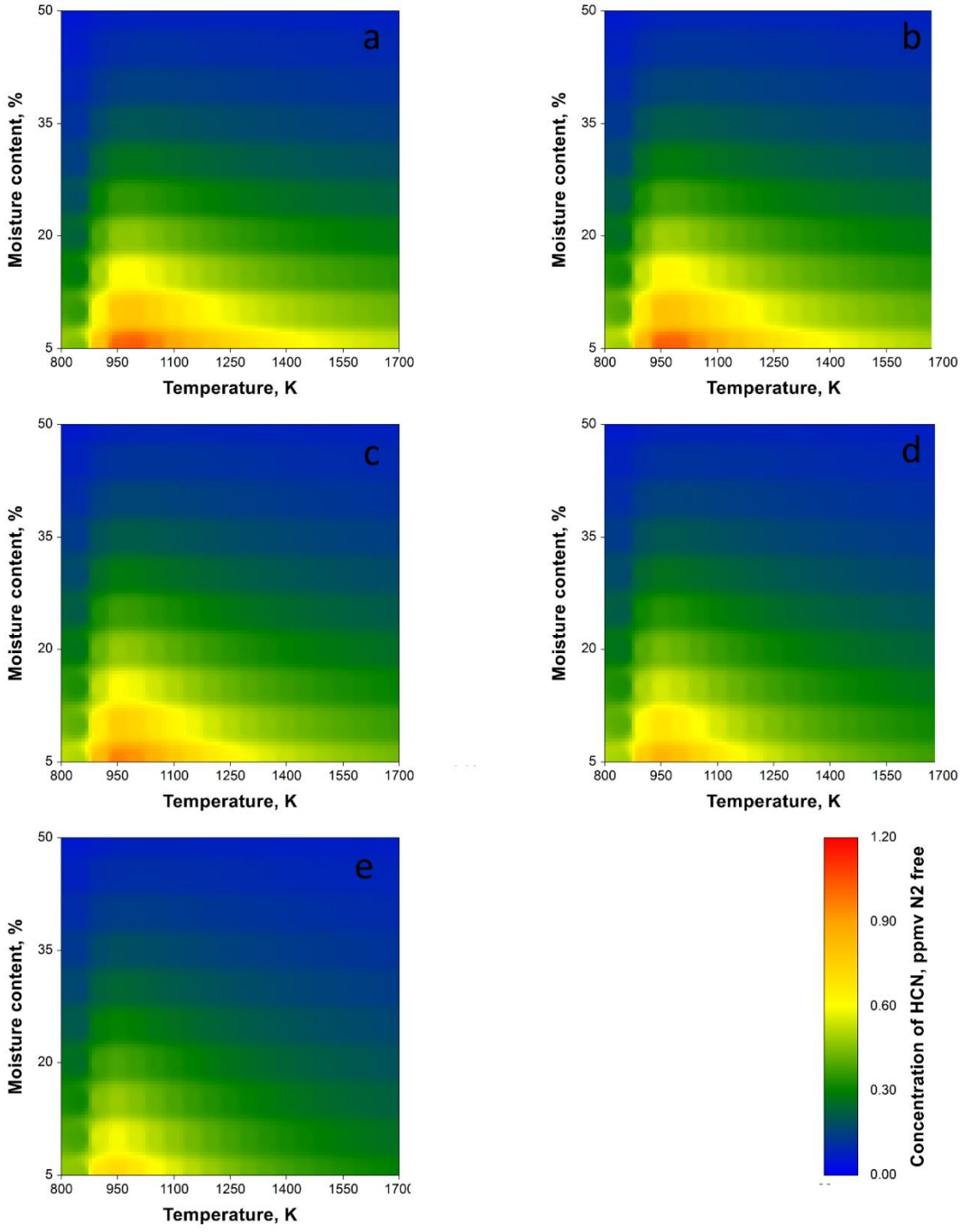

Figure 4.10. Effects of temperature, moisture content, and equivalence ratio on HCN concentration. a) ER = 0.20, b) ER = 0.25, c) ER = 0.30, d) ER = 0.35, and e) ER = 0.40. Values are reported on a % vol/vol dry, N_2-free basis.

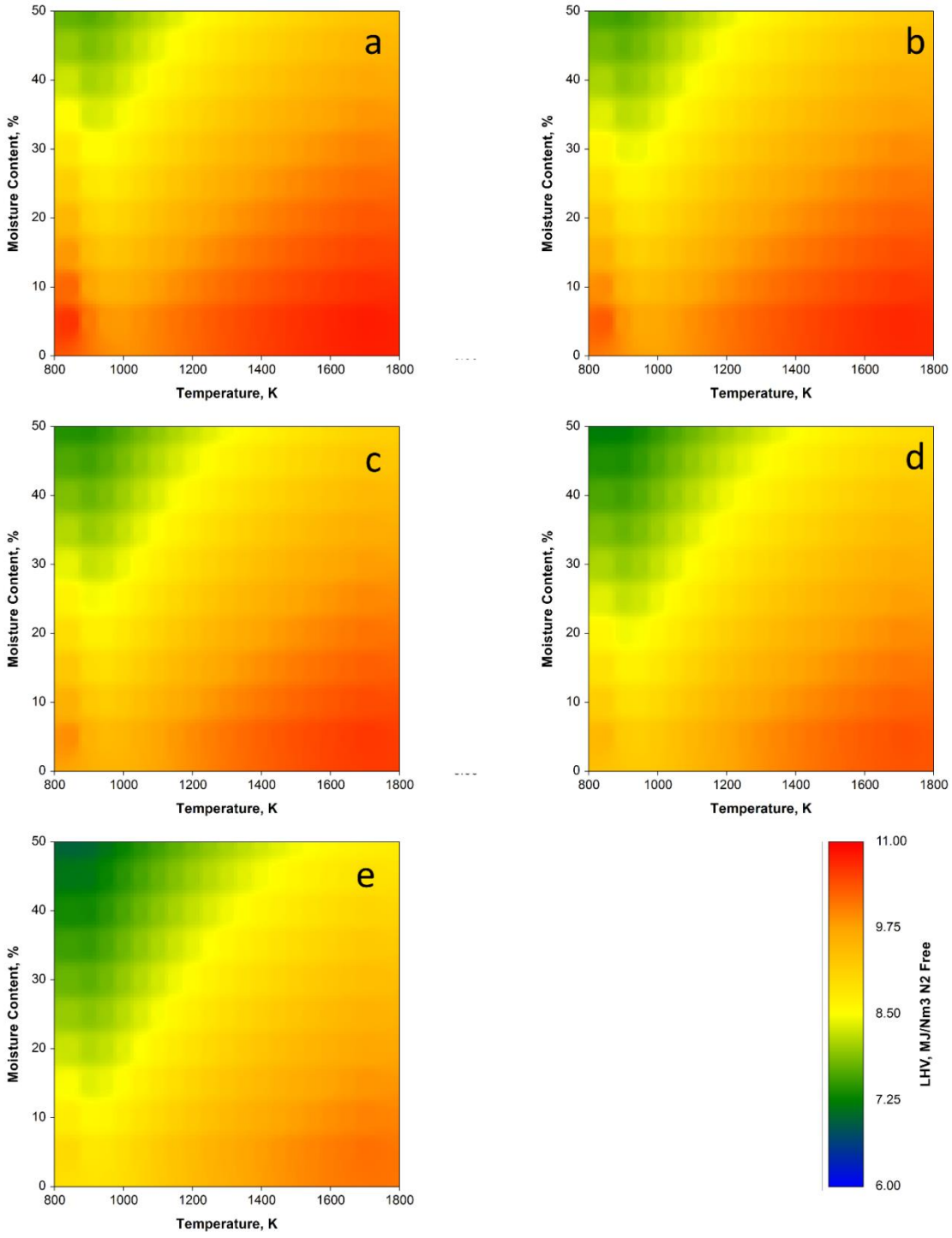

Figure 4.11. Effects of temperature, moisture content, and equivalence ratio on LHV of producer gas. a) ER = 0.20, b) ER = 0.25, c) ER = 0.30, d) ER = 0.35, and e) ER = 0.40. Values are reported on a N_2-free basis.

Conclusions

This paper presents information that is valuable in guiding the selection of gasification operating conditions and gasifier design using a comprehensive parametric study with a non-stoichiometric equilibrium model. Comparison of model prediction against experimental data shows that non-equilibrium effect is important in real systems especially for CH_4 and inorganic contaminants (NH_3, HCN, H_2S, COS). However, the predicted trends from equilibrium model of major producer gas constituents (CO, H_2, and CO_2) are comparable to those reported from experimental studies. The beta coefficient, describing the relationship between gasification operating variables and gas composition, was obtained from a multiple linear regression analysis and presented in this paper. The beta coefficient also provides a quantitative evaluation of relative importance of gasification operating variables to gas composition. The trends obtained suggest that reverse water-gas shift reaction is an important gasification reaction, especially from a CO and H_2 standpoint. Similarly, it was concluded that reaction $H_2S + CO_2 \leftrightarrow COS + H_2O$ and reaction $HCN + H_2O \leftrightarrow NH_3 + CO$ play a significant role in sulfur and nitrogen product distribution, respectively. Furthermore, decreasing ER was seen to increase the concentration of CO and H_2, as well as NH_3, HCN, H_2S, and COS. This is disadvantageous because the maximization of CO and H_2 via the reduction of air to fuel ratio with produce simultaneous increase in the yield of sulfur- and nitrogen-containing contaminants.

Nomenclature

a, b, c, d	Molar concentration of elemental hydrogen, oxygen, nitrogen, and sulfur, respectively on a unit elemental carbon basis (-)
e, f, g	Stoichiometric coefficient of water, oxygen, and nitrogen molecules, respectively, in the overall reaction
ER	Equivalence ratio (-)
$e_{i,j}$	Number of moles of jth element per mole of ith gas phase species (-)
G	Total Gibbs energy (J)
$\bar{g}_i^o$	Gibb's energy of ith gas phase species (J/mol)
$\bar{h}_i^o$	Specific enthalpy of ith gas phase species (J/mol)
i	1 = H_2, 2 = H_2O, 3 = CO, 4 = CO_2, 5 = CH_4, 6 = N_2, 7 = O2, 8 = NH_3, 9 = HCN, 10 = H_2S, and 11 = COS
LHV	Lower heating value of producer gas (J/Nm^3)
LHV_i	Lower heating value of ith gas phase species (J/Nm^3)
$M_{biomass}$	Molecular mass of biomass (kg/mol)
M_{water}	Molecular mass of water (kg/mol)
N_c	Number of gas phase species in overall reaction
N_e	Number of chemical elements in overall reaction
P	Pressure (Pa)
P^o	Reference pressure (Pa)
R	Universal gas constant (J/mol K)

$\bar{s}_i^o$	Specific entropy of ith gas phase species (J/mol K)
T	Temperature (K)
W_j	Number of moles of jth element initially in the reaction (-)
$x_1, x_2, \ldots x_{11}$	Stoichiometric coefficient of ith gas phase species (-)
x_t	Total moles of gas phase species ($\sum_{i=1}^{N_c} x_i$)
α	Carbon conversion fraction (-)
φ	Moisture content of feedstock (% wet basis)
λ_j	Underdetermined multiplier for jth chemical element (-)
μ_i	Chemical potential of ith gas phase species (J/mol)
μ_i^o	Chemical potential of ith gas phase species at reference T and P (J/mol)

Declarations

The authors declare no competing financial interest

Acknowledgments

This research was supported by Southeastern Sun Grant Center and the U.S. Department of Transportation, Research and Innovative Technology Administration, Grant No. DTO559-07-G-00050.

References

1. EIA *July 2017 - Monthly energy review*; U.S. Energy Information Administration: Washington, DC, 2017; p 3.
2. Larcher, D.; Tarascon, J.-M., Towards greener and more sustainable batteries for electrical energy storage. *Nature chemistry* **2015,** *7* (1), 19-29.
3. Oyedeji, O.; Fasina, O., Impact of drying-grinding sequence on loblolly pine chips preprocessing effectiveness. *Industrial Crops and Products* **2017,** *96* (1), 8-15.
4. Basu, P., *Biomass Gasification and Pyrolysis*. 1st ed.; Elsevier: Oxford, England, 2010.
5. Adhikari, S.; Abdoulmoumine, N.; Nam, H.; Oyedeji, O., 16 - Biomass gasification producer gas cleanup. In *Bioenergy Systems for the Future*, Woodhead Publishing: 2017; pp 541-557.
6. Abdoulmoumine, N.; Adhikari, S.; Kulkarni, A.; Chattanathan, S., A review on biomass gasification syngas cleanup. *Appl Energ* **2015,** *155* (1), 294-307.
7. Tan E. C. D.; Talmadge M.; Dutta A.; Hensley J.; Schaidle J.; Biddy M.; Humbird D.; Snowden-Swan L. J.; Ross J.; Sexton D.; Yap R.; J., L. *Process Design and Economics for the Conversion of Lignocellulosic Biomass to Hydrocarbons via Indirect Liquefaction*; 2015.
8. Liu, H.; Cattolica, R. J.; Seiser, R., CFD studies on biomass gasification in a pilot-scale dual fluidized-bed system. *International Journal of Hydrogen Energy* **2016,** *41* (28), 11974-11989.
9. Kulkarni, A.; Baker, R.; Abdoulmoumine, N.; Adhikari, S.; Bhavnani, S., Experimental study of torrefied pine as a gasification fuel using a bubbling fluidized bed gasifier. *Renewable Energy* **2016,** *93*, 460-468.
10. Hamad, M. A.; Radwan, A. M.; Heggo, D. A.; Moustafa, T., Hydrogen rich gas production from catalytic gasification of biomass. *Renewable Energy* **2016,** *85*, 1290-1300.
11. He, M.; Xiao, B.; Hu, Z.; Liu, S.; Guo, X.; Luo, S., Syngas production from catalytic gasification of waste polyethylene: influence of temperature on gas yield and composition. *International Journal of Hydrogen Energy* **2009,** *34* (3), 1342-1348.
12. Kirsanovs, V.; Zandeckis, A.; Blumberga, D.; Veidenbergs, I. In *The influence of process temperature, equivalence ratio and fuel moisture content on gasification process: A review*, Proceedings of 27th International Conference on Efficiency, Cost, Optimization, Simulation and Environmental Impact of Energy Systems, 2014; pp 15-19.
13. McKendry, P., Energy production from biomass (part 3): Gasification technologies. *Bioresource Technology* **2002,** *83* (1), 55-63.
14. Klein, S.; Nellis, G., *Thermodynamics*. 1st ed.; Cambridge University Press: New York, USA, 2012.
15. Aydin, E. S.; Yucel, O.; Sadikoglu, H., Development of a semi-empirical equilibrium model for downdraft gasification systems. *Energy* **2017,** *130*, 86-98.

16. Gautam, G.; Adhikari, S.; Bhavnani, S., Estimation of biomass synthesis gas composition using equilibrium modeling. *Energy Fuels* **2010,** *24* (4), 2692-2698.
17. Mendiburu, A. Z.; Carvalho, J. A.; Zanzi, R.; Coronado, C. R.; Silveira, J. L., Thermochemical equilibrium modeling of a biomass downdraft gasifier: Constrained and unconstrained non-stoichiometric models. *Energy* **2014,** *71*, 624-637.
18. Gambarotta, A.; Morini, M.; Zubani, A., A non-stoichiometric equilibrium model for the simulation of the biomass gasification process. *Appl Energ* **2017**.
19. Zainal, Z. A.; Ali, R.; Lean, C. H.; Seetharamu, K. N., Prediction of performance of a downdraft gasifier using equilibrium modeling for different biomass materials. *Energy Conversion and Management* **2001,** *42* (12), 1499-1515.
20. Li, X.; Grace, J.; Lim, C.; Watkinson, A.; Chen, H.; Kim, J., Biomass gasification in a circulating fluidized bed. *Biomass and bioenergy* **2004,** *26* (2), 171-193.
21. Klein, S. A., *Engineering Equation Solver (EES) for the Microsoft Windows Operating Systems*. F-Chart software: Wisconsin, USA, 2011.
22. Abdoulmoumine, N.; Kulkarni, A.; Adhikari, S., Effects of Temperature and Equivalence Ratio on Pine Syngas Primary Gases and Contaminants in a Bench-Scale Fluidized Bed Gasifier. *Ind. Eng. Chem. Res.* **2014,** *53* (14), 5767-5777.
23. Aljbour, S. H.; Kawamoto, K., Bench-scale gasification of cedar wood – Part II: Effect of Operational conditions on contaminant release. *Chemosphere* **2013,** *90* (4), 1501-1507.
24. Aljbour, S. H.; Kawamoto, K., Bench-scale gasification of cedar wood – Part I: Effect of operational conditions on product gas characteristics. *Chemosphere* **2013,** *90* (4), 1495-1500.
25. Fasina, O. O., Flow and physical properties of switchgrass, peanut hull, and poultry litter. *Transactions of the ASABE* **2006,** *49* (3), 721.
26. Silva, V. B.; Rouboa, A., Using a two-stage equilibrium model to simulate oxygen air enriched gasification of pine biomass residues. *Fuel Processing Technology* **2013,** *109*, 111-117.
27. Bates, R. B.; Ghoniem, A. F.; Jablonski, W. S.; Carpenter, D. L.; Altantzis, C.; Garg, A.; Barton, J. L.; Chen, R.; Field, R. P., Steam-air blown bubbling fluidized bed biomass gasification (BFBBG): Multi-scale models and experimental validation. *AIChE Journal* **2017,** *63* (5), 1543-1565.
28. Pepiot, P.; Dibble, C. J.; Foust, T. D., Computational fluid dynamics modeling of biomass gasification and pyrolysis. In *Computational Modeling in Lignocellulosic Biofuel Production*, 1st ed.; American Chemical Society: 2010; Vol. 1052, pp 273-298.
29. Elder, R.; Allen, R., Nuclear heat for hydrogen production: Coupling a very high/high temperature reactor to a hydrogen production plant. *Progress in Nuclear Energy* **2009,** *51* (3), 500-525.
30. Ni, M.; Leung, D. Y. C.; Leung, M. K. H.; Sumathy, K., An overview of hydrogen production from biomass. *Fuel Processing Technology* **2006,** *87* (5), 461-472.

31. Xiao, G.; Ni, M.-J.; Chi, Y.; Cen, K.-F., Low-temperature gasification of waste tire in a fluidized bed. *Energy Conversion and Management* **2008,** *49* (8), 2078-2082.
32. Broer, K. M.; Woolcock, P. J.; Johnston, P. A.; Brown, R. C., Steam/oxygen gasification system for the production of clean syngas from switchgrass. *Fuel* **2015,** *140*, 282-292.
33. Woolcock, P. J.; Brown, R. C., A review of cleaning technologies for biomass-derived syngas. *Biomass and Bioenergy* **2013,** *52* (1), 54-84.
34. Torres, W.; Pansare, S. S.; Goodwin, J. G., Hot Gas Removal of Tars, Ammonia, and Hydrogen Sulfide from Biomass Gasification Gas. *Catalysis Reviews* **2007,** *49* (4), 407-456.
35. Zhao, X.; Liu, W.; Deng, Y.; Zhu, J. Y., Indirect Biomass Fuel Cells at High Temperature. In *Lignocellulosic Biomass-Energized Fuel Cells: Cases of High-Temperature* Dunn-Rankin, D., Ed. Momentum Press: New York, 2015.
36. Zhao, H.; Draelants, D. J.; Baron, G. V., Performance of a nickel-activated candle filter for naphthalene cracking in synthetic biomass gasification gas. *Ind. Eng. Chem. Res.* **2000,** *39* (9), 3195-3201.
37. Zhou, J.; Masutani, S. M.; Ishimura, D. M.; Turn, S. Q.; Kinoshita, C. M., Release of fuel-bound nitrogen during biomass gasification. *Industrial and Engineering Chemistry Research* **2000,** *39* (3), 626-634.
38. Atnaw, S. M.; Sulaiman, S. A.; Yusup, S., Influence of fuel moisture content and reactor temperature on the calorific value of syngas resulted from gasification of oil palm fronds. *The Scientific World Journal* **2014,** *2014*.
39. Niu, M.; Huang, Y.; Jin, B.; Wang, X., Oxygen Gasification of Municipal Solid Waste in a Fixed-bed Gasifier. *Chinese Journal of Chemical Engineering* **2014,** *22* (9), 1021-1026.

CHAPTER V
CFD-DEM SIMULATION AND VALIDATION OF THE HYDRODYNAMICS BEHAVIOR OF AN INERT FLUIDIZED BED SYSTEM

This chapter is a draft version of the following article:

Oyedeji, O. A., Daw, C. S., Labbé, N., Ayers, P, D., and Abdoulmoumine, N. H. (draft). CFD-DEM simulation and validation of the hydrodynamics behavior of an inert fluidized bed system. Powder Technology.

Abstract

Fluidized bed reactors are commonly used in bioenergy processing because they create conditions favorable for excellent biomass conversion and large-scale operations. However, it is remarkably expensive and difficult to experimentally obtain internal flow information needed to optimize fluidization behavior at bioenergy processing conditions. In this study, we developed a simulation model based on Eulerian-Lagrangian approach in Open-source Field Operation and Manipulation (OpenFOAM), a computational fluid dynamics (CFD) and Discrete Element Method (DEM) software code, in which the gas phase flow was resolved by solving Navier-Stokes transport equations and the solid phase flow was calculated by applying Newton's second law of motion. The solid phase flow was linked to the gas phase flow through Gidaspow drag law. The CFD-DEM simulation was carried out for sand at different fluidization velocities (0.0 – 0.4 m/s) and particle mass (0.1 and 0.2 kg). Two hydrodynamic quantities (pressure drop and bed height) were the focus of this work because of their importance to fluidization performance. The experimental validation of the developed CFD-DEM simulation was performed using a simple experimental setup to obtain corresponding pressure drop and bed height for the fluidization conditions used in the CFD-DEM simulation. It was shown that the developed CFD-DEM model can reasonably reproduce the flow behavior inside the fluidized bed system. The developed model can therefore be used to represent the hydrodynamics of a fluidized bed and may be coupled with thermal and chemical reaction models to produce a comprehensive and realistic simulation of bioenergy processing in a fluidized bed.

Keywords: pressure drop, bed height, validation, OpenFOAM, minimum fluidization velocity

Introduction

Fluidized bed systems are widely used in various industrial applications including pharmaceutical, petrochemical, energy, and food processing because they are easy to design, scalable and have excellent mixing capability and solid mobility.[1] In the context of bioenergy processing, fluidized bed systems are also attractive because they are characterized by rapid biomass heating and produce isothermal conditions when used with carefully selected bed material.[2]

The optimum utilization and operation of fluidized bed systems for bioenergy processing require thorough understanding of the complex interaction of the hydrodynamics state with the thermal, and chemical behaviors of the system.

Information available via conventional experimental measurement is limited because the harsh operating conditions, e.g. high temperature, maintained during bioenergy processing makes it prohibitively expensive and difficult to measure the flow, thermal, and chemical properties inside the reactor.[3] There has therefore been an increasing interest in numerically modeling the hydrodynamics of fluidized bed systems with the goal of extracting useful flow, thermal, and chemical information inside the reactor.[4-6]

Computational fluid dynamics (CFD) modeling is perhaps the most important tool used in the modeling of fluidized bed systems. CFD modelers commonly use two broad approaches when analyzing fluidized bed systems. On the bulk-scale, solid particles in fluidized beds behave like fluids. Many CFD modelers therefore describe fluidized beds systems using inter-penetrating continua. This modeling approach is commonly known as Eulerian-Eulerian or two-fluid model. The interaction between the solid and gas continuum is described using drag force correlations that are coupled to localized properties of both continua. The major drawback to the Eulerian-Eulerian approach is that it does not provide detailed particle-scale behaviors like its more computationally expensive alternative—Eulerian-Lagrangian (CFD-DEM) approach. The Eulerian-Lagrangian approach to CFD model describes the solid phase in fluidized bed systems with discrete elements, which are subjected to the Newton laws of motion and solid particle contact models.[7-8] Hence, it is possible to track particle-scale properties and establish a sophisticated understanding the hydrodynamics of the gas-solid hydrodynamics of fluidized bed systems.

Several studies have investigated the simulation of the hydrodynamics of fluidized bed systems. However, some of the proposed simulations in these studies are based on the Eulerian-Eulerian approach,[9-11] which is lacking in accuracy and particle-scale information.[8] Although few studies have proposed fluidized bed simulations based on the CFD-DEM approach, the simulation setups are usually significantly different from the experimental configurations commonly reported for bioenergy application.[12-14] The mean particle size of bed materials and biomass is typically less than 1 mm in bioenergy applications[15-17] whereas most CFD-DEM simulation of the hydrodynamics of fluidized bed systems use bed materials with particle size of 4 mm.[12-14] Additionally, the fluidizing gas is injected into the fluidized bed via a slot at the base of the bed[12-14] whereas the fluidized gas is uniformly distributed across the radius of the bed in real systems.[15-17] These deviations in the simulation setup can be traced back to the pioneering study on the CFD-DEM modeling of fluidized bed systems by Tsuji, et al. [7]. It is important to develop and evaluate the prediction performance of a CFD-DEM model of the hydrodynamics of a fluidized bed for bioenergy processing.

This study was therefore undertaken to develop and validate a CFD-DEM simulation of a non-reacting fluidized bed system. Specifically, CFD-DEM simulations of sand

fluidization were implemented using Eulerian-Lagrangian approach within an open source code (OpenFOAM). The results were analyzed to obtain information on the effect of fluidizing gas velocity on two important hydrodynamics properties (pressure drop across reactor length and bed height).[18] Simultaneously, a simple experimental setup was designed to extract useful information that can be compared to the CFD-DEM simulation results to establish the accuracy of the CFD-DEM simulation.

Materials and method

Experimental setup and data collection

Figure 5.1 shows the components used in this study and how they were set up. A clear unthreaded PVC pipe with a diameter of 1.5 in (38.10 mm) was used to model a fluidized bed reactor. The pipe was fitted with an air distributor (Applied porous technologies, Tariffville, Connecticut) to uniformly supply the fluidizing agent along the cross-sectional area of the pipe. The air distributor has a uniformly distributed perforation of 20×10^{-4} m.

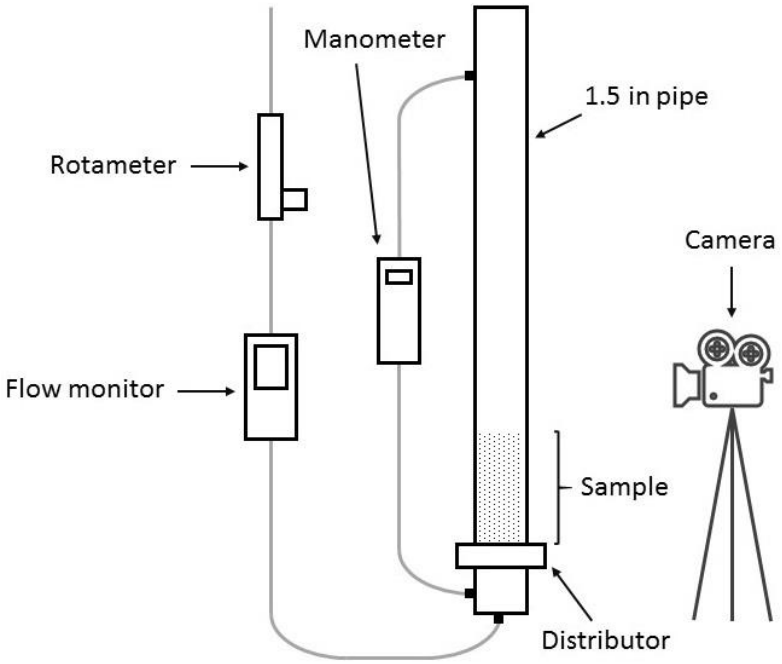

Figure 5.1. Experimental setup schematic.

The fluidizing agent was air supplied from the laboratory building compressed air system. The air flow was regulated using a rotameter (model 1250A, Brooks Instrument, Hatfield, Pennsylvania) and flow rate was validated using a totalizer input/output flow monitor (model TIO-LAA5, Aalborg, Orangeburg, New York) mounted on a mass flow rate controller (model GFC 37, Aalborg, Orangeburg, New York). The pressure drop across the reactor height was measured with a differential pressure manometer (model AR1895, Perfect prime, Rockaway, New York). The higher positive pressure port of the manometer was connected to a buckhead fitting positioned 127 mm below the distributor, whereas the lower positive pressure port of the manometer was connected to a buckhead fitting positioned 750 mm above the distributor.

The pressure drops across the empty bed (without sand) was first measured as a function of velocity (0.0 – 0.5 m/s) to obtain the baseline for the pressure drop across the distributor. Thereafter, a known mass (100 g or 200 g) of sand () was placed in the reactor and supported by the distributor. The pressure drop across the bed was measured as the flow velocity was increased from 0.0 to ~0.5 m/s (fluidization), then reduced to 0.0 m/s (defluidization). The actual pressure drop was calculated as the difference between the measured pressure drop and the baseline pressure drop. Each experimental run was recorded for about 3 seconds using a camera (Model Rebel T4i, Canon, Melville, New York) fitted with an 18 – 135 mm lens. All measurement was carried out in triplicate.

About 330 frames were extracted from each video recording, totaling 1000 frames for each sample mass. The frames were analyzed in R programming language. The image was cropped, converted to greyscale, and enhanced for contrast, as shown in Figure 5.2. The percentage of the black area along the height of the reactor was then plotted against the reactor height. A sharp reduction was observed in the value of the percentage of black area at the transition from the sample bed to the complete gas phase region. The value of bed height for each frame was recorded.

Bed height distribution charts as affected by the mass of sand and flow velocity were constructed. The effective bed height was calculated as the second quartile (median) for the bed height distribution.

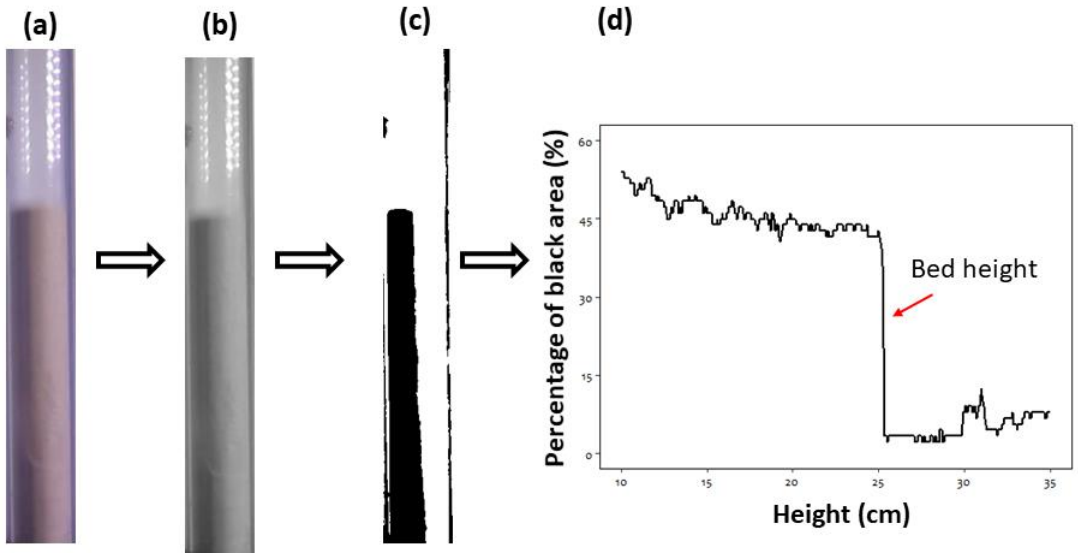

Figure 5.2. Image analysis in R programming (a) original and input bed image in full color, (b) bed image in greyscale, (c) bed image converted to white and black, and (d) graphical representation of color gradient in the bed image to identify bed height.

Mathematical models

This study used CFD-DEM model to simulate the multi-phase flow behavior in an inert fluidized bed system. The gas phase was modeled as a continuum using Eulerian framework and coupled with the solid phase, which was modeled as discrete elements using Lagrangian framework. The system was assumed to be inert, hence changes in the properties of the gas and solid phases were not considered. The mathematical representation for the gas and solid movement are described in subsequent sections.

Particle mass and momentum models

The equation governing the conservation of mass of particles is given as $\frac{dM_p}{dt}=0$ because of the inert nature of the solid particles in the fluidized bed. Particle motion during fluidization were classified as translational and rotational motions.[19] The translational and rotational accelerations were calculated as shown in Equations (5.1) and (5.2) respectively. The translational particle motion was assumed to be produced by the particle contact with fluid ($\mathbf{F}_g$), other particles and walls ($\mathbf{F}_p$), and gravity ($M_p\mathbf{g}$). The net torque ($\mathbf{T}$) on the particles produces the rotational particle motion as shown in Equation (5.3). Gidaspow drag model was used to calculate the coefficient of interphase momentum exchange (β), which is proportional to the fluid contact force on particles.[20] The Gidaspow drag model is a combination of Ergun equation[21] and Wen and Yu drag model[22]. Ergun equation describes the interphase momentum exchange behavior for dense bed ($\varepsilon_g < 0.8$) whereas Wen and Yu drag model describes the interphase momentum exchange behavior for dilute bed ($\varepsilon_g \geq 0.8$) (Equation (5.4)).

$$\frac{d\mathbf{U}_p}{dt} = \frac{\mathbf{F}_g}{M_p} + \frac{\mathbf{F_p}}{M_p} + \mathbf{g} \tag{5.1}$$

$$\frac{d\omega}{dt} = \frac{\mathbf{T}}{I} \tag{5.2}$$

$$F_g = \frac{\beta V_p}{\varepsilon_p}\left(\mathbf{U}_g - \mathbf{U}_p\right) \tag{5.3}$$

$$\beta = \begin{cases} 150\frac{\varepsilon_p^2\mu_g}{\varepsilon_g^2 d_g^2} + 1.75\frac{\varepsilon_p\rho_g}{\varepsilon_g d_p}\left|\mathbf{U}_g - \mathbf{U}_p\right| & \varepsilon_g < 0.8 \\ 0.75C_d\frac{\varepsilon_p\rho_g}{d_p}\left|\mathbf{U}_g - \mathbf{U}_p\right|\varepsilon_g^{-2.65} & \varepsilon_g \geq 0.8 \end{cases} \tag{5.4}$$

$$C_d = \begin{cases} \frac{24}{Re_p}\left(1 + 0.15Re_p^{0.687}\right) & < 1000 \\ 0.44 & Re_p \geq 1000 \end{cases} \quad (5.5)$$

$$Re_p = \frac{\varepsilon_g \rho_g d_p \left|\mathbf{U}_g - \mathbf{U}_p\right|}{\mu_g} \quad (5.6)$$

Particle contact forces (inter-particle and particle-wall collisions) were calculated using soft-sphere discrete element model. This is because soft-sphere discrete element model has been demonstrated to account for the frequently occurring inter-particle and particle-wall collisions in fluidized bed systems.[19] The momentum exchange during collisions was modeled using a combination of spring, slider, and dashpot models as illustrated in Figure 5.3.

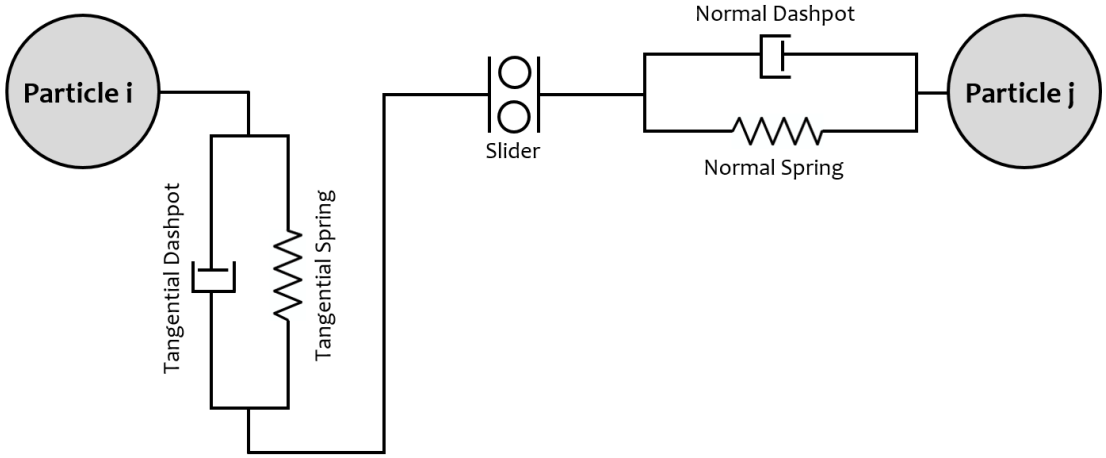

Figure 5.3. Hertz-Mindlin particle contact model (spring-slider-damper collision model).

The particle contact forces were partitioned into normal force ($F_{p,n}$) and tangential force ($F_{p,t}$) components (Figure 5.3). Equations (5.7) and (5.9) describe the mathematical models used to represent the normal and tangential particle collision forces in this study.

$$\mathbf{F}_{p,n} = -k\mathbf{d}_n - \eta\mathbf{U}_n \tag{5.7}$$

$$\mathbf{U}_n = (\mathbf{U}_r \cdot \mathbf{n})\mathbf{n} \tag{5.8}$$

$$\mathbf{F}_{p,t} = -k\mathbf{d}_t - \eta\mathbf{U}_t \tag{5.9}$$

$$\mathbf{U}_t = \mathbf{U}_r - \mathbf{U}_n \tag{5.10}$$

When $|\mathbf{F}_{p,t}| \geq \mu_f|\mathbf{F}_{p,n}|$ (particle sliding), the tangential particle collision force was be calculated as:

$$\mathbf{F}_{p,t} = -\mu_f|\mathbf{F}_{p,n}|\mathbf{t} \tag{5.11}$$

The particle contact model parameters for particle-particle and particle-wall collisions used in this study are as listed Table 5.1.

Table 5.1. Inter-particle and particle-wall collision parameters used in this work.[23]

Inter-particle collision parameters	Value
Effective Young's modulus (Pa)	1.00×10^{8}
Poisson's ratio	2.30×10^{-1}
Coefficient of restitution	9.00×10^{-1}
Coefficient of friction	3.00×10^{-1}
String stiffness (N/m)	8.00×10^{2}

Gas phase transport equations

The equations of conservation of mass, momentum, and energy are shown in Equations (5.12) – (5.15)). The exchanges between the gas and solid phases were accounted for using source terms in each transport equation. Since the solid particles used in this simulation is inert, the source term for the mass continuity equation was set to zero. Additionally, the voidage term (ε_g) was considered in the continuity equations to realistically capture the gas-solid behavior, especially in the dense regime.

$$\frac{\delta}{\delta t}\left(\varepsilon_g \rho_g\right) + \nabla \cdot \left(\varepsilon_g \rho_g \mathbf{U}_g\right) = 0 \tag{5.12}$$

$$\frac{\delta}{\delta t}\left(\varepsilon_g \rho_g \mathbf{U}_g\right) + \nabla \cdot \left(\varepsilon_g \rho_g \mathbf{U}_g \mathbf{U}_g\right) = -\nabla p + \nabla \cdot \left(\varepsilon_g \boldsymbol{\tau}\right) + \varepsilon_g \rho_g \mathbf{g} + S_m \tag{5.13}$$

$$E = h_s - \frac{p}{\rho_g} + \frac{\mathbf{U}_g^2}{2} \tag{5.14}$$

$$\frac{\delta}{\delta t}\left(\varepsilon_g \rho_g E\right) + \nabla \cdot \left(\varepsilon_g \mathbf{U}_g (\rho_g E + p)\right) = \nabla \cdot \left(\varepsilon_g \alpha_{eff} \nabla h_s\right) \tag{5.15}$$

The stress tensor ($\boldsymbol{\tau}$) was calculated as the sum of viscous and turbulent stresses. Equally, viscous and turbulent effects were accounted for in the computation of the effective dynamic thermal diffusivity (α_{eff}). Gas phase density and viscosity were determined based on the pressure and temperature values using assumed gas equation of state.

Numerical simulation setup

The governing equations for conservation of mass, momentum, and energy were resolved in OpenFOAM code (version 2.4.0), which uses finite volume discretization method. The gas flow was assumed to be compressible and k-ε turbulence model was used to describe the turbulent behavior of the gas flow. A standard pressure based PISO (pressure implicit splitting of operators) solver for variable density flow was employed to solve the fluid transport equations. The fluid density was calculated using the ideal gas equation state (p = ρRT).

Table 5.2 lists value(s) for important simulation parameters and gasification process variables. The simulated fluidized bed reactor is 38.1 mm in diameter and 749.30 mm in height. To reduce computational time and size. a quasi-three-dimensional geometry model, with its thickness equal to the initial diameter of the biomass

particle, was used (Figure 5.4). The boundary conditions were chosen to match the experimental conditions. The outlet is assumed to be fixed at atmospheric pressure and the gas inlet and reactor wall temperature were fixed at room temperature.

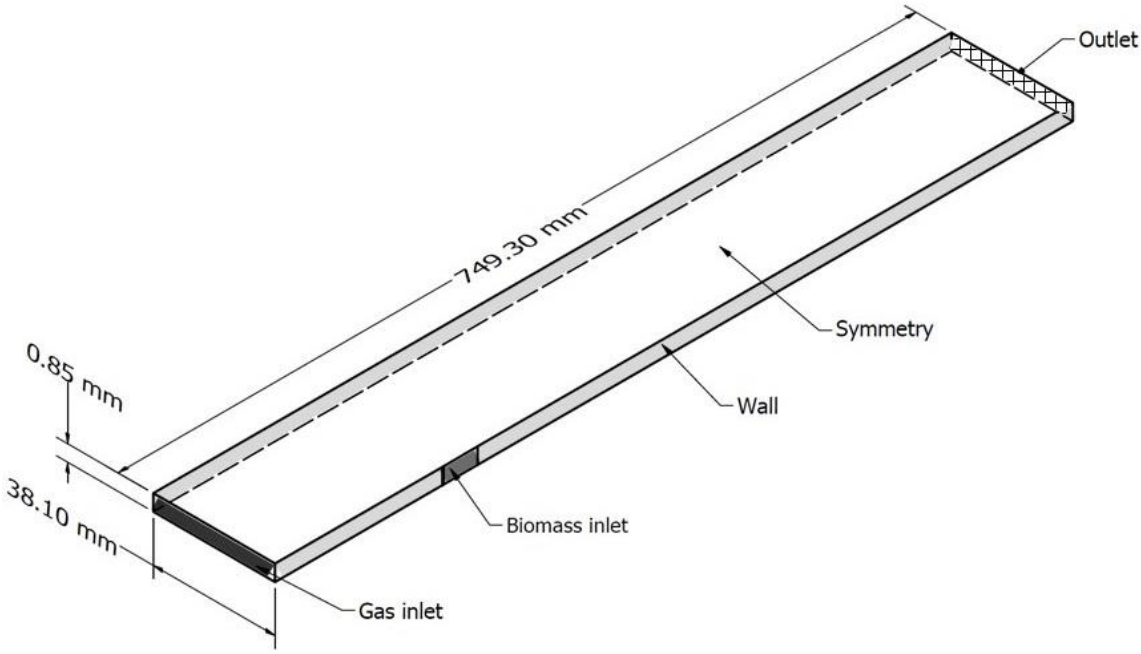

Figure 5.4. Quasi-three-dimensional geometry model with boundary conditions.

Table 5.2. Simulation parameters and gasification process variables used.

Parameter	Value
Mesh size (m)	0.0038 × 0.0049 × 0.0005
Fluid time step (s)	1.0×10^{-5}
Simulation end time (s)	20
Reactor temperature (K)	298.15
Inlet gas flow rate (m^3/s)	0.0 – 0.4
Sand quantity (kg)	0.10 – 0.20
Sand specific heat (J/kg-K)	860
Sand density (kg/m^3)	2600
Sand shape (-)	sphere
Sand diameter (m)	3.33×10^{-4}
Sand emissivity (-)	1.0

Results and discussion

Static and initial bed preparation

The static bed configuration of the CFD-DEM simulation was generated by placing 44275 and 88550 spheres (for the 1-S and 2-S case, respectively) inside the simulation geometry. Each sphere represents a sand particle with the properties listed in Table 5.2 and initial velocity equals to zero. The center of each sphere was carefully selected such that the spheres do not overlap spatially. The inlet gas stream was turned off ($\mathrm{U_{inlet}} = 0.0\ \mathrm{m/s}$) to allow the particle fall under the influence of gravity and inter-particle collision forces. The simulation for each case was run for 10 seconds. The bed configuration was fairly constant between simulation time equals 0.7 and 10 s. This observation indicate that the simulation reached steady state at about 0.7 s and the result at any time after 0.7 s is a proper representation of the simulation prediction. Figure 5.5 shows the bed configuration at simulation time equals 10 s and reveals that the static bed height was about 6.51 and 13.05 cm for the 1-S and 2-S case, respectively. These bed heights correspond to a bulk density of 1345.03 and 1344.25 kg/m^3 (for the 1-S and 2-S case, respectively) and a porosity of 0.48 regardless of the case considered.

The bulk density data obtained from the static bed simulation was compared to experimental data. It was experimentally determined that the bulk density of the sand used in this work is 1381.04 ± 4.26 kg/m^3. The comparison of the experimental to the simulated bulk density indicates that the developed CFD-DEM simulation was able to accurately predict (<3% deviation) the physical bulk density of the material used in this study. The simulated static bed configuration obtained in this section was used as the initial bed configuration for the fluidized bed simulations in subsequent sections where $\mathrm{U_{inlet}} \neq 0.0\ \mathrm{m/s}$.

Minimum fluidization velocity and pressure drop

The minimum fluidization velocity is an important characteristic in the operation of a fluidized bed system, marking the transition from static bed to fluidized bed. The minimum fluidization velocity was identified as the intersection between the proportional region and the asymptotic region of the pressure drop against velocity curve (Figure 5.6).[24] It was experimentally determined that the sand particles used has a minimum fluidization velocity of about 0.07 m/s. This was consistent for the two samples mass studied. Although the magnitude of pressure drop across the sample bed was higher for the 2-S case runs compared to the 1-S case, minimum fluidization velocity was largely unchanged. The value of the minimum fluidization velocity observed was comparable to result (0.08 m/s) reported by Patil, et al. [25] for sand with a diameter of 3.75 × 10^{-4} m.

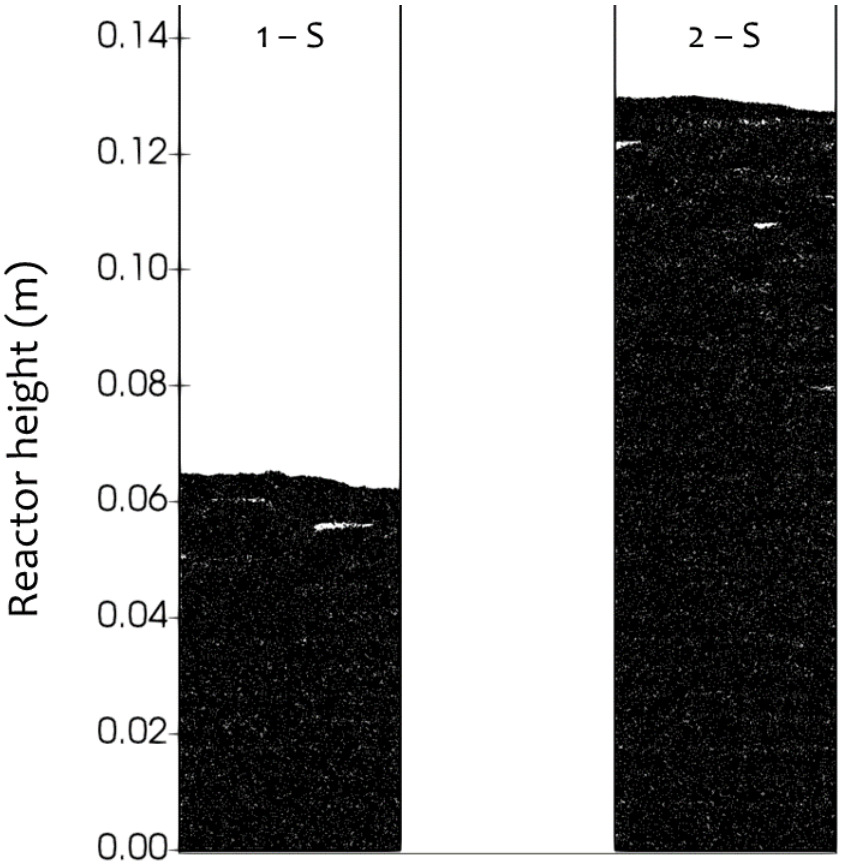

Figure 5.5. Initial bed configuration at simulation time = 10 s.

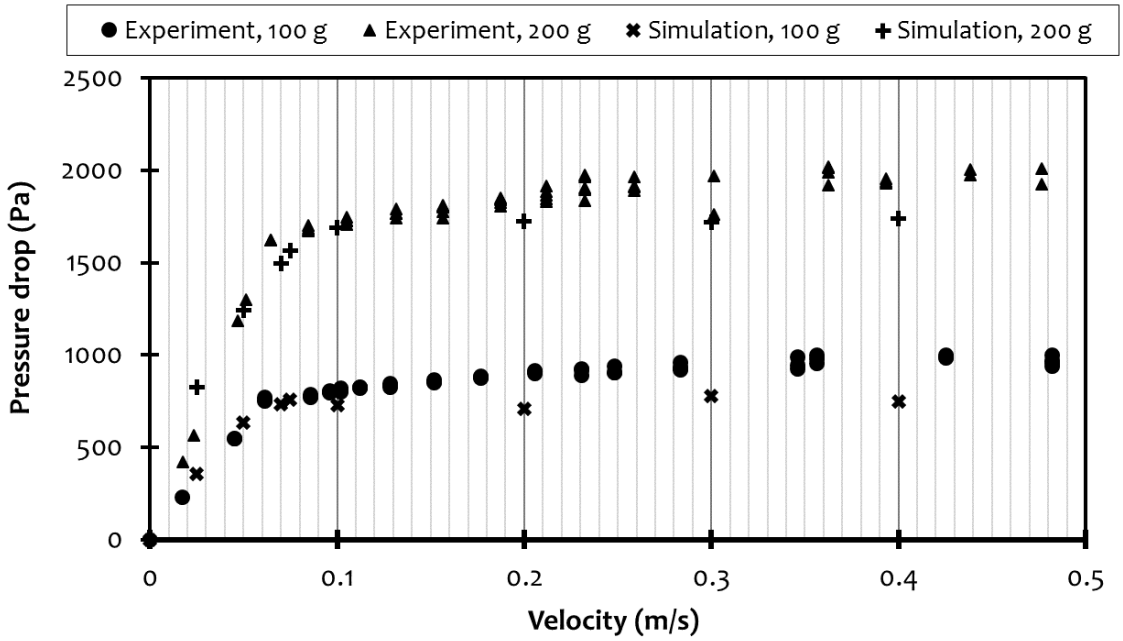

Figure 5.6. Pressure drop versus superficial velocity for sand fluidization.

Figure 5.6 shows the qualitative comparison the CFD-DEM simulation prediction to the experimental data. It reveals that the CFD-DEM simulation was able to reasonably predict the minimum fluidization velocity and pressure drop across the fluidized bed. The predicted minimum fluidization velocity was between 0.075 and 0.10 m/s because the increase in pressure drop with rising fluidization velocity continued pass the 0.075 m/s fluidization velocity but reached a plateau value at the 0.1 m/s fluidization velocity. Projecting the increasing pressure drop line against the plateau pressure drop line shows that the predicted minimum fluidization velocity in this study was about 0.085 m/s. The predicted pressure drops closely follow but were consistently lower than the measured pressure drops. The predicted plateau value of the pressure drop was 741.49 and 1717.68 Pa for the 1-S and 2-S case, respectively, whereas the measured plateau value of the pressure drop was 897.13 and 1893.77 Pa for the 1-S and 2-S case, respectively.

Bed height

The bed height of a fluidized bed system represents the interface between the dense and dilute regime. The dense regime holds significantly higher particle concentration than the dilute regime. As a result, the dense regime is characterized by high pressure drop per length as well as pyrolysis and heterogenous chemical reactions whereas the dilute regime is characterized by homogenous chemical reactions. Therefore, the bed height of a fluidized bed system is a critical and influential system feature and it is important to evaluate the ability of the developed CFD-DEM simulation to capture the bed height during fluidization.

First, the experimentally determined static bed height was compared to the expected static bed height and the CFD-DEM simulated static bed height. The expected static bed height was calculated as the quotient of the mass of sand divided by the product of its bulk density and cross-sectional area of the geometry. This comparison showed that the measured heights of the static bed were closely matched to both expected and CFD-DEM simulated static bed height (Table 5.3). For case 1-S, the static bed height of CFD-DEM simulation was slightly higher than that of the experimental setup. However, the converse relationship was observed for case 2-S, as the static bed height of CFD-DEM simulation was slightly lower than the static bed height from the experimental set up. The slight deviation of the simulation static bed height from the experimental static bed height was ascribed the monodisperse nature of the particles used in the CFD-DEM model. The excepted static bed heights were consistently slightly lower than the static bed height from the experimental and CFD-DEM simulation. However, all observation deviations were less than 3.5%, demonstrating the reliability and validity of the experimental procedure used.

Table 5.3. Comparison of the bed height values

Measurement procedure	Case 1-S (100g)	Case 2-S (200g)
Expected static bed height (cm)*	6.34	12.67
Experimental static bed height (cm)	6.40	13.11
Simulation static bed height (cm)	6.51	13.05

*The bulk density and diameter used for expected bed height calculation were 1381.04 kg/m^3 and 3.81 cm, respectively.

The frequency distribution of the static bed height as affected by the velocity of the fluidizing gas was constructed for the experimental setup and the CFD-DEM simulation. Figure 5.7 is the experimentally determined bed height frequency distribution for case 1-S at different fluidizing gas velocity. It represents the typical frequency distribution of bed height that was obtained in this work. The frequency distribution was uniform (standard deviation ≈ 0) for velocities below the minimum fluidization velocity. This means that there was no significant bed movement below the minimum fluidization velocity as commonly reported in earlier studies. However, the frequency distribution becomes wider and shorter as the fluidization velocity increases above the minimum fluidization velocity. The effective bed height was calculated as the median bed height and plotted against the fluidizing gas velocity (Figure 5.8) to better visualize the dependency of bed height on sample mass and fluidizing gas velocity. It can be seen in Figure 5.8 that the effective bed height distribution generally increased linearly with increasing superficial velocity. However, bed height was unchanged at velocities below the U_{mf}.

The snapshot of simulated particle flow for case 1-S is shown Figure 5.9. It illustrates the bed expansion behavior above the minimum fluidization velocity as well as the static bed below the minimum fluidization velocity. The CFD-DEM model was able to accurately capture the transition from static bed to moving bed as well as the dependence of bed height on fluidizing gas velocity for both cases 1-S and 2-S. The result from the CFD-DEM simulation showed that transition from static bed to moving bed occurred between 0.075 and 0.10 m/s, which is comparable to the experimental observation and consistent with the predicted minimum fluidization velocity. Qualitatively, the prediction of the CFD-DEM simulation in this study closely matches the measured response of bed height to fluidization velocity. The mean average error of the CFD-DEM model was about 1.2 cm. Figure 5.10 compares the bed height fluctuation for the experimental data to that of the simulation data. The experimental data consistently exhibited higher fluctuation frequency compared to the simulation prediction. This demonstrates that the bubbles formed in the CFD-DEM simulation do not coalesce at rate comparable to the experimental setting because the bubble growth rate is proportional to bubble size and bed fluctuation.[26]

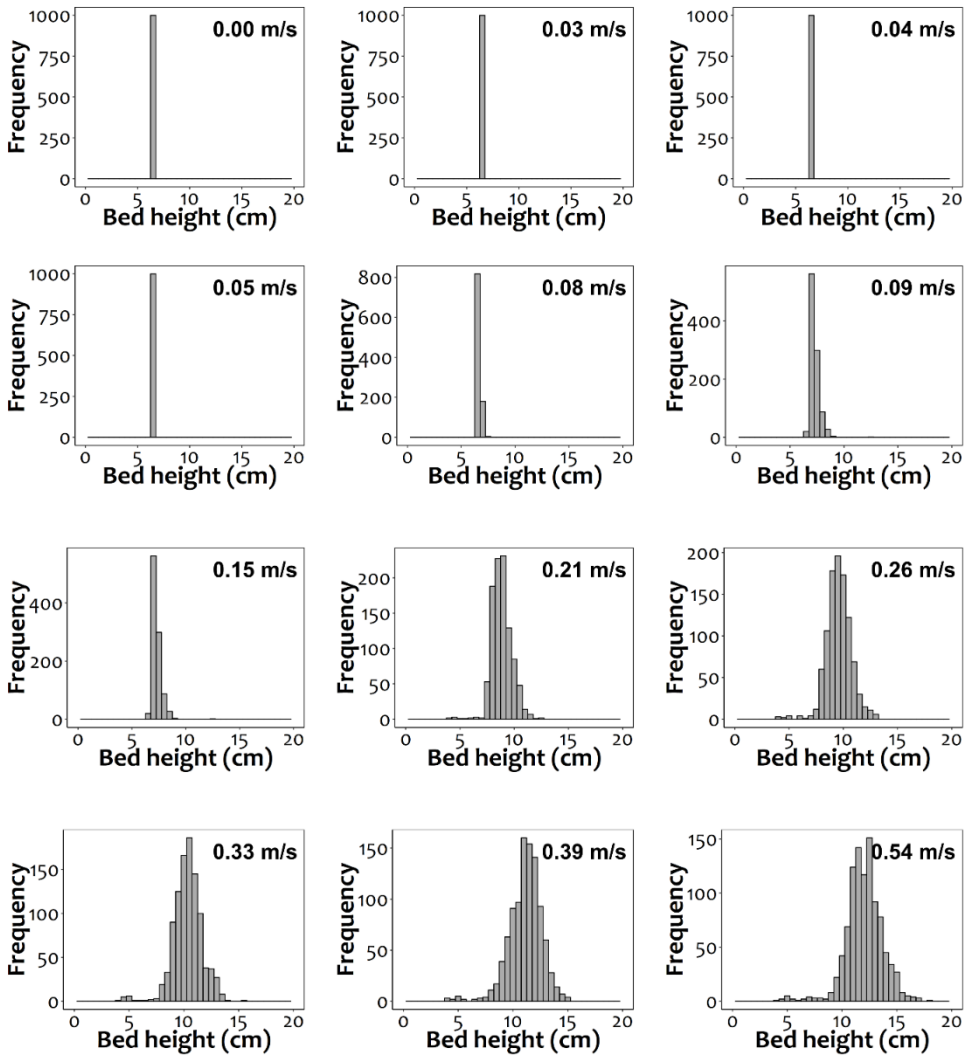

Figure 5.7. Effect of sample mass and superficial velocity on bed height distribution (case 1-S).

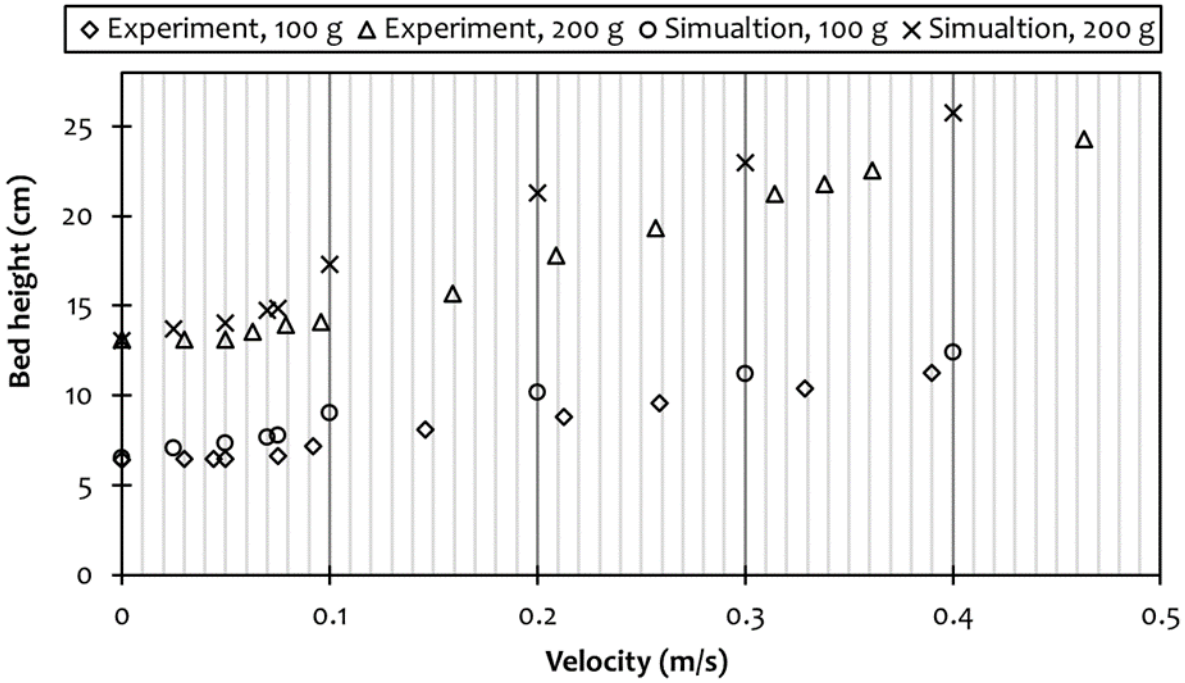

Figure 5.8. Bed height versus superficial velocity for sand fluidization.

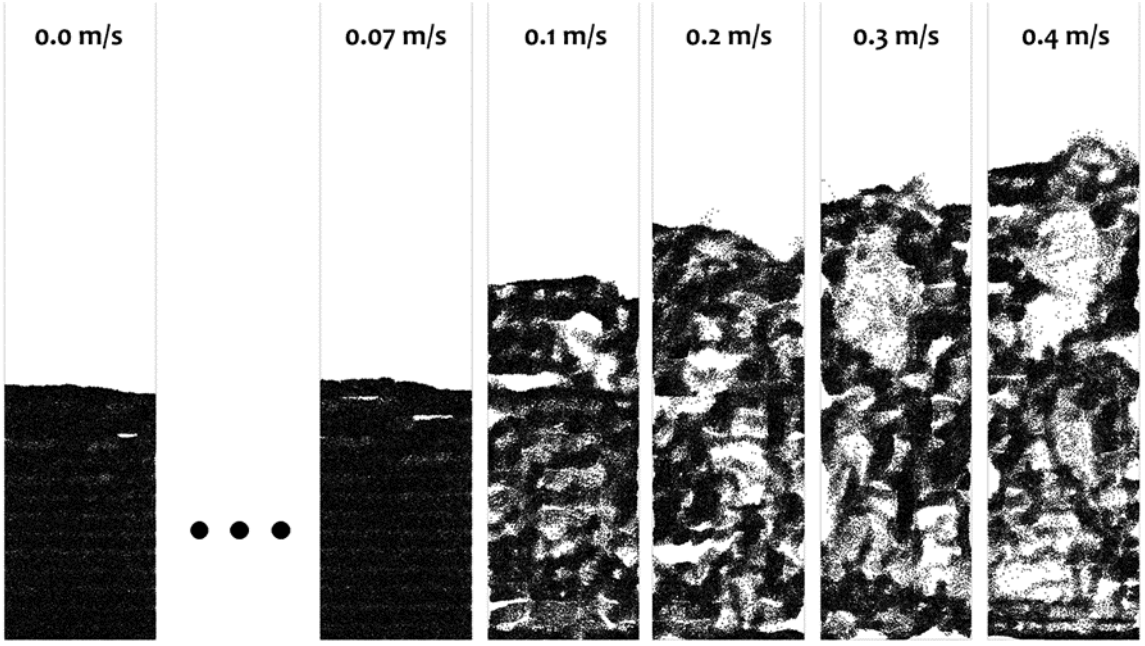

Figure 5.9. Snapshot of simulated particle flow at different fluidization velocity for case 1-S at simulation time = 20 s.

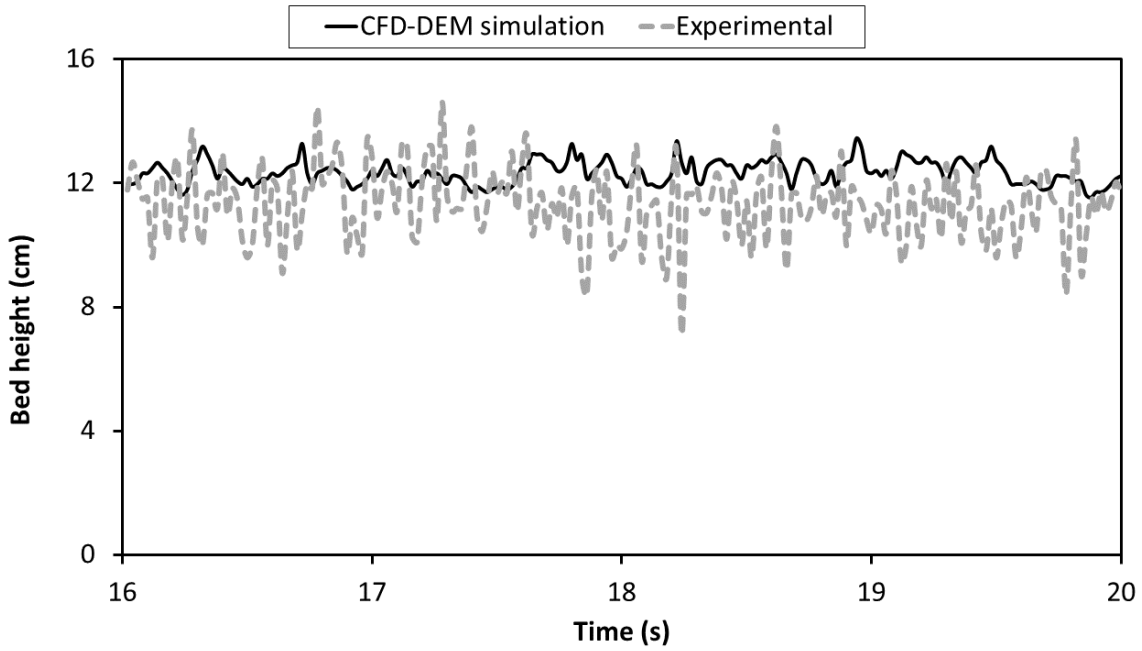

Figure 5.10. Comparison of experimental and CFD-DEM predicted bed height fluctuation for case 1-S. CFD-DEM fluidization velocity equal 0.40 m/s and experimental fluidization velocity equal ~0.39 m/s.

Conclusions

In this study, a CFD-DEM model capable of accurately representing the hydrodynamics behavior of gas-solid flow inside fluidized system was presented. Two major assumptions were introduced in the development of the CFD-DEM models. First, this study assumes a quasi-three-dimensional flow in which the thickness of the fluidized bed system was equal to the diameter of the particles, though the flow field in real fluidized bed systems is full three dimensional. Second, the particle was assumed to be monodispersed with diameter equal to the mass median diameter of the particle size distribution. The experimental validation of the simulation prediction was carried out by comparing two important hydrodynamic properties of fluidized beds (pressure drop and bed height). Despite the simplifications made in the development our model, the result of the CFD-DEM simulation closely followed the experimental observation regardless of the mass of sand used. It is expected that the developed CFD-DEM model will be coupled with thermal and chemical reaction models in future work to present a comprehensive modeling tool for describing bioenergy processing in a fluidized bed.

Nomenclature

C_d	Drag coefficient (-)
d_p	Diameter of particle (s)
E	Enthalpy (J)
$\mathbf{F}_g$	Fluid force on particle (N)
$\mathbf{F}_p$	Inter-particle collision force (N)
$\mathbf{F}_{p,n}$	Normal particle contact force (N)
$\mathbf{F}_{p,t}$	Tangential particle contact force (N)
$\mathbf{g}$	Acceleration due to gravity (m s^{-2})
h_s	Enthalpy of gas phase (J kg^{-1})
I	Moment of inertia (kg m^2)
$\mathbf{n}$	Unit vector in the direction of the line between two particles (-)
M_p	Mass of particle (kg)
p	Pressure (Pa)
Re_p	Particle Reynolds number (-)
S_m	Momentum source term (N m^{-3})
$\mathbf{T}$	Torque on particle (N m)
t	Time (s)
$\mathbf{U}_g$	Velocity of gas phase (m/s)
$\mathbf{U}_n$	Normal velocity of particle (m s^{-1})
$\mathbf{U}_p$	Velocity of particle (m/s)
$\mathbf{U}_t$	Tangential velocity of particle (m s^{-1})
$\mathbf{U}_r$	Relative velocity between particles (m s^{-1})
V_p	Particle volume (m^3)
ω	Angular velocity (rad/s)

β	Coefficient of interphase momentum exchange (kg m^{-3} s^{-1}))
ε_p	Particle fraction (-)
ε_g	Gas phase fraction (-)
ρ_g	Particle density (kg m^{-3})
μ_g	Gas phase viscosity (kg m^{-1} s^{-1})
k	Stiffness coefficient (N m^{-1})
η	Damping coefficient (kg s^{-1})
μ_f	Friction coefficient (-)
$\boldsymbol{\tau}$	Effective stress tensor (Pa)
α_{eff}	Effective thermal diffusivity (kg m^{-1} s^{-1})

Acknowledgement

This research was supported by Southeastern Sun Grant Center and the US Department of Transportation, Research and Innovative Technology Administration, Grant No. DTO559-07-G-00050.

References

1. Yang, W., *Handbook of fluidization and fluid-particle systems*. CRC press: 2003.
2. Basu, P., *Combustion and Gasification in Fluidized Beds*. 1st ed.; Taylor & Francis Group, LLC: Florida, USA, 2006.
3. Pepiot, P.; Dibble, C. J.; Foust, T. D., Computational fluid dynamics modeling of biomass gasification and pyrolysis. In *Computational Modeling in Lignocellulosic Biofuel Production*, 1st ed.; American Chemical Society: 2010; Vol. 1052, pp 273-298.
4. Anil, M.; Rupesh, S.; Muraleedharan, C.; Arun, P., Performance Evaluation of Fluidised Bed Biomass Gasifier Using CFD. *Energy Procedia* **2016,** *90*, 154-162.
5. Liu, H.; Cattolica, R. J.; Seiser, R., CFD studies on biomass gasification in a pilot-scale dual fluidized-bed system. *International Journal of Hydrogen Energy* **2016,** *41* (28), 11974-11989.
6. Xiong, Q.; Zhang, J.; Xu, F.; Wiggins, G.; Daw, C. S., Coupling DAEM and CFD for simulating biomass fast pyrolysis in fluidized beds. *Journal of Analytical and Applied Pyrolysis* **2016,** *117*, 176-181.
7. Tsuji, Y.; Kawaguchi, T.; Tanaka, T., Discrete particle simulation of two-dimensional fluidized bed. *Powder technology* **1993,** *77* (1), 79-87.
8. van der Hoef, M. A.; van Sint Annaland, M.; Deen, N.; Kuipers, J., Numerical simulation of dense gas-solid fluidized beds: a multiscale modeling strategy. *Annu. Rev. Fluid Mech.* **2008,** *40*, 47-70.
9. Esmaili, E.; Mahinpey, N., Adjustment of drag coefficient correlations in three dimensional CFD simulation of gas–solid bubbling fluidized bed. *Advances in Engineering Software* **2011,** *42* (6), 375-386.
10. Loha, C.; Chattopadhyay, H.; Chatterjee, P. K., Assessment of drag models in simulating bubbling fluidized bed hydrodynamics. *Chemical Engineering Science* **2012,** *75*, 400-407.
11. Bakshi, A.; Altantzis, C.; Bates, R. B.; Ghoniem, A. F., Eulerian–Eulerian simulation of dense solid–gas cylindrical fluidized beds: Impact of wall boundary condition and drag model on fluidization. *Powder Technology* **2015,** *277*, 47-62.
12. Kafui, K.; Thornton, C.; Adams, M., Discrete particle-continuum fluid modelling of gas–solid fluidised beds. *Chemical Engineering Science* **2002,** *57* (13), 2395-2410.
13. Hoomans, B.; Kuipers, J.; van Swaaij, W. P. M., Granular dynamics simulation of segregation phenomena in bubbling gas-fluidised beds. *Powder Technology* **2000,** *109* (1-3), 41-48.
14. Ku, X.; Li, T.; Løvås, T., Influence of drag force correlations on periodic fluidization behavior in Eulerian–Lagrangian simulation of a bubbling fluidized bed. *Chemical engineering science* **2013,** *95*, 94-106.
15. Kulkarni, A.; Baker, R.; Abdoulmoumine, N.; Adhikari, S.; Bhavnani, S., Experimental study of torrefied pine as a gasification fuel using a bubbling fluidized bed gasifier. *Renewable Energy* **2016,** *93*, 460-468.

16. Subramanian, P.; Sampathrajan, A.; Venkatachalam, P., Fluidized bed gasification of select granular biomaterials. *Bioresource Technology* **2011,** *102* (2), 1914-1920.
17. García-Labiano, F.; Gayán, P.; De Diego, L.; Abad, A.; Mendiara, T.; Adánez, J.; Nacken, M.; Heidenreich, S., Tar abatement in a fixed bed catalytic filter candle during biomass gasification in a dual fluidized bed. *Applied Catalysis B: Environmental* **2016,** *188*, 198-206.
18. Wu, X.; Li, K.; Song, F.; Zhu, X., Fluidization Behavior of Biomass Particles and its Improvement in a Cold Visualized Fluidized Bed. *BioResources* **2017,** *12* (2), 3546-3559.
19. Tsuji, Y.; Tanaka, T.; Ishida, T., Lagrangian numerical simulation of plug flow of cohesionless particles in a horizontal pipe. *Powder technology* **1992,** *71* (3), 239-250.
20. Gidaspow, D., *Multiphase flow and fluidization: continuum and kinetic theory descriptions*. Academic press: 1994.
21. Ergun, S., Fluid flow through packed columns. *Chem. Eng. Prog.* **1952,** *48*, 89-94.
22. Wen, C.; Yu, Y., A generalized method for predicting the minimum fluidization velocity. *AIChE Journal* **1966,** *12* (3), 610-612.
23. Kawaguchi, T.; Tanaka, T.; Tsuji, Y., Numerical simulation of two-dimensional fluidized beds using the discrete element method (comparison between the two-and three-dimensional models). *Powder technology* **1998,** *96* (2), 129-138.
24. Escudero, D.; Heindel, T. J., Minimum fluidization velocity in a 3D fluidized bed modified with an acoustic field. *Chemical engineering journal* **2013,** *231*, 68-75.
25. Patil, K. N.; Bowser, T. J.; Bellmer, D. D.; Huhnke, R. L. In *Fluidization characteristics of sand and chopped switchgrass-sand mixtures*, 2003 ASAE Annual Meeting, American Society of Agricultural and Biological Engineers: 2003; p 1.
26. Fan, L.; Ho, T. C.; Walawender, W., Measurements of the rise velocities of bubbles, slugs and pressure waves in a gas-solid fluidized bed using pressure fluctuation signals. *AIChE Journal* **1983,** *29* (1), 33-39.

CHAPTER VI
MULTISCALE SIMULATION OF THE FORMATION OF LIGNOCELLULOSIC BIOMASS INORGANIC SYNGAS CONTAMINANTS IN A BUBBLING FLUIDIZED BED REACTOR. PART I: NITROGEN CONTAMINANTS

This chapter is a draft version of the first part of a two-part series. The relevant paper is listed below:

Oyedeji, O. A., Daw, C. S., Labbé, N., Ayers, P, D., and Abdoulmoumine, N. H. (draft). Multiscale simulation of the formation of lignocellulosic biomass inorganic syngas contaminants in a bubbling fluidized bed reactor. Part i: nitrogen contaminants. Sustainable Chemistry & Engineering.

Abstract

A computational fluid dynamics and discrete element method (CFD-DEM) model was developed to predict the yield of deleterious nitrogen contaminants (NH_3 and HCN) during biomass gasification. Alongside, the yields of major producer gas species (CO, CO_2, CH_4, and H_2) were predicted. The formation of nitrogen contaminants was assumed to follow heterogeneous reaction producing HCN, which was later hydrolyzed to form NH_3. The effects of two important gasification process variables (temperature and equivalence ratio) were evaluated. The result of the CFD-DEM simulation was compared to experimental data reported in literature. This comparison demonstrates that the CFD-DEM model successfully predicts the syngas species (CO, CO_2, H_2, and CH_4). Furthermore, the predicted yields of NH_3 closely match experimental data whereas the predicted yields of HCN were about 30 – 50% lower than the experimental data.

Keywords: NH_3 and HCN, CFD-DEM, Eulerian-Lagrangian, particle collision, multi-phase flow

Introduction

Physiological nitrogen is present in lignocellulosic biomass in organic and inorganic forms as covalently bound proteins, inorganic free ions in the plant fluid matter and salts.[1-2] This physiological nitrogen is the origin of gaseous nitrogen species in gasification producer gas and is partitioned predominantly into nitrogen (N_2), ammonia (NH_3) and hydrogen cyanide (HCN).[3-4] Among all of them, the latter two species are regarded as producer gas impurities because they are precursors to deleterious nitrogen oxides and cause severe catalysts deactivation, which reduces post-gasification process efficiency.[5-6] Ammonia is by far the most abundant of the nitrogen impurities[6] with widely varying concentrations between 350 and 18,000ppm[3] depending on the nitrogen content in the starting feedstock.

The formation of producer gas contaminants during gasification occurs through complex interdependent processes and involves several solid-gas and gas-gas phase chemical reactions, which are highly influenced by the profile of temperature, velocity, pressure, and concentration of chemical species inside the reactor.[7] This complexity leads gasification technology operators and developers rely on insights on the state of processes and concentrations inside the gasifier for design, process control, and optimization. This insight can come by through direct measurements.

However, direct measurement applications are limited as sensors for such measurements in a harsh environment (i.e. high-temperature, turbulent flow) are prohibitively expensive. Furthermore, their application would unavoidably disturb flow patterns and would, therefore, affect the analysis.[7] These limitations make area-averaged and time-averaged data, such as gas composition, flow rate, and temperature at the gasifier inlet and outlet, the commonly available data to scientists and engineers for design, control, and optimization.[7]

Multiscale modeling approaches have been successfully applied in the analysis of complex, coupled processes and, thus, can be applied to understand lignocellulosic biomass gasification in a detailed, fast, and cost-effective manner.[8] Multiscale models have been used to simulate lignocellulosic biomass gasification by combining information on devolatilization, reactive and non-reactive particle collisions, heat transfer, and chemical reactions to produce detailed distributions of temperature, velocity, pressure, and species concentrations.[7] In the context of gasification in fluidized bed reactors, there are two general approaches used: an Eulerian-Eulerian approach and Eulerian-Lagrangian approach.[9] The Eulerian-Eulerian approach considers gas and solid as a continuous and interpenetrating continua.[10] In this case, kinetic theory of granular flow is commonly used to approximate the transport properties of the solid phase.[11] Conversely, the Eulerian-Lagrangian approach describes the gas phase as a continuum and the solid phase as a discrete phase.[12] The motions of individual particles of the solid phase are tracked throughout the flow space.[13] Eulerian-Lagrangian approach is consequently more computationally expensive and accurate than Eulerian-Eulerian approach.[14]

Commercial and non-commercial software used for biomass gasification simulation include ANSYS FLUENT, COMSOL, Barracuda, Multiphase Flow with Interphase eXchanges (MFIX), and Open-source Field Operation and Manipulation (OpenFOAM). OpenFOAM is of special interest to researchers because it is a free and open source software that allows a relatively easy platform to simulate customized problems.[15] It uses C++ libraries and finite-volume-based discretization to solve partial and ordinary differential equations.[16] Its standard distribution comes with several developed utilities and sub-models, and its object-oriented framework allows users to develop their own customized utilities and sub-models to complement existing packages. Oevermann et al.[17] used OpenFOAM code to simulate the gasification of wood in a bubbling fluidized bed gasifier with an Eulerian-Lagrangian approach. They used char as the bed material and studied the effect of wood feed rate on temperature along gasifier height and the yield of major chemical species (carbon monoxide (CO), carbon dioxide (CO_2) and hydrogen (H_2)). The solid particles of lignocellulosic biomass and bed material were described as soft spheres and Smagorinsky sub-grid model (Large-Eddy) was used to describe the turbulence behavior. The authors found that the temperature data obtained from their computational fluid dynamics (CFD) and discrete element method (DEM) simulations closely fit the experimental data. They also reported that the production

of CO and H_2 increased as the wood feed rate increased whereas CO_2 was generally unchanged. Similarly, Ku et al.[18] used OpenFOAM code to develop an Eulerian-Lagrangian model to simulate a fluidized bed biomass gasification. However, they used k-ε turbulence model to describe the turbulence behavior inside the reactor. The developed model showed that the production of CO_2 and H_2 increased as the steam to biomass ratio was raised. Also, the increase in temperature favored the formation of CO and H_2. The predicted data for CO and H_2 conformed well to the experimental data, but the predicted data for CO_2 and methane (CH_4) showed some degree of deviation. Many other works have used OpenFOAM code to develop CFD model for biomass gasification in an entrained flow reactor[19] as well as biomass pyrolysis.[20-21]

In this study, a coupled CFD and DEM simulation of lignocellulosic biomass gasification was developed in OpenFOAM to predict the concentration of nitrogen containing contaminants (NH_3 and HCN), which are rarely quantified in published experimental studies[22], as well as producer gas using a detailed reaction scheme kinetic model rather than a lumped model. The simulations were also designed to investigate the effects of two important process variables (temperature and equivalence ratio (ER)) of the aforementioned nitrogen contaminants.[23]

Materials and method

Computational approach and methodology

A Eulerian-Lagrangian approach was used in this study to simulate the multi-phase flow behavior in the fluidized bed system. The gas phase was simulated in the Eulerian framework as a continuum, whereas the particles (biomass and sand) were simulated in the Lagrangian framework. The mass, momentum, heat, and chemical species transport equations that were employed as well as the submodels to describe the gasification process are presented in subsequent sections.

Particle mass and momentum models

The equation governing the conservation of mass of biomass particles is given as:

$$\frac{\mathrm{dM_p}}{\mathrm{dt}} = \frac{\mathrm{dM_{moisture}}}{\mathrm{dt}} + \frac{\mathrm{dM_{volatile}}}{\mathrm{dt}} + \frac{\mathrm{dM_{char}}}{\mathrm{dt}} \tag{6.1}$$

We assumed that the solid particles mainly experience translational and rotational motions during fluidization.[24] The translational and rotational accelerations were calculated as equations (6.2) and (6.3) respectively. The force driving the translational particle motion is made up of fluid force ($\mathbf{F}_g$), particle force ($\mathbf{F}_p$), and gravity force ($\mathrm{M_p}\mathbf{g}$). These forces also cause a net torque ($\mathbf{T}$) on the particles, producing the rotational particle motion. The coefficient of interphase momentum

exchange (β) is proportional to the fluid force and was computed using Gidaspow drag model for solid spheres.[25] The Gidaspow drag model is a combination of Ergun equation[26] and Wen and Yu drag model[27]. Ergun equation was used to describe the drag behavior in dense bed regime ($\varepsilon_g < 0.8$) whereas Wen and Yu drag model was used to describe the drag behavior in dilute regime ($\varepsilon_g \geq 0.8$).

$$\frac{d\mathbf{U}_p}{dt} = \frac{\mathbf{F}_g}{M_p} + \frac{\mathbf{F_p}}{M_p} + \mathbf{g} \tag{6.2}$$

$$\frac{d\omega}{dt} = \frac{\mathbf{T}}{I} \tag{6.3}$$

$$F_g = \frac{\beta V_p}{\varepsilon_p}\left(\mathbf{U}_g - \mathbf{U}_p\right) \tag{6.4}$$

$$\beta = \begin{cases} 150\frac{\varepsilon_p^2\mu_g}{\varepsilon_g^2 d_g^2} + 1.75\frac{\varepsilon_p\rho_g}{\varepsilon_g d_p}\left|\mathbf{U}_g - \mathbf{U}_p\right| & \varepsilon_g < 0.8 \\ 0.75C_d\frac{\varepsilon_p\rho_g}{d_p}\left|\mathbf{U}_g - \mathbf{U}_p\right|\varepsilon_g^{-2.65} & \varepsilon_g \geq 0.8 \end{cases} \tag{6.5}$$

$$C_d = \begin{cases} \frac{24}{Re_p}\left(1 + 0.15Re_p^{0.687}\right) & < 1000 \\ 0.44 & Re_p \geq 1000 \end{cases} \tag{6.6}$$

$$Re_p = \frac{\varepsilon_g\rho_g d_p\left|\mathbf{U}_g - \mathbf{U}_p\right|}{\mu_g} \tag{6.7}$$

Particle forces are due to inter-particle and particle-wall collisions. Soft-sphere discrete element model is capable of accounting for the multiple inter-particle and particle-wall collisions, which are frequent in fluidized bed systems.[24] Therefore, a soft-sphere discrete element model was used to describe the collision dynamics in this study. The momentum exchange during collisions was modeled using a combination of spring, slider, and dashpot models as illustrated in Figure 6.1.
The particle contact force was decomposed into normal force ($F_{p,n}$) and tangential force ($F_{p,t}$) (Figure 6.1).

The models describing the normal and tangential particle collision forces can be expressed as shown in Equations ((6.8) - (6.11))

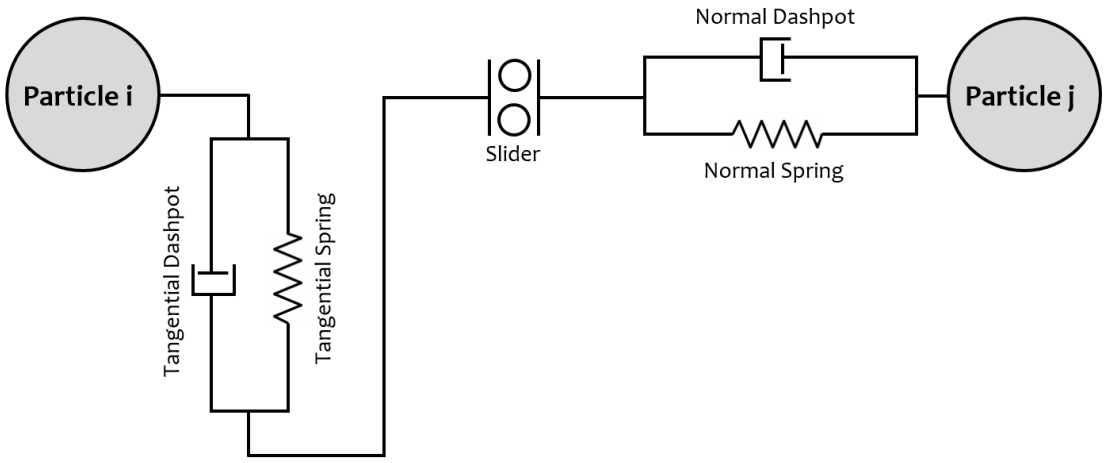

Figure 6.1. Hertz-Mindlin particle contact model (spring-slider-damper collision model).

$$\mathbf{F}_{p,n} = -k\mathbf{d}_n - \eta\mathbf{U}_n \tag{6.8}$$

$$\mathbf{U}_n = (\mathbf{U}_r \cdot \mathbf{n})\mathbf{n} \tag{6.9}$$

$$\mathbf{F}_{p,t} = -k\mathbf{d}_t - \eta\mathbf{U}_t \tag{6.10}$$

$$\mathbf{U}_t = \mathbf{U}_r - \mathbf{U}_n \tag{6.11}$$

If particle sliding is assumed to occur when $|\mathbf{F}_{p,t}| \geq \mu_f|\mathbf{F}_{p,n}|$, then tangential particle collision force can be expressed as:

$$\mathbf{F}_{p,t} = -\mu_f|\mathbf{F}_{p,n}|\mathbf{t} \tag{6.12}$$

The model parameters for particle-particle and particle-wall collisions used in this study are as listed in Table 6.1.

Table 6.1. Inter-particle and particle-wall collision parameters used in this work.[28]

Inter-particle collision parameters	Value
Effective Young's modulus (Pa)	1.0e+08
Poisson's ratio	2.3e-01
Coefficient of restitution	9.0e-01
Coefficient of friction	3.0e-01
String stiffness (N/m)	8.0e+02

Gas phase transport equations

The governing mass, momentum, energy, and chemical species transport equations were described as expressed Equations (6.13) – (6.17). The exchanges between the gas and solid phases were accounted for using source terms in each transport equation. Additionally, the gas fraction parameter was introduced into each equation to effectively model for dense gas-solid fluidization.

$$\frac{\delta}{\delta t}\left(\varepsilon_g \rho_g\right) + \nabla \cdot \left(\varepsilon_g \rho_g \mathbf{U}_g\right) = S_\rho \tag{6.13}$$

$$\frac{\delta}{\delta t}\left(\varepsilon_g \rho_g \mathbf{U}_g\right) + \nabla \cdot \left(\varepsilon_g \rho_g \mathbf{U}_g \mathbf{U}_g\right) = -\nabla p + \nabla \cdot \left(\varepsilon_g \boldsymbol{\tau}\right) + \varepsilon_g \rho_g \mathbf{g} + S_m \tag{6.14}$$

$$E = h_s - \frac{p}{\rho_g} + \frac{\mathbf{U}_g^2}{2} \tag{6.15}$$

$$\frac{\delta}{\delta t}\left(\varepsilon_g \rho_g E\right) + \nabla \cdot \left(\varepsilon_g \mathbf{U}_g (\rho_g E + p)\right) = \nabla \cdot \left(\varepsilon_g \alpha_{eff} \nabla h_s\right) + S_h + S_{p,\,h} + S_{rad} \tag{6.16}$$

$$\frac{\delta}{\delta t}\left(\varepsilon_g \rho_g Y_i\right) + \nabla \cdot \left(\varepsilon_g \rho_g \mathbf{U}_g Y_i\right) = \nabla \cdot \left(\varepsilon_g \rho_g D_{eff} \nabla Y_i\right) + S_{p,Y_i} + S_{Y_i} \tag{6.17}$$

The stress tensor ($\boldsymbol{\tau}$) was calculated as the sum of viscous and turbulent stresses. Equally, viscous and turbulent effects were accounted for in the computation of the effective dynamic thermal diffusivity (α_{eff}) and species mass diffusion (D_{eff}). Gas phase density and viscosity are determined based on the pressure and temperature values according to gas equation of state.

Chemical reaction models

Figure 6.2 illustrates the assumed chemical reaction pathway followed for the conversion of solid biomass to gaseous chemical species and char. Although drying is not considered part of the chemical reaction, it clearly releases H2O that participates in subsequent homogeneous reactions.

The major assumptions used in the implementation of the chemical reaction pathway are:

- Biomass is a composite mixture of water, volatile matter, and solid matter.
- During drying, the water component of biomass is released into the gas phase.

- The volatile matter of biomass is released as CO, CO_2, H_2, H_2O, and CH_4, leaving behind the solid matter.
- The solid matter comprises of carbon, nitrogen, and ash.
- The ash component is not chemically or mechanically removed from the particle.
- The char component undergoes heterogenous reactions to form CO, CO_2, and CH_4.
- The nitrogen component undergoes heterogeneous reaction to form HCN, which later participate in homogeneous reaction with H_2O to for NH_3.

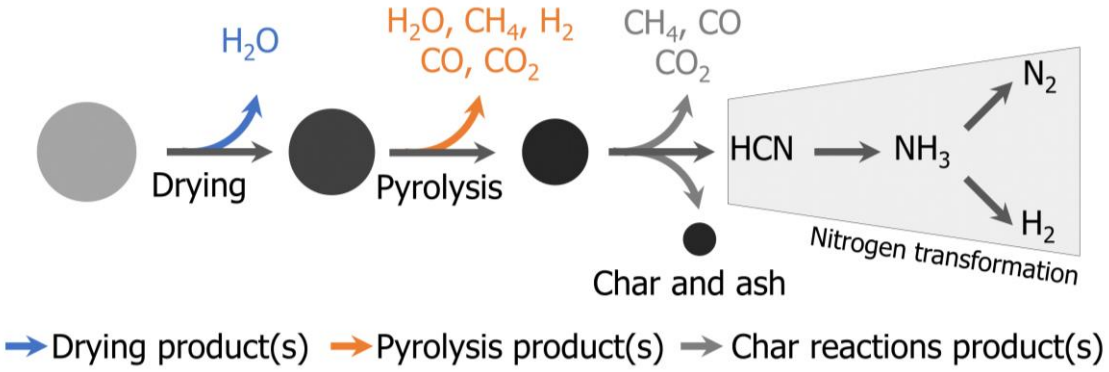

Figure 6.2. Chemical reaction pathways for the conversion of biomass.

The chemical reaction pathway and assumptions considered were carefully selected based on the availability of kinetic information in literature. Although several studies have demonstrated that some biomass nitrogen is released at the pyrolysis stage,[29-30] there is inadequate kinetic information on the formation of NH_3 and HCN during pyrolysis. Hence, this study restricts the release of biomass nitrogen to heterogenous reaction.

Pyrolysis reaction

Biomass particles are rapidly heated up and dried when they are injected into the reactor. After the moisture content of the particles has been vaporized, the dried biomass particles are pyrolyzed to release their volatile matter contents, leaving behind solid residue. The volatiles considered in the devolatilization model used in this study are CO, CO_2, H_2, H_2O, and CH_4. The fractional composition of the volatile was determined following the equilibrium reaction equation (Reaction [6.1]) subjected to elemental conservations. This followed the approach used by Ku et al.[18] and consistent with our findings in Chapter 4 of this dissertation.

$$\mathrm{Biomass_{volatile}} \rightarrow \alpha_1 \mathrm{CO} + \alpha_2 \mathrm{CO_2} + \alpha_3 \mathrm{CH_4} + \alpha_4 \mathrm{H_2} + \alpha_5 \mathrm{H_2O} \qquad [6.1]$$

A single step first-order Arrhenius devolatilization reaction model will be used to compute the rate of devolatilization (Equation (6.18)). Similar to the modeling approach used by Abani and Ghoniem[31], a net zero energy consumption during devolatilization was assumed because the heat required for devolatilization is negligible as compared to heat produced during subsequent char oxidation reactions.

$$\frac{\mathrm{dM_{volatile}}}{\mathrm{dt}} = \mathrm{A} \exp\left(\frac{-\mathrm{E_a}}{\mathrm{RT_p}}\right) \mathrm{M_{volatile}} \qquad (6.18)$$

Heterogeneous reactions

The solid residue resulting from the devolatilization reaction participate in several heterogeneous chemical reactions. The heterogeneous char reactions examined in this study are listed in Figure 6.2. These reactions include the conversion of solid carbon to CO, CO_2, and CH_4 and the conversion of solid nitrogen to HCN.

Table 6.2. Kinetics parameter for heterogeneous chemical reactions.

Stoichiometry	Reaction rate	No.
$C_{(S)} + H_2O \rightarrow CO + H_2$	$A_1 = 2.00 \times 10^{-3};\ E_{a,1} = 1.96 \times 10^{8}$	[6.2] [18]
$C_{(S)} + CO_2 \rightarrow 2CO$	$A_2 = 3.00 \times 10^{-1};\ E_{a,2} = 2.00 \times 10^{8}$	[6.3] [18]
$C_{(S)} + O_2 \rightarrow CO_2$	$A_3 = 2.51 \times 10^{-3};\ E_{a,3} = 7.48 \times 10^{7}$	[6.4] [18]
$2C_{(S)} + 2H_2 \rightarrow 2CH_4$	$A_4 = 1.18 \times 10^{-5};\ E_{a,4} = 1.48 \times 10^{8}$	[6.5] [11]
$N_{(S)} \rightarrow HCN$	$A_N = 2.63 \times 10^{1};\ E_{a,N} = 1.43 \times 10^{5}$	[6.6] [32]

No.: reaction number.

The overall conversion of solid carbon was assumed to be diffusion limited.[11] Therefore, to model these heterogeneous reactions, the effect of diffusion on the overall reaction was accounted for by using an overall reaction scheme (Equation (6.19)), which expresses the rate of char consumption as a function of reaction rate and diffusion rate. The conversion of solid nitrogen was assumed to be limited by the amount of available solid nitrogen and volatile matter content (Equation (6.22)).[32]

$$\frac{dC_{(s)}}{dt} = \sum_{i=1}^{4} -A_p p_i \frac{r_{diff,i} r_{kin,i}}{r_{diff,i} + r_{kin,i}} \tag{6.19}$$

$$r_{diff,i} = 5.00 \times 10^{-12} \frac{\left(0.5\left(T_p + T_g\right)\right)^{0.75}}{d_p} \tag{6.20}$$

$$r_{kin,i} = A_i \exp\left(\frac{-E_{a,i}}{RT_p}\right) \tag{6.21}$$

$$\frac{dN_{(s)}}{dt} = A_N \exp\left(\frac{-E_{a,N}}{RT_p}\right) N_C \frac{VM^{0.364}}{VM_\infty} \tag{6.22}$$

Homogenous reactions

All the hundreds of homogeneous reactions that take place during biomass gasification cannot be evaluated mainly due to the computational intensity and the paucity of kinetic data in literature. Hence, significant homogeneous reactions involving primary gases and contaminant gases were selected (Reactions [6.7] – [6.13]). Table 6.3 lists the chemical reactions considered and their corresponding reaction rate information as deduced from relevant literature.

Table 6.3. Kinetics parameter for homogenous chemical reactions.

Stoichiometry	Reaction rate	No.
$CH_4 + 2O_2 \rightarrow CO_2 + 2H_2O$	$5.16 \times 10^{13}\ \mathrm{T}^{-1} \exp\left(\frac{-1.56 \times 10^4}{\mathrm{T}}\right)$	[6.7] [18]
$CH_4 + H_2O \rightarrow CO + 3H_2$	$7.00 \times 10^6 \exp\left(\frac{-1.54 \times 10^4}{\mathrm{T}}\right)$	[6.8] [18]
$H_2 + 0.5O_2 \rightarrow H_2O$	$2.20 \times 10^9 \exp\left(\frac{-2.20 \times 10^9}{\mathrm{RT}}\right)$	[6.9] [18]
$CO + H_2O \rightarrow CO_2 + H_2$	$2.78 \times 10^3 \exp\left(\frac{-1.52 \times 10^3}{\mathrm{T}}\right)$	[6.10] [18]
$CO_2 + H_2 \rightarrow CO + H_2O$	$9.59 \times 10^4 \exp\left(\frac{-5.34 \times 10^3}{\mathrm{T}}\right)$	[6.11] [18]
$HCN + H_2O \rightarrow NH_3 + CO$	$1.94 \times 10^{20} \exp\left(\frac{-3.95 \times 10^4}{\mathrm{T}}\right)$	[6.12] [32]
$NH_3 \rightarrow 0.5N_2 + 1.5H_2$	$3.29 \times 10^{-2} \exp\left(\frac{-8.31 \times 10^3}{\mathrm{T}}\right)$	[6.13] [33]

No.: reaction number.

Particle shrinkage

Vaporization, devolatilization, and char-gasification processes cause biomass particles to shrink in size. Simulating this phenomenon is important to effectively describe the fluidization behavior as well as particle residence time and entrainment rate. A mass-proportional shrinkage model was used to evaluate the instantaneous diameter of each biomass particle (Equation (6.23)).[34]

$$d_p = \sqrt[3]{\frac{6M_p}{\pi\rho_p}} \tag{6.23}$$

Heat transfer model

The heat conservation equation for each particle (Equation (6.24)) considers the effect of radiation, gas-solid convection, vaporization, and heterogeneous reactions on temperature change. Equation (6.24) was therefore used to determine the instantaneous particle temperature.

$$M_p C_p \frac{dT_p}{dt} = hA_p(T_g - T_p) + \frac{e_p A_p}{4}(G - 4\sigma T_p^4) + Q_{moisture} + Q_{char} \tag{6.24}$$

$$h = \frac{6 \propto_p k_g Nu_p}{d_p^2} \tag{6.25}$$

$$Nu_p = 2 + 0.6Re_p^{0.5}Pr^{0.33} \tag{6.26}$$

$$Pr = \frac{C_{pg}\mu_g}{k_g} \tag{6.27}$$

Numerical simulation setup

The governing equations for conservation of mass, momentum, energy, and chemical species were resolved in OpenFOAM code (version 2.4.0), which uses finite volume discretization method. The gas flow was assumed to be compressible and k-ε turbulence model was used to describe the turbulent behavior of the gas flow. A standard pressure based PISO (pressure implicit splitting of operators) solver for variable density flow was employed to solve the fluid transport equations. The fluid density was calculated using the ideal gas equation state (p = ρRT).

Table 6.4 lists value(s) for important simulation parameters and gasification process variables. The simulated fluidized bed reactor is 38.1 mm in diameter and 749.30 mm in height. To reduce computational time and size. a quasi-three-dimensional geometry model, with its thickness equal to the initial diameter of the biomass

particle, was used (Figure 6.3). The boundary conditions were chosen to match the experimental conditions used by Abdoulmoumine, et al. [35]. The outlet is assumed to be fixed at atmospheric pressure. Simulations were carried out to study the effect of temperature (1063.15, 1207.15, and 1351.15 K) and ER (0.15, 0.25, and 0.35), respectively.

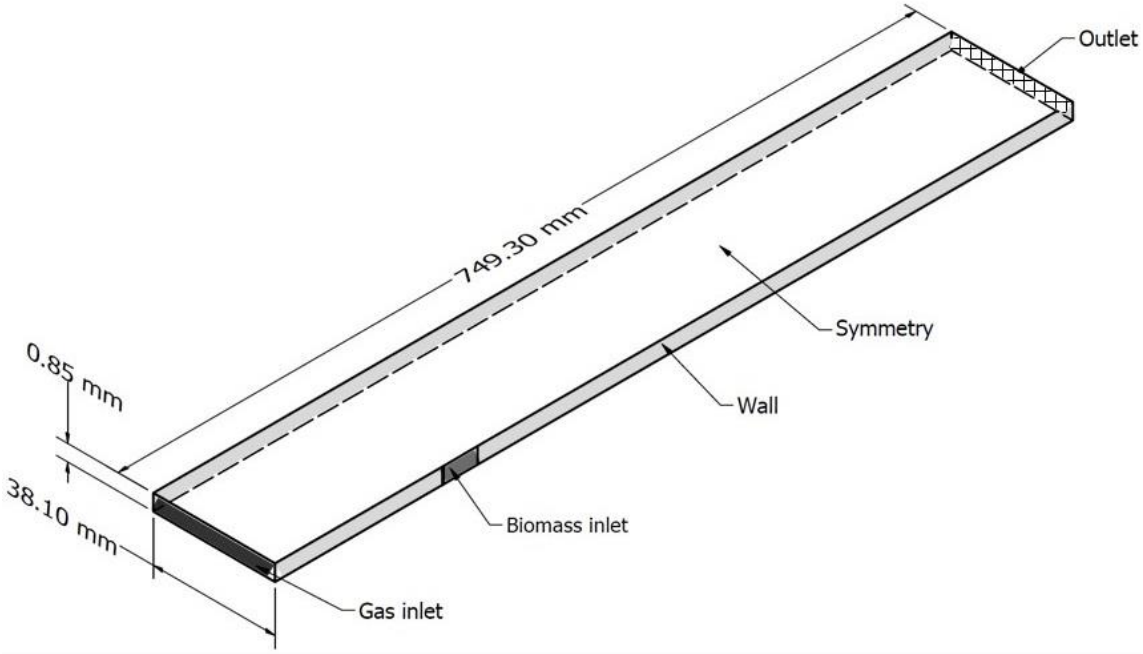

Figure 6.3. Quasi-three-dimensional geometry model with boundary conditions.

Table 6.4. Simulation parameters and gasification process variables used.

Parameter	Value
Mesh size (m)	0.0038 × 0.0049 × 0.0005
Fluid time step (s)	1.00×10^{-5}
Simulation end time (s)	20
Reactor temperature (K)	1063.15, 1207.15, 1351.15
Inlet gas velocity (m/s)	0.15
Biomass feed rate (kg/s)	8.33×10^{-5}
Biomass initial temperature (K)	298.15
Biomass specific heat (J/kg-K)	1500
Biomass density (kg/m^3)	600
Biomass shape (-)	sphere
Biomass diameter (m)	8.50×10^{-4}
Sand quantity (kg)	0.20
Sand specific heat (J/kg-K)	860
Sand density (kg/m^3)	2600
Sand shape (-)	sphere
Sand diameter (m)	5.0×10^{-4}
Sand emissivity (-)	1.0

Results and discussion

Fluidization and particle motion behavior

Understanding how particles behave during fluidization is essential to optimizing the gasification process in a fluidized bed reactor. In this study, the particles were tracked in terms of position, composition, temperature, and size. Each simulation was initialized by placing 19650 sand particles in the reactor and allowed to be fluidized for 30 secs before the injection of biomass particles was implemented. The temperature of the sand particles at the start of each simulation was set to the gasification temperature whereas the temperature of the biomass particles was set to room temperature.

Figure 6.4 is the snapshot of the particle flow with corresponding voidage profile at three different simulation times. During simulation, a typical upward movement of bubbles, displacing solid particle was observed.[36] As the bubbles breakup on the bed surface, the displaced solid particles drifts towards the wall and return to lower regions within the bed. This observation was continued throughout the simulation duration, generating mixing effect within the bed. Figure 6.4 (D, E, and F) represents the voidage profile inside the reaction at simulation time = 15.0, 15.1, and 15.2, respectively. It shows that at simulation time = 15.1s, Bubbles 1 and 2 coalesce to form Bubble 4, which then displaced the particles around it. At simulation time = 15.2s Bubble 4 broke through the bed surface, displacing the particles above it upwards and towards the wall. Additionally, bubbles can also be fragmented, as seen in the case of Bubble 3 dividing to form Bubbles 5 and 6. The biomass particles that enter the reactor are heated up and dried, then undergo pyrolysis and char reactions, causing particle shrinkage as described in Equation (6.23). After the biomass particle diameter have been reduced beyond a threshold diameter where terminal velocity equals operating velocity, the biomass particles are elutriated and subsequently discharged from the reactor (Figure 6.4).

Temperature and gas composition profiles

We assumed that the reactor was continuously heated to maintain its temperature at the set gasification temperature. To satisfy this assumption, a constant temperature boundary condition was imposed on the reactor walls ($\mathrm{T_{wall}} = \mathrm{T_{operation}}$). The simulation result shows that temperature of the region surrounding the biomass inlet was lower than other regions in the reactor because the injected biomass particles are rapidly dried and undergo incipient pyrolysis in this region. The notion that injected biomass particles are rapidly dried and undergo incipient pyrolysis is supported by the corresponding increase in H_2O and volatile gases concentration in the region surrounding the biomass inlet (Figure 6.5).

As expected, the gas phase velocity was increased within the dense bed region because of the reduction area available to fluid flow because of the presence of particulates.

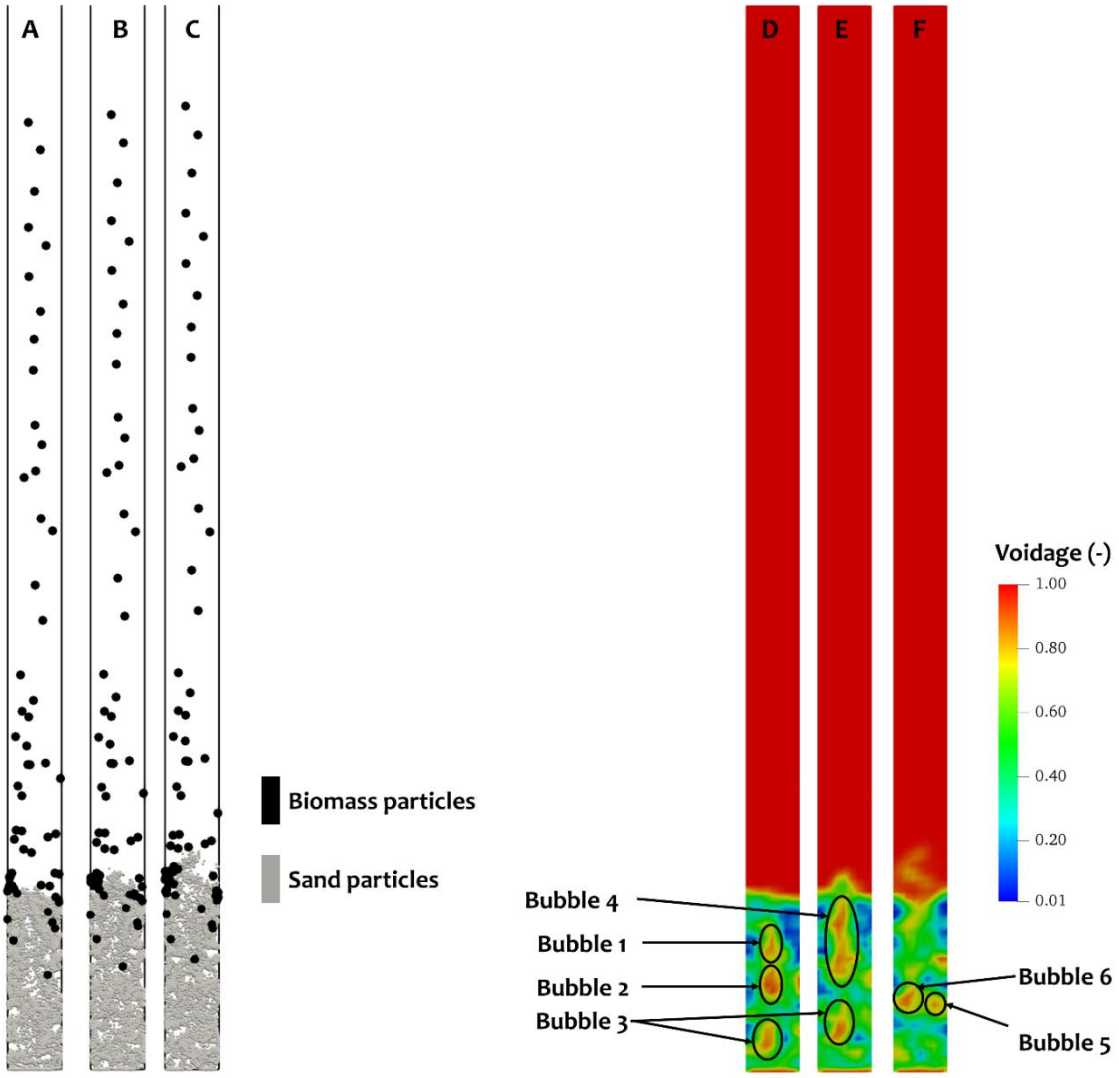

Figure 6.4. Fluidization pattern of particles during simulation with corresponding voidage inside the reactor (temperature = 1207.15 K, ER = 0.25, gas velocity = 0.15 m/s). a) particle flow at simulation time = 15.0 s, b) particle flow at simulation time = 15.1 s, c) particle flow at simulation time = 15.2 s, d) voidage profile at simulation time = 15.0 s, e) voidage profile at simulation time = 15.1 s, and f) voidage profile at simulation time = 15.2 s.

Furthermore, additional gas released during particle drying and pyrolysis increases the flow rate of the gas phase. The gas phase velocity gradually reduced in the dilute bed region and as it rises towards the reactor outlet. A plot of the pressure at the reactor inlet clearly shows the transient nature of the fluidization process (Figure 6.6).

A careful observation of gas species concentrations reveals three classes of gas species based on where they were mainly formed and/or consumed. Class I includes gas species formed within and around the bed. However, as class I gases approach the reactor outlet, they are consumed mainly due to the activities of heterogenous reactions. Class II includes gas species that are mainly formed between the bed and reactor outlet from heterogenous reactions consuming class I gas species. The net formation of class III gas species is generally positive throughout the length of the reactor. Therefore, class III gas species were described as continuously formed throughout the length of the reactor. For the temperature and ER ranges considered in this study, CH_4 and HCN were categorized as class I gas species whereas NH_3 and CO_2 were categorized as class II. Class III gas species were CO and H_2.

Effects of temperature and ER on H_2, CO, CO_2, and CH_4

Figure 6.7 show a typical example of the time-averaged concentration of the major gas compositions of producer gas as observed by Abdoulmoumine, et al. [35] and predicted in this study. The reported CFD-DEM predicted concentration throughout this work represent the time-averaged concentration for simulations between simulation time = 10.0 and 20.0 s. A 95% confidence interval for each set of experimental data was calculated to account for sampling error and provide a robust qualitative comparison between predicted and experimental data. Figure 6.7 shows that the H_2 concentration was directly proportional to the gasification temperature. This observation closely matches the experimental trend. The predicted H_2 concentrations were higher but comparable to the average experimental data from Abdoulmoumine, et al. [35], regardless of gasification temperature. The mean absolute deviation of the CFD-DEM prediction of H_2 concentration data was 5.27% (Table 6.5), indicating good fit of the CFD-DEM model to the experimental data.

When the gasification temperature was raised, CO concentration increased, which is consistent with the idea that water gas and Boudouard reactions are more favored at higher temperature. The rate of increase of CO concentration with temperature was lower between 1063.15 and 1207.15 K compared to the rate of increase of CO concentration with temperature between 1207.15 and 1351.15 K. The predicted value of CO concentration was within the experimental range at 1351.15 K. However, the predicted CO concentration was higher than the experimental CO concentration at 1063.15 and 1207.15 K, as in the case of H_2. The higher concentrations of H_2 and CO_2 from the simulation data compared to experimental data may be due to the fact that Abdoulmoumine, et al. [35] included the concentration for minor gases such as C_2H_2 and C_2H_4.

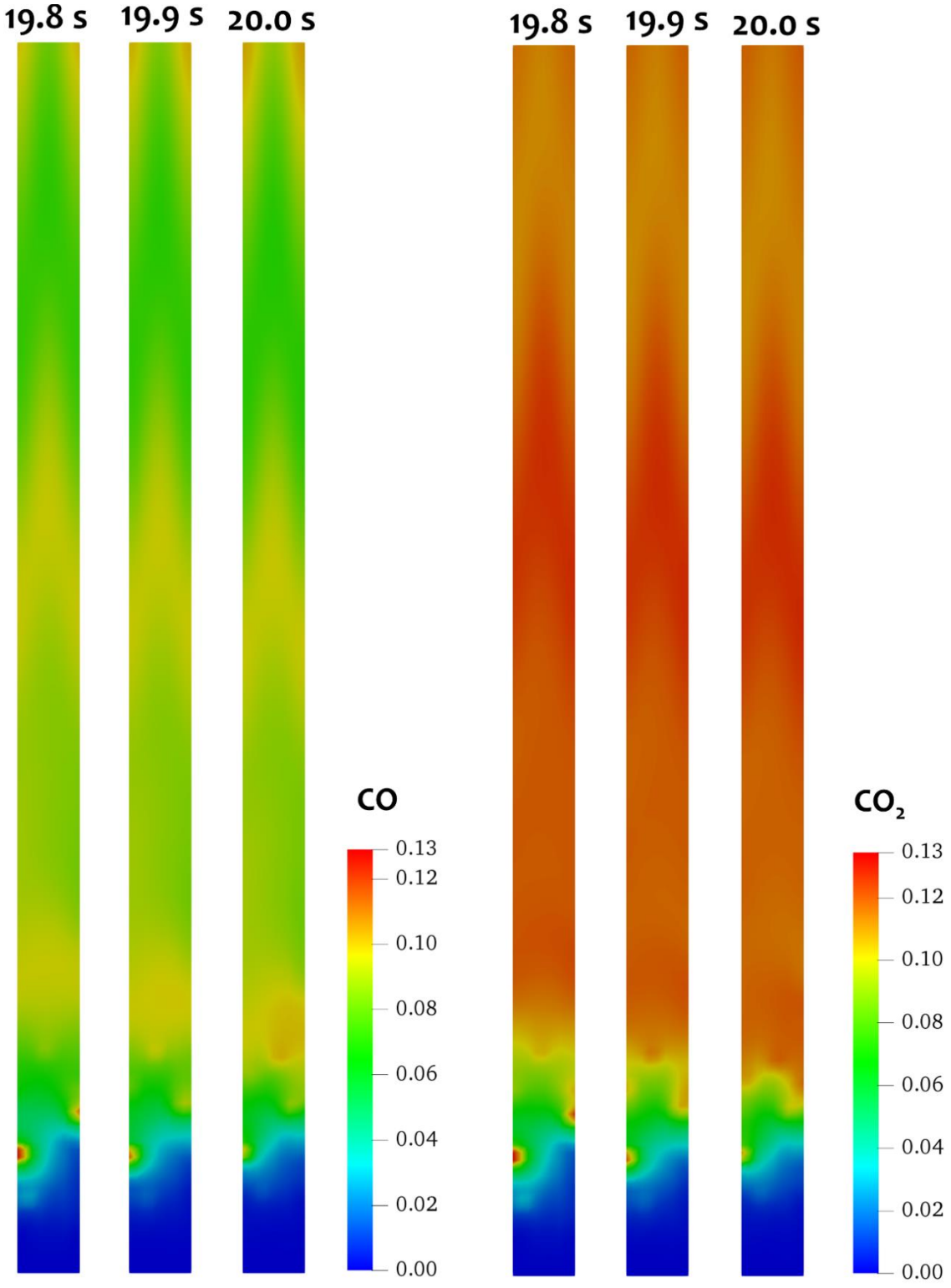

Figure 6.5. Snapshot of gas phase flow characteristics (temperature = 1207.15 K, ER = 0.25, gas velocity = 0.15 m/s). Concentration of chemical species is in mass fraction.

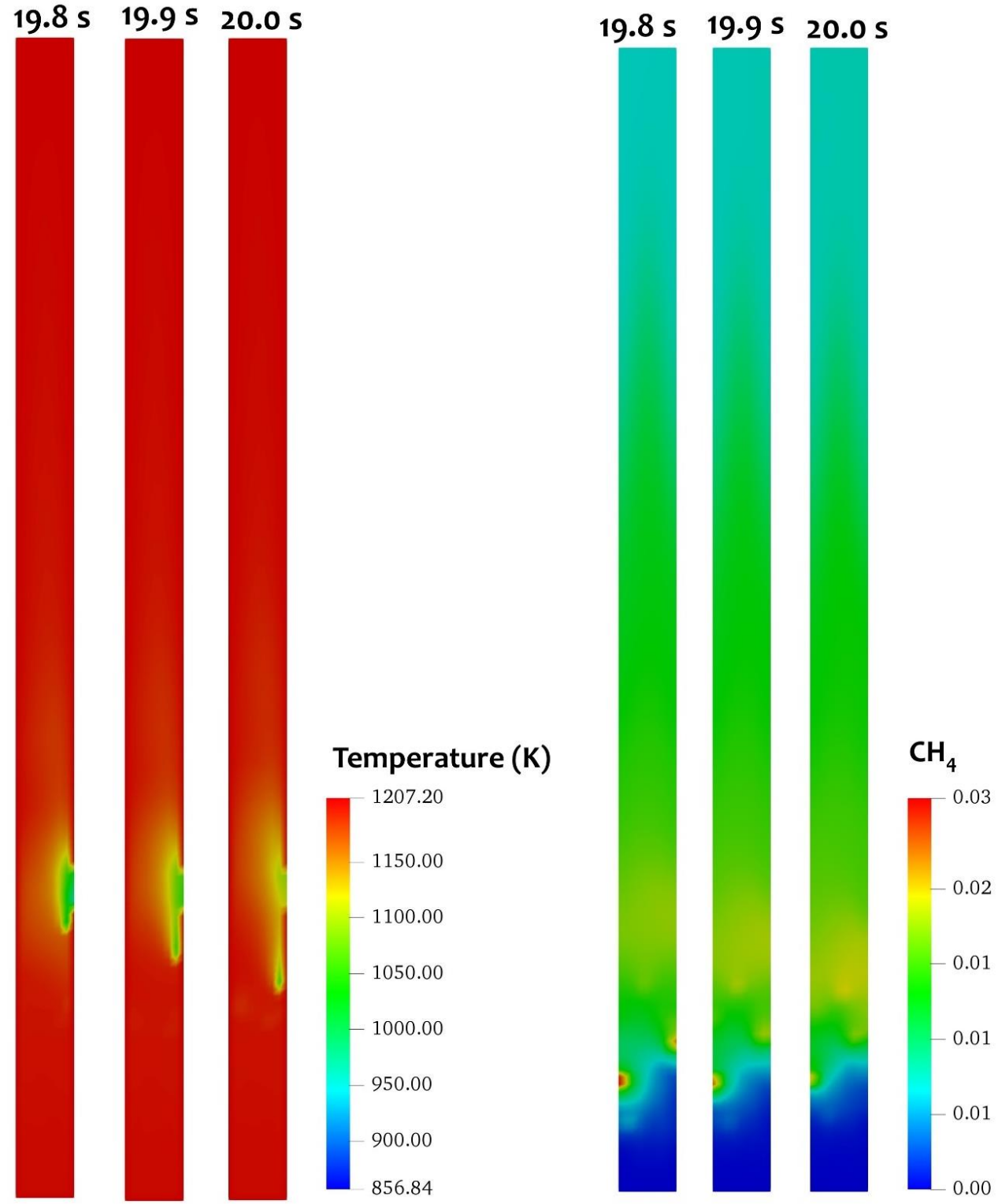

Figure 6.5. Continued.

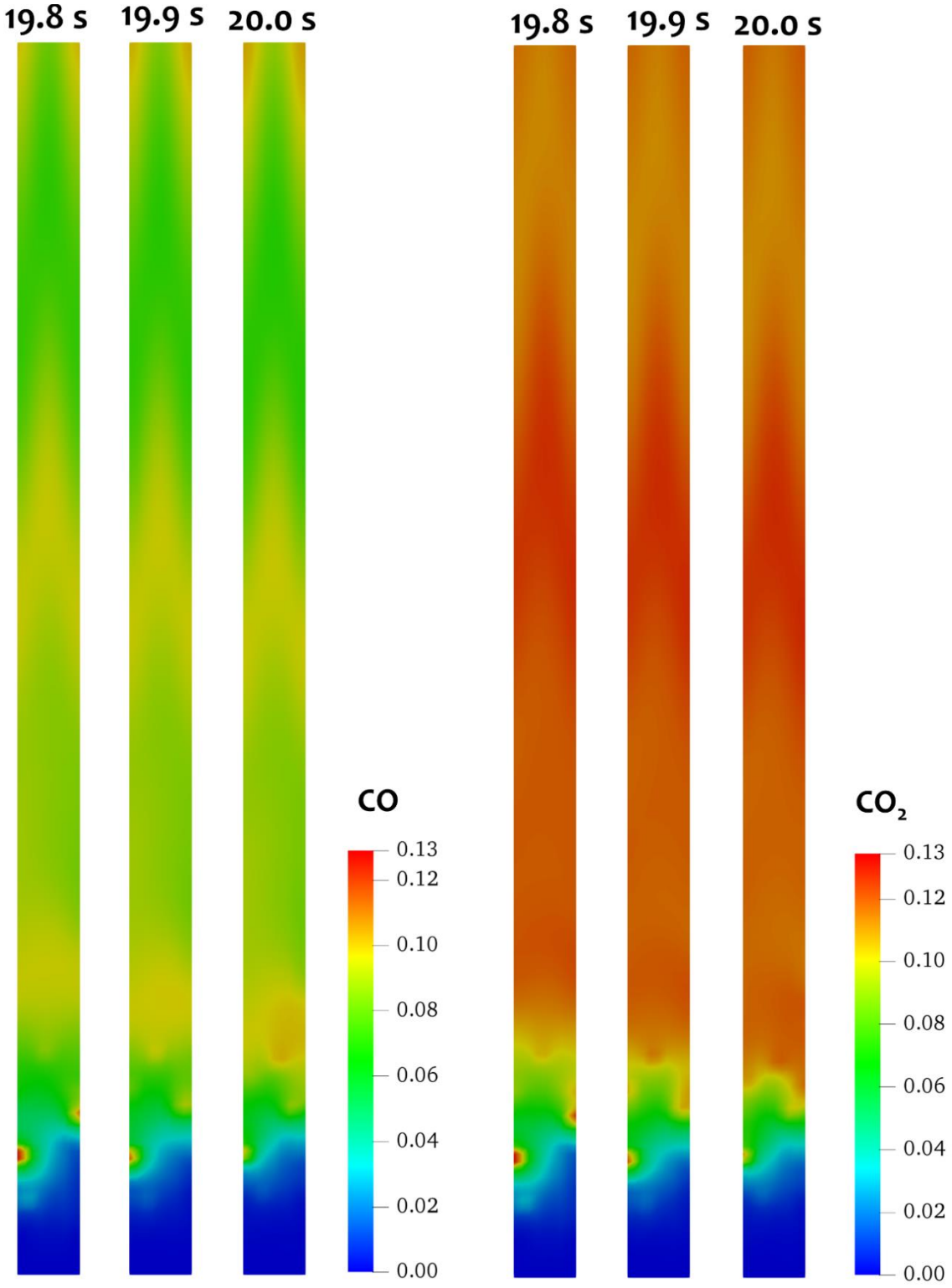

Figure 6.5. Continued.

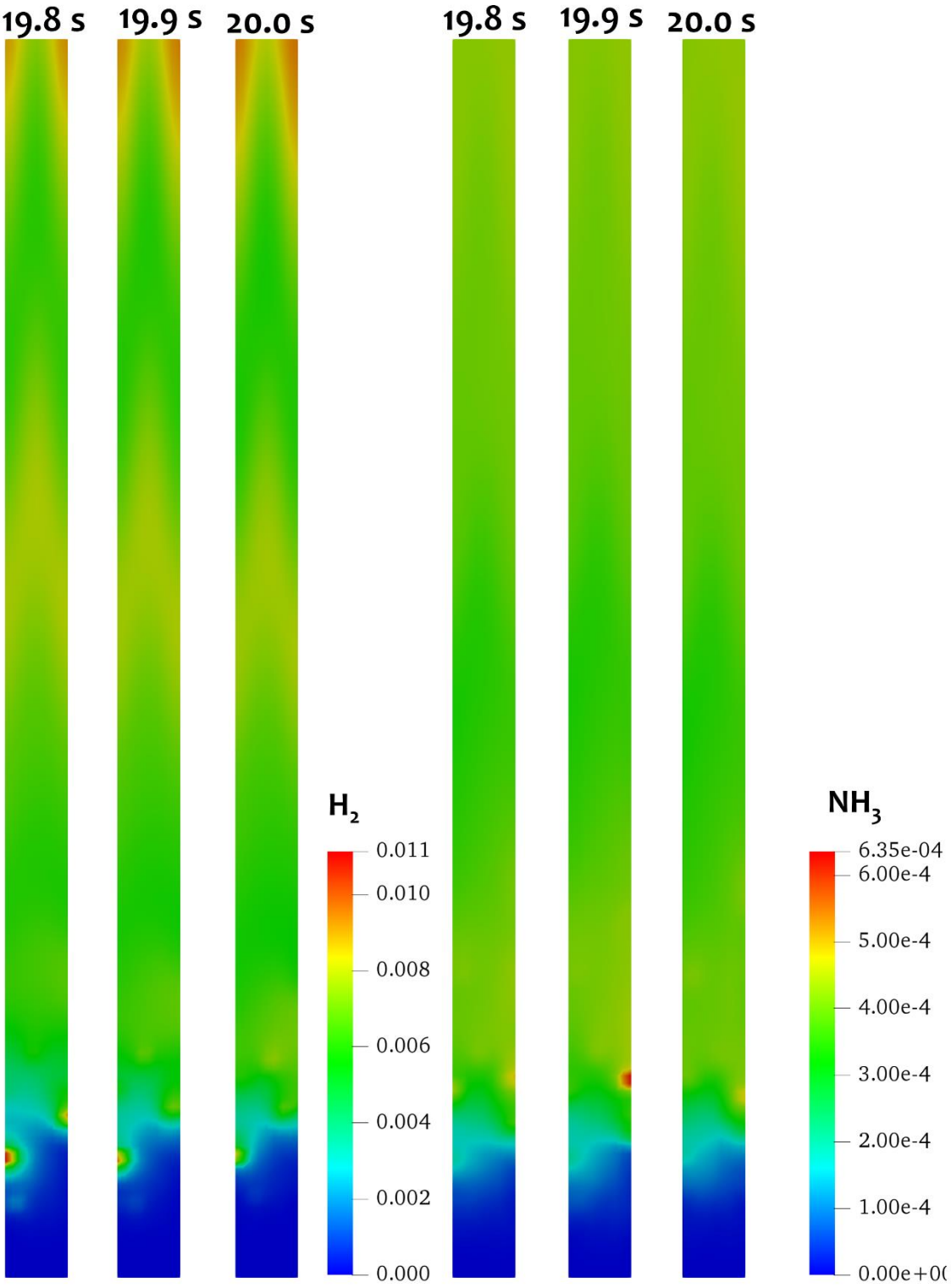

Figure 6.5. Continued.

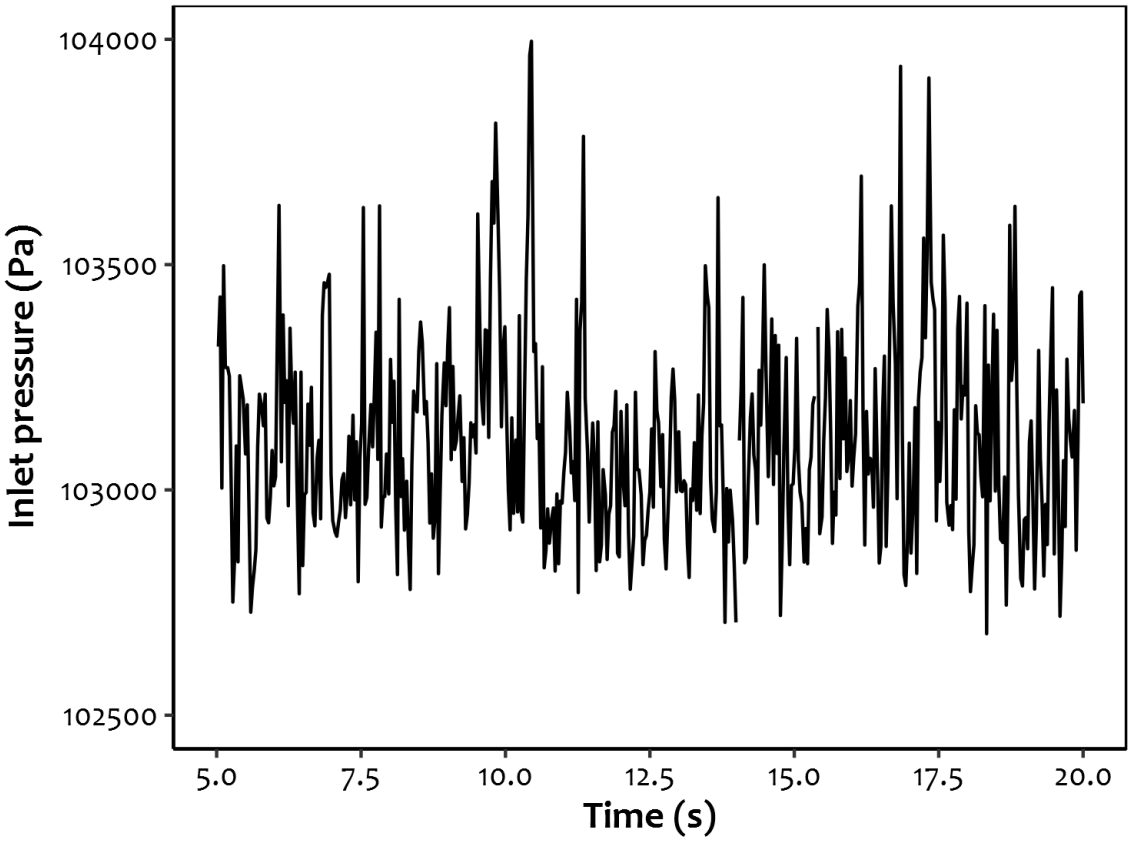

Figure 6.6. Transient inlet pressure (temperature = 1207.15 K, ER = 0.25, gas velocity = 0.15 m/s)

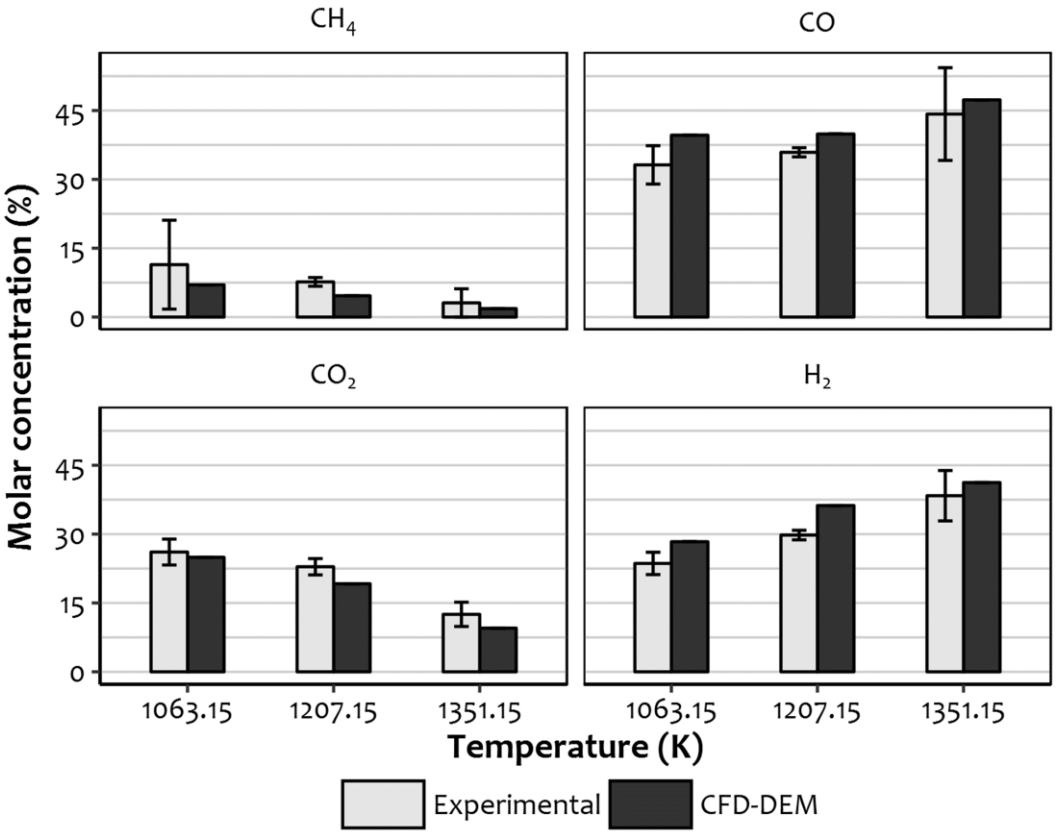

Figure 6.7. Comparison between the predicted and experiment concentration of H_2, CO, CO_2, and CH_4 as affected by gasification temperature. Error bar indicates 95% confidence interval.

There were negative linear correlations between CO_2 concentration and gasification temperature and between CH_4 concentration and gasification temperature (Figure 6.7). The observed reduction in CH_4 concentration with increasing temperature has been commonly attributed to the amplification of methane steam reforming reaction.[37] Predicted CH_4 concentrations were lower than experimental values (Table 6.5) and may be because tar formation during the pyrolysis stage is not included in this modeling work. Experimental studies have shown that some portion of pyrolysis tar is usually cracked in subsequent reactions to form additional CH_4.[38]

Table 6.5. Simulation prediction accuracy metrics

Species	Accuracy metric	
	MAE	RMSE
H2 (%)	5.27	5.73
CO (%)	4.38	5.04
CO2 (%)	2.86	3.30
CH4 (%)	2.50	3.12
NH3 (ppm)	92.50	111.02
HCN (ppm)	22.75	24.03

MAE: mean absolute error, RMSE: root mean square error

Figure 6.8 compares the simulation data with experimental data for different ER. Equivalence ratio significantly influenced CO_2 concentration, with the predicted CO_2 concentration rising by 14.36% when ER was increased from 0.15 to 0.35. Abdoulmoumine, et al. [35] demonstrated that CO_2 concentration increased by 17.07% within the same ER range. CH_4 concentration dropped when ER was increased because methane oxidation reaction is more favored at higher ER values. There was decrease in H_2 concentration with increasing ER. In contrast to the experimental trend, CO concentration slightly increased when ER was raised. The reason for this inconsistency is unclear, however the predicted CO trend vis-à-vis ER corroborate the findings several previous works in this area of study.[22, 39-40]

Overall, the simulation was able to reasonably predict the effect of ER on the major gas composition of producer gas. This is supported by qualitative proofs in Figure 6.7 and Figure 6.8, and evident in the prediction accuracy analysis using mean absolute error and root mean square error (Table 6.5). This demonstrates that the developed CFD-DEM simulation can produce reliable predictions for the major gas composition of producer gas during biomass gasification.

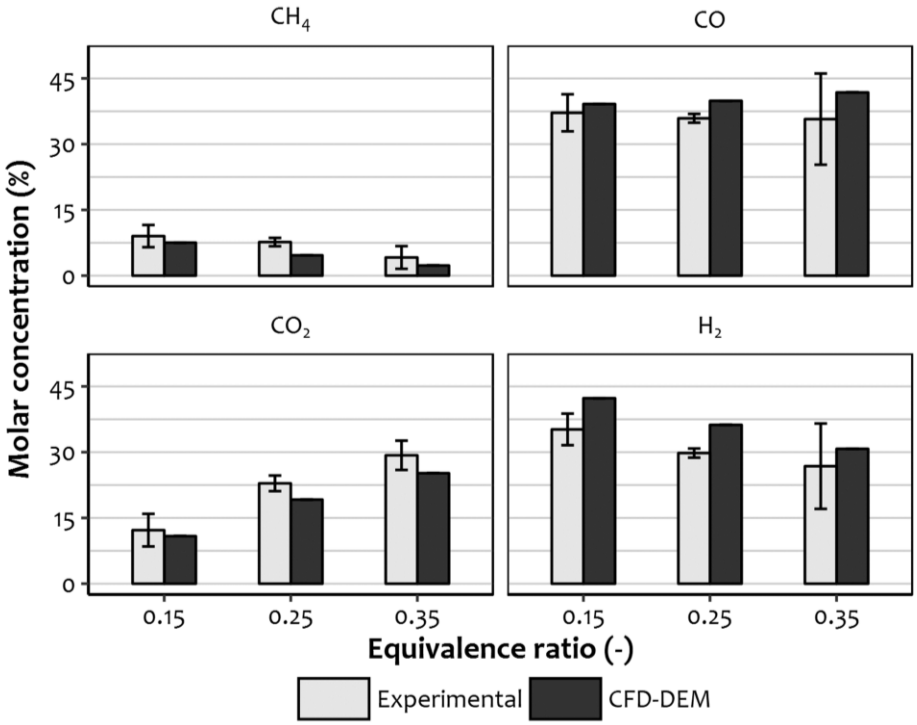

Figure 6.8. Comparison between the predicted and experiment concentration of H_2, CO, CO_2, and CH_4 as affected by equivalence ratio. Error bar indicates 95% confidence interval.

Effects of temperature and ER on NH_3 and HCN

NH_3 and HCN concentrations in producer gas are typically in the ppm range. This minute concentrations however can lead to air pollution and severe catalyst deactivation and are highly damaging to some post-gasification process. For instance, Fisher-Tropsch synthesis requires that the level of nitrogen-containing contaminant be less than 1 ppm for efficient operation.[41] It is therefore important to develop useful tools such as CFD-DEM simulations to predict and understand, and possibly prevent, the yield of NH_3 are HCN, being the two most abundant nitrogen-containing contaminants.

Our simulation shows that NH_3 concentration is reduced when gasification temperature or ER was augmented ((Figure 6.9 and Figure 6.10, respectively). The temperature associated NH_3 destruction was ascribed to the decomposition of NH_3 to N_2 and H_2. This is in consonant with the work of Makepeace et al.[42] However, the reduction in NH_3 concentration with increasing ER was ascribed mainly to dilution effect because the total yield of the major gas composition of producer gas substantially increased with increasing ER. The predicted NH_3 concentration was close the upper 95% confidence bound. The CFD-DEM simulation yielded reasonable predictions. At the lowest temperature and ER considered in this study, the predicted NH_3 values were within the 95% confidence interval of experimental data. On an average, the simulated NH_3 concentrations are within 92.50 ppm of the experimental data. Table 6.5 reveals that the CFD-DEM simulation was able to predict NH_3 concentration as a function of ER better than NH_3 as a function of temperature.

Figure 6.9 shows a clear trend of decreasing HCN concentration with increasing temperature. However, Abdoulmoumine, et al. [35] experimentally demonstrated that the average HCN initially increased as temperature was raised from 1063.15 to 1207.15 K before the average HCN concentrated decreased as temperature was further raised to 1351.15 K. Regardless of the gasification temperature and equivalence ratio, our CFD-DEM simulation underpredicted HCN concentration (Figure 6.9 and Figure 6.10). There are two possible explanation for this observation. The first possibility is that the mechanism and kinetic information adopted for describing the evolution of biomass-nitrogen does not sufficiently capture HCN formation. Studies have shown that substantial quantities of HCN are formed at the pyrolysis stage.[29] However, there are no available kinetic information to describe this process. The second, and not mutually exclusive, possibility is that the experimental measurement may be flawed, as commonly observed in experimental measurement of HCN.[43]

The originality of this work lies in the fact that it is a pilot study into the development of a CFD-DEM model to predict NH_3 and HCN during gasification. The model configuration and data presented gives engineers and scientists in this area of study a valuable understanding needed to envisage necessary gas clean up approach as

well as optimum operating conditions for reducing nitrogen-containing contaminant to tolerable limits. Furthermore, the observations in this study highlight that importance of developing robust mathematical models to describe the mechanism for biomass nitrogen evolution during gasification. Such model needs to properly consider the nature of biomass-nitrogen and track its evolution. Since this current study has only examined specific kinetic parameter values for biomass-nitrogen evolution. It is recommended that sensitivity analysis should be carried out using wide-range kinetic parameter values and experimental data to establish a suitable set of kinetic parameter values for describing biomass-nitrogen evolution without carrying out expensive and laborious experimental studies.

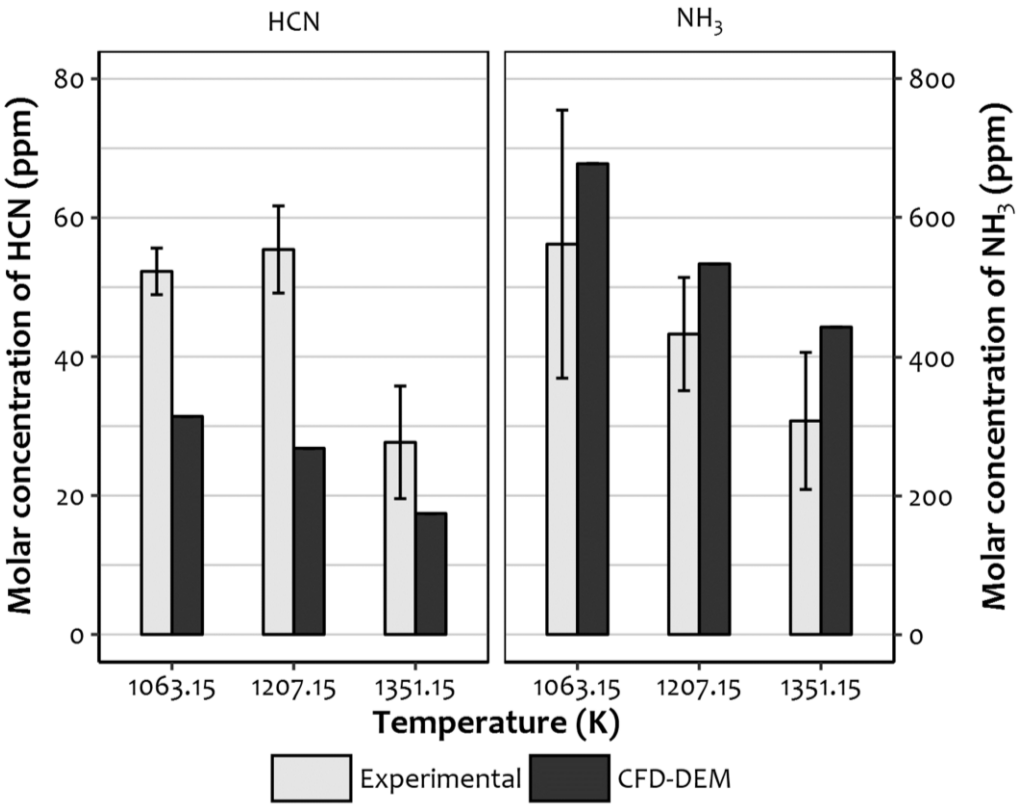

Figure 6.9. Comparison between the predicted and experiment concentration of NH_3 and HCN as affected by gasification temperature. Error bar indicates 95% confidence interval.

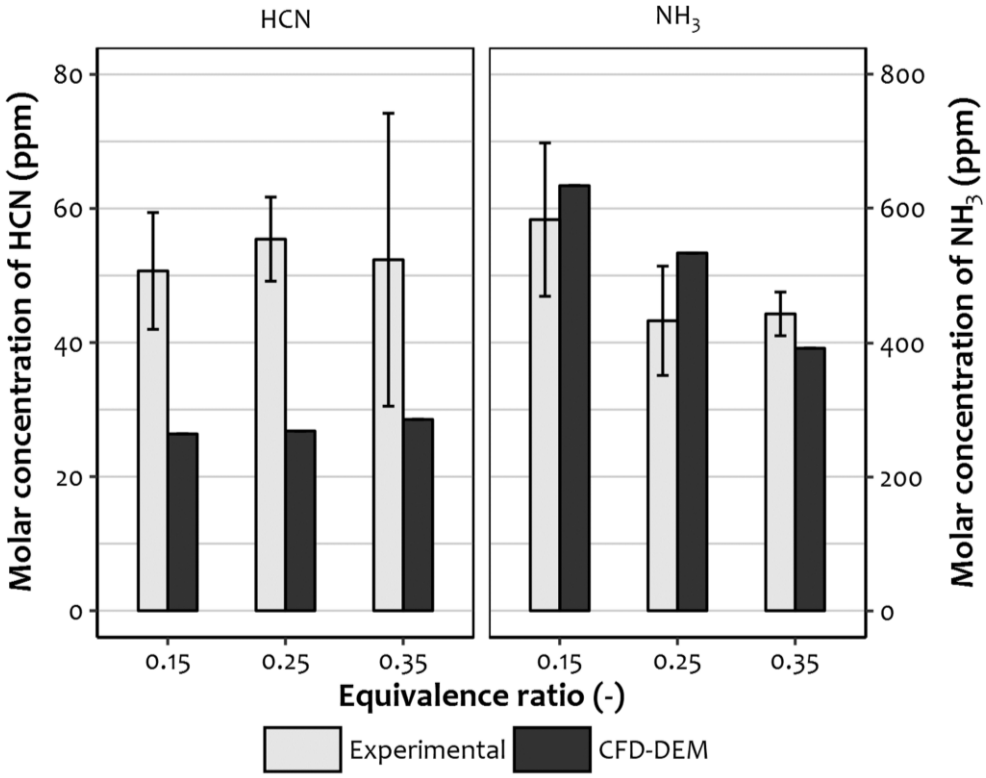

Figure 6.10. Comparison between the predicted and experiment concentration of NH_3 and HCN as affected by equivalence ratio. Error bar indicates 95% confidence interval.

Conclusions

In this study, we developed a CFD-DEM model to simulate biomass gasification and predict the concentration of the gas compositions of producer gas as well as nitrogen-containing contaminants (NH_3 and HCN). The developed CFD-DEM model provides valuable physical, thermal, and chemical flow pattern inside the reactor. We were able to track the position and chemical composition of each biomass particle through its residence inside the reactor and compare the predict gas species to experimental data qualitatively and quantitatively. The predicted concentrations of H_2, CH_4, CO, and CO_2 were good-quality fit to corresponding experimental data obtained from literature. The predicted NH_3 concentration with mean absolute error of 92.50 ppm provides a reasonable comparison to experimental data, especially the experimental upper confidence bound (95%). The predicted HCN concentration was about 30 - 50% lower than corresponding experimental data. An important issue for future research is the implementation of wide-range of kinetic parameters to

predict nitrogen-containing contaminants and establish a suitable set of kinetic information to account for the large deviation in the predicted data for HCN.

Nomenclature

A	Pre-exponential term (s^{-1})
A_i	Pre-exponential term of chemical species i (s^{-1})
A_p	Surface area of particle (m^2)
C_d	Drag coefficient (-)
C_p	Specific heat capacity of particle (J kg^{-1} K^{-1})
d_p	Diameter of particle (s)
E	Enthalpy (J)
E_a	Activation energy (J/mol)
$E_{a,i}$	Activation energy of chemical species i (J/mol)
e_p	Particle emissivity (-)
$\mathbf{F}_g$	Fluid force on particle (N)
$\mathbf{F}_p$	Inter-particle collision force (N)
$\mathbf{F}_{p,n}$	Normal particle contact force (N)
$\mathbf{F}_{p,t}$	Tangential particle contact force (N)
G	Incident radiation (kg s^{-1})
$\mathbf{g}$	Acceleration due to gravity (m s^{-2})
h	Convective heat transfer coefficient (W m^{-2} K^{-1})
h_s	Enthalpy of gas phase (J kg^{-1})
I	Moment of inertia (kg m^2)
k_g	Thermal conductivity (W m^{-1} K^{-1})
$\mathbf{n}$	Unit vector in the direction of the line between two particles (-)
N_C	Nitrogen content of particle at time t (-)
Nu_p	Nusselt number (-)
M_{char}	Mass of particle fixed carbon (kg)
$M_{moisture}$	Mass of particle moisture (kg)
M_p	Total mass of particle (kg)
$M_{volatile}$	Mass of particle volatile (kg)
Q_{char}	Heat transfer due to pyrolysis and heterogenous reactions (W)
$Q_{moisture}$	Heat transfer due to drying (W)
p	Pressure (Pa)
Pr	Prandtl number (-)
Re_p	Particle Reynolds number (-)
$r_{diff,i}$	Rate of diffusion of chemical species i (mol s^{-1})
$r_{kin,i}$	Rate of reaction of chemical species i (mol s^{-1})
S_h	Enthalpy source due to homogenous reactions (W m^{-3})
$S_{p,h}$	Enthalpy source due to drying, heterogenous and pyrolysis reactions (W m^{-3})
S_m	Momentum source term (N m^{-3})

S_{rad}	Enthalpy source due to radiation (W m^{-3})
S_{p,y_i}	Chemical species source due to drying, pyrolysis, and heterogenous reactions (kg m^{-3} s^{-1})
S_{y_i}	Chemical species source due to homogenous reactions (kg m^{-3} s^{-1})
S_ρ	Mass source term (kg m^{-3} s^{-1})
$\mathbf{T}$	Torque on particle (N m)
T_p	Temperature of particle (K)
T_g	Temperature of gas phase (K)
t	Time (s)
$\mathbf{U}_g$	Velocity of gas phase (m/s)
$\mathbf{U}_n$	Normal velocity of particle (m s^{-1})
$\mathbf{U}_p$	Velocity of particle (m/s)
$\mathbf{U}_t$	Tangential velocity of particle (m s^{-1})
$\mathbf{U}_r$	Relative velocity between particles (m s^{-1})
V_p	Particle volume (m^3)
VM	Volatile matter content at time t (-)
VM_∞	Initial volatile matter content (-)
ω	Angular velocity (rad/s)
β	Coefficient of interphase momentum exchange (kg m^{-3} s^{-1}))
ε_p	Particle fraction (-)
ε_g	Gas phase fraction (-)
ρ_g	Particle density (kg m^{-3})
ρ_i	Density of chemical species i (kg m^{-3})
μ_g	Gas phase viscosity (kg m^{-1} s^{-1})
k	Stiffness coefficient (N m^{-1})
η	Damping coefficient (kg s^{-1})
μ_f	Friction coefficient (-)
$\boldsymbol{\tau}$	Effective stress tensor (Pa)
α_{eff}	Effective thermal diffusivity (kg m^{-1} s^{-1})
σ	Stefan-Boltzmann constant (W m^{-2} K^{-4})

Acknowledgement

This research was supported by Southeastern Sun Grant Center and the US Department of Transportation, Research and Innovative Technology Administration, Grant No. DTO559-07-G-00050.

References

1. Liu, Q.; Chmely, S. C.; Abdoulmoumine, N., Biomass treatment strategies for thermochemical conversion. *Energy & Fuels* **2017,** *31* (4), 3525-3536.
2. Leijenhorst, E. J.; Wolters, W.; van de Beld, L.; Prins, W., Inorganic element transfer from biomass to fast pyrolysis oil: Review and experiments. *Fuel Processing Technology* **2016,** *149*, 96-111.
3. Zhou, J.; Masutani, S. M.; Ishimura, D. M.; Turn, S. Q.; Kinoshita, C. M., Release of Fuel-Bound Nitrogen during Biomass Gasification. *Industrial & Engineering Chemistry Research* **2000,** *39* (3), 626-634.
4. Wilk, V.; Hofbauer, H., Conversion of fuel nitrogen in a dual fluidized bed steam gasifier. *Fuel* **2013,** *106* (0), 793-801.
5. Adhikari, S.; Abdoulmoumine, N.; Nam, H.; Oyedeji, O., Biomass gasification producer gas cleanup. In *Bioenergy Systems for the Future : Prospects for Biofuels and Biohydrogen*, 1st ed.; Dalena, F.; Basile, A.; Rossi, C., Eds. Elsevier Ltd.: Cambridge, United States, 2017; pp 514-555.
6. Cui, H.; Turn, S. Q.; Keffer, V.; Evans, D.; Tran, T.; Foley, M., Contaminant Estimates and Removal in Product Gas from Biomass Steam Gasification. *Energy & Fuels* **2010,** *24* (2), 1222-1233.
7. Pepiot, P.; Dibble, C. J.; Foust, T. D., Computational fluid dynamics modeling of biomass gasification and pyrolysis. In *Computational Modeling in Lignocellulosic Biofuel Production*, 1st ed.; American Chemical Society: 2010; Vol. 1052, pp 273-298.
8. Tu, J.; Yeoh, G. H.; Liu, C., *Computational Fluid Dynamics: A Practical Approach*. 2nd ed.; Butterworth-Heinemann: Oxford, United Kingdom, 2013.
9. Su, X.; Jin, H.; Guo, S.; Guo, L., Numerical study on biomass model compound gasification in a supercritical water fluidized bed reactor. *Chemical Engineering Science* **2015,** *134* (1), 737-745.
10. Benyahia, S.; Arastoopour, H.; Knowlton, T.; Massah, H., Simulation of particles and gas flow behavior in the riser section of a circulating fluidized bed using the kinetic theory approach for the particulate phase. *Powder Technology* **2000,** *112* (1), 24-33.
11. Liu, H.; Elkamel, A.; Lohi, A.; Biglari, M., Computational fluid dynamics modeling of biomass gasification in circulating fluidized-bed reactor using the Eulerian–Eulerian approach. *Ind. Eng. Chem. Res.* **2013,** *52* (51), 18162-18174.
12. Kozic, S. R.; Puharic, M.; Katavic, B. In *Comparison Of Euler-Euler And Euler-Lagrange Approach In Numerical Simulation Of Multiphase Flow In Ventilation Mill-Air Mixing Duct*, 2011 Congress on Theoretical and Applied Mechanics, Vlasina lake, Serbia, Vlasina lake, Serbia, 2011.
13. Reddy, R. K.; Joshi, J. B., CFD modeling of solid–liquid fluidized beds of mono and binary particle mixtures. *Chemical Engineering Science* **2009,** *64* (16), 3641-3658.
14. Zhang, Y.; Lei, F.; Xiao, Y., Computational fluid dynamics simulation and parametric study of coal gasification in a circulating fluidized bed reactor. *Asia-Pac. J. Chem. Eng.* **2015,** *10* (2), 307-317.

15. Chen, G.; Xiong, Q.; Morris, P. J.; Paterson, E. G.; Sergeev, A.; Wang, Y., OpenFOAM for computational fluid dynamics. *Not. AMS* **2014,** *61* (4), 354-363.
16. OpenFOAM, *The Open Source CFD Toolbox*. 2014; Vol. 2.3.1.
17. Oevermann, M.; Gerber, S.; Behrendt, F., Euler–Lagrange/DEM simulation of wood gasification in a bubbling fluidized bed reactor. *Particuology* **2009,** *7* (4), 307-316.
18. Ku, X.; Li, T.; Løvås, T., CFD–DEM simulation of biomass gasification with steam in a fluidized bed reactor. *Chemical Engineering Science* **2015,** *122*, 270-283.
19. Ku, X.; Li, T.; Løvås, T., Eulerian–lagrangian simulation of biomass gasification behavior in a high-temperature entrained-flow reactor. *Energy Fuels* **2014,** *28* (8), 5184-5196.
20. Xiong, Q.; Aramideh, S.; Passalacqua, A.; Kong, S.-C., BIOTC: an open-source CFD code for simulating biomass fast pyrolysis. *Computer Physics Communications* **2014,** *185* (6), 1739-1746.
21. Xiong, Q.; Kong, S.-C., Modeling effects of interphase transport coefficients on biomass pyrolysis in fluidized beds. *Powder Technology* **2014,** *262*, 96-105.
22. Broer, K. M.; Woolcock, P. J.; Johnston, P. A.; Brown, R. C., Steam/oxygen gasification system for the production of clean syngas from switchgrass. *Fuel* **2015,** *140*, 282-292.
23. Basu, P., *Biomass Gasification and Pyrolysis*. 1st ed.; Elsevier: Oxford, England, 2010.
24. Tsuji, Y.; Tanaka, T.; Ishida, T., Lagrangian numerical simulation of plug flow of cohesionless particles in a horizontal pipe. *Powder technology* **1992,** *71* (3), 239-250.
25. Gidaspow, D., *Multiphase flow and fluidization: continuum and kinetic theory descriptions*. Academic press: 1994.
26. Ergun, S., Fluid flow through packed columns. *Chem. Eng. Prog.* **1952,** *48*, 89-94.
27. Wen, C.; Yu, Y., A generalized method for predicting the minimum fluidization velocity. *AIChE Journal* **1966,** *12* (3), 610-612.
28. Kawaguchi, T.; Tanaka, T.; Tsuji, Y., Numerical simulation of two-dimensional fluidized beds using the discrete element method (comparison between the two-and three-dimensional models). *Powder technology* **1998,** *96* (2), 129-138.
29. Lee, S.-B.; Fasina, O., TG-FTIR analysis of switchgrass pyrolysis. *Journal of analytical and applied pyrolysis* **2009,** *86* (1), 39-43.
30. Oyedeji, O.; Daw, C. S.; Labbe, N.; Ayers, P.; Abdoulmoumine, N., Kinetics of the release of elemental precursors of syngas and syngas contaminants during devolatilization of switchgrass. *Bioresource Technology* **2017,** *244*, 525-533.
31. Abani, N.; Ghoniem, A. F., Large eddy simulations of coal gasification in an entrained flow gasifier. *Fuel* **2013,** *104*, 664-680.
32. Mitchell, J. W.; Tarbell, J., A kinetic model of nitric oxide formation during pulverized coal combustion. *AIChE journal* **1982,** *28* (2), 302-311.

33. Liu, H.; Gibbs, B. M., Modeling NH3 and HCN emissions from biomass circulating fluidized bed gasifiers. *Fuel* **2003,** *82* (13), 1591-1604.
34. Bruchmüller, J.; van Wachem, B.; Gu, S.; Luo, K.; Brown, R., Modeling the thermochemical degradation of biomass inside a fast pyrolysis fluidized bed reactor. *AIChE Journal* **2012,** *58* (10), 3030-3042.
35. Abdoulmoumine, N.; Kulkarni, A.; Adhikari, S., Effects of Temperature and Equivalence Ratio on Pine Syngas Primary Gases and Contaminants in a Bench-Scale Fluidized Bed Gasifier. *Ind. Eng. Chem. Res.* **2014,** *53* (14), 5767-5777.
36. Wang, J.; Ren, C.; Yang, Y.; Hou, L., Characterization of particle fluidization pattern in a gas solid fluidized bed based on acoustic emission (AE) measurement. *Ind. Eng. Chem. Res.* **2009,** *48* (18), 8508-8514.
37. Mokheimer, E. M. A.; Ibrar Hussain, M.; Ahmed, S.; Habib, M. A.; Al-Qutub, A. A., On the Modeling of Steam Methane Reforming. *Journal of Energy Resources Technology* **2014,** *137* (1), 012001-012001-11.
38. Tao, J.; Dong, C.; Lu, Q.; Liao, H.; Du, X.; Yang, Y.; Dahlquist, E., Catalytic cracking of biomass high-temperature pyrolysis tar using NiO/AC catalysts. *International journal of green energy* **2015,** *12* (8), 773-779.
39. Aljbour, S. H.; Kawamoto, K., Bench-scale gasification of cedar wood – Part I: Effect of operational conditions on product gas characteristics. *Chemosphere* **2013,** *90* (4), 1495-1500.
40. Kulkarni, A.; Baker, R.; Abdoulmomine, N.; Adhikari, S.; Bhavnani, S., Experimental study of torrefied pine as a gasification fuel using a bubbling fluidized bed gasifier. *Renewable Energy* **2016,** *93*, 460-468.
41. Abdoulmoumine, N.; Adhikari, S.; Kulkarni, A.; Chattanathan, S., A review on biomass gasification syngas cleanup. *Appl Energ* **2015,** *155* (1), 294-307.
42. Makepeace, J. W.; Wood, T. J.; Hunter, H. M.; Jones, M. O.; David, W. I., Ammonia decomposition catalysis using non-stoichiometric lithium imide. *Chemical science* **2015,** *6* (7), 3805-3815.
43. Broer, K. M.; Johnston, P. A.; Haag, A.; Brown, R. C., Resolving inconsistencies in measurements of hydrogen cyanide in syngas. *Fuel* **2015,** *140*, 97-101.

CHAPTER VII
MULTISCALE SIMULATION OF THE FORMATION OF LIGNOCELLULOSIC BIOMASS INORGANIC SYNGAS CONTAMINANTS IN A BUBBLING FLUIDIZED BED REACTOR. PART II: SULFUR CONTAMINANTS

This chapter is a draft version of the second part of a two-part series. The relevant paper is listed below:

Oyedeji, O. A., Daw, C. S., Labbé, N., Ayers, P, D., and Abdoulmoumine, N. H. (draft). Multiscale simulation of the formation of lignocellulosic biomass inorganic syngas contaminants in a bubbling fluidized bed reactor. Part ii: sulfur contaminants. Sustainable Chemistry & Engineering.

Abstract

In this study, we presented a computational fluid dynamics and discrete element method (CFD-DEM) model of biomass gasification in a fluidized bed to evaluate the yields of H_2S, COS, and SO_2. The developed model was used to investigate the effects of gasification temperature and equivalence ratio on the yields H_2S, COS, and SO_2. The gas flow was obtained by solving Navier–Stokes equations coupled with standard k–ε turbulence model and the particle flow was obtained by solving Newton's equations of motion. The CFD-DEM model also accounted for particle collisions and shrinkage; pyrolysis, heterogeneous, and homogeneous reactions; and heat transfers. Experimental validation showed that the CFD-DEM prediction of H_2S concentrations closely match the experimental data, with mean absolute error of about 9.1 ppmV. The production of H_2S was higher at higher temperatures and lower ER whereas the concentration of SO_2 was higher at lower temperatures and higher ER. COS formation was favored by higher temperature and ER. Additionally, the analysis of particle entrainment showed that particle residence time was reduced when temperature and ER were increased.

Keywords: H_2S and COS, CFD-DEM, Eulerian-Lagrangian, particle collision, multi-phase flow

Introduction

Biomass feedstocks contain low but consequential amounts of elemental sulfur (<0.1 %wt.) that can make its way into biomass-derived producer gas during gasification.[1] H_2S and COS are the most common sulfur species found in biomass-derived producer gas, with H_2S being the most prominent and most deleterious. Biomass-derived producer gas can contain about 20 - 320 ppmv H_2S and <2 - 50 ppm COS.[2-3] Even in parts per million concentrations, sulfur species in biomass-derived producer gas present severe downstream-related problems ranging from emission of regulated environmental pollutants, operational safety concerns and, catalyst poisoning, to equipment corrosion and failure.[4] Efficient sulfur abatement strategies are therefore unavoidable for the successful commercial deployment of biomass gasification technologies to meet stringent standards for emission and avoid troublesome downstream operation.

Several in-situ and ex-situ strategies have been suggested and/or deployed for reducing the concentration of sulfur species in biomass-derived producer gas to

levels tolerable for downstream operation. These strategies use one or a combination of wet scrubbing, physical absorption, and chemical absorption to desulfurize biomass-derived producer gas.[4-5] However, studies have shown that current strategies are either expensive, inefficient, ineffective, unadaptable, or require additional treatment process for resulting waste water stream. To improve producer gas desulfurization strategies and effectively plan for ex-situ producer gas cleanup, considerable amount of data on the concentration of sulfur species in biomass-derived producer gas is required. This is because several gasification process variables can influence the quantity of sulfur species in producer gas. These factors include gasification temperature, pressure, equivalence ratio, gasifying agent, and biomass properties.

Most experimental studies do not sufficiently evaluate the formation of sulfur species in producer gas because they are considered as peripheral species and their measurement are laborious and expensive.[3, 6] Hence, comprehensive experimental data on sulfur contaminant yield during gasification is scarce. Computational fluid dynamics and discrete element method (CFD-DEM) simulation of biomass gasification is increasingly becoming an essential element of biomass gasification research because it offers in-depth information of the process variables (temperature, pressure, gas species concentration, velocity, and particle properties) throughout the gasifier in a cost-effective and fast manner.[6] The information obtained from CFD-DEM simulation as well as the area-average concentration at the outlet of the gasifier is useful to engineers and researchers in developing efficient and cost-effective desulfurization strategy for biomass-derived producer gas.

The objective of this study, the second of a two-part series, was to construct a CFD-DEM model of biomass gasification capable of predicting three major sulfur species commonly found in biomass-derived producer gas (H_2S, COS, and SO_2). The simulations result will be compared to experimental data to determine the accuracy of the CFD-DEM prediction. The constructed CFD-DEM model can be used to provide a realistic and reliable understanding of the formation of sulfur species in biomass-derived producer gas in fluidized bed reactor.

Mathematical models

The multi-phase flow simulated in this study consists of gas phase and solid phase (biomass and bed material). The developed CFD-DEM model described the gas flow as an interpenetrating continuum and the particle flow as discrete elements. Navier-Stokes equations and Newton's second equation of motion were solved to obtain the gas and particle flow characteristics, respectively. The bed material used was sand and was modeled as inert particles, which was not allowed to undergo physical and chemical changes. The biomass particles were however modeled as reactive particles and were allowed to undergo physical and chemical changes such as drying, devolatilization reactions, gasification reactions, and shrinkage. The

mathematical models used to describe the gas and particle motion, particle shrinkage, particle heat transfer, and pyrolysis reaction are extensively presented in Chapter 6 and are briefly summarized in the next few sections for continuity and reference. Necessary model addition to describe the formation of sulfur contaminants are also provided.

Particle mass and momentum models

The change in the mass of the biomass particles during gasification was assumed to be the linear combination of changes due to drying ($dM_{moisture}$), pyrolysis ($dM_{volatile}$), and char gasification (dM_{char}). Therefore, the rate of mass change was calculated as given in Equation (7.1). After mass change has been implemented, Equation (7.2) was used to calculate the current particle diameter. The instantaneous linear and angular accelerations of particles were calculated as equations (7.3) and (7.4) respectively. The momentum exchange between the gas and particle flow was model using Gidaspow drag model for solid spheres.[7] Particle-particle and particle-wall collisions were computed using Hertz-Mindlin particle contact model (see Figure 6.1 in Chapter 6). Heat transfer through the particle accounts for conduction, convection, and radiation and was modeled using Equation (7.9).

$$\frac{dM_p}{dt} = \frac{dM_{moisture}}{dt} + \frac{dM_{volatile}}{dt} + \frac{dM_{char}}{dt} \tag{7.1}$$

$$d_p = \sqrt[3]{\frac{6M_p}{\pi\rho_p}} \tag{7.2}$$

$$\frac{d\mathbf{U}_p}{dt} = \frac{\mathbf{F}_g}{M_p} + \frac{\mathbf{F_p}}{M_p} + \mathbf{g} \tag{7.3}$$

$$\frac{d\omega}{dt} = \frac{\mathbf{T}}{I} \tag{7.4}$$

$$F_g = \frac{\beta V_p}{\varepsilon_p}\left(U_g - U_p\right) \tag{7.5}$$

$$\beta = \begin{cases} 150\frac{\varepsilon_p^2\mu_g}{\varepsilon_g^2 d_g^2} + 1.75\frac{\varepsilon_p\rho_g}{\varepsilon_g d_p}\left|\mathbf{U}_g - \mathbf{U}_p\right| & \varepsilon_g < 0.8 \\ 0.75C_d\frac{\varepsilon_p\rho_g}{d_p}\left|\mathbf{U}_g - \mathbf{U}_p\right|\varepsilon_g^{-2.65} & \varepsilon_g \geq 0.8 \end{cases} \tag{7.6}$$

$$C_d = \begin{cases} \frac{24}{Re_p}\left(1 + 0.15Re_p^{0.687}\right) & < 1000 \\ 0.44 & Re_p \geq 1000 \end{cases} \tag{7.7}$$

$$\mathrm{Re_p} = \frac{\varepsilon_g \rho_g d_p \left|\mathbf{U_g} - \mathbf{U_p}\right|}{\mu_g} \tag{7.8}$$

$$M_p C_p \frac{dT_p}{dt} = hA_p\left(T_g - T_p\right) + \frac{e_p A_p}{4}\left(G - 4\sigma T_p^4\right) + Q_{moisture} + Q_{char} \tag{7.9}$$

$$h = \frac{6 \propto_p k_g Nu_p}{d_p^2} \tag{7.10}$$

$$Nu_p = 2 + 0.6 Re_p^{0.5} Pr^{0.33} \tag{7.11}$$

$$Pr = \frac{C_{pg}\mu_g}{k_g} \tag{7.12}$$

Gas phase transport equations

Gas flow behavior was described using continuity and Navier-Stokes equations coupled with porosity term, k-ε turbulence model, effective dynamic thermal diffusivity (Equations (7.13) – (7.17)).

$$\frac{\delta}{\delta t}\left(\varepsilon_g \rho_g\right) + \nabla \cdot \left(\varepsilon_g \rho_g \mathbf{U_g}\right) = S_\rho \tag{7.13}$$

$$\frac{\delta}{\delta t}\left(\varepsilon_g \rho_g \mathbf{U_g}\right) + \nabla \cdot \left(\varepsilon_g \rho_g \mathbf{U_g U_g}\right) = -\nabla p + \nabla \cdot \left(\varepsilon_g \boldsymbol{\tau}\right) + \varepsilon_g \rho_g \mathbf{g} + S_m \tag{7.14}$$

$$E = h_s - \frac{p}{\rho_g} + \frac{\mathbf{U_g^2}}{2} \tag{7.15}$$

$$\frac{\delta}{\delta t}\left(\varepsilon_g \rho_g E\right) + \nabla \cdot \left(\varepsilon_g \mathbf{U_g}(\rho_g E + p)\right) = \nabla \cdot \left(\varepsilon_g \alpha_{eff} \nabla h_s\right) + S_h + S_{p,h} + S_{rad} \tag{7.16}$$

$$\frac{\delta}{\delta t}\left(\varepsilon_g \rho_g Y_i\right) + \nabla \cdot \left(\varepsilon_g \rho_g \mathbf{U_g} Y_i\right) = \nabla \cdot \left(\varepsilon_g \rho_g D_{eff} \nabla Y_i\right) + S_{p,Y_i} + S_{Y_i} \tag{7.17}$$

Chemical reaction models

The overall mechanism used in this present study is shown in Figure 7.1. It is similar to the chemical mechanism in Chapter 6 and used to describe the formation of the major producer gas species and sulfur contaminants during biomass gasification following the assumptions listed below:

1. Biomass is made up of three major fractions, namely moisture, volatile matter, and solid matter.
2. Moisture is released as H_2O via drying into the gas phase.
3. The volatile matter fraction is decomposed to form CO, CO_2, H_2, H_2O, and CH_4 during pyrolysis.
4. The solid matter has carbon, sulfur, and ash components.
5. The ash component of the solid fraction is inert, hence does not leave the particle.
6. The carbon component of the solid fraction reacts with gas phase chemical species to form additional CO, CO_2, and CH_4.
7. The sulfur component of the solid fraction is release as H_2S (Reaction [7.5]).

In the gas phase, H_2S may undergo two major reactions are shown in Figure 7.1. H_2S can react with CO_2 to form COS and H_2O (Reaction [7.11]) or O_2 to form SO_2 and H_2O (Reaction [7.12]). Details of the kinetic models used to describe the chemical reactions highlighted in Figure 7.1 including the kinetics information for the conversion of biomass sulfur to H_2S and H_2S to COS and SO_2 are listed in Table 7.1.

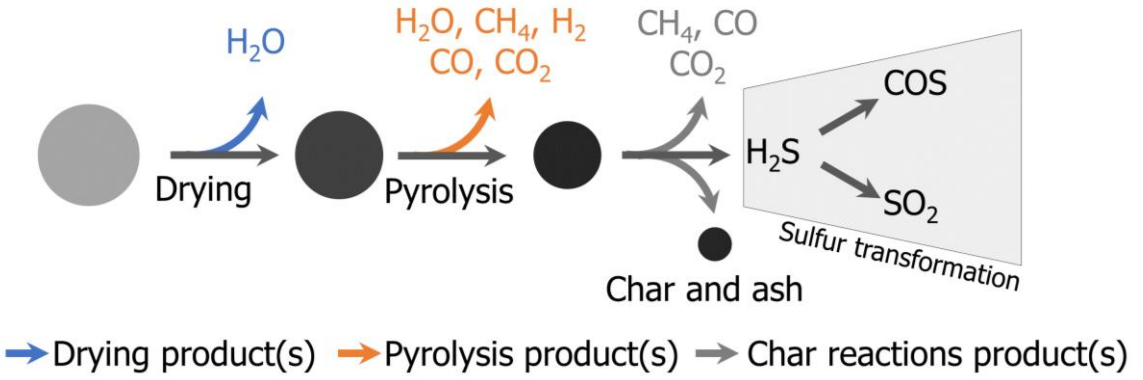

Figure 7.1. Chemical reaction mechanism leading to the formation producer gas and sulfur contaminant species.

Table 7.1. Kinetic information for sulfur contaminant formation

Stoichiometry	Reaction rate	No.
$C_{(S)} + H_2O \rightarrow CO + H_2$	$A_1 = 2.00 \times 10^{-3};\ E_{a,1} = 1.96 \times 10^{8}$	[7.1] [8]
$C_{(S)} + CO_2 \rightarrow 2CO$	$A_2 = 3.00 \times 10^{-1};\ E_{a,2} = 2.00 \times 10^{8}$	[7.2] [8]
$C_{(S)} + O_2 \rightarrow CO_2$	$A_3 = 2.51 \times 10^{-3};\ E_{a,3} = 7.48 \times 10^{7}$	[7.3] [8]
$2C_{(S)} + 2H_2 \rightarrow 2CH_4$	$A_4 = 1.18 \times 10^{-5};\ E_{a,4} = 1.48 \times 10^{8}$	[7.4] [9]
$S_{(S)} \rightarrow H_2S$	$A_N = 8.0 \times 10^{9};\ E_{a,S} = 1.81 \times 10^{4}$	[7.5] [10]
$CH_4 + 2O_2 \rightarrow CO_2 + 2H_2O$	$5.16 \times 10^{13}\ T^{-1} \exp\left(\frac{-1.56 \times 10^{4}}{T}\right)$	[7.6] [8]
$CH_4 + H_2O \rightarrow CO + 3H_2$	$7.00 \times 10^{6} \exp\left(\frac{-1.54 \times 10^{4}}{T}\right)$	[7.7] [8]
$H_2 + 0.5O_2 \rightarrow H_2O$	$2.20 \times 10^{9} \exp\left(\frac{-2.20 \times 10^{9}}{RT}\right)$	[7.8] [8]
$CO + H_2O \rightarrow CO_2 + H_2$	$2.78 \times 10^{3} \exp\left(\frac{-1.52 \times 10^{3}}{T}\right)$	[7.9] [8]
$CO_2 + H_2 \rightarrow CO + H_2O$	$9.59 \times 10^{4} \exp\left(\frac{-5.34 \times 10^{3}}{T}\right)$	[7.10] [8]
$H_2S + CO_2 \rightarrow COS + H_2O$	$2.40 \times 10^{6} \exp\left(\frac{-2.03 \times 10^{6}}{T}\right)$	[7.11] [11]
$2H_2S + 3O_2 \rightarrow 2SO_2 + 2H_2O$	$1.50 \times 10^{10} \exp\left(\frac{-1.56 \times 10^{7}}{T}\right)$	[7.12] [12]

No.: reaction number.

The pyrolysis reaction rate of biomass was calculated using a single step first-order Arrhenius devolatilization reaction (Equation (7.18)).

$$\frac{dM_{volatile}}{dt} = A \exp\left(\frac{-E_a}{RT_p}\right) M_{volatile} \tag{7.18}$$

Finally, the overall conversion rate of solid carbon was assumed to be limited by diffusion rate as expressed in Equation (7.19).[9]

$$\frac{dC_{(s)}}{dt} = \sum_{i=1}^{4} -A_p p_i \frac{r_{diff,i} r_{kin,i}}{r_{diff,i} + r_{kin,i}} \tag{7.19}$$

$$r_{diff,i} = 5.00 \times 10^{-12} \frac{\left(0.5\left(T_p + T_g\right)\right)^{0.75}}{d_p} \tag{7.20}$$

$$r_{kin,i} = A_i \exp\left(\frac{-E_{a,i}}{RT_p}\right) \tag{7.21}$$

Numerical simulation setup

All equations for gas and particle flow were solved in OpenFOAM code (version 2.4.0). The gas phase governing equations were discretized using finite volume method and solved in the order of mass, momentum, chemical species, and energy with the standard pressure based PISO (pressure implicit splitting of operators) solver for variable density flow. Turbulence model solution was implemented within the momentum continuity equation. The gas flow behavior was assumed to be compressible and obey idea gas equation of state. The interphase exchanges were determined using source terms. For instance, the gas phase mass and momentum continuity equations were coupled with Equation (7.1) and Equation (7.5), respectively.

The properties of the biomass feedstock used, and gasification operation variables are listed in Table 7.2. At simulation time = 0.0 s, sand particles were positioned inside the reactor and allowed to fall and settle before biomass particles were injected into the reactor. All mathematical models used in this work were implemented in a quasi-three-dimensional coordinate, in which the thickness of the geometry was set to the initial particle diameter. This approach was implemented mainly to reduce computational cost and has been used by several modelers for biomass gasification[8, 13] Fluidizing gas velocity and chemical composition were set across the bottom of the gasification. Similarly, gasification temperature and biomass feed rate were set at the wall and biomass inlet, respectively. The top of the gasifier was assumed to be open to the atmosphere (pressure = 1 atm).

Table 7.2. Simulation parameters and gasification process variables used in this study.

Parameter	Value
Mesh size (m)	0.0038 × 0.0049 × 0.0005
Fluid time step (s)	1.0×10^{-5}
Simulation end time (s)	20
Reactor temperature (K)	1063.15, 1207.15, 1351.15
Inlet gas velocity (m/s)	0.15
Biomass feed rate (kg/s)	8.33×10^{-5}
Biomass initial temperature (K)	298.15
Biomass specific heat (J/kg-K)	1500
Biomass density (kg/m^3)	600
Biomass shape (-)	sphere
Biomass diameter (m)	8.50×10^{-4}
Sand quantity (kg)	0.20
Sand specific heat (J/kg-K)	860
Sand density (kg/m^3)	2600
Sand shape (-)	sphere
Sand diameter (m)	5.0×10^{-4}
Sand emissivity (-)	1.0

Bounded, first-order Euler scheme were used to solve all time derivative terms and unbounded, second-order Gauss scheme was used to discretize all gradient terms. Each simulation ran till simulation time = 20 s (time step = 1.0×10^{-5} s), which corresponds to actual execution time of approximately 3 weeks using 8 nodes per simulation on a high-performance computing cluster.

Results and discussion

In Chapter 6 of this work, we discussed the CFD-DEM predicted yields for the major producer gas species (CO, CO_2, CH_4, and H_2) as affected by temperature and equivalence ratio. Additionally, we discussed the gas and particle flow characteristics inside the fluidized bed reactor. In this present study, we will discuss particle flow pattern and residence time and study more specially the yield of sulfur contaminants (H_2S, COS, and SO_2).

Particle residence time distribution

Particle residence time was calculated as the amount of time taken by particles to travel through the reactor. Since fluidization is a stochastic process, the particle trajectory is not specific and particle residence time is therefore best defined by probability distribution. Particle residence time distribution (RTD) is a vital fluidized bed characteristic that highly impact gasification performance, especially carbon conversion efficiency and producer gas yield. Nevertheless, RTD measurement in biomass gasification studies are limited because they are protracted and, in some cases, expensive. The prediction of RTD is one of the unique benefits of CFD-DEM simulations and highlights the importance of this work to biomass gasification research.

Figure 7.2 shows the RTD as affected by gasification temperature. The median particle residence time was approximately 10.2, 9.52, and 9.41 s for 1063.15, 1207.15, 1351.15 K gasification temperature, respectively. This clearly demonstrates that the particle residence time decreased as the gasification temperature was raised. This observation correlates with the rate of particle shrinkage. Hence, the decrease in particle residence time with increasing gasification temperature was ascribed to the fact that drying and chemical reaction rates are higher at higher gasification temperature and causes the particle to shrink and attain terminal velocity faster. Similarly, it was observed that higher ER caused the biomass particles to travel through the reactor faster. This was ascribed to increased $C_s + O_2 \rightarrow CO_2$ reaction, which also resulted in increased particle shrinkage.

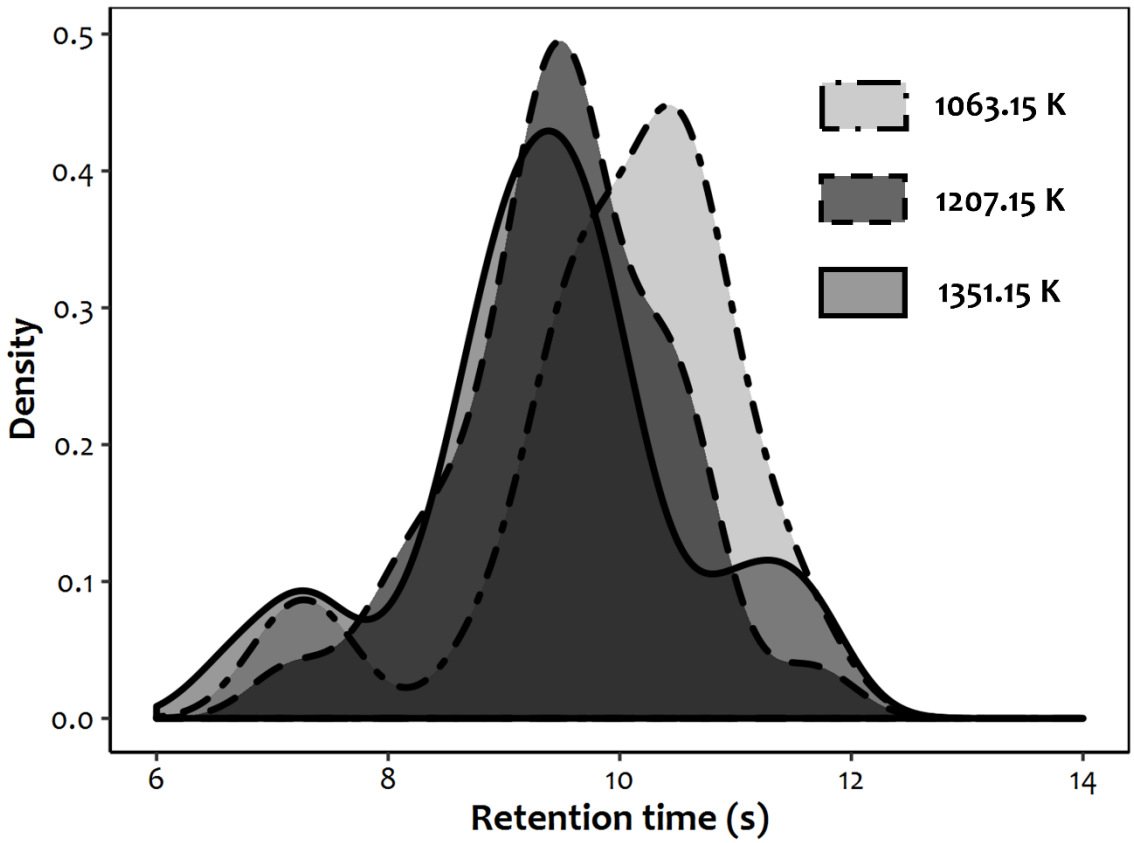

Figure 7.2. Effect of gasification temperature on particle residence time.

Effects of temperature and ER on sulfur contaminants

Three sulfur contaminant species (H_2S, COS, and SO_2) were tracked during the CFD-DEM simulation and thereafter analyzed for yield. Additionally, entrained particles were examined for their sulfur concentration to provide a complete picture of sulfur partitioning during gasification. Figure 7.3 and Figure 7.4 are comparisons of the CFD-DEM predicted yield to experimentally measured concentration data. This comparison of the predicted yield to experimental yield is only shown for H_2S because of experimental data availability. Predicted H_2S yield closely follow the experimental data with mean absolute error of about 9.1 ppmV. This ascertains that the developed CFD-DEM model is reasonably accurate. The developed CFD-DEM model can therefore be relied on to provide a good indication of the expected sulfur contaminants level during biomass gasification, especially for new biomass feedstocks and conceptual gasification technologies.

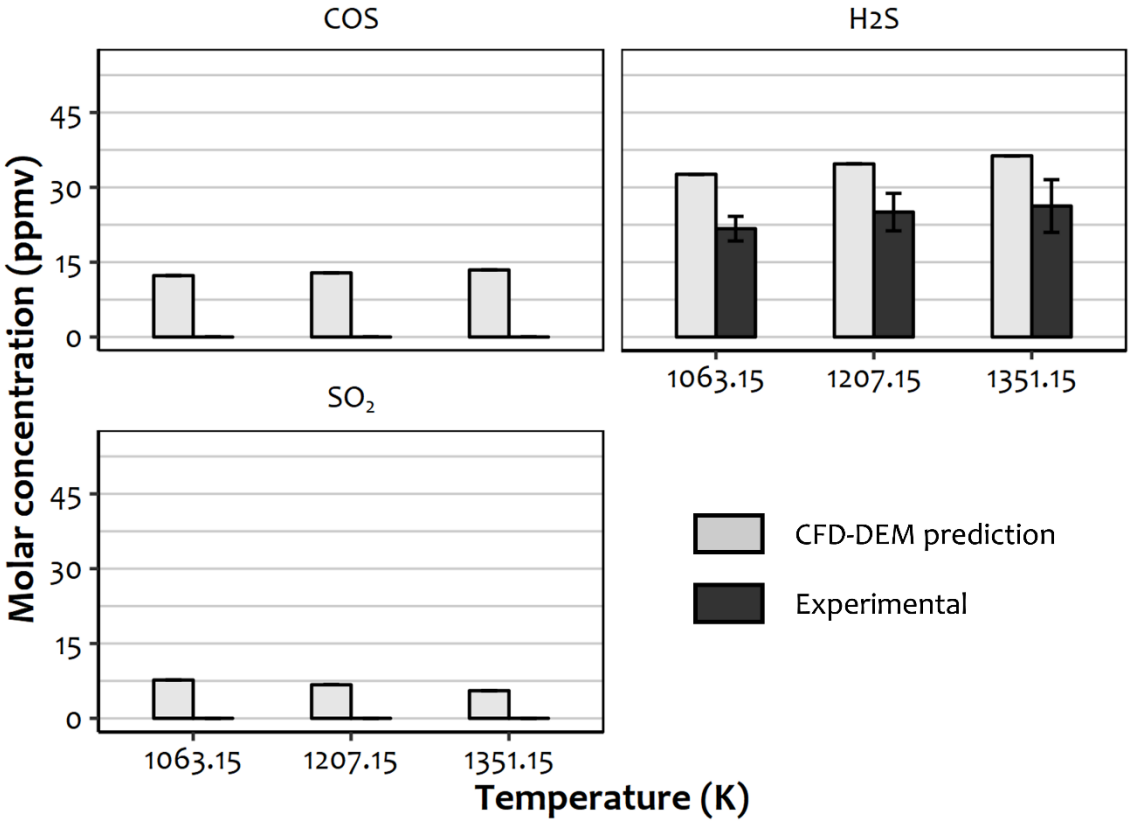

Figure 7.3. Effects of gasification temperature on sulfur contaminant concentrations during biomass gasification.

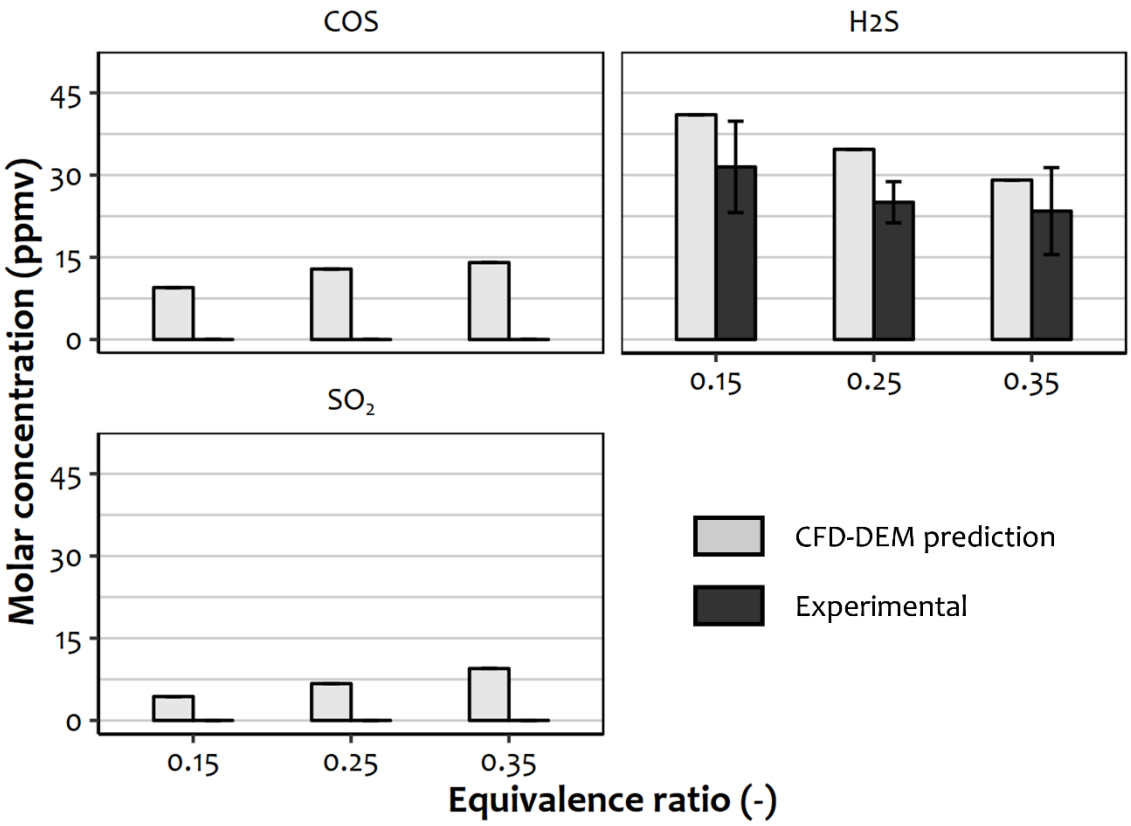

Figure 7.4. Effects of equivalence ratio on sulfur contaminant concentrations during biomass gasification.

Gasification temperature played an impactful role in the partitioning of biomass-sulfur during gasification. It was observed that the extent biomass sulfur conversion increased when gasification temperature was raised (Table 7.3). The implication of this observation is that more sulfur contaminants are released into the gas phase at higher temperature, increasing the severity and cost of producer gas remediation. This trend is in consonant with the finding in our earlier work on the conversion of biomass elements during pyrolysis stage of biomass gasification.[14] However the predicted range of sulfur conversion extent was even lower than the range of sulfur conversion extent for the pyrolysis stage in our previous work. This is because biomass sulfur partitioning to other sulfur-gases are considered in this present work. Furthermore, sulfur conversion during gasification slightly increased with increasing ER. This may be associated with increasing particle entrainment rate at higher ERs.

Table 7.3. Effects of temperature and equivalence ratio on biomass sulfur conversion during gasification.

Temperature (K)	Equivalence ratio (-)	Sulfur conversion extent (%)
1063.15	0.25	27.25
1207.15	0.25	28.01
1351.15	0.25	29.25
1207.15	0.15	28.27
1207.15	0.35	27.25

The partitioning of the released sulfur in the gas phase was also influenced by temperature. Here, we assumed that sulfur released from biomass is partitioned into H_2S, COS, and SO_2 (Figure 7.1). This assumption is reasonable because studies have shown that the concentrations of other sulfur species such as thiophene and methanethiol are usually unstable and/or at ppbV levels.[15-16] Generally, the predicted concentrations of H_2S, COS, and SO_2 increased when temperature was raised. The predicted concentration of H_2S in this study increased from 32.6 to 36.3 ppmV when gasification temperature was raised from 1063.15 to 1351.15 K. Similarly, the predicted concentration COS increased from 12.3 to 14.1 ppmV, respectively, when gasification temperature was raised from 1063.15 to 1351.15 K. The increase seen in the concentration of H_2S was due to the aforementioned increased conversion rate of biomass sulfur at higher gasification temperature. Consequently, the higher concentrations of COS and SO_2 can be attributed the acceleration of $H_2S + CO_2 \rightarrow COS + H_2O$ reaction because of increased H_2S concentration. However, the concentration of SO_2 decreased as the temperature was raised.

The concentrations of H_2S was inversely proportional to the ER. However, the concentration of SO_2 was directly proportional to ER. These observations demonstrate that the increased formation of H_2S (as result increased conversion of biomass sulfur) was lower compared to the consumption of H_2S via oxidation reaction. We found that this observation deviates from the findings of Kulkarni et al. [17], in which the mean concentration of SO_2 decreased (though not statistically significant) with increasing ER. The concentration of COS also increased with increasing ER. This specific trend is consistent with the work of Kulkarni et al.[17] and Salah Aljbour and Kawamoto.[2] and can be explained by the fact that the increasing

ER causes an intermediate increase in H_2S, which is subsequently consumed to form COS and SO_2. Additionally, the concentration of COS is thermodynamically expected to increase when ER is raised, as seen in our earlier work on thermodynamic modeling of biomass gasification (Chapter 4).

CFD-DEM modeling of biomass gasification: challenges and future perspective

This study demonstrates the capability of CFD-DEM model vis-à-vis biomass gasification. However, several challenges remain to be solved to improve the prediction accuracy of CFD-DEM simulation of biomass gasification. In this section, we pinpoint some existing challenges and future opportunities for researchers in this subject area.

Based on literature survey,[8, 13, 18-19] it could be concluded that the state-of-the-art of CFD-DEM modeling studies of biomass gasification assumes that biomass particles are perfect spheres (sphericity = 1). However, studies have shown that particulate biomass is rod- or ribbon-shaped, with sphericity < 1.[20-21] It is therefore essential to appropriately describe biomass shape in CFD-DEM models to obtain more accurate particulate flow behavior. This can be achieved by coupling available discrete element method (DEM) software packages (such as LIGGGHTS and EDEM), which have capability for modeling non-spherical particle geometries), with CFD software packages.

One of the challenges associated with the DEM modeling of biomass flow during gasification is the lack of mathematical models to describe the evolution of biomass particulate properties during biomass gasification. Therefore, CFD-DEM models of biomass gasification generally set several biomass particulate properties (such as specific heat, density, emissivity, young modulus, and Poisson's ratio) to a constant value (typically using the properties of fresh biomass). Consequently, the implementation of experimental studies and development of robust empirical models are needed to facilitate the estimation of accurate biomass properties as a function of time and extent chemical reaction in CFD-DEM models. In addition to changes in biomass particulate properties during gasification, biomass particle collisions with sand particles and reactor wall can attrite and fragment biomass particles. This phenomenon is typically not accounted for in CFD-DEM studies and may play an important role in reducing the deviation of CFD-DEM flow predictions from experimental data.

Published experimental studies on biomass gasification only measure and provide partial data, limiting the potential for thorough validation of existing CFD-DEM models. Hence, there is need for well-designed experimental studies to provide comprehensive data on concentrations of major producer gas composition and contaminants as affected by gasification process variables (temperature, ER, and flowrate) and biomass properties for extensive validation of CFD-DEM model.

Additionally, it is necessary to obtain particle flow data inside a fluidized bed gasifier to validate CFD-DEM predicted hydrodynamics.

Conclusions

A computational fluid dynamics and discrete element method (CFD-DEM) model was constructed to simulate the flow behavior inside a fluidized bed reactor during biomass gasification and predict the yield of major sulfur contaminants. In our analysis, we demonstrated that the predicted yield of hydrogen sulfide during biomass gasification reasonably follows experimental data reported in literature. The concentration of hydrogen sulfide was found to increase with rising temperature and reduce with rising ER. Conversely, the concentration of sulfur dioxide decreased with rising temperature and increased with rising ER. The concentration of carbonyl sulfide increased with rising temperature and ER. Additionally, the proposed model can track the particle properties and flow pattern throughout the simulation domain. Hence, we were able to evaluate the effects of temperature and ER on the particle residence time. It was observed that particle was entrained faster at higher temperature and ER. To our knowledge, this is the first proposed CFD-DEM model for biomass gasification that addresses the production of sulfur contaminants. Therefore, the significance of the proposed model is that it can be used to provide valuable insight to biomass gasification engineers and scientists. In summary, the propose model is a powerful tool for understanding the realistic amounts of sulfur contaminants to expect during biomass gasification, hence de-risking the commercial deployment of biomass gasification from sulfur contaminant standpoint.

Nomenclature

A	Pre-exponential term (s^{-1})
A_i	Pre-exponential term of chemical species i (s^{-1})
A_p	Surface area of particle (m^2)
C_d	Drag coefficient (-)
C_p	Specific heat capacity of particle (J kg^{-1} K^{-1})
d_p	Diameter of particle (s)
E	Enthalpy (J)
E_a	Activation energy (J/mol)
$E_{a,i}$	Activation energy of chemical species i (J/mol)
e_p	Particle emissivity (-)
$\mathbf{F}_g$	Fluid force on particle (N)
$\mathbf{F}_p$	Inter-particle collision force (N)
$\mathbf{F}_{p,n}$	Normal particle contact force (N)
$\mathbf{F}_{p,t}$	Tangential particle contact force (N)
G	Incident radiation (kg s^{-1})
$\mathbf{g}$	Acceleration due to gravity (m s^{-2})
h	Convective heat transfer coefficient (W m^{-2} K^{-1})

h_s	Enthalpy of gas phase (J kg^{-1})
I	Moment of inertia (kg m^2)
k_g	Thermal conductivity (W m^{-1} K^{-1})
$\mathbf{n}$	Unit vector in the direction of the line between two particles (-)
Nu_p	Nusselt number (-)
M_{char}	Mass of particle fixed carbon (kg)
$M_{moisture}$	Mass of particle moisture (kg)
M_p	Total mass of particle (kg)
$M_{volatile}$	Mass of particle volatile (kg)
Q_{char}	Heat transfer due to pyrolysis and heterogenous reactions (W)
$Q_{moisture}$	Heat transfer due to drying (W)
p	Pressure (Pa)
Pr	Prandtl number (-)
Re_p	Particle Reynolds number (-)
$r_{diff,i}$	Rate of diffusion of chemical species i (mol s^{-1})
$r_{kin,i}$	Rate of reaction of chemical species i (mol s^{-1})
S_h	Enthalpy source due to homogenous reactions (W m^{-3})
$S_{p,h}$	Enthalpy source due to drying, heterogenous and pyrolysis reactions (W m^{-3})
S_m	Momentum source term (N m^{-3})
S_{rad}	Enthalpy source due to radiation (W m^{-3})
S_{p,y_i}	Chemical species source due to drying, pyrolysis, and heterogenous reactions (kg m^{-3} s^{-1})
S_{y_i}	Chemical species source due to homogenous reactions (kg m^{-3} s^{-1})
S_ρ	Mass source term (kg m^{-3} s^{-1})
$\mathbf{T}$	Torque on particle (N m)
T_p	Temperature of particle (K)
T_g	Temperature of gas phase (K)
t	Time (s)
$\mathbf{U}_g$	Velocity of gas phase (m/s)
$\mathbf{U}_n$	Normal velocity of particle (m s^{-1})
$\mathbf{U}_p$	Velocity of particle (m/s)
$\mathbf{U}_t$	Tangential velocity of particle (m s^{-1})
$\mathbf{U}_r$	Relative velocity between particles (m s^{-1})
V_p	Particle volume (m^3)
ω	Angular velocity (rad/s)
β	Coefficient of interphase momentum exchange (kg m^{-3} s^{-1}))
ε_p	Particle fraction (-)
ε_g	Gas phase fraction (-)
ρ_g	Particle density (kg m^{-3})
ρ_i	Density of chemical species i (kg m^{-3})
μ_g	Gas phase viscosity (kg m^{-1} s^{-1})

k	Stiffness coefficient (N m^{-1})
η	Damping coefficient (kg s^{-1})
μ_f	Friction coefficient (-)
$\boldsymbol{\tau}$	Effective stress tensor (Pa)
α_{eff}	Effective thermal diffusivity (kg m^{-1} s^{-1})

Acknowledgement

This research was supported by Southeastern Sun Grant Center and the US Department of Transportation, Research and Innovative Technology Administration, Grant No. DTO559-07-G-00050.

References

1. Stevens, D. J., Hot gas conditioning: recent progress with larger-scale biomass gasification systems. *NREL Subcontractor Report (NREL/SR-510-29952)* **2001**.
2. Aljbour, S. H.; Kawamoto, K., Bench-scale gasification of cedar wood – Part II: Effect of Operational conditions on contaminant release. *Chemosphere* **2013,** *90* (4), 1501-1507.
3. Broer, K. M.; Woolcock, P. J.; Johnston, P. A.; Brown, R. C., Steam/oxygen gasification system for the production of clean syngas from switchgrass. *Fuel* **2015,** *140*, 282-292.
4. Woolcock, P. J.; Brown, R. C., A review of cleaning technologies for biomass-derived syngas. *Biomass and Bioenergy* **2013,** *52* (1), 54-84.
5. Abdoulmoumine, N.; Adhikari, S.; Kulkarni, A.; Chattanathan, S., A review on biomass gasification syngas cleanup. *Appl Energ* **2015,** *155* (1), 294-307.
6. Pepiot, P.; Dibble, C. J.; Foust, T. D., Computational fluid dynamics modeling of biomass gasification and pyrolysis. In *Computational Modeling in Lignocellulosic Biofuel Production*, 1st ed.; American Chemical Society: 2010; Vol. 1052, pp 273-298.
7. Gidaspow, D., *Multiphase flow and fluidization: continuum and kinetic theory descriptions*. Academic press: 1994.
8. Ku, X.; Li, T.; Løvås, T., CFD–DEM simulation of biomass gasification with steam in a fluidized bed reactor. *Chemical Engineering Science* **2015,** *122*, 270-283.
9. Liu, H.; Elkamel, A.; Lohi, A.; Biglari, M., Computational fluid dynamics modeling of biomass gasification in circulating fluidized-bed reactor using the Eulerian–Eulerian approach. *Ind. Eng. Chem. Res.* **2013,** *52* (51), 18162-18174.
10. Maffei, T. Kinetics of Coal Combustion. Politecnico di Milano, Milano, Italy, 2013.
11. Ströhle, J.; Chen, X.; Zorbach, I.; Epple, B., Validation of a detailed reaction mechanism for sulfur species in coal combustion. *Combustion Science and Technology* **2014,** *186* (4-5), 540-551.
12. Müller, M.; Schnell, U.; Scheffknecht, G., Modelling the fate of sulphur during pulverized coal combustion under conventional and oxy-fuel conditions. *Energy Procedia* **2013,** *37*, 1377-1388.
13. Oevermann, M.; Gerber, S.; Behrendt, F., Euler–Lagrange/DEM simulation of wood gasification in a bubbling fluidized bed reactor. *Particuology* **2009,** *7* (4), 307-316.
14. Oyedeji, O.; Daw, C. S.; Labbe, N.; Ayers, P.; Abdoulmoumine, N., Kinetics of the release of elemental precursors of syngas and syngas contaminants during devolatilization of switchgrass. *Bioresource Technology* **2017,** *244*, 525-533.
15. Meng, X.; De Jong, W.; Fu, N.; Verkooijen, A. H., Biomass gasification in a 100 kWth steam-oxygen blown circulating fluidized bed gasifier: Effects of operational conditions on product gas distribution and tar formation. *Biomass and Bioenergy* **2011,** *35* (7), 2910-2924.

16. Cui, H.; Turn, S. Q.; Keffer, V.; Evans, D.; Tran, T.; Foley, M., Contaminant estimates and removal in product gas from biomass steam gasification. *Energy Fuels* **2010,** *24* (2), 1222-1233.
17. Kulkarni, A.; Baker, R.; Abdoulmomine, N.; Adhikari, S.; Bhavnani, S., Experimental study of torrefied pine as a gasification fuel using a bubbling fluidized bed gasifier. *Renewable Energy* **2016,** *93*, 460-468.
18. Ku, X.; Li, T.; Løvås, T., Eulerian–lagrangian simulation of biomass gasification behavior in a high-temperature entrained-flow reactor. *Energy Fuels* **2014,** *28* (8), 5184-5196.
19. Wu, Y.; Zhang, Q.; Yang, W.; Blasiak, W., Two-dimensional computational fluid dynamics simulation of biomass gasification in a downdraft fixed-bed gasifier with highly preheated air and steam. *Energy Fuels* **2013,** *27* (6), 3274-3282.
20. Miao, Z.; Grift, T. E.; Hansen, A. C.; Ting, K. C., Energy requirement for comminution of biomass in relation to particle physical properties. *Industrial Crops and Products* **2011,** *33* (2), 504-513.
21. Oyedeji, O.; Fasina, O., Impact of drying-grinding sequence on loblolly pine chips preprocessing effectiveness. *Industrial Crops and Products* **2017,** *96* (1), 8-15.

CHAPTER VIII
DISSERTATION CONCLUSIONS AND RECOMMENDATIONS

Conclusions

The overall objective of this dissertation was to identify the formation behavior of inorganic contaminants of biomass-derived producer gas and develop relevant modeling tools to predict their formation. Special attention was devoted to the yields of NH_3, HCN, H_2S, and COS because they are the most abundant inorganic contaminants found in biomass-derived producer gas. The formation of major producer gas composition (CO, CO_2, H_2, and CH_4) were also investigated as an attendant benefit of the study approach used in this dissertation. Five different studies were carried out to achieve the objectives of this dissertation and the conclusions reached are as follows:

1. A comprehensive picture of the release of elemental precursors of producer gas and contaminants during the pyrolysis step of biomass gasification was presented in Chapter 3. The analysis of the total mass loss measurements revealed two distinct stages. The first stage was ascribed to moisture and extractive conversion whereas the second stage was ascribed to cellulose, hemicellulose, and lignin decomposition. The estimates for the kinetic parameters varied with temperature due to the activation of different chemical reactions at the different temperatures. Kinetics modeling shows that non-first-order Arrhenius reaction kinetics fit the observed conversion rates for total volatiles and biomass elements. However, the order of reaction approached first-order as temperature was increased from 600 to 800 °C.

2. The formation of the major producer gas composition (CO, CO_2, and H_2, except CH_4) was equilibrium controlled, hence can be predicted using equilibrium models. However, the formation of inorganic contaminants (NH_3, HCN, H_2S, and COS) was kinetics controlled. This means that the formation of NH_3, HCN, H_2S, and COS is more depended on gasification process variables than the formation of CO, CO_2, and H_2. Therefore, multiscale modeling tools involving kinetic models (such as computational fluid dynamics and discrete element method (CFD-DEM)) are needed to adequately capture the formation of NH_3, HCN, H_2S, and COS. The formation of nitrogen containing contaminants is thermodynamically influenced by $HCN + H_2O \leftrightarrow NH_3 + CO$. Likewise, the formation of sulfur containing contaminants is thermodynamically influenced by $H_2S + CO_2 \leftrightarrow COS + H_2O$ reaction.

3. The proposed CFD-DEM model described in Chapter 5 of this work, despite the assumption of quasi-three-dimensional flow and homogeneous particle size, can accurately predict the hydrodynamic behavior of gas-solid flow inside an inert fluidized bed system. Therefore, can be coupled with thermal and chemical reaction models in future work to present a comprehensive modeling tool for describing bioenergy processing in a fluidized bed.

4. The developed CFD-DEM model provides information on the physical, thermal, and chemical flow pattern inside the reactor. Additionally, the model tracked the position and chemical composition of each biomass particle through its residence inside the reactor and compare the predict gas species to experimental data qualitatively and quantitatively. The predicted concentrations of H_2, CH_4, CO, and CO_2 closely fits corresponding experimental data obtained from literature. Similarly, the predicted NH_3 concentration, with mean absolute error of 92.50 ppm, provides a reasonable comparison to experimental data. The prediction was closer to the experimental upper confidence bound (95%). The predicted HCN concentration was about 30 - 50% lower than corresponding experimental data, suggesting over-consumption of HCN in the CFD-DEM model.

5. In our analysis, we demonstrated that the CFD-DEM predicted yield of hydrogen sulfide during biomass gasification reasonably follows experimental data reported in literature. The concentration of hydrogen sulfide was directly proportional to temperature, but inversely proportional to ER. The concentration of sulfur dioxide decreased with rising temperature and increased with rising ER. However, the concentration of carbonyl sulfide increased with rising temperature and ER. Additionally, the proposed model can track the particle properties and flow pattern throughout the simulation domain. Hence, we were able to evaluate the effects of temperature and ER on the particle residence time. The augmentation of gasification temperature and ER caused faster entrainment of biomass particles from the reactor.

Recommendations

The collection of studies in this dissertation provides relevant information and tools for understanding the formation of inorganic contaminant species (mainly NH_3, HCN, H_2S, and COS) during biomass gasification. Nevertheless, there still exist several research gaps and opportunities, which need to be addressed regarding this subject area. To inform future research studies in this subject area, we will highlight the research gaps and opportunities we identified during the implementation of the experimental and simulation studies in this dissertation.

Tracking and modeling properties of biomass solid during biomass pyrolysis and char-gasification

In the first study, we tracked the conversion profile for the major chemical elements of switchgrass during the pyrolysis stage of biomass gasification. This study provided relevant insight into the extent and rate of conversion for major chemical elements of switchgrass. However, there is an excepted simultaneous change in the physio-thermal properties of biomass particles during pyrolysis and char-gasification, which was not captured in this study. The development of a robust model to describe how the particle properties such as size, shape, density, specific heat capacity, and emissivity change during pyrolysis and char-gasification will

significantly enhance the prediction accuracy of multiscale simulation tools. The collection of relevant modeling data can be achieved by utilizing the simple thermo-gravimetric procedure used in this work coupled with appropriate testing equipment such as pycnometers, particle size and shape analyzer, and differential thermal analyzer.

Development of temperature specific pyrolysis mechanism

The results from the first study also shows that the conversion rate and extent for the chemical elements in switchgrass (C, H, N, O, S) were temperature specific. Additionally, it was observed that biomass pyrolysis exhibits a non-first-order Arrhenius kinetics behavior within the temperatures considered (600 – 800 °C). However, the deviation of the pyrolysis kinetics from first-order Arrhenius kinetics decreased with increasing temperature. This suggest that the mechanisms of the chemical bond cleavage and formation during the pyrolysis stage of biomass gasification is highly dependent on temperature and higher temperature pyrolysis may exhibit first-order Arrhenius kinetics behavior. There are two important research questions that need to be answered here. First, is whether the mechanism of reaction during pyrolysis is temperature specific? Second, is the rate of pyrolysis at temperature above 800 °C approximately first-order?

Quantify the kinetic parameter for the formation of H_2S, COS, NH_3, and HCN during pyrolysis

This study show that pyrolysis is important to the overall conversion of biomass-nitrogen and -sulfur. Up to about 66% and 80% of biomass-nitrogen and -sulfur can be released into the gas phase during pyrolysis. Although this study provided kinetic information on the release of biomass-nitrogen and -sulfur, it did not explicitly quantify the distribution of specific species. Hence, there are still no available kinetic information for describing the formation of the major nitrogen and sulfur species (NH_3, HCN, H_2S, and COS) during the pyrolysis stage of gasification. It would be beneficial to explore thermo-gravimetric methods coupled with gas analyzers (such as gas chromatography and mass spectrometer) to quantify and model the release of NH_3, HCN, H_2S, and COS during the pyrolysis stage of biomass gasification.

Establish models to describe deviation from thermodynamic equilibrium

In the second study, we demonstrated that the yields of CO, CO_2, and H_2 during gasification are comparable to thermodynamic equilibrium expectations. However, the yields of CH_4 and contaminant species (NH_3, HCN, H_2S, and COS) were more kinetically limited, hence deviate from thermodynamic equilibrium expectations. Nevertheless, we found that the equilibrium model was computationally inexpensive and able to accurately predict the relationships between the yield of each species and operating variable. It is therefore imperative to leverage the good qualities of equilibrium modeling by developing robust models capable of accounting for the deviation between real systems and thermodynamically equilibrium system. Machine learning algorithm like neural network and decision trees are possible tools

for developing such deviation model, which has the potential to improve the prediction accuracy of the equilibrium model.

Chemical mechanism and kinetics parameter tuning

Presenting a complete picture of biomass gasification mechanisms and identifying appropriate kinetics parameters would be a substantial and positive addition to the field of biomass gasification. Based on literature review and our experience implementing the experimental and simulation works in this dissertation, it appears that it is unviable to draw the complete picture of all chemical mechanisms during biomass gasification via experimental studies. This is because of several limitations ranging from high cost, safety concerns, and operational impracticality to process complexity and technological deficiencies of sensors. We therefore would recommend developing an approximate overall picture of biomass gasification via synergy of experimental and CFD-DEM simulation works. This will involve manual construction of an exhaustive list of chemical mechanisms with wide ranges of kinetics parameters. Then validating each set of mechanism and kinetic parameter by statistically comparing the CFD-DEM prediction to experimentally measured data.

VITA

Oluwafemi A. Oyedeji is from Ekiti State, Nigeria. He earned his B.Eng. in Agricultural Engineering from the Federal University of Technology, Akure in 2011. He then received his M.S. degree in Biosystems Engineering from Auburn University in 2015 under the supervision of Dr. Oladiran Fasina. His M.S. thesis was focused on the effects of drying and storage process on the grindability of woody biomass. After that, He joined Dr. Erin Webb's group at the Energy and Environmental Sciences Division of Oak Ridge National Laboratory as a post-masters researcher. He studied the field drying potential of corn stover for bioenergy production during this period. He was a PhD student in the Department of Biosystems Engineering and Soil Science at the University of Tennessee. There, he worked on understanding the formation of syngas contaminants during biomass gasification. His research interests include biomass characterization and preprocessing, and cost-effective thermo-chemical conversion of biomass to transportation fuels, chemicals, and materials. He is a member of the American Society of Agricultural and Biological Engineers and the Nigerian Institution of Agricultural Engineers.